

Universidade do Minho
Escola de Engenharia

Paulo Jorge da Rocha Soares Antunes

Constitutive Modelling of Cork-Polyurethane Gel Composites

Tese de Doutoramento
Engenharia de Polímeros / Ciência de Materiais Poliméricos

Trabalho efectuado sob a orientação do
Doutor Gustavo Alexandre O. Rodrigues Dias

Co-Orientador
Engenheiro José António Teixeira Coelho

Dezembro de 2008

This page is intentionally left blank.

Agradecimentos

A primeira palavra de agradecimento vai dirigida à minha família e amigos, cujo apoio foi fundamental para a conclusão deste trabalho, tendo servido de motivação adicional para ultrapassar os momentos de maior desânimo.

Aos meus orientadores, Doutor Gustavo Rodrigues Dias e Engenheiro António Teixeira Coelho, envio uma sincera palavra de agradecimento, pela forma como souberam orientar e coordenar o meu trabalho.

Aos docentes e funcionários do DEP - Departamento de Engenharia de Polímeros da Universidade do Minho, em particular ao Doutor João Pedro Nunes e ao Professor António Magalhães da Cunha, dirigo uma palavra de apreço pessoal.

Gostaria de dirigir uma palavra de agradecimento ao Doutor Rui Magalhães, Director Geral do PIEP - Pólo de Inovação em Engenharia de Polímeros, por ter facilitado a utilização das instalações e equipamentos informáticos da instituição, durante o último ano do plano de trabalhos. Agradeço também a todos os colaboradores do PIEP a forma como me receberam e colaboraram comigo.

Ao Dr. Victor Hugo, Dr. Tiago Pereira e Professor Francisco Rebelo agradeço o apoio técnico prestado durante a modelação FEM do pé, nomeadamente a disponibilização dos meios técnicos necessários à sua realização.

A todos os colaboradores da ACC - Amorim Cork Composites, que partilharam comigo os últimos quatro anos de trabalho, gostaria de agradecer a disponibilidade que sempre demonstraram e o interesse que depositaram no meu trabalho.

Gostaria de agradecer o apoio financeiro concedido pela FCT - Fundação para a Ciência e a Tecnologia, através da Bolsa de Doutoramento em Empresa SFHR/BDE/15526/2004, e pela ACC - Amorim Cork Composites.

Uma última palavra de agradecimento a todas as pessoas que durante a minha vida profissional colaboraram comigo e souberam partilhar experiência e conhecimento.

Paulo Antunes

This page is intentionally left blank.

Abstract

Constitutive Modelling of Cork-Polyurethane Gel Composites

The CPGC - Cork-Polyurethane Gel Composite is a rubber-like material produced by ACC-Amorim Cork Composites. The non-conventional combination of cork with polyurethane gel results in a composite material with particular mechanical characteristics that must be clearly understanded for potentiate new applications or optimize products already produced with CPGC. The application of CPGC in products such as comfort enhancement devices and vibration damping or other applications, must be supported by Computer Aided Enginnering (CAE) tools, that can predict the mechanical response of the CPGC and its adequacy for particular loading case scenarios.

The mechanical behaviour of the CPGC was evaluated from experimental tests conducted at different temperatures, that furnished crucial information for the constitutive modelling procedure. From the experimental tests was possible to conclude that CPGC is mechanically characterized by a nonlinear elastic behaviour at large deformations (hyperelastic behaviour) and a dissipative behaviour evidenced by the hysteretic effect that occurs during loading-unloading cycles.

The nonlinear elastic behaviour was modelled by hyperelastic constitutive models based on phenomenological strain energy functions what enabled a structured framework for CPGC's material modelling. A new methodology for modelling hysteretic cycles and consequent material heat build-up, is proposed in this work. This proposed methodology accounts separately the dissipative effects arising from purely deviatoric and volumetric deformations.

The calibration of material parameters and the development of specific material subroutines for the modelling of the CPGC's mechanical behaviour, allowed a more versatile way of simulate the material mechanical behaviour through the use of the Finite Element Method (FEM/FEA).

In order to simulate the mechanical response of the CPGC in real case applications, two case-studies were modelled during this work. The first case-study corresponds to a anatomically detailed FEM model of the human foot. This model is a tool for evaluating the mechanical performance of CPGC shoe insoles, through the monitoring of the contact pressure (normal stress) values at the insole/foot interface. The second case-study corresponds to an initial approach in the modelling of hysteretic cycles and consequent material heat build-up during cyclic loading, applying nonlinear FEM techniques. Within this context the specifically developed material user subroutines assumed a particular importance for the modelling of the CPGC's mechanical behaviour.

Resumo

Modelação Constitutiva de Materiais Compósitos de Cortiça com Matriz em Gel de Poliuretano

O CPGC - *Cork-Polyurethane Gel Composite* é um material *rubber-like* produzido em Portugal pela ACC-Amorim Cork Composites. A combinação não convencional de cortiça com gel de poliuretano traduz-se na obtenção de um material compósito com características mecânicas particulares. Estas características devem ser estudadas e compreendidas de forma a potenciar novas aplicações em CPGC ou a optimização do desempenho mecânico de componentes já produzidos em CPGC. A aplicação de CPGC em produtos tais como dispositivos de conforto, amortecimento de vibrações e outros, deverá ser suportada por ferramentas de engenharia assistida por computador (CAE) que permitam prever a resposta mecânica do CPGC e a sua adequabilidade a casos particulares de carregamento mecânico.

O comportamento mecânico do CPGC foi avaliado através de ensaios experimentais, tendo sido consideradas diferentes temperaturas de ensaio. Esta informação foi crucial para o desenrolar do processo de modelação constitutiva do material. Através dos resultados experimentais obtidos foi possível concluir que o CPGC é um material caracterizado mecanicamente por um comportamento elástico não-linear a grandes deformações (comportamento hiperelástico) e por um comportamento dissipativo, evidenciado pelo efeito histerético originado pelos ciclos de carregamento e descarregamento.

O comportamento elástico não-linear foi modelado através de modelos constitutivos hiperelásticos baseados em funções fenomenológicas de energia de deformação. Uma nova metodologia para a modelação de ciclos histeréticos e consequente geração interna de calor, é proposta no presente trabalho. Através desta metodologia é possível separar os efeitos de desvio e volumétricos na resposta dissipativa do material, decorrentes do processo de

deformação cíclica do CPGC.

A calibração de parâmetros de material dos modelos constitutivos e o desenvolvimento de sub-rotinas específicas para a modelação do comportamento mecânico do CPGC, permitiram uma mais versátil forma de simular o comportamento do material através do Método dos Elementos Finitos (FEM/FEA).

Com o objectivo de simular a resposta mecânica do CPGC em potenciais aplicações prácticas, foram considerados dois casos de estudo no presente trabalho. O primeiro caso, corresponde a um modelo FEM de um pé, considerando na sua modelação um elevado detalhe anatómico. Este modelo servirá como ferramenta de avaliação do desempenho mecânico de palmilhas de CPGC, através da monitorização dos valores de pressão do contacto (tensão normal à superfície de contacto) na interface palmilha/pé. O segundo caso de estudo corresponde a uma primeira aproximação à modelação FEM de ciclos histeréticos originados por solicitações cíclicas de carregamento. Neste contexto, a implementação de subrotinas de comportamento material especificamente desenvolvidas para modelação do comportamento histerético do CPGC, assume um papel particularmente importante.

Table of Contents

List of Figures **xiii**

List of Tables **xxi**

List of Algorithms **xxiii**

List of Symbols **xxv**

1 Introduction **1**

1.1 Outline of the thesis 3

2 State of the Art **5**

2.1 Overview of Continuum Mechanics 5

2.1.1 Kinematics 6

2.1.1.1 Configuration 6

2.1.1.2 Motion 7

2.1.1.3 Displacement 8

2.1.1.4 Deformation gradient 8

2.1.1.5 Displacement gradient 11

2.1.1.6 Jacobian determinant 11

2.1.1.7 Finite strain tensors 12

2.1.1.8 Polar decomposition 14

2.1.1.9 Eigenvalues and eigenvectors of strain tensors 15

2.1.2 Stress 16

2.1.2.1 Stress tensors 16

2.1.2.2 Alternative stress tensors 18

2.1.3 Balance equations 19

2.1.3.1 Mechanical balance 19

2.1.3.2 Thermomechanical balance . . . 22
2.2 Constitutive equations . . . 24
2.2.1 Hyperelasticity . . . 24
2.2.2 Isotropic hyperelasticity . . . 26
2.2.3 Incompressible hyperelastic materials . . . 30
2.2.4 Isotropic incompressible hyperelasticity . . . 31
2.2.5 Compressible hyperelasticity . . . 33
2.2.6 Compressible hyperelasticity in terms of invariants . . . 35
2.3 Strain energy functions . . . 37
2.3.1 Phenomenological models . . . 37
2.3.1.1 Rivlin's polynomial model . . . 37
2.3.1.2 Reduced polynomial form . . . 39
2.3.1.3 Gent model . . . 40
2.3.1.4 Ogden model . . . 40
2.3.1.5 Valandis and Landel hypothesis . . . 41
2.3.1.6 Varga model . . . 41
2.3.1.7 Hyperfoam model . . . 42
2.3.1.8 Blatz and Ko model . . . 42
2.3.2 Physical models . . . 42
2.3.2.1 Arruda and Boyce model . . . 42
2.3.2.2 Van der Waals model . . . 43
2.4 Modelling hysteresis . . . 43
2.4.1 Pseudo-elasticity theory . . . 45
2.4.1.1 Isotropic material's behaviour . . . 46
2.4.1.2 Pseudo-elastic behaviour . . . 47
2.4.1.3 Modelling the hysteretic cycle (uniaxial compression case) 48
2.5 Heat generation . . . 51

3 New Formulations 55
3.1 Modelling hysteresis in nonlinear elastic materials with deviatoric and volumetric dissipative behaviour . . . 55
3.1.1 Specialization to isotropic pseudo-elasticity . . . 59
3.1.1.1 Simple uniaxial compression case (unconfined deformation) 61
3.1.1.2 Uniaxial volumetric compression case (confined deformation) . . . 62
3.1.2 Modelling the hysteretic cycle . . . 63
3.1.2.1 Simple uniaxial compression cycle (unconfined deformation) 66
3.1.2.2 Volumetric deformation cycle (confined deformation) . . . 69

3.1.3 Modified Dorfmann-Ogden model 70
3.1.4 Modified Zúñiga model 71
3.2 Modelling heat generation in nonlinear elastic materials 72
3.2.1 Heat build-up modelling 73

4 Constitutive Modelling **75**
4.1 Experimental methodology and results 76
4.1.1 Simple uniaxial compression 76
4.1.1.1 Simple uniaxial compression results (loading path) 76
4.1.1.2 Simple uniaxial compression results (loading-unloading path) 80
4.1.2 Volumetric compression 83
4.1.2.1 Volumetric compression results (loading path) 83
4.1.2.2 Volumetric compression results (loading-unloading path) . 84
4.2 Material parameters fitting 85
4.2.1 Fitting the loading path 86
4.2.1.1 Simple uniaxial compression stress 86
4.2.1.2 Volumetric compression stress 88
4.2.1.3 Numerical fitting procedure 89
4.2.2 Interpolation of material parameters 102
4.2.2.1 Simple uniaxial compression behaviour 102
4.2.2.2 Volumetric compression behaviour 105
4.2.3 Modelling the hysteretic cycle 107
4.2.3.1 Unconfined deformation hysteretic cycle (purely deviatoric behaviour) 108
4.2.3.2 Confined deformation hysteretic cycle (purely volumetric behaviour) 115
4.3 Constitutive modelling implementation 118
4.3.1 Modelling the loading path 118
4.3.1.1 Simple uniaxial compression case 118
4.3.1.2 Volumetric compression case 125
4.3.2 Modelling hysteretic cycles using a modified pseudo-elasticity theory 129
4.3.2.1 Simple uniaxial compression (unconfined deformation) . . 133
4.3.2.2 Volumetric compression (confined deformation) 136
4.3.3 Modelling heat generation 138
4.3.3.1 Thermomechanical finite element model description 138
4.3.3.2 Thermomechanical FEA results 140

5 Applications/Examples **147**
5.1 Comfort evaluation of CPGC shoe insoles (FE model of the foot) 147
5.1.1 Background 148
5.1.2 3D modelling methodology 149
5.1.2.1 Medical image data generation 150
5.1.2.2 Density segmentation operations 150
5.1.2.3 3D CAD modelling 152
5.1.3 Nonlinear FE foot model definition 153
5.1.3.1 Geometrical definition 153
5.1.3.2 Loads and boundary conditions 154
5.1.3.3 Material properties 155
5.1.4 FEA results 157
5.1.5 Experimental validation 158
5.1.6 Contact stiffness dependence 159
5.1.6.1 Material properties 160
5.1.6.2 FEA results 161
5.1.7 Results discussion 162
5.2 Vibration control 163
5.2.1 FE model 163
5.2.1.1 Material properties 164
5.2.1.2 Loads and boundary conditions 165
5.2.1.3 Mechanical and thermal interactions 166
5.2.2 FEA results 167

6 Conclusions/Further work **171**

Bibliography **173**

List of Figures

1.1 CPGC material detailing a) its visual aspect and b) a practical application in shoe insoles. 1

2.1 Motion of a continuum body 7
2.2 Displacement vector field $\mathbf{U}_d$. 9
2.3 Deformation of a continuum body. 10
2.4 Traction vector acting at the referencial and current configurations of the body. 17
2.5 System of forces acting in the current configuration. 20
2.6 Heat fluxes acting in the current configuration. 23
2.7 Loading-unloading cycle for a hystereric material. 44
2.8 Loading-unloading curves in simple tension, in: Ogden & Roxburgh [1999]. 45
2.9 Pseudo-elastic strain energy function describing the uniaxial mechanical behaviour of a hysteretic material. 50

4.1 Uniaxial nominal stress plotted against nominal strain, considering $T = 23^oC$. 77
4.2 Uniaxial nominal stress plotted against nominal strain, considering $T = 100^oC$. 78
4.3 Uniaxial nominal stress plotted against nominal strain, considering $T = -10^oC$. 78
4.4 Uniaxial nominal stress plotted against nominal strain considering formulation *A,* with $T = 23^oC$, $T = 100^oC$ and $T = -10^oC$. 79
4.5 Uniaxial nominal stress plotted against nominal strain considering formulation *B,* with $T = 23^oC$, $T = 100^oC$ and $T = -10^oC$. 79
4.6 Uniaxial nominal stress plotted against nominal strain considering formulation *F,* with $T = 23^oC$, $T = 100^oC$ and $T = -10^oC$. 80

4.7 Uniaxial loading-unloading cycle obtained for formulation A, considering $T = 23^oC$. 81
4.8 Uniaxial loading-unloading cycle obtained for formulation B, considering $T = 23^oC$. 81
4.9 Uniaxial loading-unloading cycle obtained for formulation D, considering $T = 23^oC$. 82
4.10 Uniaxial loading-unloading cycle obtained for formulation F, considering $T = 23^oC$. 82
4.11 Volume ratio plotted against hydrostatic pressure for formulations of CPGC, considering $T = 23^oC$. 84
4.12 Volumetric (confined deformation) loading-unloading curve for formulation A, considering $T = 23^oC$. 85
4.13 Simple uniaxial compression stress state (unconfined deformation). 87
4.14 Uniaxial volumetric stress compression case (confined deformation). 88
4.15 Fit to the uniaxial compression experimental data from formulation A to the second order polynomial hyperelastic model, considering $T = 23^oC$. . . 91
4.16 Relative error plotted against nominal strain, for the fit of uniaxial compression data from formulation A. 92
4.17 Fit to the uniaxial compression experimental data from formulation B to the second order polynomial hyperelastic model, considering $T = 23^oC$. . . 92
4.18 Relative errors plotted against nominal strain, for the fit of uniaxial compression data from formulation B. 93
4.19 Fit to the uniaxial compression experimental data from formulation D to the second order polynomial hyperelastic model, considering $T = 23^oC$. . . 93
4.20 Relative error plotted against nominal strain, for the fit of uniaxial compression data from formulation D. 94
4.21 Fit to the uniaxial compression experimental data from formulation F to the second order polynomial hyperelastic model, considering $T = 23^oC$. . . 94
4.22 Relative error plotted against nominal strain, for the fit of uniaxial compression data from formulation F. 95
4.23 Effect of the expansion order in the fit of the volumetric experimental data from formulation A to the volumetric polynomial model, considering $N = 2$ and $N = 4$. 97
4.24 Relative error plotted against volume ratio for the fit of volumetric data from formulation A to the volumetric polynomial model, considering $N = 2$ and $N = 4$. 97

4.25 Effect of the expansion order in the fit of the volumetric experimental data from formulation B to the volumetric polynomial model, considering $N = 2$ and $N = 4$. 98
4.26 Relative error plotted against volume ratio for the fit of volumetric data from formulation B to the volumetric polynomial model, considering $N = 2$ and $N = 4$. 99
4.27 Effect of the expansion order in the fit of the volumetric experimental data from formulation C to the volumetric polynomial model, considering $N = 2$ and $N = 4$. 99
4.28 Relative error plotted against volume ratio for the fit of volumetric data from formulation C to the volumetric polynomial model, considering $N = 2$ and $N = 4$. 100
4.29 Tangent bulk modulus plotted against volume ratio for formulations A, B and C, considering $N = 4$. 101
4.30 Deviatoric material parameters C_{ij} plotted against incorporation of cork, considering $T = 23^oC$. 103
4.31 Nominal stress plotted against stretch for interpolated CPGC formulation with 35*php* in cork *(represented with dashed line)*. 103
4.32 Deviatoric strain energy density plotted against stretch for interpolated CPGC formulation with *35php* in cork *(represented with dashed line)*. . . 104
4.33 Deviatoric material parameters C_{ij} plotted against incorporation of cork, considering $T = 100^oC$. 104
4.34 Deviatoric material parameters C_{ij} plotted against incorporation of cork, considering $T = -10^oC$. 105
4.35 Volumetric material parameters D_i plotted against incorporation of cork, considering $T = 23^oC$. 106
4.36 Hydrostatic pressure plotted against volume ratio for interpolated CPGC formulation with 35*php* in cork *(represented with dashed line)*. 106
4.37 Volumetric strain energy density plotted against volume ratio for interpolated CPGC formulation with 35*php* in cork *(represented with dashed line)*. 107
4.38 Modelling the uniaxial (unconfined deformation) hysteretic cycle of formulation *A,* considering a) the modified Dorfmann-Ogden model and b) the modified Zúñiga model. 109
4.39 Relative error plotted against nominal strain for the fit of uniaxial data from formulation A to the modified Dorfmann-Ogden and Zúñiga models. . 109

4.40 Modelling the uniaxial (unconfined deformation) hysteretic cycle of formulation *B,* considering a) the modified Dorfmann-Ogden model and b) the Modified Zúñiga model. 110
4.41 Relative error plotted against nominal strain for the fit of uniaxial data from formulation *B* to the modified Dorfmann-Ogden and Zúñiga models. . 110
4.42 Modelling the uniaxial (unconfined deformation) hysteretic cycle of formulation *D,* considering a) the Dorfmann-Ogden model and b) the Zúñiga model. 111
4.43 Relative error plotted against nominal strain for the fit of uniaxial data from formulation *D* to the modified Dorfmann-Ogden and Zúñiga models. . 111
4.44 Modelling the uniaxial (unconfined deformation) hysteretic cycle of formulation *F,* considering a) the modified Dorfmann-Ogden model and b) the modified Zúñiga model. 112
4.45 Relative error plotted against nominal strain for the fit of uniaxial data from formulation *F* to the modified Dorfmann-Ogden and Zúñiga models. . 112
4.46 Plot of the pseudo-energy function against the nominal strain during loading-unloading cycle, considering formulation *A* at $T = 23^oC$. 113
4.47 Plot of the pseudo-energy function against the nominal strain during loading-unloading cycle, considering formulation *B* at $T = 23^oC$. 114
4.48 Plot of the pseudo-energy function against the nominal strain during loading-unloading cycle, considering formulation *D* at $T = 23^oC$. 114
4.49 Plot of the pseudo-energy function against the nominal strain during loading-unloading cycle, considering formulation *F* at $T = 23^oC$. 115
4.50 Modelling the volumetric (confined deformation) hysteretic cycle of formulation *A*, considering a) the Dorfmann-Ogden model and b) the Zúñiga model. 116
4.51 Relative error plotted against nominal strain for the fit of volumetric data from formulation *A* to the modified Dorfmann-Ogden and Zúñiga models. . 116
4.52 Plot of the pseudo-energy function against the volume ratio during a loading-unloading (confined deformation) cycle considering formulation *A* at $T = 18^oC$. 117
4.53 Axisymetrical FE model (simple uniaxial compression case). 118
4.54 Nodal axial displacement FEA values (mm) obtained for the simple uniaxial compression case. 119
4.55 Comparison of FEA results with uniaxial compression experimental data from formulation *A*, considering $T = 23^oC$. 120

4.56 Comparison of FEA results with uniaxial compression experimental data from formulation *B*, considering $T = 23^oC$. 120
4.57 Comparison of FEA results with uniaxial compression experimental data from formulation *D*, considering $T = 23^oC$. 121
4.58 Comparison of FEA results with uniaxial compression experimental data from formulation *F*, considering $T = 23^oC$. 121
4.59 Comparison of FEA results with uniaxial compression experimental data from formulation *A*, considering $T = 100^oC$. 122
4.60 Comparison of FEA results with uniaxial compression experimental data from formulation *B*, considering $T = 100^oC$. 123
4.61 Comparison of FEA results with uniaxial compression experimental data from formulation *F*, considering $T = 100^oC$. 123
4.62 Comparison of FEA results with uniaxial compression experimental data from formulation *A*, considering $T = -10^oC$. 124
4.63 Comparison of FEA results with uniaxial compression experimental data from formulation *B*, considering $T = -10^oC$. 124
4.64 Comparison of FEA results with uniaxial compression experimental data from formulation *F*, considering $T = -10^oC$. 125
4.65 Boundary conditions applied to the hexahedral finite element for reproducing a volumetric (confined) deformation state. 127
4.66 FEA results obtained for formulation *A,* considering $N_{vol} = 2$ and $N_{vol} = 4$, plotted against volumetric deformation experimental data at $T = 23^oC$. . . 128
4.67 FEA results obtained for formulation *B,* considering $N_{vol} = 2$ and $N_{vol} = 4$, plotted against volumetric deformation experimental data at $T = 23^oC$. . . 128
4.68 FEA results obtained for formulation *C,* considering $N_{vol} = 2$ and $N_{vol} = 4$, plotted against volumetric deformation experimental data at $T = 23^oC$. . . 129
4.69 Boundary conditions defined to simulate loading-unloading uniaxial compression cycles. 130
4.70 FEA results plotted against experimental data considering a total loading-unloading compression cycle. 134
4.71 Pseudo-energy plotted against nominal strain, considering simultaneously numerical data obtained from the fitting process and FEA data. 135
4.72 Deviatoric and volumetric dissipation factors plotted against nominal strain, considering a uniaxial (unconfined) compression case. 135
4.73 FEA results plotted against experimental data considering a total loading-unloading volumetric compression cycle. 136

4.74 Pseudo-energy plotted against volume ratio considering simultaneously numerical data obtained from the fitting process and FEA data. 137
4.75 Deviatoric and volumetric dissipation factors plotted against volume ratio considering a volumetric deformation state. 137
4.76 Nominal stress plotted against nominal strain for formulation *A,* considering a nested cycle loading condition. 140
4.77 Material temperature plotted against simulation time for 10 loading-unloading cycles, considering $f = 1Hz$ *(models 1 and 2).* 141
4.78 Material temperature plotted against simulation time for 10 loading-unloading cycles, considering $f = 10Hz$ *(models 4 and 5).* 141
4.79 Material temperature plotted against simulation time for 10 loading-unloading cycles, considering $f = 100Hz$ *(models 8 and 9).* 142
4.80 Temperature plotted against simulation time considering multiple loading-unloading cycles, for $f = 1Hz$, $f = 10Hz$ and $f = 100Hz$ *(models 2, 7 and 11).* 143
4.81 Temperature plotted against simulation time considering multiple and nested loading-unloading cycles, for $f = 1Hz$ *(models 2 and 3).* 143
4.82 Temperature plotted against simulation time considering multiple and nested loading-unloading cycles, for $f = 10Hz$ *(models 5 and 6).* 144
4.83 Temperature plotted against simulation time considering multiple and nested loading-unloading cycles, for $f = 100Hz$ *(models 9 and 10).* 144
4.84 Nominal stress plotted against nominal strain for multiple cycles ($f = 10Hz$), considering the effect of temperature on the material parameters C_{ij}.146
4.85 Temperature plotted against time for multiple loading-unloading cycles ($f = 10Hz$), considering thermal and no thermal effect on the material parameters C_{ij}. 146

5.1 Modelling methodology applied in the FE model definition. 149
5.2 Medical image data aquisition detailing a) the CT scan equipment and b) a CT scan medical image. 150
5.3 Density segmentation masks detailing a) sagittal view and b) coronal view. 151
5.4 Density segmentation 3D models considering a) the bone structure and b) the soft tissues volume. 151
5.5 Density segmentation model incorporating both bone structure and soft tissues volume. 152
5.6 Final CAD models detailing a) bone and cartilaginous structure and b) encapsulated soft tissues volume, bone and cartilaginous structure. 152

5.7 Mesh discretization of the foot geometry with a) corresponding to the volumetric meshes of bone and cartilaginous structure and b) to the encapsulated soft tissues. 153
5.8 FE modelling procedures detailing a) plantar fascia modelling through the definition of truss elements and b) modelling of Achilles tendon incorporating axial connector elements. 154
5.9 Balanced standing loading case scheme. 154
5.10 Soft tissues nonlinear mechanical behaviour obtained from *in vivo* experimental tests of the heel pad in: Lemmon *et al.* [1997]. 156
5.11 Foot plantar contact pressure values (MPa) obtained through FE analysis. 157
5.12 von Mises stress criteria at the bone structure detailing a) upper view and b) posterior view. 158
5.13 Experimental measuring of foot plantar contact pressure values detailing a) the podologic pressure measuring equipment and b) the experimentally obtained foot plantar contact pressure values. 159
5.14 Foot FE model with incorporation of a CPGC flat insole. 160
5.15 Nodal contact pressure values beneath the 1^{st} metatarsal head plotted against insole thickness. 161
5.16 Foot plantar contact area plotted against insole thickness. 162
5.17 FE model assembly with indication of the principal parts. 164
5.18 Mechanical boundary conditions applied in the definition of the FE model. 166
5.19 Nodal axial displacement FEA values (mm). 166
5.20 Reaction force values obtained for FE model 1 plotted against nodal displacement *(model 1)*. 167
5.21 Final nodal temperatures obtained in the material sample detailing a) facet temperature and b) internal temperature (cross-section). 168
5.22 Nodal temperature values plotted against loading time *(model 1)*. 168
5.23 Reaction force plotted against displacement considering the first and the last loading-unloading cycle *(model 2)*. 169
5.24 Temperature at the internal node plotted against loading time, considering thermal and no thermal effect on the material parameters *(models 1 and 2)*. 169

This page is intentionally left blank.

List of Tables

2.1 Transformation of stress tensors. 19
2.2 Representative values of initial modulus ratio and correspondence with initial Poisson's ratio. 30

4.1 CPGC formulations characteristics. 75
4.2 Hysteresis (dissipated energy density per deformation cycle) values for CPGC formulations. 83
4.3 Numerical fit of CPGC uniaxial experimental data, considering $T = 23^oC$. 90
4.4 Numerical fit of CPGC uniaxial experimental data to the second order polynomial model, considering $T = 100^oC$ and $T = -10^oC$. 95
4.5 Deviatoric material parameter values (MPa) for the second order polynomial model, considering $T = 23^oC$. 96
4.6 Deviatoric material parameter values (MPa) for the second order polynomial model, considering $T = 100^oC$. 96
4.7 Deviatoric material parameter values (MPa) for the second order polynomial model, considering $T = -10^oC$. 96
4.8 Mean relative errors considering different polynomial expansion orders. . . 98
4.9 Volumetric material parameters values (MPa^{-1}) for formulation A, considering different polynomial expansion orders. 101
4.10 Volumetric material parameters values (MPa^{-1}) for formulation B, considering different polynomial expansion orders. 101
4.11 Volumetric material parameter values (MPa^{-1}) for formulation C, considering different polynomial expansion orders. 102
4.12 Interpolated deviatoric material parameters (MPa) for a non-tested formulation with $35php$ in cork. 105
4.13 Interpolated volumetric material parameters (MPa^{-1}) for a non-tested formulation with $35php$ in cork. 107

4.14 Material parameters obtained for the modified Dorfmann-Ogden and Zúñiga models, considering a purely deviatoric behaviour. 108
4.15 Mean relative errors for the fit of the uniaxial unloading path, considering the Dorfmann-Ogden and Zúñiga models. 108
4.16 Material parameters obtained for the modified Dorfmann-Ogden and Zúñiga models, considering a purely volumetric behaviour. 115
4.17 Mean relative errors for the fit of the volumetric unloading path considering, the Dorfmann-Ogden and Zúñiga models. 117
4.18 Volumetric material parameter values (MPa^{-1}) for formulation A and correspondent initial Poisson's ratio. 133
4.19 Material thermal properties [Silva *et al.*, 2005] and density applied in the definition of the FE thermomechanical model. 139
4.20 Thermomechanical characteristics of the FE models. 140

5.1 Material properties and element topology/formulation. 156
5.2 Material parameters of the hyperelastic model used for the soft tissues [Cheung *et al.*, 2005]. 157
5.3 FEA nodal contact pressure values (MPa) beneath metatarsal heads and calcaneus bones. 158
5.4 Interpolated material parameter values (MPa) for non-tested CPGC formulations G and H. 161
5.5 Thermomechanical characteristics of the FE models. 164
5.6 Material properties and element topology/formulation. 165
5.7 Material thermal properties [Incropera & DeWitt, 1996] used in the definition of the FE model. 165

List of Algorithms

1 Pseudo-code user subroutine for an independent control of the volumetric polynomial expansion order, N_{vol} 126
2 Pseudo-code for modelling hysteretic cycles 131
3 Pseudo-code for modelling hysteretic cycles (continued) 132
4 Pseudo-code for modelling heat generation 139
5 Pseudo-code for interpolation of material parameters 145

This page is intentionally left blank.

List of Symbols

Roman letters

$\mathbf{b}$	Left Cauchy-Green deformation tensor, *page (13).*
$\mathbf{b}_f$	Body force, *page (19).*
$\mathbf{d}$	Rate of deformation tensor (or strain velocity), *page (21).*
$\mathbf{e}$	Euler-Almansi strain tensor, *page (14).*
$\mathbf{f}$	Force, *page (16).*
$\mathbf{l}$	Spatial velocity gradient, *page (21).*
$\mathbf{n}$	Unit normal vector in the current configuration, *page (16).*
$\mathbf{q}$	heat flux per unit time and current area, *page (23).*
$\mathbf{t}$	Cauchy traction vector, *page (16).*
$\mathbf{u}_d$	Displacement vector in the current configuration, *page (8).*
$\mathbf{v}$	Left stretch tensor, *page (14).*
$\mathbf{v}_f$	Spatial velocity field, *page (21).*
$\mathbf{x}$	Position vector in the current configuration, *page (6).*
a	Parameter of the Van der Waals model, *page (43).*
b	Material parameter of the Zúñiga model, *page (50).*
b_T	Material parameter for the modelling of heat build-up in rubber materials, *page (53).*
b_{dev}	Deviatoric material parameter for the modified Zúñiga model, *page (71).*
b_{vol}	Volumetric material parameter for the modified Zúñiga model, *page (71).*
c	Material parameter for the modelling of heat build-up in rubber materials, *page (53).*

c_1 Material parameter of the Varga model, *page (41).*

c_p Specific heat, *page (139).*

e_a Unit vector set in the current configuration, *page (6).*

f Blatz and Ko interpolation parameter, *page (42).*

f Linear frequency, *page (140).*

h Height, *page (76).*

h_{air} Convection heat transfer coefficient, *page (138).*

h_{con} Thermal conductance, *page (167).*

k Boltzmann's constant, *page (39).*

k_t Thermal conductivity, *page (139).*

l Vector lenght in the current configuration, *page (12).*

m Material parameter for the Dorfmann-Ogden model, *page (49).*

m_{dev} Deviatoric material parameter for the modified Dorfmann-Ogden model, *page (70).*

m_{vol} Volumetric material parameter for the modified Dorfmann-Ogden model, *page (70).*

n Number of molecular chains, *page (39).*

n_a Principal directions at the current configuration, *page (15).*

p Hydrostatic pressure, *page (30).*

p^0 Ummodified hydrostatic pressure, *page (57).*

p_{theo} Theoretical hydrostatic pressure, *page (89).*

r Material parameter for the Dorfmann-Ogden model, *page (49).*

r_h Volumetric heat source, *page (23).*

r_{dev} Deviatoric material parameter for the modified Dorfmann-Ogden model, *page (70).*

r_{vol} Volumetric material parameter for the modified Dorfmann-Ogden model, *page (70).*

s Surface in the current configuration, *page (16).*

t Time, *page (6).*

u Specific internal energy, *page (22).*

v Volume in the current configuration, *page (11).*

v_f Volume fraction of filler, *page (53).*

$\mathfrak{g}$ Response function, *page (25).*

$\mathfrak{p}$ Response function, *page (26).*

$\overline{\mathbf{b}}$ Modified left Cauchy-Green strain tensor, *page (34).*

Capital roman letters

$\mathbb{P}$ Fourth order projection tensor, *page (34).*

$\mathbf{C}$ Right Cauchy-Green deformation tensor, *page (12).*

$\mathbf{E}$ Green-Lagrange strain tensor , *page (13).*

$\mathbf{F}$ Deformation gradient, *page (9).*

$\mathbf{I}$ Identity tensor, *page (11).*

$\mathbf{N}$ Unit normal vector in the reference configuration, *page (16).*

$\mathbf{P}$ First Piola-Kirchhoff (or nominal) stress tensor, *page (16).*

$\mathbf{P}^0$ Unmodified first Piola-Kirchhoff stress tensor, *page (57).*

$\mathbf{P}^0_{dev}$ Deviatoric term of the unmodified first Piola-Kirchhoff stress tensor, *page (57).*

$\mathbf{P}^0_{vol}$ Volumetric term of the unmodified first Piola-Kirchhoff stress tensor, *page (57).*

$\mathbf{P}_E$ Extra stress, *page (30).*

$\mathbf{P}_{dev}$ Deviatoric term of the first Piola-Kirchhoff stress tensor, *page (57).*

$\mathbf{P}_{vol}$ Volumetric (or dilatational) term of the first Piola-Kirchhoff stress tensor, *page (57).*

$\mathbf{Q}$ Proper orthogonal tensor, *page (26).*

$\mathbf{R}$ Rotation tensor, *page (14).*

$\mathbf{S}$ Second Piola-Kirchhoff stress tensor, *page (18).*

$\mathbf{S}_{dev}$ Deviatoric term of the second Piola-Kirchhoff stress tensor, *page (34).*

$\mathbf{S}_{vol}$ Volumetric term of the second Piola-Kirchhoff stress tensor, *page (34).*

$\mathbf{T}$ First Piola-Kirchhoff traction vector, *page (16).*

$\mathbf{T}_B$ Biot stress tensor, *page (18).*

$\mathbf{U}$ Right stretch tensor, *page (14).*

$\mathbf{U}_d$ Displacement vector in the reference configuration, *page (8).*

$\mathbf{X}$ Position vector in the reference configuration, *page (6).*

C_2 Material parameter of the Pucci-Saccomandi model, *page (40).*

C_i Constants of the Arruda-Boyce model, *page (43).*

C_{ij} Deviatoric material parameters of the Rivlin model, *page (38).*

D_i Volumetric material parameters, *page (38).*

E Fit error, *page (86).*

E^* Complex modulus, *page (52).*

E'' Dissipative modulus, *page (52).*

E' Storage modulus, *page (52).*

E_a Unit vector set in the reference configuration, *page (6).*

H Dissipated energy per deformation cycle, *page (51).*

I_1, I_2, I_3 Strain invariants, *page (27).*

J Jacobian determinant (volume ratio), *page (11).*

J_m Material parameter of the Gent model, *page (40).*

J_{max} Volume ratio at the unloading point, *page (68).*

K Bulk modulus, *page (30).*

K_0 Initial bulk modulus, *page (30).*

L Vector lenght in the reference configuration, *page (12).*

N Polynomial expansion order, *page (38).*

N_a Principal directions at the reference configuration, *page (15).*

N_{dev} Polynomial expansion order of the deviatoric term, *page (89).*

N_{vol} Polynomial expansion order of the volumetric term, *page (89).*

O Fixed origin, *page (6).*

P First Piola-Kirchhoff uniaxial stress, *page (48).*

P_{dev} First Piola-Kirchhoff uniaxial deviatoric stress, *page (67).*

P_{test} Experimental nominal stress, *page (86).*

P_{theo} Theoretical nominal stress, *page (86).*

S Surface in the reference configuration, *page (16).*

T Temperature, *page (39).*

T_1 Steady-state temperature, *page (53).*

V Volume in the reference configuration, *page (11).*

V_0 Initial sample's volume, *page (83).*

V_c Current sample's volume, *page (83).*

P Material point (or particle), *page (6).*

X Point in space, *page (6).*

Y Point in space, *page (9).*

$\mathcal{K}$ Kinetic energy, *page (20).*

$\mathcal{P}_{ext}$ External mechanical power, *page (20).*

$\mathcal{P}_{int}$ Internal mechanical power, *page (20).*

$\mathcal{Q}$ Thermal power, *page (22).*

$\mathcal{U}$ Total internal energy, *page (22).*

$\mathfrak{G}$ Response function, *page (25).*

$\overline{\mathbf{C}}$ Modified right Cauchy-Green strain tensor, *page (33).*

$\overline{\mathbf{F}}$ Modified deformation gradient, *page (33).*

$\overline{\mathbf{S}}$ Fictious second Piola-Kirchhoff stress tensor, *page (34).*

$\overline{I}_1, \overline{I}_2, \overline{I}_3$ Modified strain invariants, *page (35).*

Greek letters

ϵ Strain tensor, *page (86).*

$\boldsymbol{\kappa}$ Map function acting on body β, *page (7).*

$\boldsymbol{\kappa}_0$ Map function acting on body β, *page (7).*

$\boldsymbol{\sigma}$ Cauchy (or true) stress tensor, *page (16).*

$\boldsymbol{\sigma}_{dev}$ Deviatoric part of the Cauchy stress tensor, *page (34).*

$\boldsymbol{\sigma}_{vol}$ Volumetric part of the Cauchy stress tensor, *page (34).*

$\boldsymbol{\sigma}^0_{vol}$ Unmodified volumetric part of the Cauchy stress tensor, *page (60).*

$\boldsymbol{\tau}$ Kirchhoff stress tensor, *page (18).*

$\boldsymbol{\chi}$ Motion, *page (7).*

α_i Material parameters of the Ogden model, *page (40).*

β Continuum body, *page (6).*

β_v Parameter of the Van der Waals model, *page (43).*

δ Phase angle, *page (52).*

ϵ_0 Imposed strain amplitude, *page (52).*

ϵ_{rad} Thermal radiation heat transfer coefficient, *page (139).*

ϵ_u Uniaxial nominal strain, *page (50).*

η Internal scalar variable (dissipation factor), *page (45).*

η_{dev} Deviatoric term of the internal scalar variable, *page (56).*

η_{vol} Volumetric term of the internal scalar variable, *page (56).*

η_{dev}^{min} Minimum value for the deviatoric term of the internal scalar variable, *page (69).*

η_{vol}^{min} Minimum value for the volumetric term of the internal scalar variable, *page (69).*

ϑ Strain energy function components of the Valanis and Landel model, *page (41).*

λ Uniaxial stretch, *page (47).*

λ_a Principal stretches, *page (15).*

λ_m Locking stretch, *page (43).*

λ_v Volumetric stretch, *page (62).*

μ Shear modulus, *page (30).*

μ_0 Initial shear modulus, *page (30).*

μ_i Material parameters of the Ogden model, *page (40).*

ξ Fraction of the critical damping factor, *page (53).*

ϱ Material density, *page (21).*

σ Cauchy uniaxial stress, *page (47).*

σ^0 Unmodified Cauchy uniaxial stress, *page (48).*

σ_{dev} Deviatoric Cauchy uniaxial stress, *page (61).*

σ_{dev}^0 Unmodified deviatoric Cauchy uniaxial stress, *page (62).*

σ_0 Stress amplitude, *page (52).*

υ Poisson's ratio, *page (30).*

υ_0 Initial Poisson's ratio, *page (30).*

ϕ Dissipation function, *page (48).*

ϕ_{dev} Deviatoric term of the dissipation function, *page (65).*

ϕ_{vol} Volumetric term of the dissipation function, *page (66).*

ϕ_{total} Total dissipated energy, *page (73).*

φ Strain energy function, *page (59).*

ω Radial frequency, *page (52).*

$\bar{\lambda}_a$ Modified principal stretches, *page (33).*

$\bar{\lambda}_{max}$ Modified stretch at the unloading point, *page (68).*

$\overline{\boldsymbol{\sigma}}$ Fictious Cauchy stress tensor, *page (35).*

Capital greek letters

Υ_{int} Internal potential energy, *page (21).*

Ψ Strain energy density function, *page (21).*

Ψ^0 Primary (or unmodified) strain energy function, *page (46).*

Ψ_{dev} Deviatoric term of the strain energy density function, *page (34).*

Ψ_{vol} Volumetric (or dilatational) term of the strain energy density function, *page (34).*

Ψ^{max} Maximum strain energy density obtained at the unloading point, *page (49).*

Ψ^{rec} Recoverable strain energy density per deformation cycle, *page (49).*

${}^{\star}\Psi$ Incompressible strain energy function for a biaxial state of deformation, *page (47).*

${}^{*}\Psi$ Incompressible strain energy function for an uniaxial state of deformation, *page (47).*

$\bar{\Psi}$ Decoupled strain energy function, *page (56).*

$\bar{\Psi}^0$ Unmodified decoupled strain energy function, *page (57).*

$\bar{\Psi}^0_{dev}$ Unmodified deviatoric term of the decoupled strain energy function, *page (57).*

$\bar{\Psi}^0_{vol}$ Unmodified volumetric term of the decoupled strain energy function, *page (57).*

$\bar{\Psi}^{max}_{dev}$ Deviatoric strain energy at the unloading point, *page (70).*

$\bar{\Psi}^{max}_{vol}$ Volumetric strain energy at the unloading point, *page (70).*

${}^{\diamond}\bar{\Psi}$ Decoupled strain energy function for a purely volumetric state of deformation, *page (62).*

${}^{\diamond}\bar{\Psi}^0$ Unmodified decoupled strain energy function for a purely volumetric state of deformation, *page (63).*

${}^{\bullet}\bar{\Psi}$ Decoupled strain energy function for an uniaxial volumetric state of deformation, *page (62).*

${}^{\star}\bar{\Psi}$ Decoupled strain energy function for a biaxial state of deformation, *page (60).*

${}^{\star}\bar{\Psi}^0$ Unmodified decoupled strain energy function for a biaxial state of deformation, *page (60).*

${}^{\star}\bar{\Psi}_{dev}$ Deviatoric term of the decoupled strain energy function for a biaxial state of deformation, *page (60).*

${}^{\star}\bar{\Psi}_{vol}$ Volumetric term of the decoupled strain energy function for a biaxial state of deformation, *page (60).*

$^{\star}\bar{\Psi}^{0}_{dev}$ Unmodified deviatoric term of the decoupled strain energy function for a biaxial state of deformation, *page (60).*

$^{\star}\bar{\Psi}^{0}_{vol}$ Unmodified volumetric term of the decoupled strain energy function for a biaxial state of deformation, *page (60).*

$^{*}\bar{\Psi}$ Decoupled strain energy function for an uniaxial state of deformation, *page (61).*

$^{*}\bar{\Psi}^{0}$ Unmodified decoupled strain energy function for an uniaxial state of deformation, *page (61).*

$^{*}\bar{\Psi}_{dev}$ Deviatoric term of the decoupled strain energy function for an uniaxial state of deformation, *page (61).*

$^{*}\bar{\Psi}_{vol}$ Volumetric term of the decoupled strain energy function for an uniaxial state of deformation, *page (61).*

$^{*}\bar{\Psi}^{0}_{dev}$ Unmodified deviatoric term of the decoupled strain energy function for an uniaxial state of deformation, *page (66).*

$^{*}\bar{\Psi}^{0}_{vol}$ Unmodified volumetric term of the decoupled strain energy function for an uniaxial state of deformation, *page (66).*

$^{*}\bar{\Psi}^{max}_{dev}$ Deviatoric strain energy at the unloading point for an uniaxial state of deformation, *page (68).*

$^{*}\bar{\Psi}^{max}_{vol}$ Volumetric strain energy at the unloading point for an uniaxial state of deformation, *page (68).*

$\tilde{\Psi}^{0}$ Unmodified incompressible strain energy function for a biaxial state of deformation, *page (63).*

Ω Geometrical region in the current configuration, *page (6).*

Ω_0 Geometrical region in the reference configuration, *page (6).*

Special symbols

$\beth_a$ Response coefficients, *page (27).*

$\otimes$ Tensor product, *page (29).*

$\varnothing$ Diameter, *page (76).*

Chapter 1

Introduction

The main focus of this thesis is to validate and develop a constitutive law for describing the mechanical behaviour of *CPGC (Cork Polyurethane Gel Composite)* material that can support the on-going industrial projects developed at *ACC-Amorim Cork Composites*. The CPGC material whose visual appearance is shown in figure 1.1(a) is based on a heterogeneous mixture of a *Polyurethane gel* with *cork particles* and is characterized by *nonlinear elastic* behaviour at large deformations and *strong hysteretic behaviour*. The empirical knowledge derived from the practical applications of the CPGC makes this material promising for *human comfort enhancement* as seen in figure 1.1(b) and *dynamic damping/control applications*.



(a) (b)

Figure 1.1: CPGC material detailing a) its visual aspect and b) a practical application in shoe insoles.

The use of constitutive modelling to describe and analyze materials behaviour has been an important issue since the beginning of modern engineering. The ability to predict the material's mechanical behaviour under complex stress fields, and its relation to other physical entities such as temperature or electromagnetic fields, is mandatory for

the analysis of demanding engineering problems. For any new material is necessary an assessment programme to analyze if actual constitutive models are satisfactory or if more effort is needed to improve such models or develop new ones.

The constitutive modelling of *hyperelastic materials* can be traced back to the early work of Mooney [Mooney, 1940] where a formulation was derived for incompressible solids, mainly rubbers. This model is quite simplistic when compared with the actual more demanding necessities of engineering problems. The actual models try to reproduce more efficiently the different material behaviors, essentially: the anisotropy [Diani *et al.*, 2004; Itskov & Askel, 2004], the introduction of compressibility [Attard, 2004] and the hysteretic phenomena present in some hyperelastic materials [Bergström & Boyce, 1999, 2000; Dorfmann & Ogden, 2003]. Their formulation framework is based on polyconvex *strain energy functions*. However, all of them require extensive material testing in order determine the material parameters that calibrated the model for a particular experimental behaviour [Gendy & Saleeb, 2000; Ogden *et al.*, 2004]. That is considered a drawback in the generalization of many of the models. More specifically it is usually needed to perform at least one experiment in the loading conditions that will be applied to the material in the real case situation. If anisotropy is a relevant feature the number of experiments must be increased.

The form of hyperelastic models is based on strain energy potentials that can be based on structural (micromechanical) aspects of the material (physical models) such as the Arruda-Boyce [Arruda & Boyce, 1993] or Van der Waals [Kilian *et al.*, 1986] models. Other models are based on material parameters that generally have no known physically meaningful basis (phenomenological models) and they serve as curve fitting parameters. Ogden [Ogden, 1972b], Mooney-Rivlin [Rivlin, 1948; Rivlin & Saunders, 1951] and Neo-Hookean models are examples of phenomenological strain energy functions.

Usually the potentials for slightly compressible materials are divided in two terms: one associated with incompressible behaviour, normally a function of the general deformation invariants or a function of principal stretches and an additional term to include the contribution of compressibility typically an isotropic function of the change in volume. These strain energy functions can take different forms in order to capture the particular behaviour of a material. For instance, the Yeoh model [Yeoh, 1990] is indicated to reproduce the mechanical behaviour of carbon-black filled rubber that are characterized by an highly nonlinear elastic behaviour at large deformations while the Mooney-Rivlin model is a more general model applied in the modelling of isotropic rubber-like materials at moderate deformations. There are however intrinsic postulates that are applied to all the hyperelastic models in order to assure the correctness of the strain energy potential in the considered deformation range in order to avoid numerical instabilities and consequently

non-physical behaviour [Bilgili, 2004].

The other fundamental type of behaviour that appears frequently in several engineering materials is the hysteretic behaviour. Different paths of loading and unloading characterize this behaviour. This phenomenon is associated with mechanical energy dissipation and is often used to determine damping properties of materials. The treatment of hysteresis can be done using different approaches. The work of Bergström & Boyce [1999, 2000] deal with time and strain rate dependence associated with loading-unloading hysteretic cycles, using a physical model approach. Phenomenological approaches to model material hysteresis are described in the literature by Banks *et al.* [1999], Kaliske & Rothert [1998] and Dorfmann & Ogden [2003]. This last authors used the pseudo-elastic theory originally developed by Ogden & Roxburgh [1999] for the modelling of the Mullins effect to describe purely hysteretic cycles in nonlinear elastic materials.

1.1 Outline of the thesis

In the chapter 2 is described the relevant theory for the constitutive modelling of nonlinear elastic materials. Concepts such as motion and deformation (kinematics), the concept of stress, hyperelasticity and several forms of strain energy functions are discussed. The basis of pseudo-elastic theory is also introduced in chapter 2 as a tool for modelling hysteretic cycles developed in the CPGC. In chapter 3, new formulations developed during this thesis are discussed, what enabled the modelling of hysteretic cycles (loading-unloading cycles) and the consequent heat build-up due to energy dissipation. The constitutive modelling of CPGC is outlined in chapter 4 where is discussed the experimental methodology followed for the mechanical evaluation of the material, the material parameters fitting procedure and the finite element implementation of the proposed constitutive laws. In chapter 5 are shown two practical examples, namely, the finite element model of the human foot to serve as tool for comfort optimization of CPGC shoe insoles and a preliminary study in the potentialities of the proposed hysteretic model for the reproduction of loading-unloading case scenarios, using nonlinear finite element tools. Conclusions and further work that must arise from this thesis are outlined in chapter 6.

This page is intentionally left blank.

Chapter 2

State of the Art

In this chapter, theoretical aspects associated with *continuum mechanics* are outlined. Important concepts such as kinematics, stress and finite strain tensors, mechanical and thermomechanical balance equations are discussed in section 2.1.

Other important concepts for the constitutive modelling of the CPGC, such as *hyperelasticity*, *constitutive equations* and *strain energy functions* are also discussed in this chapter, namely, at sections 2.2 and 2.3.

In section 2.4 is introduced the concept of *pseudo-elasticity* that is used for the modelling of the CPGC's *hysteretic* behaviour (loading-unloading cycles). The last section of this chapter (section 2.5) is dedicated to the *heat generation* effect that characterize *dissipative* or *hysteretic* materials.

2.1 Overview of Continuum Mechanics

The behaviour of a body when subjected to external forces and moments must be understood. *Continuum mechanics* is a powerful tool to explain various physical phenomena such as stress and strain developed within a body without the need of knowing the internal (or microscopic) structure. From a practical point of view, the internal material structure composed by a very large number of particles (or molecules) is replaced by a continuous description that can represent the underlying microscopic behaviour of the body. In other words, continuum mechanics confines itself to the *macroscopic phenomena*, neglecting the structure of the material in a smaller scale [see Truesdell & Noll, 2004, Section 3]. For these cases, the material is assumed to be continuously distributed throughout its volume and completely fills the space that occupies [see Mase, 1970, Section 2.1].

In order to understand the macroscopic behaviour of elastic bodies when subjected to motions and deformations that can cause stress in the material, the concept of body motion and deformation arising from continuum mechanics and nonlinear elasticity theory

must be well understood. In section 2.1.1 is discussed the kinematics associated with continuum bodies; here are outlined important concepts of motion of continuum bodies, such as the *deformation gradient, displacement gradient* and *finite strain tensors*. In section 2.1.2 the concept of *stress* and *stress tensors* such as *Cauchy, first Piola-Kirchhoff* (nominal stress) and *second Piola-Kirchhoff* stress tensors are described. More detailed information about continuum mechanics and nonlinear elasticity theory can be found in the books from Holzapfel [2005], Ogden [2005], Truesdell & Noll [2004], Fu & Ogden [2002], Mase [1970] and Dunne & Petrinic [2005].

2.1.1 Kinematics

2.1.1.1 Configuration

Body β is composed by set of *particles* (or *material points*[1]) $\mathsf{P} \in \beta$ as seen in figure 2.1, and is assumed to have a continuous distribution of matter in space and time. Such a body is called a *continuum body* or just a *continuum* [see Holzapfel, 2005, Section 2.1].

In figure 2.1 is represented the three-dimensional Euclidean space where the continuum body β is emerged at a given instant of time t. The reference frame has its origin in O with orthogonal unit vectors set $\{E_a\}$ and $\{e_a\}$, $a = 1, 2, 3$. As body β moves, it occupies different regions in space that are denoted by the *geometrical regions* Ω_0,..., Ω.These regions occupied by body β at each instant of time t are known as *configurations* of body β.

The *reference configuration* of body β is obtained for time $t = 0$ and we state that this configuration corresponds to the *undeformed state*. Point[2] X occupies the same position as particle $\mathsf{P} \in \beta$ in the reference configuration ($t = 0$). Position vector $\mathbf{X}$ indicates the initial position of particle $\mathsf{P} \in \beta$ relative to the fixed origin O.

For instants of time t, body β occupies the region Ω in space. For this region, particle $\mathsf{P} \in \beta$, is associated with point x and the corresponding position vector $\mathbf{x}$ indicates the current position of point x relative to origin O.

Relative to the rectangular Cartesian axes $OX_1X_2X_3$ we can write the position vector $\mathbf{X}$ as

$$\mathbf{X} = X_1E_1 + X_2E_2 + X_3E_3, \tag{2.1}$$

denoting the *referential* (or *material*) coordinates of point X. Following the same procedure for position vector $\mathbf{x}$ we can then write

[1] material point or particle refers to a infinitesimal part of the continuum body.
[2] a point is used to designate a place in the considered space.

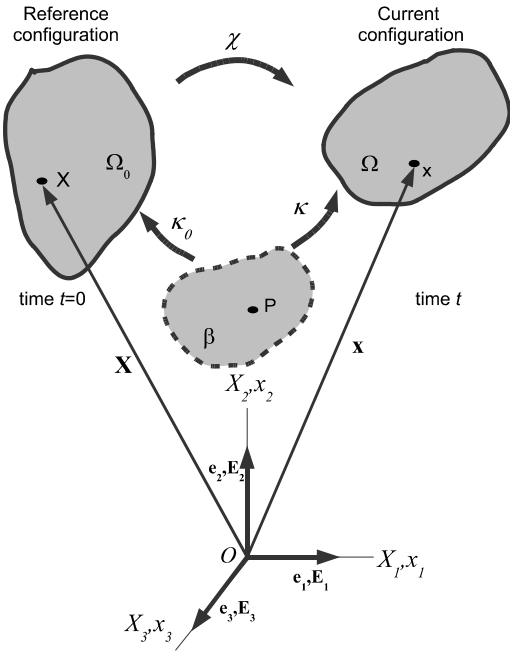


Figure 2.1: Motion of a continuum body.

$$\mathbf{x} = x_1 e_1 + x_2 e_2 + x_3 e_3, \tag{2.2}$$

relative to the rectangular Cartesian axes $Ox_1x_2x_3$, denoting the *spatial* (or *current*) coordinates of point x.

2.1.1.2 Motion

Focusing again on figure 2.1 we associate for every instant of time t, a position vector $\mathbf{X} \in \Omega_0$ for each particle $\mathsf{P} \in \beta$ by the one to one map $\mathbf{X} = \boldsymbol{\kappa}_0(\mathsf{P}, t)$. The map $\boldsymbol{\kappa}_0$ acting on body β produces the geometrical region Ω_0 for $t = 0$. If, for other hand, map $\boldsymbol{\kappa}$ acts on body β it will produce the geometrical region Ω occupied by body β at a given instant of time t. The place $\mathbf{x} = \boldsymbol{\kappa}(\mathsf{P}, t)$ occupied by particle P at time t is then given by

$$\mathbf{x} = \boldsymbol{\kappa}\left[\boldsymbol{\kappa}_0^{-1}(\mathbf{X}, t)\right] = \boldsymbol{\chi}(\mathbf{X}, t). \tag{2.3}$$

In equation (2.3) the vector field $\boldsymbol{\chi}$ specifies the place $\mathbf{x}$ of $\mathbf{X}$ for time instants t. Vector field $\boldsymbol{\chi}$ is often called as *motion* [Holzapfel, 2005, Section 2.1; Truesdell & Noll, 2004, Section 15] of the body β and carries points in material position $\mathbf{X} \in \Omega_0$ to new spatial positions in region Ω described by the position vector $\mathbf{x}$. The successive positions $\mathbf{x}$ derived from equation 2.3 define a *trajectory* (or *path line*) of a material point P in the

Euclidean space.

Motion $\boldsymbol{\chi}$ is assumed to be invertible [see Truesdell & Noll, 2004, Section 15]. Using this property is possible to associate a reference position $\mathbf{X} \in \Omega_0$ by means of a current position $\mathbf{x} \in \Omega$ at time t, using an inverse transformation written by

$$\mathbf{X} = \boldsymbol{\chi}^{-1}(\mathbf{x}, t). \tag{2.4}$$

where $\boldsymbol{\chi}^{-1}$ is called the *inverse motion*.

Position vector $\mathbf{X}$ and time t serve as independent variables for the geometrical region Ω_0 as seen in equation (2.3) and for this case, fields are defined in the referential description. In the case of region Ω, position vector $\mathbf{X}$ is defined in terms of the independent variables $\mathbf{x}$ and time t as expressed by equation (2.4). In this case the description is said to be spatial or current. In some text books it is usual to call the material description the *Lagrangian form* and the spatial description the *Eulerian form* [see Mase, 1970, Section 3.4].

2.1.1.3 Displacement

Observing figure 2.2 the *displacement vector field* $\mathbf{U}_d$ of a point in the material description (or Lagrangian form) relates its position $\mathbf{X}$ in the initial (undeformed) configuration to its position $\mathbf{x}$ in the current (deformed) configuration at time t. Displacement field $\mathbf{U}_d$ can be written performing vector algebra operations as stated by

$$\mathbf{U}_d(\mathbf{X}, t) = \mathbf{x}(\mathbf{X}, t) - \mathbf{X}. \tag{2.5}$$

The displacement vector field $\mathbf{u}_d$ in the spatial description (or Eulerian form) is given by

$$\mathbf{u}_d(\mathbf{x}, t) = \mathbf{x} - \mathbf{X}(\mathbf{x}, t). \tag{2.6}$$

Expression (2.6) specifies the displacement of a material point as a function of the current position $\mathbf{x}$ and time t. The two forms can be related by means of inverse motion $\boldsymbol{\chi}^{-1}$. This relation can be expressed by

$$\mathbf{U}_d(\mathbf{X}, t) = \mathbf{U}_d\left(\chi^{-1}(\mathbf{x}, t), t\right) = \mathbf{u}_d(\mathbf{x}, t). \tag{2.7}$$

2.1.1.4 Deformation gradient

Transformation of geometrical region Ω_0 in region Ω can result in changes of the infinitesimal material elements that constitutes the continuum body β. Deformation can be quantified by monitoring the distance between two neighboring points during the motion

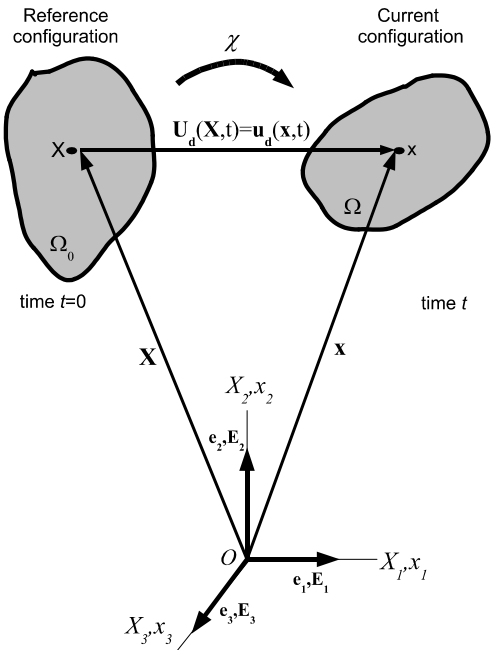


Figure 2.2: Displacement vector field $\mathbf{U}_d$.

of the body as seen in figure 2.3. In the reference (undeformed) configuration, the distance between material points $\mathsf{X} \in \Omega_0$ and $\mathsf{Y} \in \Omega_0$ is given by the infinitesimal vector (or material line) $d\mathbf{X}$, expressed by

$$d\mathbf{X} = \mathbf{Y} - \mathbf{X}. \tag{2.8}$$

In the current (deformed) configuration, the distance between the same particles but now expressed by x and y is given by

$$d\mathbf{x} = \mathbf{y} - \mathbf{x}. \tag{2.9}$$

Infinitesimal vector $d\mathbf{x}$ can be expressed in terms of the infinitesimal vector $d\mathbf{X}$ by the use of the *deformation gradient tensor*, $\mathbf{F}$, expressed by the relation

$$d\mathbf{x} = \mathbf{F}\left(\mathbf{X}, t\right) d\mathbf{X} \tag{2.10}$$

[Holzapfel, 2005, Section 2.4; Fu & Ogden, 2002, Section 1.2.1].

Analyzing expression (2.10) we can observe that this is clearly a linear transformation which generates a spatial infinitesimal vector $d\mathbf{x}$ by the action of the second order tensor $\mathbf{F}$ on the infinitesimal material vector $d\mathbf{X}$. The deformation gradient $\mathbf{F}$ is a primary measure of deformation given by

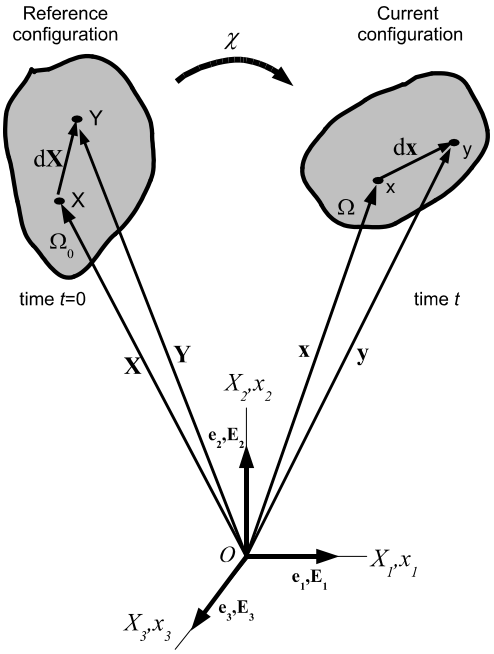


Figure 2.3: Deformation of a continuum body.

$$\mathbf{F}\left(\mathbf{X},t\right)=\frac{\partial\boldsymbol{\chi}\left(\mathbf{X},t\right)}{\partial\mathbf{X}}=\frac{\partial\mathbf{x}\left(\mathbf{X},t\right)}{\partial\mathbf{X}}=\operatorname{Grad}\mathbf{x}(\mathbf{X},t)\cdot \tag{2.11}$$

In indicial notation we can write the deformation gradient tensor as

$$\mathbf{F}_{aA}=\frac{\partial\chi_a}{\partial X_A}=\operatorname{Grad}X_A x_a\cdot \tag{2.12}$$

In (2.12) the capital index A describes material (referential) coordinates and the minor index a spatial (current) coordinates.

As stated in section 2.1.1.2, motion $\boldsymbol{\chi}$ is assumed to be invertible which requires the deformation gradient tensor $\mathbf{F}$ to be non singular (i.e., $\det\mathbf{F}\neq 0$) and we adopt the usual convention that $\det\mathbf{F}>0$ [see Fu & Ogden, 2002, Section 1.2.1]. The inverse of the deformation gradient $\mathbf{F}^{-1}$ is written by

$$\mathbf{F}^{-1}\left(\mathbf{x},t\right)=\frac{\partial\boldsymbol{\chi}^{-1}\left(\mathbf{x},t\right)}{\partial\mathbf{x}}=\frac{\partial\mathbf{X}\left(\mathbf{x},t\right)}{\partial\mathbf{x}}=\operatorname{grad}\mathbf{X}(\mathbf{x},t)\ , \tag{2.13}$$

or in indicial form by

$$\mathbf{F}^{-1}_{Aa}=\frac{\partial\chi_A^{-1}}{\partial X_a}=\operatorname{grad}x_a X_A\cdot \tag{2.14}$$

Performing simple algebraic manipulations on equation (2.10) we obtain the following

linear transformation written in terms of the inverse deformation gradient $\mathbf{F}^{-1}$ by

$$d\mathbf{X} = \mathbf{F}^{-1}(\mathbf{x}, t)d\mathbf{x} \ , \tag{2.15}$$

which is a linear transformation operation that transforms the spatial infinitesimal vector $d\mathbf{x}$ into the material infinitesimal vector $d\mathbf{X}$ by means of the inverse deformation gradient tensor $\mathbf{F}^{-1}$.

2.1.1.5 Displacement gradient

Applying the gradient operator in equation (2.5) we obtain a relation between the deformation gradient $\mathbf{F}$ and the displacement gradient tensor $\operatorname{Grad}\mathbf{U}_d$ in the material description, given by

$$\begin{aligned} \operatorname{Grad}\mathbf{U}_d(\mathbf{X}, t) &= \operatorname{Grad}\mathbf{x}(\mathbf{X}, t) - \operatorname{Grad}\mathbf{X} \\ &= \mathbf{F}(\mathbf{X}, t) - \mathbf{I}. \end{aligned} \tag{2.16}$$

The same methodology can be followed for obtaining the displacement gradient tensor $\operatorname{grad}\mathbf{u}_d$ in the spatial description. Using equation 2.6 we can write that

$$\begin{aligned} \operatorname{grad}\mathbf{u}_d(\mathbf{x}, t) &= \operatorname{grad}\mathbf{x} - \operatorname{grad}\mathbf{X}(\mathbf{x}, t) \\ &= \mathbf{I} - \mathbf{F}^{-1}(\mathbf{x}, t). \end{aligned} \tag{2.17}$$

2.1.1.6 Jacobian determinant

The change in volume during the deformation process is given by the *Jacobian* determinant (volume ratio), expressed by

$$J(\mathbf{X}, t) = \det\mathbf{F}(\mathbf{X}, t) > 0 \tag{2.18}$$

[see Truesdell & Noll, 2004, Section 21].

Assuming that the body have continuous distribution of matter, $dV = dX_1dX_2dX_3$ and $dv = dx_1dx_2dx_3$ denote infinitesimal volume elements in reference and current configurations, respectively. Is possible to relate the material volume element dV to the spatial volume element dv, through the Jacobian determinant J, as

$$dv = J(\mathbf{X}, t)\, dV \tag{2.19}$$

[see Holzapfel, 2005, Section 2.4].

As stated in expression (2.18), and due to the nonsingularity of the deformation gradient tensor $\mathbf{F}$ as stated in section 2.1.1.4, we conclude that $\det \mathbf{F}(\mathbf{X}, t) = J(\mathbf{X}, t) \neq 0$. Knowing that volume elements cannot have negative volumes we must reject $J(\mathbf{X}, t) < 0$.

2.1.1.7 Finite strain tensors

In section 2.1.1.4 we defined the deformation gradient tensor $\mathbf{F}$ as a crucial measure for characterization of changes in material elements during motion. In this section are introduced the concept of strain tensors that relate the changes in the material elements with the effective strain developed in the body.

Observing again figure 2.3 we can consider for the reference configuration Ω_0, that the length of material infinitesimal vector $d\mathbf{X}$ is given by dL. Same methodology can be applied for the current configuration Ω, assigning the infinitesimal length dl to the infinitesimal spatial vector $d\mathbf{x}$. We can write the square magnitude of spatial vector dl as

$$dl^2 = d\mathbf{x} \cdot d\mathbf{x}. \tag{2.20}$$

Applying expression (2.10) we can rewrite equation (2.20) as

$$\begin{aligned} dl^2 = d\mathbf{x} \cdot d\mathbf{x} = (\mathbf{F}d\mathbf{X}) \cdot (\mathbf{F}d\mathbf{X}) = d\mathbf{X}^T \underbrace{\mathbf{F}^T\mathbf{F}}_{\mathbf{C}} d\mathbf{X} \\ = d\mathbf{X}^T \mathbf{C} d\mathbf{X}. \end{aligned} \tag{2.21}$$

From expression (2.21), we obtain that

$$\mathbf{C} = \mathbf{F}^T\mathbf{F} \qquad \text{or} \qquad C_{AB} = (F_{aA}F_{aB}) \ , \tag{2.22}$$

which is known as the right *Cauchy-Green deformation tensor*. Strain tensor $\mathbf{C}$ is an important deformation measure in material coordinates. Note that $\mathbf{C}$ is a symmetric and definite positive tensor at each $\mathbf{X} \in \Omega_0$ [see Holzapfel, 2005, Section 2.5].

Considering now the material vector length dL, we can write

$$\begin{aligned} dL^2 = d\mathbf{X} \cdot d\mathbf{X} = \left(\mathbf{F}^{-1}d\mathbf{x}\right)^T \left(\mathbf{F}^{-1}d\mathbf{x}\right) = d\mathbf{x}^T \underbrace{\left(\mathbf{F}^{-1}\right)^T \mathbf{F}^{-1}}_{\mathbf{b}^{-1}} d\mathbf{x} \\ = d\mathbf{x}^T \mathbf{b}^{-1} d\mathbf{x} \ , \end{aligned} \tag{2.23}$$

with

$$\mathbf{b}^{-1} = \left(\mathbf{F}^{-1}\right)^T \mathbf{F}^{-1} \qquad \text{or} \qquad b_{ab}^{-1} = (F_{Aa}^{-1} F_{Ab}^{-1}) \ , \tag{2.24}$$

corresponding to the inverse of the *left Cauchy-Green deformation tensor* given by $\mathbf{b} = \mathbf{F}\mathbf{F}^T$. This tensor is a fundamental strain measure in the spatial coordinates. The left Cauchy-Green tensor $\mathbf{b}$ is symmetric and positive definite for all $\mathbf{x} \in \Omega$ [see Holzapfel, 2005, Section 2.5].

The difference in vector lenghts dL and dl gives another strain measure in material elements between the reference (undeformed) configuration and the current (deformed) configuration. We can write from equations (2.21) and (2.23) the difference between vector lenghts as

$$\begin{aligned} dl^2 - dL^2 &= d\mathbf{x}^T d\mathbf{x} - d\mathbf{X}^T d\mathbf{X} = (\mathbf{F}d\mathbf{X})^T \mathbf{F}d\mathbf{X} - d\mathbf{X}^T d\mathbf{X} \\ &= d\mathbf{X}^T \mathbf{F}^T \mathbf{F} d\mathbf{X} - d\mathbf{X}^T d\mathbf{X} = d\mathbf{X}^T (\underbrace{\mathbf{F}^T \mathbf{F}}_{\mathbf{C}} - \mathbf{I}) d\mathbf{X} \\ &= d\mathbf{X}^T \left(\mathbf{C} - \mathbf{I}\right) d\mathbf{X} = d\mathbf{X}^T \left(\mathbf{2E}\right) d\mathbf{X} \ , \end{aligned} \tag{2.25}$$

where

$$\mathbf{E} = \frac{1}{2}\left(\mathbf{C} - \mathbf{I}\right) = \frac{1}{2}\left(\mathbf{F}^T\mathbf{F} - \mathbf{I}\right) \qquad \text{or} \qquad \mathbf{E}_{AB} = \frac{1}{2}(F_{aA}F_{aB} - \delta_{AB}). \tag{2.26}$$

In expression (2.26) $\mathbf{I}$ is the identity tensor and δ_{AB} is the Kronecker delta.

Strain tensor $\mathbf{E}$ expressed in equation (2.26) is known as the *Green-Lagrange strain tensor* and like strain tensor $\mathbf{C}$, is referred as a *material strain tensor*. Knowing that $\mathbf{C} = \mathbf{C}^T$ and $\mathbf{I} = \mathbf{I}^T$ we conclude that strain tensor $\mathbf{E}$ is also symmetric ($\mathbf{E} = \mathbf{E}^T$).

The same methodology applied in (2.25) can be followed to define a new strain measure in spatial coordinates. Writing equation (2.25) in terms of the spatial vector $d\mathbf{x}$, we obtain

$$\begin{aligned} dl^2 - dL^2 &= d\mathbf{x}^T d\mathbf{x} - d\mathbf{X}^T d\mathbf{X} = d\mathbf{x}^T d\mathbf{x} - \left(\mathbf{F}^{-1} d\mathbf{x}\right)^T \left(\mathbf{F}^{-1} d\mathbf{x}\right) \\ &= d\mathbf{x}^T d\mathbf{x} - d\mathbf{x}^T \mathbf{F}^{-T} \mathbf{F}^{-1} d\mathbf{x} = d\mathbf{x}^T (\mathbf{I} - \underbrace{\mathbf{F}^{-T}\mathbf{F}^{-1}}_{\mathbf{b}^{-1}}) d\mathbf{x} \\ &= d\mathbf{x}^T \left(\mathbf{I} - \mathbf{b^{-1}}\right) d\mathbf{x} = d\mathbf{x}^T \left(2\mathbf{e}\right) d\mathbf{x} \ , \end{aligned} \tag{2.27}$$

with

$$\mathbf{e} = \frac{1}{2}\left(\mathbf{I} - \mathbf{b^{-1}}\right) = \frac{1}{2}\left(\mathbf{I} - \mathbf{F}^{-T}\mathbf{F}^{-1}\right) \qquad \text{or} \qquad \mathbf{e}_{ab} = \frac{1}{2}(F_{aA}F_{bA} - \delta_{ab}) \ , \tag{2.28}$$

where $\mathbf{e}$ is a second order tensor called the *Euler-Almansi strain tensor*. Both $\mathbf{e}$ and $\mathbf{b}$ are spatial strain tensors operating on spatial vectors $\mathbf{x}$.

Strain tensors $\mathbf{E}$ and $\mathbf{e}$ have important characteristics in terms of strain measuring since this measures are invariant with respect to rigid-body motion, i.e. $\mathbf{e}$ and $\mathbf{E}$ vanish during rigid-body motion [see Dunne & Petrinic, 2005, Section 3.4].

2.1.1.8 Polar decomposition

The deformation gradient tensor $\mathbf{F}(\mathbf{X},t)$ can be decomposed into a pure stretch and a pure rotation by using the *polar decomposition theorem* [Holzapfel, 2005, Section 2.6; Truesdell & Noll, 2004, Section 24]. At each point $\mathbf{X}$, the deformation gradient $\mathbf{F}$ can be written by

$$\mathbf{F} = \mathbf{RU} = \mathbf{vR} \ , \tag{2.29}$$

where $\mathbf{U}$ and $\mathbf{v}$ are the *material stretch tensor* and the *spatial stretch tensor*, respectively. $\mathbf{R}$ is the *proper orthogonal rotation tensor*[3]. The stretch tensors measures stretching along the mutually orthogonal eigenvectors. *Right stretch tensor* $\mathbf{U}$ acts on the reference configuration while the *left stretch tensor* $\mathbf{v}$ is defined in the current configuration.

Rotation tensor $\mathbf{R}$ is responsible for local rotation resulting from the body's orientation changing. If $\mathbf{U} = \mathbf{v} = \mathbf{I}$, the body motion is considered as a *pure rigid-body rotation*, resulting from (2.29) in $\mathbf{F} = \mathbf{R}$. Considering a pure rigid-body rotation, equation (2.10) becomes

$$d\mathbf{x} = \mathbf{R}(\mathbf{X}, t)d\mathbf{X}. \tag{2.30}$$

For a pure stretch we have $\mathbf{R} = \mathbf{I}$ and consequently $\mathbf{F} = \mathbf{U} = \mathbf{v}$. The spatial vector $d\mathbf{x}$ is then given by

$$d\mathbf{x} = \mathbf{U}(\mathbf{X}, t)d\mathbf{X}. \tag{2.31}$$

The combination of rotation and stretch in the definition of the spatial line vector can be written using the *right polar decomposition,* expressed by (2.29). From expressions (2.10) and (2.29) we obtain

[3] a proper orthogonal tensor must obey to the properties: $\mathbf{R}\mathbf{R}^T = \mathbf{R}^T\mathbf{R} = \mathbf{I}$ and $\det \mathbf{R} = \mathbf{1}$

$$d\mathbf{x} = \mathbf{R}(\mathbf{U}d\mathbf{X}) \tag{2.32}$$

or using the *left polar decomposition*,

$$d\mathbf{x} = \mathbf{v}(\mathbf{R}d\mathbf{X}). \tag{2.33}$$

From the polar decomposition theorem in (2.29), we can write that

$$\mathbf{U}^2 = \mathbf{F}^T\mathbf{F} = \mathbf{C} \qquad \text{and} \qquad \mathbf{v}^2 = \mathbf{F}\mathbf{F}^T = \mathbf{b}. \tag{2.34}$$

2.1.1.9 Eigenvalues and eigenvectors of strain tensors

The eigenvalues $\lambda_a,\ a = 1, 2, 3$ of the stretch tensor $\mathbf{U}$ are the *principal stretches* [see Fu & Ogden, 2002, Section 1.2.1]. Using *spectral decomposition*, the material right stretch tensor $\mathbf{U}$ is expressed by

$$\mathbf{U} = \sum_{a=1}^{3} \lambda_a N_a \otimes N_a \ , \tag{2.35}$$

where N_a, $a = 1, 2, 3$, corresponds to the principal referential directions and $\otimes$ denotes the *tensor product*. From identity (2.34) we can express the deformation tensor $\mathbf{C}$ as

$$\mathbf{C} = \mathbf{U}^2 = \sum_{a=1}^{3} \lambda_a^2 N_a \otimes N_a. \tag{2.36}$$

Following the same methodology we can write the spatial left stretch tensor $\mathbf{v}$ as

$$\mathbf{v} = \sum_{a=1}^{3} \lambda_a n_a \otimes n_a \ , \tag{2.37}$$

where n_a, $a = 1, 2, 3$, corresponds to the principal spatial directions. Based on expression (2.37) and identity (2.34), the left Cauchy-Green deformation tensor $\mathbf{b}$ is expressed as

$$\mathbf{b} = \mathbf{v}^2 = \sum_{a=1}^{3} \lambda_a^2 n_a \otimes n_a. \tag{2.38}$$

From expressions (2.35) and (2.36) we conclude that $\mathbf{C}$ and $\mathbf{U}$ have the same eigenvectors λ_a, $a = 1, 2, 3$.

2.1.2 Stress

In the previous section some aspects related with motion and deformation of a continuum body were outlined. On this section relevant aspects associated with stress measuring such as *traction vectors* and *stress tensors* are discussed.

Stress is responsible for the deformation of materials and must be well understood. A deformable material when subjected to external or internal forces is deformed as result of the interaction between material and neighboring material in the interior part of the body as result of the forces being transmitted from one portion of the continuum to another portion.

Stress measures can be defined in the current configuration leading to the well-known *Cauchy stress tensor* (current force per unit current area). Alternativelly, for the reference configuration, *nominal stress* or *engineering stress* (initial force per unit initial area) is defined, also expressed by the *first Piola-Kirchhoff stress tensor.*

2.1.2.1 Stress tensors

The body represented in figure 2.4 was cut by a plane that passes in any given $\mathbf{x} \in \Omega$. The infinitesimal resultant force denoted by $d\mathbf{f}$ acting on a point $\mathbf{x} \in \Omega$ is given by

$$d\mathbf{f} = \mathbf{t}ds = \mathbf{T}dS \ , \tag{2.39}$$

where, through *Cauchy's postulate* [see Holzapfel, 2005, Section 3.1], $\mathbf{t} = \mathbf{t}(\mathbf{x}, t, \mathbf{n})$ corresponds to the spatial *Cauchy traction vector* and $\mathbf{T} = \mathbf{T}(\mathbf{X}, t, \mathbf{N})$ is known as the *first Piola-Kirchhoff traction vector.* Vectors $\mathbf{n}$ and $\mathbf{N}$ are the unit normal vectors to the infinitesimal surfaces ds and dS (see figure 2.4), respectively.

Following *Cauchy's stress theorem* [Holzapfel, 2005, Section 3.1; Truesdell & Noll, 2004, Section 16; Mase, 1970, Section 2.6], we can write that

$$\mathbf{t}(\mathbf{x}, t, \mathbf{n}) = \boldsymbol{\sigma}(\mathbf{x}, t)\mathbf{n} \tag{2.40}$$

and

$$\mathbf{T}(\mathbf{X}, t, \mathbf{N}) = \mathbf{P}(\mathbf{X}, t)\mathbf{N}. \tag{2.41}$$

In equation (2.40) $\boldsymbol{\sigma}$ is the second order spatial *Cauchy (or true) stress tensor.* Tensor $\mathbf{P}$ in equation (2.41) is called the *first Piola-Kirchhoff (or nominal) stress tensor.*

These two stress tensors can be related by the use of relations (2.39), (2.40) and (2.41). Applying this relations we can write

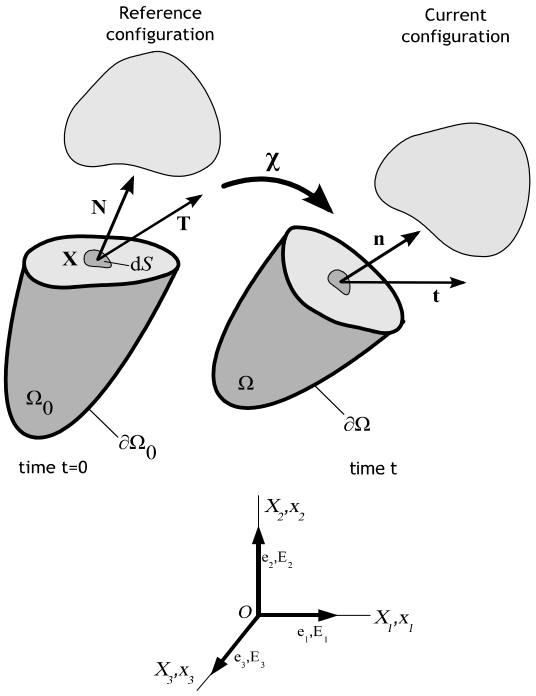


Figure 2.4: Traction vector acting at the referencial and current configurations of the body.

$$\boldsymbol{\sigma}(\mathbf{x},t)\mathbf{n}ds = \mathbf{P}(\mathbf{X},t)\mathbf{N}dS. \tag{2.42}$$

Using *Nanson's formula* [see Holzapfel, 2005, Section 2.4] expressed by $\mathbf{n}ds = J\mathbf{F}^{-T}\mathbf{N}dS$, that describes how area elements deforms during motion, we obtain

$$\mathbf{P} = J\boldsymbol{\sigma}\mathbf{F}^{-T} \qquad \text{or} \qquad P_{aA} = J\sigma_{ab}F^{-1}_{Ab}. \tag{2.43}$$

The transformation of $\mathbf{P}$ into $\boldsymbol{\sigma}$ and the converse is called *Piola transformation.* From equation (2.43), the symmetric Cauchy stress tensor $\boldsymbol{\sigma}$ is expressed by

$$\boldsymbol{\sigma} = J^{-1}\mathbf{P}\mathbf{F}^{T} = \boldsymbol{\sigma}^{T} \qquad \text{or} \qquad \sigma_{ab} = J^{-1}P_{aA}F_{bA} = \sigma_{ba}. \tag{2.44}$$

First Piola-Kirchhoff $\mathbf{P}$ is not, in general, a symmetric tensor [Holzapfel, 2005, Section 3.1; Truesdell & Noll, 2004, Section 43A]. The symmetry of the Cauchy stress tensor $\boldsymbol{\sigma}$ follows from the angular momentum conservation in the current configuration [see Truesdell & Noll, 2004, Section 43A].

2.1.2.2 Alternative stress tensors

Cauchy stress $\boldsymbol{\sigma}$ and the first Piola-Kirchhoff tensor $\mathbf{P}$ are the most widely used stress tensors in the field of nonlinear continuum mechanics but some alternative stress tensors such as the *Kirchhoff stress tensor* $\boldsymbol{\tau}$, the *second Piola-Kirchhoff stress tensor* $\mathbf{S}$ and the *Biot stress tensor* $\mathbf{T}_B$ are often used for practical cases. The second Piola-Kirchhoff tensor $\mathbf{S}$ for instance, is wide used in the formulation of nonlinear constitutive equations, which will be seen in section 2.2.

The spatial *Kirchhoff stress tensor* $\boldsymbol{\tau}$ can be written in function of the Cauchy stress tensor. This relation is expressed by

$$\boldsymbol{\tau} = J\boldsymbol{\sigma} \qquad \text{or} \qquad \tau_{ab} = J\sigma_{ab} \ , \tag{2.45}$$

differing from the Cauchy stress tensor σ by the volume ratio J already defined in (2.18).

The symmetric second Piola-Kirchhoff stress tensor $\mathbf{S}$ can be written in terms of the Cauchy stress tensor σ as

$$\mathbf{S} = J\mathbf{F}^{-1}\boldsymbol{\sigma}\mathbf{F}^{-T} = \mathbf{S}^T \qquad \text{or} \qquad S_{AB} = JF_{Aa}F_{Bb}\sigma_{ab} \tag{2.46}$$

[see Truesdell & Noll, 2004, Section 44].

Using equation (2.43) and substituting in equation (2.46) we obtain the expression

$$\mathbf{S} = \mathbf{F}^{-1}\mathbf{P} \qquad \text{or} \qquad S_{AB} = F^{-1}_{Aa}P_{aB} = S_{BA} \ , \tag{2.47}$$

as a fundamental expression relating the non-symmetrical tensor $\mathbf{P}$ with the symmetrical stress tensor $\mathbf{S}$.

Another alternative stress measuring tensor is the material *Biot stress tensor* $\mathbf{T}_B$ defined as

$$\mathbf{T}_B = \mathbf{R}^T\mathbf{P} \qquad \text{or} \qquad T_{B\,AB} = R_{aA}P_{aB}. \tag{2.48}$$

The Biot stress tensor $\mathbf{T}_B$ differs from the first Piola-Kirchhoff tensor $\mathbf{P}$ by the transpose of the rotation tensor $\mathbf{R}$.

In table 2.1 are summarized some useful transformations of stress tensors.

Table 2.1: Transformation of stress tensors.

	1^{st}Piola-Kirchhoff stress $\mathbf{P}$	Cauchy stress $\boldsymbol{\sigma}$	2^{nd}Piola-Kirchhoff stress $\mathbf{S}$	Biot stress $\mathbf{T}_B$	Kirchhoff stress $\boldsymbol{\tau}$
$\mathbf{P} =$	-	$J\sigma\mathbf{F}^{-T}$	$\mathbf{FS}$	$\mathbf{RT}_B$	$\tau\mathbf{F}^{-T}$
$\boldsymbol{\sigma} =$	$J^{-1}\mathbf{PF}^T$	-	$J^{-1}\mathbf{FSF}^T$	$J^{-1}\mathbf{RT}_B\mathbf{F}^T$	$J^{-1}\boldsymbol{\tau}$
$\mathbf{S} =$	$\mathbf{F}^{-1}\mathbf{P}$	$\mathbf{JF}^{-1}\boldsymbol{\sigma}\mathbf{F}^{-T}$	-	$\mathbf{U}^{-1}\mathbf{T}_B$	$\mathbf{F}^{-1}\boldsymbol{\tau}\mathbf{F}^{-T}$
$\mathbf{T}_B =$	$\mathbf{R}^T\mathbf{P}$	$\mathbf{JR}^T\boldsymbol{\sigma}\mathbf{F}^{-T}$	$\mathbf{US}$	-	$\mathbf{R}^T\boldsymbol{\tau}\mathbf{F}^{-T}$
$\boldsymbol{\tau} =$	$\mathbf{PF}^T$	$J\boldsymbol{\sigma}$	$\mathbf{FSF}^T$	$\mathbf{RT}_B\mathbf{F}^T$	-

2.1.3 Balance equations

This section intends to introduce some concepts associated with balance of energy in *purely mechanical systems* and systems where mechanical and thermal energy are present. The balance of energy in *thermomechanical systems* is extremely important for hysteretic materials where phenomena such as heat generation are important to predict, as they influences the material's mechanical behaviour. In section 3.2 the thermomechanical behaviour of the CPGC material associated with hysteretic (dissipative) behaviour will be discussed in detail, and where a new approach is presented for the modelling of *heat generation* in nonlinear elastic hysteretic materials.

In purely mechanical energy conservative problems (no associated energy dissipation) all the external work done in the material is transformed into mechanical work considering a static or quasi-static (null or approximately null values of kinetic energy) loading case [see Holzapfel, 2005, Section 4.4], however, in the case of *non-conservative systems*, irreversibilities associated with internal heat generation do not allow the use of purely mechanical balance equations due to the thermal (or non-mechanical) power developed. Heat flux terms must be used to accounted for irreversible processes and be included in energy balance laws.

Note that the energy balance equations described during in this section will be referred to the spatial description. More information about this issue can be found in the books by Truesdell & Noll [2004], Holzapfel [2005], Incropera & DeWitt [1996], Çengel & Boles [1989], and Mase [1970].

2.1.3.1 Mechanical balance

In figure 2.5, vector $\mathbf{t}(\mathbf{x}, t, \mathbf{n})$ corresponds to the spatial Cauchy traction vector already introduced in section 2.1.2.1, while the spatial vector field $\mathbf{b}_f(\mathbf{x}, t)$ is known as the *body force* and expressed as force per unit current volume. The resultant force $\mathbf{f}$ applied in body can be express in integrand form by

$$\mathbf{f}(t) = \int_{\partial\Omega} \mathbf{t} ds + \int_{\Omega} \mathbf{b}_f dv. \tag{2.49}$$

Considering the kinetic energy term $\mathcal{K}$ for simulation of both static and dynamic loading cases we obtain the following *balance of energy rate* for purely mechanical (no thermal power induced) problems [Holzapfel, 2005, Section 4.4; Mase, 1970, Section 5.4],

$$\frac{d}{dt}\mathcal{K}(t) + \mathcal{P}_{int}(t) = \mathcal{P}_{ext}(t) \ , \tag{2.50}$$

where $\mathcal{P}_{int}$ and $\mathcal{P}_{ext}$ correspond to the *rate of internal* and *external work,* respectively, expressed in units of energy per unit time.

External mechanical power $\mathcal{P}_{ext}$ (or *rate of external mechanical work)* is the power input generated by the external forces represented in figure 2.5, when applied on the geometrical region Ω occupied by the body β at time t, and given by

$$\mathcal{P}_{ext}(t) = \int_{\partial\Omega} \mathbf{t} \cdot \mathbf{v}_f ds + \int_{\Omega} \mathbf{b}_f \cdot \mathbf{v}_f dv. \tag{2.51}$$

In the spatial form the *internal mechanical power* $\mathcal{P}_{int}$ (or *rate of internal mechanical work)* describes the mechanical response of a region Ω occupied by the body β at time t

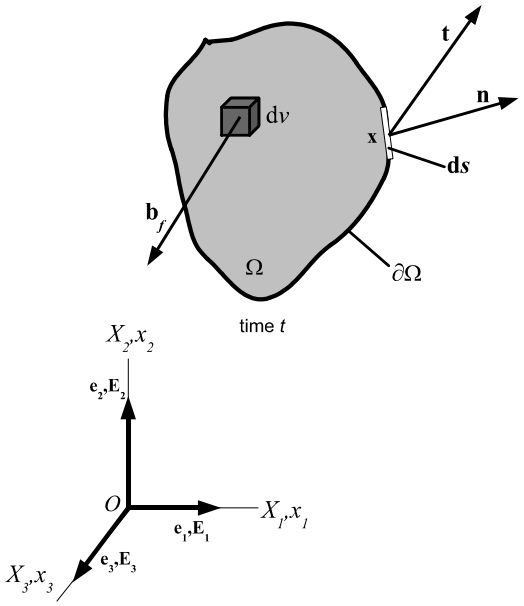


Figure 2.5: System of forces acting in the current configuration.

done by the Cauchy stress field σ, and is expressed by

$$\mathcal{P}_{int}(t) = \int_{\Omega} \boldsymbol{\sigma} : \mathbf{d} dv = \int_{\Omega} \mathrm{tr}(\boldsymbol{\sigma}^T \mathbf{d}) dv. \tag{2.52}$$

In (2.52), $\mathbf{d} = \frac{1}{2}(\mathbf{l} + \mathbf{l}^T)$ is the *rate of deformation tensor* (or strain velocity) corresponding to the symmetric part of *spatial velocity gradient* $\mathbf{l}$, given by $\mathbf{l} = \partial \mathbf{v}_f(\mathbf{x},t)/\partial \mathbf{x}$, where the *spatial velocity field* is given by $\mathbf{v}_f = \partial \mathbf{x}/\partial t$ [Holzapfel, 2005, Section 2.7; Belytschko *et al.*, 2006, Section 3.3.3]

Internal mechanical power $\mathcal{P}_{int}$ is expressed by the variation in *internal potential energy* Υ_{int} with time [see Holzapfel, 2005, Section 4.4], expressed by

$$\mathcal{P}_{int}(t) = \frac{d\Upsilon_{int}}{dt}. \tag{2.53}$$

Internal potential energy Υ_{int} can be viewed as the *strain energy* (or *stored energy*) developed in the interior of the body during the deformation process resulted from the action of the applied system of forces. We can calculate the total value of Υ_{int} as

$$\Upsilon_{int}(t) = \int_{\Omega} \Psi dV \ , \tag{2.54}$$

where Ψ is the *strain energy density function* defined per unit reference volume. Some forms of strain energy density functions will be analyzed in more detail in section 2.3.

The kinetic energy $\mathcal{K}$ of a body β occupying a region Ω in a time instant t is given by

$$\mathcal{K}(t) = \frac{1}{2} \int_{\Omega} \varrho \mathbf{v}_f^2 dv \ , \tag{2.55}$$

where scalar ϱ corresponds to the material density at the current configuration and $\mathbf{v}_f$ is the spatial velocity field.

Considering a *stationary system* [see Çengel & Boles, 1989, Section 1.4] we can state that the change in kinetic energy is null and consequently $\frac{d\mathcal{K}(t)}{dt} = 0$. For this particular case, equation (2.50) reduces to

$$\mathcal{P}_{int}(t) = \mathcal{P}_{ext}(t) \ , \tag{2.56}$$

which states that in a stationary case all the external power introduced in the system (by external forces) is converted into internal power.

Internal power $\mathcal{P}_{int}(t)$ generated in function of the applied external power $\mathcal{P}_{ext}(t)$ alter the state of energy in the material. In microscopic terms the contribution of each material structure for the developed internal energy must be a sum of all energy forms

[Çengel & Boles, 1989, Section 1.4; Holzapfel, 2005, Section 4.4; Mase, 1970, Section 5.4]. The thermodynamical state variable $u(\mathbf{x}, t)$ is known as the *specific internal energy* [see Truesdell & Noll, 2004, Section 79] defined as energy per unit of current volume. The *total internal energy* $\mathcal{U}(t)$ of a body β, occupying a region Ω in the time instant t is given by

$$\mathcal{U}(t) = \int_{\Omega} u(x,t)dv. \tag{2.57}$$

Considering a purely mechanical system we can state that the internal power $\mathcal{P}_{int}$ (work done in the body by the internal stress) equals the rate of internal energy $\mathcal{U}$ [see Holzapfel, 2005, Section 4.4]. It follows that

$$\frac{d\mathcal{U}(t)}{dt} = \mathcal{P}_{int}(t)\cdot \tag{2.58}$$

The balance of mechanical energy expressed in (2.50) can now be rewritten in terms of total internal energy $\mathcal{U}(t)$ by

$$\frac{d\mathcal{K}(t)}{dt} + \frac{d\mathcal{U}(t)}{dt} = \mathcal{P}_{ext}(t)\ , \tag{2.59}$$

or expressed in integrand form by

$$\underbrace{\frac{d}{dt}\int_{\Omega}(\frac{1}{2}\varrho\mathbf{v}_f^2 + u)dv}_{Total\ energy} = \underbrace{\int_{\partial\Omega}\mathbf{t}\cdot\mathbf{v}_f ds + \int_{\Omega}\mathbf{b}\cdot\mathbf{v}_f dv}_{\mathcal{P}_{ext}}\,. \tag{2.60}$$

The sum of the terms (kinetic $\mathcal{K}$ and internal energy $\mathcal{U}$) in the left hand side give us the *total energy* of the system that equals the external power $\mathcal{P}_{ext}$ (see expression 2.60). It means that for a purely mechanical system all the contributions to the total energy of a system are due to external sources.

2.1.3.2 Thermomechanical balance

In section 2.1.3.1 we analyzed the balance equations for a purely mechanical case. In the present section we analyze the case where a continuum possesses both mechanical and thermal energy that can be induced by external sources (heat fluxes) or internally, by energy dissipative phenomena such as hysteresis.

The thermomechanical system possesses thermal and mechanical derived energies. *Thermal (non-mechanical) power* $\mathcal{Q}$ in the spatial form is defined by

$$\mathcal{Q}(t) = -\int_{\partial\Omega} \mathbf{q} \cdot \mathbf{n} ds + \int_{\Omega} r_h dv. \tag{2.61}$$

Vector field $\mathbf{q}$ is known as *heat flux per unit time and current area* entering the body Ω. *External or internal volumetric heat sources* defined per unit time and unit volume are denoted by the scalar variable r_h. The integrand term $-\int_{\partial\Omega} \mathbf{q} \cdot \mathbf{n} ds$ computes the rate at which heat enters the body across the current boundary surface $\partial\Omega$ of the body Ω. The rate at which heat is internally generated in the body Ω is given by $\int_{\Omega} r_h dv$.

In figure 2.6 is presented a scheme with the heat fluxes acting in the current configuration Ω of the continuum body β.

Adding the thermal power $\mathcal{Q}(t)$ term to expression (2.58) we obtain

$$\frac{d\mathcal{U}(t)}{dt} = \mathcal{P}_{int}(t) + \mathcal{Q}(t). \tag{2.62}$$

Substituting $\mathcal{P}_{int}(t)$ in equation (2.50), we obtain

$$\frac{d\mathcal{K}(t)}{dt} + \frac{d\mathcal{U}(t)}{dt} = \mathcal{P}_{ext}(t) + \mathcal{Q}(t). \tag{2.63}$$

Equation (2.63) postulates a *thermomechanical energy balance*, known as the *first law of thermodynamics* [Çengel & Boles, 1989, Chapter 3; Mase, 1970, Section 5.4] in the rate

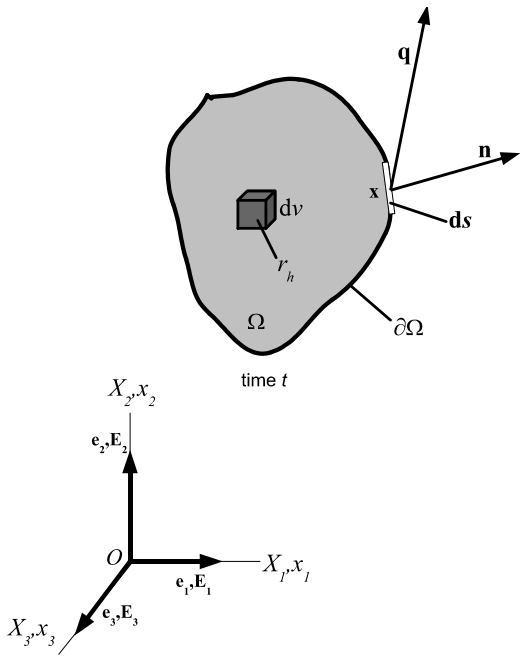


Figure 2.6: Heat fluxes acting in the current configuration.

form. In the integrand form, the first law of thermodynamics is given by the expression

$$\frac{d}{dt}\int_{\Omega}(\frac{1}{2}\varrho\mathbf{v}_f^2+u)dv=\int_{\partial\Omega}(\mathbf{t}\cdot\mathbf{v}_f-\mathbf{q}\cdot\mathbf{n})ds+\int_{\Omega}(\mathbf{b}_f\cdot\mathbf{v}_f+r_h)dv\ , \tag{2.64}$$

based in equation (2.60).

2.2 Constitutive equations

In section 2.1 we introduced fundamental concepts associated with continuum mechanics, namely, kinematics, strain and stress tensors and energy balance equations. In the present section we will discuss *constitutive equations* that model the mechanical behaviour of nonlinear elastic materials. Concepts such as hyperelasticity and strain energy functions will be discussed in this section.

The material mechanical response to applied external forces is defined mathematically by a *constitutive equation*. A constitutive equation establish a mathematical relationship among mechanical or thermal (or other) variables and must predict the observed behaviour of the material that intends to model.

Constitutive equations must obey to the *principle of objectivity*[4] [Ogden, 2005, Section 4.1; Holzapfel, 2005, Section 5.4; Truesdell & Noll, 2004, Section 19]. Succinctly, this principle state that the mechanical response must be invariant under changes of frame of reference. In other words, constitutive equations must be invariant to rigid-body motions. If this principle is violated, constitutive equations are affected by rigid-body motions producing meaningless results.

In section 2.2.1 we will treat constitutive equations for *simple materials*[5] assuming pure nonlinear mechanical problems (no temperature dependence), disregarding all non-mechanical influences.

A more detailed review of nonlinear constitutive equations can be found in the books from [Truesdell & Noll, 2004, Sections 26, 27 and 28], Ogden [2005], [Holzapfel, 2005, Chapter 6] and Fu & Ogden [2002].

2.2.1 Hyperelasticity

For many materials such as rubber or rubber-like materials such as CPGC - Cork Polyurethane Gel Composite, the stress-strain response is nonlinear which invalidate the

[4] also refered as the principle of material objectivity or principle of material-frame indiference.

[5] a simple material is dependent only on the history of the deformation gradient [see Truesdell & Noll, 2004, Section 28].

use of linear elasticity theories to describe their mechanical behaviour in practical situations.

Large deformation problems can be modelled using the *hyperelasticity* (or *finite elasticity*) *theory* that enables the numerical modelling of nonlinear elastic materials that undergoes large (or finite) deformations. This theory postulate that the stress-strain response of a *hyperelastic* material derives from a *strain energy density function* (defined as strain energy per unit volume).

For an elastic material the constitutive equation is of the form

$$\mathbf{P} = \mathfrak{G}(\mathbf{F}) \ , \tag{2.65}$$

where $\mathfrak{G}$ represents the *response function* of a *simple elastic material*[6] [Truesdell & Noll, 2004, Section 43; Holzapfel, 2005, Section 6.1] and $\mathbf{P}$ represents the first Piola-Kirchhoff stress tensor as described in expression (2.43).

Hyperelastic materials are a subclass of elastic materials. For the special case of hyperelastic materials, expression (2.65) is given by

$$\mathbf{P} = \mathfrak{G}(\mathbf{F}) = \frac{\partial \Psi(\mathbf{F})}{\partial \mathbf{F}} \ , \tag{2.66}$$

where Ψ refers to the strain energy density function [Holzapfel, 2005, Section 6.1; Truesdell & Noll, 2004, Section 82].

Cauchy stress $\boldsymbol{\sigma}$ can be expressed by response function $\mathfrak{G}(\mathbf{F})$, combining expression (2.43) with (2.66). It follows that

$$\boldsymbol{\sigma} = \mathfrak{g}(\mathbf{F}) = J^{-1} \underbrace{\frac{\partial \Psi(\mathbf{F})}{\partial \mathbf{F}}}_{\mathbf{P}} \mathbf{F}^T = J^{-1} \mathbf{F} \left(\frac{\partial \Psi(\mathbf{F})}{\partial \mathbf{F}} \right)^T = \boldsymbol{\sigma}^T. \tag{2.67}$$

Is evident from constitutive equations (2.66) and (2.67), that the state of stress is determined based on strain energy values derived from kinematic variables such as the deformation gradient $\mathbf{F}$.

Knowing that the strain energy function Ψ must be *objective*[7] [Holzapfel, 2005, Section 6.1; Truesdell & Noll, 2004, Section 84] we can write

$$\Psi(\mathbf{F}) = \Psi(\mathbf{C}) = \Psi(\mathbf{E}). \tag{2.68}$$

Important *reduced constitutive equations* in terms of the symmetrical right Cauchy-Green deformation tensor $\mathbf{C}$ are obtained

[6] in the work from Ogden [2005] the definition of *Cauchy elastic material* is used.

[7] objectivity implies that under a rigid body motion the strain energy remains unchanged.

$$\boldsymbol{\sigma} = 2J^{-1}\mathbf{F}\frac{\partial\Psi(\mathbf{C})}{\partial\mathbf{C}}\mathbf{F}^T \ , \tag{2.69}$$

$$\mathbf{P} = 2\mathbf{F}\frac{\partial\Psi(\mathbf{C})}{\partial\mathbf{C}} \ , \tag{2.70}$$

and

$$\mathbf{S} = 2\frac{\partial\Psi(\mathbf{C})}{\partial\mathbf{C}} = \frac{\partial\Psi(\mathbf{E})}{\partial\mathbf{E}}. \tag{2.71}$$

[Truesdell & Noll, 2004, Section 84; Holzapfel, 2005, Section 6.1].

2.2.2 Isotropic hyperelasticity

In this section we will outline some concepts associated to isotropy and isotropic hyperelasticity such as strain invariants, representation theorem for invariants and spectral decomposition of isotropic tensors.

In a practical point of view a material is considered *isotropic* if its mechanical response is not dependent on the direction of the applied load. Materials such as rubber, unreinforced polymers and steel for instance, can be considered isotropic or quasi-isotropic. In experimental tests these materials behave similarly in all directions. By other hand, materials such as fibre-reinforced composites or biological materials have different mechanical properties in function of the direction of the applied load. These materials are called *anisotropic*.

Anisotropy will not be considered in the present section since we are interested in constitutive equations that predict the mechanical behaviour of nonlinear elastic isotropic materials.

A reduced form of constitutive equation representing the Cauchy's stress state for isotropic elastic materials is expressed by

$$\boldsymbol{\sigma} = \mathfrak{p}(\mathbf{b}) \ , \tag{2.72}$$

where $\mathbf{b}$ is the symmetric left Cauchy-Green deformation tensor [see Truesdell & Noll, 2004, Section 47]. A material that can be represented by equation (2.72) and obey to the property derived from the principle of objectivity expressed by

$$\mathbf{Q}\mathfrak{p}(\mathbf{b})\mathbf{Q}^T = \mathfrak{p}(\mathbf{Q}\mathbf{b}\mathbf{Q}^T) \ , \tag{2.73}$$

is considered *isotropic* [Holzapfel, 2005, Section 5.4; Truesdell & Noll, 2004, Section 47; Ogden, 2005, Section 4.2.6; Fu & Ogden, 2002, Section 1.2.3.2]. In expression (2.73) $\mathbf{Q}$ is a proper orthogonal tensor (rotation tensor).

Since the tensor-valued function $\mathfrak{p}$ is an isotropic function and following the *Rivlin-Ericksen representation theorem* [Truesdell & Noll, 2004, Section 13, 47; Holzapfel, 2005, Section 5.4] we obtain for the response function $\mathfrak{p}$ the following expression

$$\boldsymbol{\sigma} = \mathfrak{p}(\mathbf{b}) = \beth_0\mathbf{I} + \beth_1\mathbf{b} + \beth_2\mathbf{b}^2 \qquad \text{with} \qquad \beth_a = \beth_a[I_1(\mathbf{b}), I_2(\mathbf{b}), I_3(\mathbf{b})]. \tag{2.74}$$

In expression (2.74) the coefficients $\beth_a, a = 0, 1, 2$, functions of the *strain invariants* $I_b(\mathbf{b}), b = 1, 2, 3$, are called the *response coefficients*. The strain invariants $I_b(\mathbf{b}), b = 1, 2, 3$ of tensor $\mathbf{b}$ are expressed by

$$I_1(\mathbf{b}) = \lambda_1^2 + \lambda_2^2 + \lambda_3^2 \ , \tag{2.75}$$

$$I_2(\mathbf{b}) = \frac{1}{2}[(\operatorname{tr}\mathbf{b})^2 - \operatorname{tr}(\mathbf{b}^2)] = \lambda_1^2\lambda_2^2 + \lambda_1^2\lambda_3^2 + \lambda_2^2\lambda_3^2 \ , \tag{2.76}$$

$$I_3(\mathbf{b}) = \det\mathbf{b} = J^2 = \lambda_1^2\lambda_2^2\lambda_3^2. \tag{2.77}$$

where scalars $\lambda_a^2,\ a = 1, 2, 3$ are the squared eigenvalues[8] of the stretch tensor $\mathbf{U}$.

For an isotropic hyperelastic material the strain energy density function Ψ can be expressed by the identity [Holzapfel, 2005, Section 6.2; Truesdell & Noll, 2004, Section 85]

$$\Psi(\mathbf{C}) = \Psi(\mathbf{b}). \tag{2.78}$$

Following the *representation theorem for invariants* [see Truesdell & Noll, 2004, Section 10] the scalar-valued isotropic tensor function expressed in (2.78) can be written in terms of the strain invariants of the symmetric deformation tensors $\mathbf{C}$ and $\mathbf{b}$. It follows that

$$\Psi = \Psi[I_1(\mathbf{C}),\ I_2(\mathbf{C}),\ I_3(\mathbf{C})] = \Psi[I_1(\mathbf{b}),\ I_2(\mathbf{b}),\ I_3(\mathbf{b})]. \tag{2.79}$$

Since deformation tensors $\mathbf{C}$ and $\mathbf{b}$ have the same eigenvalues (principal stretches squared) $\lambda_a^2,\ a = 1, 2, 3$, we can express the following identities:

$$I_1(\mathbf{C}) = I_1(\mathbf{b}),\ I_2(\mathbf{C}) = I_2(\mathbf{b}),\ I_3(\mathbf{C}) = I_3(\mathbf{b}). \tag{2.80}$$

The second Piola-Kirchhoff stress tensor $\mathbf{S}$ is given by the reduced constitutive equation expressed in (2.71). It follows for an isotropic material that

[8] see definition in section 2.1.1.9.

$$\mathbf{S} = 2\frac{\partial \Psi(\mathbf{C})}{\partial \mathbf{C}} \qquad \text{with} \qquad \frac{\partial \Psi(\mathbf{C})}{\partial \mathbf{C}} = \frac{\partial \Psi}{\partial I_b}\frac{\partial I_b}{\partial \mathbf{C}} \ , \ b = 1, 2, 3. \tag{2.81}$$

To calculate $\mathbf{S}$ in (2.81) we need to know the derivatives of strain invariants $I_b(\mathbf{b}), b = 1, 2, 3$, with respect to the tensor $\mathbf{C}$. These derivatives are expressed as follows [see Holzapfel, 2005, Section 6.2]:

$$\frac{\partial I_1}{\partial \mathbf{C}} = \frac{\partial \operatorname{tr} \mathbf{C}}{\partial \mathbf{C}} = \mathbf{I} \ , \tag{2.82}$$

$$\frac{\partial I_2}{\partial \mathbf{C}} = \left(2 \operatorname{tr} \mathbf{C}\mathbf{I} - \frac{\partial \operatorname{tr}(\mathbf{C}^2)}{\partial \mathbf{C}}\right) = I_1\mathbf{I} - \mathbf{C} \ , \tag{2.83}$$

$$\frac{\partial I_3}{\partial \mathbf{C}} = I_3\mathbf{C}^{-1}. \tag{2.84}$$

Rewriting expression (2.81) using expressions (2.82), (2.83) and (2.84) we obtain the general constitutive equation form for the second Piola-Kirchhoff stress tensor $\mathbf{S}$, expressed by

$$\mathbf{S} = 2\left[\left(\frac{\partial \Psi}{\partial I_1} + I_1\frac{\partial \Psi}{\partial I_2}\right)\mathbf{I} - \frac{\partial \Psi}{\partial I_2}\mathbf{C} + I_3\frac{\partial \Psi}{\partial I_3}\mathbf{C}^{-1}\right]\cdot \tag{2.85}$$

Using expression (2.46) we obtain the Piola transformation $\boldsymbol{\sigma} = J^{-1}\mathbf{F}\mathbf{S}\mathbf{F}^T$. Applying this transformation to expression (2.85) we obtain the general constitutive equation for the Cauchy stress tensor $\boldsymbol{\sigma}$, given by

$$\boldsymbol{\sigma} = 2J^{-1}\left[\left(\frac{\partial \Psi}{\partial I_1} + I_1\frac{\partial \Psi}{\partial I_2}\right)\mathbf{b} - \frac{\partial \Psi}{\partial I_2}\mathbf{b}^2 + I_3\frac{\partial \Psi}{\partial I_3}\mathbf{I}\right]\cdot \tag{2.86}$$

Relating expressions (2.86) and (2.74) we can conclude that the response coefficients $\beth_a, a = 0, 1, 2$, are expressed as

$$\beth_0 = 2J\frac{\partial \Psi}{\partial I_3}, \tag{2.87}$$

$$\beth_1 = 2J^{-1}\left(\frac{\partial \Psi}{\partial I_1} + I_1\frac{\partial \Psi}{\partial I_2}\right), \tag{2.88}$$

$$\beth_2 = -2J^{-1}\frac{\partial \Psi}{\partial I_2}. \tag{2.89}$$

Until now we outlined constitutive equations based on strain invariants for isotropic hyperelastic materials but it is often the case in isotropic hyperelasticity that the constitutive equations are obtained based in the principal stretches $\lambda_a, \ a = 1, 2, 3$, (eigenvalues of the strain tensors)

From expression (2.79) we may represent the strain energy density Ψ function as

$$\Psi(\mathbf{C}) = \Psi(\mathbf{b}) = \Psi(\lambda_1,\ \lambda_2,\ \lambda_3). \tag{2.90}$$

Based on expression (2.90) we can obtain new constitutive laws for the material's isotropic mechanical response with respect to the principal stretches. The first Piola-Kirchhoff stress components $P_a,\ a = 1,\ 2,\ 3$ are given by

$$P_a = \frac{\partial \Psi}{\partial \lambda_a}, \qquad a = 1,\ 2,\ 3, \tag{2.91}$$

(compare with expression (2.66)). The constitutive equation for the Cauchy stresses $\sigma_a,\ a = 1,\ 2,\ 3$ is expressed by

$$\sigma_a = J^{-1}\lambda_a \frac{\partial \Psi}{\partial \lambda_a}, \qquad a = 1,\ 2,\ 3, \tag{2.92}$$

(compare with expression (2.67)). For the components of the second Piola-Kirchhoff stress tensor $\mathbf{S}$ we obtain the expression

$$S_a = \frac{1}{\lambda_a}\frac{\partial \Psi}{\partial \lambda_a}, \qquad a = 1,\ 2,\ 3. \tag{2.93}$$

Based on expressions (2.43) and (2.46) we can write the components of the stress tensors $\mathbf{P}$ and $\mathbf{S}$ as

$$P_a = J\lambda_a^{-1}\sigma_a \qquad \text{and} \qquad S_a = J\lambda_a^{-2}\sigma_a, \qquad a = 1,\ 2,\ 3. \tag{2.94}$$

Using spectral decomposition in the same way used for the decomposition of strain tensors in section 2.1.1.9 we obtain for the stress tensors $\mathbf{P}$, $\mathbf{S}$ and $\boldsymbol{\sigma}$ the following expressions:

$$\mathbf{P} = \sum_{a=1}^{3} P_a \mathbf{n}_a \otimes \mathbf{N}_a = \sum_{a=1}^{3} \frac{\partial \Psi}{\partial \lambda_a}\mathbf{n}_a \otimes \mathbf{N}_a\ , \tag{2.95}$$

$$\mathbf{S} = \sum_{a=1}^{3} S_a \mathbf{N}_a \otimes \mathbf{N}_a = \sum_{a=1}^{3} \frac{1}{\lambda_a}\frac{\partial \Psi}{\partial \lambda_a}\mathbf{N}_a \otimes \mathbf{N}_a \tag{2.96}$$

and

$$\boldsymbol{\sigma} = \sum_{a=1}^{3} \sigma_a \mathbf{n}_a \otimes \mathbf{n}_a = J^{-1}\sum_{a=1}^{3} \lambda_a \frac{\partial \Psi}{\partial \lambda_a}\mathbf{n}_a \otimes \mathbf{n}_a. \tag{2.97}$$

2.2.3 Incompressible hyperelastic materials

Some materials such as rubber, can sustain large deformations conserving the volume during the deformation process. Most elastomers are characterized by a large *bulk modulus* K (low compressibility) when compared with its *shear modulus* μ. The relative compressibility of a material can be indirectly measured by the ratio between the initial bulk modulus and the initial shear modulus K_0/μ_0, related with the material's initial Poisson's ratio υ_0 by

$$\upsilon_0 = \frac{3K_0/\mu_0 - 2}{6K_0/\mu_0 + 2} \tag{2.98}$$

[see ABAQUS®, 2006, Analysis User's Manual, Section 17.5.1].

In table 2.2 are summarized indicative values for the ratio K_0/μ_0 and correspondent values of initial Poisson's ratio. A linear elastic material is considered incompressible if its Poisson's coefficient υ is set equal to 0.5.

In continuum mechanics a material is considered *incompressible* if its susceptible only of *isochoric* motions. A motion is considered isochoric if

$$\det \mathbf{F} = J = 1 \ , \tag{2.99}$$

where J is the volume ratio expressed by equation (2.19).

For an incompressible elastic material the first Piola-Kirchhoff stress tensor $\mathbf{P}$ defined in (2.65) is replaced by an extra stress component $\mathbf{P}_E$ [see Truesdell & Noll, 2004, Section 43] given by

$$\mathbf{P}_E = \mathbf{P} + p\mathbf{F}^{-T} \ , \tag{2.100}$$

where the scalar p is a *Lagrange multiplier* known as the *hydrostatic pressure* [Truesdell & Noll, 2004, Section 30, 43, Holzapfel, 2005, Section 6.3; Ogden, 2005, Section 4.2.7; Fu & Ogden, 2002, Section 1.2.4].

Table 2.2: Representative values of initial modulus ratio and correspondence with initial Poisson's ratio.

K_0/μ_0	Initial Poisson's ratio υ_0
10	0.452
20	0.475
50	0.490
100	0.495
1000	0.4995
10000	0.49995

For incompressible hyperelastic materials the general stress response $\mathfrak{G}(\mathbf{F})$ defined in (2.66) is reformulated and given by

$$\mathbf{P} = \mathfrak{G}(\mathbf{F}) - p\mathbf{F}^{-T} = \frac{\partial \Psi(\mathbf{F})}{\partial \mathbf{F}} - p\mathbf{F}^{-T}. \tag{2.101}$$

The Cauchy stress tensor $\boldsymbol{\sigma}$ can be calculated from expression (2.101) using the stress transformation in (2.44).We find that

$$\boldsymbol{\sigma} = \frac{\partial \Psi(\mathbf{F})}{\partial \mathbf{F}}\mathbf{F}^T - p\underbrace{\mathbf{F}^{-T}\mathbf{F}^T}_{\mathbf{I}} = \frac{\partial \Psi(\mathbf{F})}{\partial \mathbf{F}}\mathbf{F}^T - p\mathbf{I}. \tag{2.102}$$

Applying expression (2.47) to (2.101) and using (2.71) we obtain the second Piola-Kirchhoff stress tensor $\mathbf{S}$ for incompressible materials expressed by

$$\mathbf{S} = \mathbf{F}^{-1}\frac{\partial \Psi(\mathbf{F})}{\partial \mathbf{F}} - p\underbrace{\mathbf{F}^{-1}\mathbf{F}^{-T}}_{\mathbf{C}^{-1}} = 2\frac{\partial \Psi}{\partial \mathbf{C}} - p\mathbf{C}^{-1}. \tag{2.103}$$

2.2.4 Isotropic incompressible hyperelasticity

As stated in section (2.2.2) isotropic materials can be expressed in function of three strain invariants[9] of the symmetric strain tensors $\mathbf{C}$ and $\mathbf{b}$ (see equation 2.79). For the particular case of incompressible materials the dependence of the strain energy function in the third invariant I_3 vanishes due to the incompressibility constraint ($I_3(\mathbf{C}) = I_3(\mathbf{b}) = 1$). Reformulating expression (2.79) for the particular case of isotropic incompressible materials, we obtain

$$\Psi = \Psi[I_1(\mathbf{C}),\ I_2(\mathbf{C})] - \frac{1}{2}p(I_3 - 1) = \Psi[I_1(\mathbf{b}),\ I_2(\mathbf{b})] - \frac{1}{2}p(I_3 - 1) \tag{2.104}$$

[see Holzapfel, 2005, Section 6.3].

In equation (2.104) the scalar $p/2$ acts as a Lagrange multiplier.

The second Piola-Kirchhoff stress tensor $\mathbf{S}$ for incompressible materials is obtained in a similar manner used for the calculus of (2.85). It follows that

$$\mathbf{S} = 2\frac{\partial \Psi[I_1(\mathbf{C}),\ I_2(\mathbf{C})]}{\partial \mathbf{C}} - \frac{\partial [p(I_3 - 1)]}{\partial \mathbf{C}}. \tag{2.105}$$

Applying the chain rule and using the derivatives expressed in (2.82), (2.83) and (2.84) we find that

$$\mathbf{S} = 2\left[\left(\frac{\partial \Psi}{\partial I_1} + I_1\frac{\partial \Psi}{\partial I_2}\right)\mathbf{I} - \frac{\partial \Psi}{\partial I_2}\mathbf{C}\right] - p\mathbf{C}^{-1}. \tag{2.106}$$

[9] following the representation theorem for invariants.

Applying the transformation $\mathbf{P} = \mathbf{FS}$ [see Holzapfel, 2005, Section 3.4] in expression (2.106) we obtain

$$\mathbf{P} = 2\mathbf{F}\left[\left(\frac{\partial\Psi}{\partial I_1} + I_1\frac{\partial\Psi}{\partial I_2}\right)\mathbf{I} - \frac{\partial\Psi}{\partial I_2}\mathbf{C}\right] - p\mathbf{F}^{-T}. \tag{2.107}$$

The Cauchy stress tensor $\boldsymbol{\sigma}$ for incompressible materials is computed using relation expressed in (2.44). With the incompressibility constraint $J = 1$, we obtain

$$\boldsymbol{\sigma} = 2\left[\left(\frac{\partial\Psi}{\partial I_1} + I_1\frac{\partial\Psi}{\partial I_2}\right)\mathbf{b} - \frac{\partial\Psi}{\partial I_2}\mathbf{b}^2\right] - p\mathbf{I}. \tag{2.108}$$

Comparing the constitutive equation for incompressible materials expressed in (2.108) with the general form expressed in (2.86) we conclude that the response coefficients expressed in (2.88) and (2.89) are now expressed by

$$\beth_1 = 2\left(\frac{\partial\Psi}{\partial I_1} + I_1\frac{\partial\Psi}{\partial I_2}\right) , \tag{2.109}$$

$$\beth_2 = -2\frac{\partial\Psi}{\partial I_2}. \tag{2.110}$$

In terms of the principal stretches $\lambda_a,\ a = 1, 2, 3$, the constitutive equation (2.91) is now expressed by

$$P_a = -\frac{1}{\lambda_a}p + \frac{\partial\Psi}{\partial\lambda_a}, \qquad a = 1,\ 2,\ 3. \tag{2.111}$$

The components of the second Piola-Kirchhoff stress tensor $\mathbf{S}$ are given by

$$S_a = -\frac{1}{\lambda_a^2}p + \frac{1}{\lambda_a}\frac{\partial\Psi}{\partial\lambda_a}, \qquad a = 1,\ 2,\ 3. \tag{2.112}$$

The Cauchy stress components are obtained through

$$\sigma_a = -p + \lambda_a\frac{\partial\Psi}{\partial\lambda_a}, \qquad a = 1,\ 2,\ 3. \tag{2.113}$$

Considering the incompressibility constraint ($J = \lambda_1\lambda_2\lambda_3 = 1$), relations in (2.94) are replaced by

$$P_a = \lambda_a^{-1}\sigma_a \qquad \text{and} \qquad S_a = \lambda_a^{-2}\sigma_a\ , \qquad a = 1,\ 2,\ 3. \tag{2.114}$$

2.2.5 Compressible hyperelasticity

In section 2.2.3 the incompressible behaviour of hyperelastic materials was presented. For these materials the change in volume during the deformation is considered to be null ($J = 1$). By other hand, some materials such as foamed elastomers can undergo changes in volume during the deformation process that must be accounted for the correct prediction of the real mechanical behaviour of the material.

Some constitutive equations that characterize the mechanical behaviour of *compressible hyperelastic materials* will be outlined in this section. We will discuss in this section the decoupled approach used for the modelling of compressible materials and compressible hyperelasticity in terms of strain invariants, considering isotropic behaviour.

In compressible hyperelasticity is common to split the deformation gradient tensor $\mathbf{F}$ and respective strain measures such as $\mathbf{C} = \mathbf{F}^T\mathbf{F}$ into *deviatoric* (volume-preserving) and *volumetric* (volume-changing) terms [Holzapfel, 2005, Section 6.4; Ogden, 2005, Section 2.2.6]. The multiplicative decomposition of the deformation gradient $\mathbf{F}$ is given by

$$\mathbf{F} = (J^{1/3}\mathbf{I})\overline{\mathbf{F}} \ , \tag{2.115}$$

where $\overline{\mathbf{F}}$ is the *modified deformation gradient* that conforms to the constraint

$$\det \overline{\mathbf{F}} = \bar{\lambda}_1\bar{\lambda}_2\bar{\lambda}_3 = 1 \ , \tag{2.116}$$

with

$$\bar{\lambda}_a = J^{-1/3}\lambda_a \qquad a = 1,\ 2,\ 3. \tag{2.117}$$

The right Cauchy-Green strain tensor $\mathbf{C}$ can be decomposed using the same methodology followed in (2.115). It follows that

$$\mathbf{C} = (J^{2/3}\mathbf{I})\overline{\mathbf{C}} \ , \tag{2.118}$$

where $\overline{\mathbf{C}}$ is the modified right Cauchy-Green strain tensor characterized by

$$\det \overline{\mathbf{C}} = (\det \overline{\mathbf{F}})^2 = 1. \tag{2.119}$$

From expressions (2.116) and (2.118) we can say that the terms $J^{1/3}\mathbf{I}$ and $J^{2/3}\mathbf{I}$ model the the volumetric (volume-changing) deformations while the components $\overline{\mathbf{F}}$ and $\overline{\mathbf{C}}$ are associated with deviatoric (volume-preserving) deformations as defined kinematically in (2.116) and (2.119), respectively.

Writing the strain energy density function Ψ in terms of the symmetrical strain tensor $\mathbf{C}$ as outlined in (2.68) and based on the kinematical assumptions made in (2.118) we

obtain a decoupled representation [see Holzapfel, 2005, Section 6.4] of the strain energy function $\Psi = \Psi(\mathbf{C})$ as sum of strain energy developed during the volumetric and deviatoric deformation processes. This decoupled representation is given by

$$\Psi(\mathbf{C}) = \Psi_{dev}(\overline{\mathbf{C}}) + \Psi_{vol}(J). \tag{2.120}$$

In (2.120), $\Psi_{dev}(\overline{\mathbf{C}})$ is the scalar-valued function that describes the purely deviatoric behaviour of the material and $\Psi_{vol}(J)$ is the term of the function that enables the characterization of the purely volumetric material's mechanical response.

The split of the strain energy function in (2.120) leads to the split of the constitutive equations. For the second Piola-Kirchhoff stress tensor we obtain

$$\mathbf{S} = 2\frac{\partial \Psi(\mathbf{C})}{\partial \mathbf{C}} = 2\left(\frac{\partial \Psi_{dev}(\overline{\mathbf{C}})}{\partial \mathbf{C}} + \frac{\partial \Psi_{vol}(J)}{\partial \mathbf{C}}\right) = \mathbf{S}_{dev} + \mathbf{S}_{vol}. \tag{2.121}$$

The components of (2.121), based on expression (2.81), are given by

$$\mathbf{S}_{vol} = 2\frac{\partial \Psi_{vol}(J)}{\partial \mathbf{C}} = 2\underbrace{\frac{\partial \Psi_{vol}(J)}{\partial J}}_{p}\frac{\partial J}{\partial \mathbf{C}} = pJ\mathbf{C}^{-1}\ , \tag{2.122}$$

$$\mathbf{S}_{dev} = 2\frac{\partial \Psi_{dev}(\overline{\mathbf{C}})}{\partial \mathbf{C}} = J^{-2/3}\underbrace{\left(\mathbb{I} - \frac{1}{3}\mathbf{C}^{-1}\otimes\mathbf{C}\right)}_{\mathbb{P}} : \underbrace{2\frac{\partial \Psi_{dev}(\overline{\mathbf{C}})}{\partial \overline{\mathbf{C}}}}_{\overline{\mathbf{S}}} \tag{2.123}$$

$$= J^{-2/3}\mathbb{P} : \overline{\mathbf{S}} = J^{-2/3}\,\mathrm{Dev}\,\overline{\mathbf{S}}, \tag{2.124}$$

[see Holzapfel, 2005, Section 6.4, pag. 230].

In expression (2.122) the scalar p represents the *hydrostatic pressure*. The deviatoric part of tensor $\mathbf{S}$ in (2.124) is obtained by applying the deviatoric operator Dev (through the fourth order projection tensor $\mathbb{P}$) to the so called *fictious second Piola-Kirchhoff stress tensor* $\overline{\mathbf{S}}$.[see Holzapfel, 2005, Sections 1.3 and 6.4].

In analogy with assumption (2.120), we can write for an isotropic compressible hyperelastic material a decoupled form of the strain energy density function Ψ in order to the left Cauchy-Green strain tensor $\mathbf{b}$. It follows that

$$\Psi(\mathbf{b}) = \Psi_{dev}(\overline{\mathbf{b}}) + \Psi_{vol}(J). \tag{2.125}$$

From expression (2.121) we can express the additive decomposition of the Cauchy stress tensor $\boldsymbol{\sigma}$ as

$$\boldsymbol{\sigma} = 2J^{-1}\mathbf{b}\frac{\partial \Psi(\mathbf{b})}{\partial \mathbf{b}} = \boldsymbol{\sigma}_{dev} + \boldsymbol{\sigma}_{vol}\ , \tag{2.126}$$

where the volumetric and deviatoric terms of the Cauchy stress tensor are given respectively by

$$\boldsymbol{\sigma}_{vol} = 2J^{-1}\mathbf{b}\frac{\partial\Psi(J)}{\partial\mathbf{b}} = 2J^{-1}\mathbf{b}\underbrace{\frac{\partial\Psi_{vol}(J)}{\partial J}}_{p}\frac{\partial J}{\partial\mathbf{C}} = p\mathbf{I} \tag{2.127}$$

and

$$\begin{aligned}\boldsymbol{\sigma}_{dev} &= 2J^{-1}\mathbf{b}\frac{\partial\Psi_{dev}(\overline{\mathbf{b}})}{\partial\mathbf{b}} = \mathbf{b}\left(J^{-2/3}\mathbb{I}-\frac{1}{3}\mathbf{b}^{-1}\otimes\overline{\mathbf{b}}\right)\overline{\mathbf{b}}^{-1} : \underbrace{2J^{-1}\frac{\partial\Psi_{dev}(\overline{\mathbf{b}})}{\partial\overline{\mathbf{b}}}\overline{\mathbf{b}}}_{\overline{\boldsymbol{\sigma}}} \\ &= \underbrace{\left(\mathbb{I}-\frac{1}{3}\mathbf{I}\otimes\mathbf{I}\right)}_{\mathbb{P}} : \overline{\boldsymbol{\sigma}} = \mathbb{P} : \overline{\boldsymbol{\sigma}} = \operatorname{dev}\overline{\boldsymbol{\sigma}}\end{aligned} \tag{2.128}$$

[see Holzapfel, 2005, Section 6.4, pag. 232].

In expression (2.128) has been introduced the so called *fictious Cauchy stress tensor* $\overline{\boldsymbol{\sigma}}$.

2.2.6 Compressible hyperelasticity in terms of invariants

As mentioned in section 2.2.2 an isotropic scalar-valued strain energy density function can be expressed in terms of the strain invariants of the symmetric strain tensors $\mathbf{C}$ and $\mathbf{b}$.

For a decoupled representation of the strain energy function Ψ and following identities (2.79), (2.120) and (2.125), we can write

$$\Psi = \Psi_{dev}[\overline{I}_1(\overline{\mathbf{C}}),\ \overline{I}_2(\overline{\mathbf{C}})] + \Psi_{vol}(J) = \Psi[\overline{I}_1(\overline{\mathbf{b}}),\ \overline{I}_2(\overline{\mathbf{b}})] + \Psi_{vol}(J).$$

where $\overline{I}_1$ and $\overline{I}_2$ are the *modified strain invariants* of the modified symmetric strain tensors $\overline{\mathbf{C}}$ and $\overline{\mathbf{b}}$. Since $\mathbf{C}$ and $\mathbf{b}$ have the same eigenvalues as expressed in section 2.2.2, it follows that

$$\overline{I}_1(\overline{\mathbf{C}}) = \overline{I}_1(\overline{\mathbf{b}}),\ \overline{I}_2(\overline{\mathbf{C}}) = \overline{I}_2(\overline{\mathbf{b}}).$$

By means of expressions (2.75), (2.76) and (2.77) we can define the modified strain invariants $\overline{I}_a,\ a = 1, 2, 3$, as

$$\overline{I}_1(\overline{\mathbf{C}}) = \overline{I}_1(\overline{\mathbf{b}}) = \operatorname{tr}(\overline{\mathbf{C}}) = \operatorname{tr}\overline{\mathbf{b}} = \bar{\lambda}_1^2 + \bar{\lambda}_2^2 + \bar{\lambda}_3^2\ , \tag{2.129}$$

$$\overline{I}_2(\overline{\mathbf{C}}) = \overline{I}_2(\overline{\mathbf{b}}) = \frac{1}{2}[(\operatorname{tr}\overline{\mathbf{C}})^2 - \operatorname{tr}(\overline{\mathbf{C}}^2)] = \frac{1}{2}[(\operatorname{tr}\overline{\mathbf{b}})^2 - \operatorname{tr}(\overline{\mathbf{b}}^2)] = \overline{\lambda}_1^2\overline{\lambda}_2^2 + \overline{\lambda}_1^2\overline{\lambda}_3^2 + \overline{\lambda}_2^2\overline{\lambda}_3^2 \quad (2.130)$$

and

$$\overline{I}_3(\overline{\mathbf{C}}) = \overline{I}_3(\overline{\mathbf{b}}) = \det\overline{\mathbf{C}} = \det\overline{\mathbf{b}}. \quad (2.131)$$

From expressions (2.117) and (2.118) we conclude that

$$\overline{I}_1(\overline{\mathbf{C}}) = \overline{I}_1(\overline{\mathbf{b}}) = J^{-2/3}I_1\ , \quad (2.132)$$

$$\overline{I}_2(\overline{\mathbf{C}}) = \overline{I}_2(\overline{\mathbf{b}}) = J^{-4/3}I_2 \quad (2.133)$$

and from (2.119) that

$$\overline{I}_3(\overline{\mathbf{C}}) = \overline{I}_3(\overline{\mathbf{b}}) = 1. \quad (2.134)$$

Using the decoupled representation of the second Piola-Kirchhoff stress tensor $\mathbf{S}$ we obtain

$$\begin{aligned}\mathbf{S}_{dev} &= 2\frac{\partial\Psi_{dev}(\overline{I}_1,\overline{I}_2)}{\partial\mathbf{C}} = J^{-2/3}\mathbb{P} : \underbrace{2\frac{\partial\Psi_{dev}(\overline{I}_1,\overline{I}_2)}{\partial\overline{\mathbf{C}}}}_{\overline{\mathbf{S}}} \\ &= J^{-2/3}\mathbb{P} : \overline{\mathbf{S}}\ = J^{-2/3}\operatorname{Dev}\overline{\mathbf{S}}\ , \end{aligned} \quad (2.135)$$

where the fictious second Piola-Kirchhoff stress tensor $\overline{\mathbf{S}}$ is given by

$$\overline{\mathbf{S}} = 2\left[\left(\frac{\partial\Psi_{dev}(\overline{I}_1,\overline{I}_2)}{\partial\overline{I}_1} + \overline{I}_1\frac{\partial\Psi_{dev}(\overline{I}_1,\overline{I}_2)}{\partial\overline{I}_2}\right)\mathbf{I} - \frac{\partial\Psi_{dev}(\overline{I}_1,\overline{I}_2)}{\partial\overline{I}_2}\overline{\mathbf{C}}\right], \quad (2.136)$$

[see Holzapfel, 2005, Section 6.4, pag. 234].

The volumetric part $\mathbf{S}_{vol}$ is given by expression (2.122).

Writing the Cauchy stress $\boldsymbol{\sigma}$ in the decoupled form in order to the strain invariants we obtain

$$\boldsymbol{\sigma}_{dev} = 2J^{-1}\mathbf{b}\frac{\partial \Psi_{dev}(\overline{I}_1, \overline{I}_2)}{\partial \mathbf{b}} = \mathbb{P} : \underbrace{2J^{-1}\overline{\mathbf{b}}\frac{\partial \Psi_{dev}(\overline{I}_1, \overline{I}_2)}{\partial \overline{\mathbf{b}}}}_{\overline{\boldsymbol{\sigma}}}$$

$$= \mathbb{P} : \overline{\boldsymbol{\sigma}} = \operatorname{dev} \overline{\boldsymbol{\sigma}} \tag{2.137}$$

with the fictious Cauchy stress $\overline{\boldsymbol{\sigma}}$ given by

$$\overline{\boldsymbol{\sigma}} = 2J^{-1}\left[\left(\frac{\partial \Psi_{dev}(\overline{I}_1, \overline{I}_2)}{\partial \overline{I}_1} + \overline{I}_1\frac{\partial \Psi_{dev}(\overline{I}_1, \overline{I}_2)}{\partial \overline{I}_2}\right)\overline{\mathbf{b}} - \frac{\partial \Psi_{dev}(\overline{I}_1, \overline{I}_2)}{\partial \overline{I}_2}\overline{\mathbf{b}}^2\right] \tag{2.138}$$

[see Holzapfel, 2005, Section 6.4, pag. 235].

2.3 Strain energy functions

In section 2.2.1 we find that the stress response of a hyperelastic material is dependent on a strain energy density function Ψ. In the literature we can found several forms of strain energy functions that can be based on *phenomenological* (macroscopic) or in *physical* (mesoscopic) aspects. Phenomenological strain energy functions such as the Rivlin model [Rivlin & Saunders, 1951] try to reproduce in a purely mathematical way the experimentally observed mechanical behaviour leading to adjustable material parameters that can have no physical meaning but mathematically reproduce the real behaviour of the material.

By other hand, physical strain energy functions predict the macroscopic behaviour of the material based on molecular aspects of the material. This approach have the advantage of computing material parameters that have a physical sense but the disadvantage of being extremely difficult to implement in theoretical terms [Marckmann, 2004].

In this section are outlined the most popular isotropic strain energy functions published in the literature and divided by the two referred approaches.

2.3.1 Phenomenological models

2.3.1.1 Rivlin's polynomial model

The Rivlin's model [Rivlin, 1948; Rivlin & Saunders, 1951] consists in a polynomial series of invariant terms $(I_1 - 3)$ and $(I_2 - 3)$, described by

$$\Psi = \sum_{i+j=1}^{N} C_{ij}(I_1 - 3)^i (I_2 - 3)^j, \tag{2.139}$$

where the scalar C_{ij} represents the adjustable *material parameters* and obtained through numerical fitting techniques.

The Rivlin's model in practical situations is truncated at 2^{nd} or 3^{th} expansion in order to avoid numerical instabilities normally associated with high order polynomials. Setting $N = 1$ in (2.139) we obtain the so called *Mooney-Rivlin model* given by

$$\Psi = C_{10}(I_1 - 3) + C_{01}(I_2 - 3), \tag{2.140}$$

that is a wide used model for the prediction of the mechanical behaviour of natural rubber at moderate deformations.

Setting now $N = 2$ in (2.139), we obtain the *second order polynomial model*, expressed by

$$\Psi = C_{10}(I_1 - 3) + C_{01}(I_2 - 3) + C_{20}(I_1 - 3)^2 + C_{11}(I_1 - 3)(I_2 - 3) + C_{02}(I_2 - 3)^2, \tag{2.141}$$

and characterized by five adjustable material parameters which increases the fitting capability of the model.

A third-order expansion of (2.139) was considered in the work by James *et al.* [1975].

In section 2.2.5 we discussed the possibility of a compressible strain energy function be written in the decoupled form $\bar{\Psi}$. By so, and for model in (2.139) we can write that

$$\Psi = \underbrace{\sum_{i+j=1}^{N} C_{ij}(\overline{I}_1 - 3)^i (\overline{I}_2 - 3)^j}_{\Psi_{dev}} + \underbrace{\sum_{i+j=1}^{N} \frac{1}{D_i}(J-1)^{2i}}_{\Psi_{vol}}, \tag{2.142}$$

where D_i and Cij are the *adjustable volumetric* and *deviatoric material parameters*, respectively. The decoupled form of strain energy functions is widelly used in nonlinear finite element packages [see ABAQUS®, 2006, Analysis User's Manual, Section 17.5] as it is often advantageous to separate the numerical treatments of the deviatoric and volumetric parts of the deformation gradient $\mathbf{F}$ [see Holzapfel, 2005, Sections 6.4, 8.5 and 8.6].

The *initial shear modulus* μ_0 and *initial bulk modulus* K_0 can be expressed in terms of the adjustable material parameters [see ABAQUS®, 2006, Analysis User's Manual, Section 17.5.1]. For the models expressed in (2.140) and (2.141) we have that the initial shear modulus μ_0 is given by

$$\mu_0 = 2(C_{10} + C_{01}), \tag{2.143}$$

and the initial bulk modulus K_0 expressed by

$$K_0 = \frac{2}{D_1}\cdot \tag{2.144}$$

2.3.1.2 Reduced polynomial form

The reduced polynomial models is expressed in terms of polynomial series of the first invariant I_1, and written by

$$\Psi = \sum_{i=1}^{N} C_{i0}(I_1 - 3)^i. \tag{2.145}$$

Neo-Hookean model The Neo-Hookean's model is the simplest models as it is expressed in terms of the first strain invariant I_1. It corresponds to the first order expansion of expression (2.145), given by

$$\Psi = C_{10}(I_1 - 3). \tag{2.146}$$

This model is suitable for modelling the material's response at low-moderate strains due to the limited fitting capabilities of this model arising from the existence of only one adjustable material parameter C_{10}.

Neo-Hookean model can also be derived from the *Gaussian statistical theory* of elasticity giving to this model special characteristics as it is derivable either from phenomenological or from physical theories. In other words, the adjustable material parameter C_{10} in (2.146) has a physical meaning as it is dependent on molecular aspects of the material.

Considering a vulcanized rubber composed of a three-dimensional molecular structure linked at some points in the structure, the Neo-Hookean model is given by

$$\Psi = \frac{1}{2}nkT(\lambda_1^2 + \lambda_2^2 + \lambda_3^2 - 3) = \frac{1}{2}\underbrace{nkT}_{\mu_0}(I_1 - 3)\ , \tag{2.147}$$

where n is the *number of chains* in a unit volume in the network, k is the *Boltzmann's constant* and T is the *absolute temperature* [see Holzapfel, 2005, Section 7.2].

Yeoh model Yeoh [Yeoh, 1990] published a model capable of representing the nonlinear mechanical behaviour of carbon-black filled rubber with the typical stiffening at large strains. The *Yeoh model* is obtained by setting $N = 3$ in (2.145) and expressed by

$$\Psi = C_{10}(I_1 - 3) + C_{20}(I_1 - 3)^2 + C_{30}(I_1 - 3)^3. \tag{2.148}$$

For the models based on the general form of reduced polynomial model, the initial shear modulus is given by

$$\mu_0 = 2C_{10} \ , \tag{2.149}$$

and the initial bulk modulus expressed by

$$K_0 = \frac{2}{D_1}\cdot \tag{2.150}$$

2.3.1.3 Gent model

The *Gent model* [Gent, 1996] is a non-polynomial model based on the first strain invariant I_1. It is a very popular model due to its mathematical simplicity and fitting capabilities [Bilgili, 2004]. The Gent model is expressed by

$$\Psi = -\frac{\mu_0}{2} J_m \ln\left(1 - \frac{I_1 - 3}{J_m}\right) \ , \tag{2.151}$$

where μ_0 corresponds to the initial shear modulus and J_m is a positive material parameter that identifies the upper limit of I_1 that can be associated to the molecular chain extensibility of the material.

Other models based on the Gent model were published in the literature such as the Pucci-Saccomandi model [Pucci & Saccomandi, 2002], expressed by

$$\Psi = -\frac{\mu_0}{2} J_m \ln\left(1 - \frac{I_1 - 3}{J_m}\right) + C_2 \ln\left(\frac{I_2}{3}\right) \ , \tag{2.152}$$

that differs from the model expressed in (2.151) by the inclusion of the adjustable material parameter C_2 at the second term of the equation associated with the contribution of the second strain invariant I_2.

2.3.1.4 Ogden model

In 1972, Ogden [Ogden, 1972b] published a model based on the principal stretches λ_a, $a = 1, 2, 3$. The *Ogden model* is given by

$$\Psi = \sum_{i=1}^{N} \frac{\mu_i}{\alpha_i} (\lambda_1^{\alpha_i} + \lambda_2^{\alpha_i} + \lambda_3^{\alpha_i} - 3) \ , \tag{2.153}$$

where the adjustable parameters μ_i and α_i corresponds to the shear moduli and to dimensionless adjustable constants, respectively. The initial shear modulus μ_0 is given by

$$2\mu_0 = \sum_{i=1}^{N} \mu_i \alpha_i. \tag{2.154}$$

For particular values of material constants, the Ogden model will reduce to either the Neo-Hookean model ($N = 1, \alpha = 2$) in (2.146) or to the Mooney-Rivlin model ($N = 2,\ \alpha_1 = 2,\ \alpha_2 = -2$) in (2.140).

As an example and setting $N = 1$ and $\alpha_1 = 2$ in (2.153) and based on expressions (2.149) and (2.75) we obtain

$$\Psi = \underbrace{\frac{\mu_1}{2}}_{C_{10}} (\underbrace{\lambda_1^2 + \lambda_2^2 + \lambda_3^2}_{I_1} - 3) = C_{10}(I_1 - 3)\ , \tag{2.155}$$

corresponding to the Neo-Hookean model expressed in (2.146).

An interesting study on the nonlinear fitting procedure of the Ogden model parameters can be found in Ogden *et al.* [2004]

2.3.1.5 Valandis and Landel hypothesis

Valandis and Landel [Valanis & Landel, 1967] postulated the hypothesis of a strain energy density function $\Psi = \Psi(\lambda_1,\ \lambda_2,\ \lambda_3)$ be expressed as the sum of its principal stretch components, i.e.

$$\Psi = \vartheta(\lambda_1) + \vartheta(\lambda_2) + \vartheta(\lambda_3). \tag{2.156}$$

Following the *Valanis and Landel hypothesis* we can write the Ogden model expressed in (2.153) as an additive decomposition, expressed by

$$\Psi = \Psi(\lambda_1,\ \lambda_2,\ \lambda_3) = \sum_{a=1}^{3} \vartheta(\lambda_a) \qquad \text{with} \qquad \vartheta(\lambda_a) = \sum_{b=1}^{3} \frac{\mu_b}{\alpha_b}(\lambda_a^{\alpha_b} - 1)\cdot \tag{2.157}$$

2.3.1.6 Varga model

The model proposed by Varga [Varga, 1966] is based on principal stretches $\lambda_a,\ a = 1, 2, 3$ and can be obtained through the Ogden model in (2.153), by setting $N = 1$ and $\alpha = 1$

$$\Psi = \sum_{i=1}^{N} c_1(\lambda_1 + \lambda_2 + \lambda_3 - 3)\ , \tag{2.158}$$

with the constant $c_1 = \mu_1$.

As expressed in (2.154) the initial shear modulus is obtained through $\mu_0 = c_1/2$.

2.3.1.7 Hyperfoam model

Cellular solids, such as elastomeric foams, are characterized by excellent energy absorption properties and high compressibility (some foams can have zero Poisson's coefficient at large strains). The energy absorbed by elastomeric foams is substantially greater than that absorbed by other rubbery materials for a certain stress level.

Ogden [Ogden, 1972a], proposed a strain energy function for slightly compressible materials. This model has been used sucessefuly for describing the mechanical behaviour of highly compressible elastomeric foams [ABAQUS®, 2006; Mills & Gilchrist, 2000]. The hyperfoam model (or Ogden foam model) is described by

$$\Psi = \sum_{i=1}^{N} \frac{\mu_i}{\alpha_i} \left[J^{\alpha_i/3} \left(\bar{\lambda}_1^{\alpha_i} + \bar{\lambda}_2^{\alpha_i} + \bar{\lambda}_3^{\alpha_i} \right) - 3 \right] + \sum_{i=1}^{N} \frac{\mu_i}{\alpha_i \beta_i} \left(J^{-\alpha_i \beta_i} - 1 \right), \tag{2.159}$$

with

$$\beta_i = \frac{\upsilon_i}{1 - 2\upsilon_i}. \tag{2.160}$$

2.3.1.8 Blatz and Ko model

Blatz & Ko [1962], proposed a strain energy function for compressible foam rubber undergoing large deformations, especially, certain solid polyurethane rubbers and foamed polyurethane elastomers. The Blatz and Ko model is given by

$$\Psi = f \frac{\mu}{2} \left[(I_1 - 3) + \frac{1}{\beta} \left(I_3^{-\beta} - 1 \right) \right] + (1 - f) \frac{\mu}{2} \left[\left(\frac{I_2}{I_3} - 3 \right) + \frac{1}{\beta} \left(I_3^{\beta} - 1 \right) \right], \tag{2.161}$$

with

$$\beta = \frac{\upsilon}{1 - 2\upsilon}. \tag{2.162}$$

In the Blatz and Ko model, constants μ and υ correspond to the material shear modulus and Poisson's coefficient, respectively. The constant $f \in [0, 1]$, is an interpolation parameter.

2.3.2 Physical models

2.3.2.1 Arruda and Boyce model

The Arruda and Boyce model [Arruda & Boyce, 1993] also known as the *eight-chain model* is based in the assumption of *affine motion* between the material and the molecular chains

and that the deformation of the molecular chains can be measured by the deformation gradient **F**. The strain energy function is given by

$$\Psi = \mu_0 \sum_{i=1}^{N} \frac{C_i}{\lambda_m^{2i-2}} (I_1^i - 3^i) \ , \tag{2.163}$$

where μ_0, λ_m are adjustable materials parameters corresponding to the initial a shear modulus and locking stretch respectively. The constants C_i up to the fifth term are obtained through the inverse *Langevin distribution function*[10], and expressed by

$$C_1 = \frac{1}{2}, \qquad C_2 = \frac{1}{20}, \qquad C_3 = \frac{11}{1050}, \qquad C_4 = \frac{19}{7000}, \qquad C_5 = \frac{519}{673750}\cdot \tag{2.164}$$

2.3.2.2 Van der Waals model

This physical model is based the work of Kilian [1981] and Kilian *et al.* [1986] who formulated the model based on the van der Waals forces generated during interaction between molecular chains. The model is given by

$$\Psi = \mu_0 \left\{ -(\lambda_m^2 - 3)\left[\ln(1-\eta_v) + \eta_v\right] - \frac{2}{3} a \left(\frac{\widetilde{I} - 3}{2} \right)^{3/2} \right\} \ , \tag{2.165}$$

where

$$\widetilde{I} = (1-\beta_v) I_1 + \beta_v I_2 \qquad \text{and} \qquad \eta_v = \sqrt{\frac{\widetilde{I} - 3}{\lambda_m^2 - 3}}\cdot \tag{2.166}$$

In expressions (2.165) and (2.166), μ_0 is the initial shear modulus, λ_m is the locking stretch, a is a global identification parameter and β_v is an invariant mixture parameter [see ABAQUS®, 2006, Analysis User's Manual, Section 17.5.1].

2.4 Modelling hysteresis

Rubber and rubber-like materials are nowadays widely used material in industrial applications such as gaskets, shock absorbers, vibration dampers and tyres. The common approach in modelling the rubber mechanical behaviour as a purely elastic material for some of the mentioned applications may give incorrect results, especially, when cyclic loads are imposed to the rubber or rubber-like material. In fact, energy dissipation mechanisms associated with material internal damage and viscoelastic effects such as hysteresis

[10] related with Non-Gaussian statistical theory

(figure 2.7) alter considerably the mechanical behaviour and must be accounted in order to model accurately the material behaviour during the deformation process.

Internal damage in rubber, especially in filled rubber, induces stress softening in the material. This stress softening phenomena known as the *Mullins effect* [Mullins, 1947] is an inelastic effect and can be explained as an irreversible softening of the stress-strain curve. The inelastic behaviour associated with the Mullins effect is related with molecular damage that is dependent on the submaximal strain energy achieved in a previous deformation process (see figure 2.8). This behaviour is evident when a simple virgin rubber band is cyclically loaded/unloaded to a given strain level (pre-conditioning),.where after some load cycles the material mechanical behaviour stabilize and the material is *"demullinized"*. Some authors published work concerning the modelling of stress-softening, namely: Ogden & Roxburgh [1999], Elías-Zúñiga [2005], Dorfmann *et al.* [2003] and Dorfmann & Ogden [2004].

Energy dissipation associated with viscoelastic hysteresis on the other hand is related to material internal damping due to viscous flow and not with mesoscopic damage associated with the Mullins effect. The term hysteresis means that during a loading-unloading cycle the respective loading and unloading paths not coincide and the correspondent dissipated energy is calculated by the area between the loading and unloading stress-strain curves (see figure 2.7). Works from Bergström & Boyce [1999, 2000] deal with time and strain rate dependence associated with loading-unloading hysteretic cycles, using a phys-

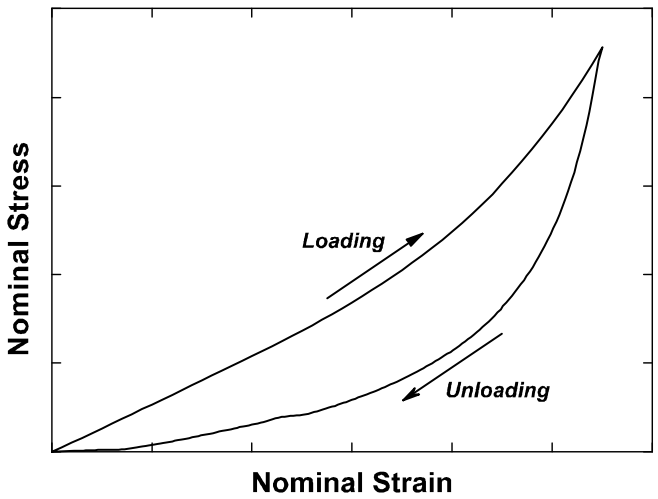


Figure 2.7: Loading-unloading cycle for a hystereric material.

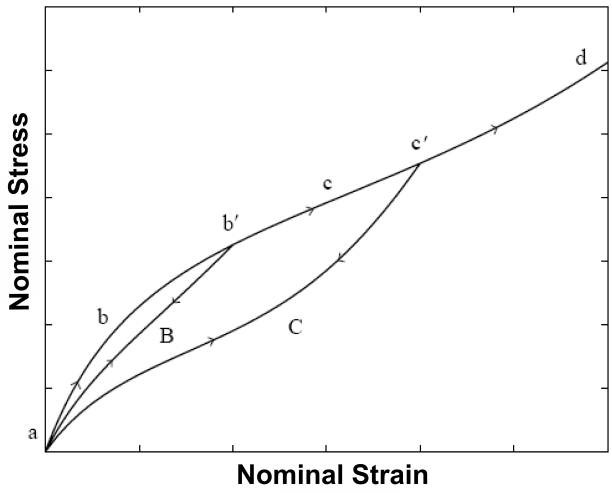


Figure 2.8: Loading-unloading curves in simple tension, in: Ogden & Roxburgh [1999].

ical model approach. Phenomenological approaches to model hysteresis are described in the works by Banks *et al.* [1999] and Kaliske & Rothert [1998].

In a purely phenomenological point of view these two phenomena (internal damage and hysteresis) can be treated using same theoretical assumptions, because both are energy dissipative and can be viewed as dependent on the modification (during unloading) of a purely elastic strain energy function defined for modelling the loading or primary hyperelastic behaviour. In the work from Dorfmann & Ogden [2003], the *pseudo-elasticity* theory used to describe the Mullins effect in a filled rubber, was the starting point to describe quasi-static hysteretic cycles in a *"demullinized"* elastomeric material. In the present work we consider that the CPGC material, due to its intrinsic nature, is not affected with stress softening due to internal damage mechanisms and the same methodology can be applied for the modelling of loading-unloading cycles.

Our new approach to model the material behaviour is discussed in chapter 3.

2.4.1 Pseudo-elasticity theory

In the context of biomechanics Fung [1981] published a work where the modelling of the loading and unloading behaviour of a soft biological material was made with the definition of two different strain energy functions accounting the hysteretic (dissipative) effect. This assumption is the basis of the *pseudo-elasticity theory.* In the work from Ogden & Roxburgh [1999], a strain energy function is modified through the inclusion of a internal scalar variable η that, when active, modifies the strain energy function during the unloading process. The material behaviour is governed by different forms of the

strain energy function during the loading and unloading phases through the modification of a *primary strain energy function* (or unmodified). Energy dissipation is accounted introducing a *damage function* or *dissipation function* [Ogden & Roxburgh, 1999] which depends on a damage scalar parameter η to model dissipative phenomena. A pseudo-energy function Ψ can be described by

$$\Psi = \Psi(\mathbf{F}, \eta). \tag{2.167}$$

The internal variable η in the context of Mullins effect is a scalar that accounts material microscopic damage which allows the modelling of stress softening process. When the parameter η turns active, the deformation is altered through the modification of the primary strain energy function resulting in a different mechanical behaviour in subsequent sub-maximal loadings. On the other hand if the parameter η is inactive the material behaves as an pure nonlinear elastic material.

The variable η can be active or inactive depending on the deformation status. The change of status may be induced, for example, by the unloading starting point in an uniaxial test [Dorfmann & Ogden, 2003], which directly affects the mechanical behaviour in the subsequent unloading phase. When the variable η is active we can set it to the unity [Dorfmann & Ogden, 2003] value and write

$$\Psi^0 = \Psi(\mathbf{F}, 1) \ , \tag{2.168}$$

where Ψ^0 represents the *unmodified* or *primary* strain energy function.

From Ogden & Roxburgh [1999] we obtain the important relation

$$\frac{\partial \Psi(\mathbf{F}, \eta)}{\partial \eta} = 0. \tag{2.169}$$

2.4.1.1 Isotropic material's behaviour

For a better understanding of the new formulations associated to this work discussed at chapter 3, we will outline here some theoretical aspects associated with the pseudo-elastic theory.

In order to simplify this approach a specialization to a simple uniaxial case will be discussed assuming an isotropic incompressible behaviour. A more detailed review about the pseudo-elastic theory can be found in the book by [Fu & Ogden, 2002, Chapter 13].

Simple uniaxial tension or compression (basic equations) Assuming an incompressible isotropic material behaviour the pseudo-elastic energy function in (2.167) can be written in order to the principal stretches $\lambda_a, \ a = 1, 2, 3$, as outlined in section 2.2.2,

through

$$\Psi = \Psi(\lambda_1,\ \lambda_2,\ \lambda_3). \tag{2.170}$$

On the use of incompressibility constraint in (2.99) we can write (2.170) in terms of two independent stretches (biaxial deformation state). We obtain

$$^{\star}\Psi(\lambda_1,\ \lambda_2) \equiv \Psi(\lambda_1,\ \lambda_2,\ \lambda_1^{-1}\lambda_2^{-1}).$$

From expression (2.113) we can compute the Cauchy stress differences as

$$\sigma_1 - \sigma_3 = \lambda_1 \frac{\partial^{\star}\Psi}{\partial\lambda_1}\ , \qquad \text{and} \qquad \sigma_2 - \sigma_3 = \lambda_2 \frac{\partial^{\star}\Psi}{\partial\lambda_2}\cdot \tag{2.171}$$

For a biaxial state of deformation we consider $\sigma_3 = 0$, [see Ogden, 2005, Section 7.2.1] resulting in

$$\sigma_1 = \lambda_1 \frac{\partial^{\star}\Psi}{\partial\lambda_1}\ , \qquad \text{and} \qquad \sigma_2 = \lambda_2 \frac{\partial^{\star}\Psi}{\partial\lambda_2}\cdot \tag{2.172}$$

In simple uniaxial tension (or compression), $\sigma_2 = \sigma_3 = 0$ and $\sigma_1 = \sigma$ with $\lambda_1 = \lambda$ and $\lambda_2 = \lambda_3 = \lambda^{-1/2}$ From expressions in (2.172) we obtain for the uniaxial case that

$$\sigma = \lambda \frac{\partial^{*}\Psi(\lambda)}{\partial\lambda}\ , \tag{2.173}$$

with strain energy function $^{*}\Psi$ given by

$$^{*}\Psi(\lambda) \equiv\ ^{\star}\Psi(\lambda,\ \lambda^{-1/2}). \tag{2.174}$$

2.4.1.2 Pseudo-elastic behaviour

Including the internal variable η in the definition of the strain energy function we obtain the pseudo-elastic strain energy function expressed by

$$^{*}\Psi(\lambda,\eta) \equiv \Psi(\lambda,\ \lambda^{-1/2},\eta). \tag{2.175}$$

From (2.173) we obtain the Cauchy stress component for the uniaxial tension case, given by

$$\sigma = \lambda \frac{\partial^{*}\Psi(\lambda,\eta)}{\partial\lambda}\cdot \tag{2.176}$$

The specialization of equation (2.169) for the uniaxial case is given by

$$\frac{\partial^* \Psi(\lambda, \eta)}{\partial \eta} = 0. \tag{2.177}$$

For the case of inactive η (set equal to unity) we obtain the unmodified strain energy function ${}^*\Psi^0$, i.e.

$${}^*\Psi^0(\lambda) \equiv {}^*\Psi(\lambda, 1). \tag{2.178}$$

The unmodified Cauchy uniaxial stress σ^0 components is expressed by

$$\sigma^0 = \lambda \frac{\partial^* \Psi^0(\lambda)}{\partial \lambda}. \tag{2.179}$$

2.4.1.3 Modelling the hysteretic cycle (uniaxial compression case)

The hysteretic cycle can be modeled using a pseudo-elastic constitutive law that enables a suitable scheme to describe loading and unloading paths. The starting point for this approach was the work of Ogden & Roxburgh [1999] for the analysis of stress softening related with the Mullins effect. The pseudo-elasticity theory is used for modelling the purely hysteretic behaviour associated with loading-unloading cycles. This approach is similar to that used in the work of Dorfmann & Ogden [2003] who model the hysteretic behaviour for an incompressible material assuming that the Mullins effect is not present as been removed by pre-conditioning. The pseudo-elastic model proposed by Ogden & Roxburgh [1999] for an incompressible material in a uniaxial state defined with a primary strain energy function ${}^*\Psi^0$, is given by

$${}^*\Psi(\lambda, \eta) = \eta {}^*\Psi^0(\lambda) + \phi(\eta) \ , \tag{2.180}$$

where $\phi(\eta)$ is a smooth function of η that is subjected to the condition

$$\phi(1) = 0. \tag{2.181}$$

The respective Cauchy uniaxial stress σ component is given by

$$\sigma = \eta \underbrace{\left(J^{-1} \lambda \frac{\partial^* \bar{\Psi}^0_{dev}(\bar{\lambda})}{\partial \lambda} \right)}_{\sigma^0}. \tag{2.182}$$

The deviatoric uniaxial nominal (or first Piola-Kirchhoff) stress P component are obtained through

$$P = \eta \underbrace{\left(\frac{\partial^* \bar{\Psi}^0_{dev}(\bar{\lambda})}{\partial \lambda} \right)}_{P^0}. \tag{2.183}$$

Regarding the uniaxial compression case we can write the dissipation function $\phi(\eta)$ as

$$\phi(\eta) = {}^{*}\Psi(\lambda, \eta) - \eta^{*}\Psi^{0}(\lambda). \tag{2.184}$$

Performing the derivative of ϕ in terms of η and regarding the condition expressed by (2.177) we obtain

$$\frac{\partial \phi(\eta)}{\partial \eta} = \phi'(\eta) = -{}^{*}\Psi^{0}(\lambda). \tag{2.185}$$

Dorfmann-Ogden Model In their work, Dorfmann & Ogden [2003] proposed a dissipation function $\phi(\eta)$ based on the dissipation function used by Ogden & Roxburgh [1999] to model the energy dissipation in incompressible rubber, given by

$$-\phi'(\eta) = m \, \tanh^{-1}[r(\eta - 1)] + \Psi_{max} \ , \tag{2.186}$$

where r and m are adjustable material parameters and Ψ_{max} represents the maximum strain energy density achieved during the loading (see figure 2.9).

From (2.186) and applying (2.185) and we obtain, after some algebraic manipulations a expression for the scalar variable η, given by

$$\eta = 1 - \frac{1}{r} \tanh \left[\frac{{}^{*}\Psi^{max} - {}^{*}\Psi^{0}(\lambda)}{m} \right] . \tag{2.187}$$

Integrating (2.186)

$$\begin{aligned} \phi(\eta) &= \int_{1}^{\eta} (-m \, \tanh^{-1}[r(\eta - 1)] - \ {}^{*}\Psi^{max}) \ d\eta = \\ &= -\frac{m}{2r} \ln \left[1 - (\eta r - r)^2 \right] - \ {}^{*}\Psi^{max}(\eta - 1) \\ &- m \tanh^{-1} \left[r(\eta - 1) \right] (\eta - 1). \end{aligned} \tag{2.188}$$

The minimum value for η is obtained for the unstressed configuration given by $\lambda = 1$ with ${}^{*}\Psi^{0}(1) = 0$. Substituting in (2.187), we obtain

$$\eta^{min} = 1 - \frac{1}{r} \tanh \left[\frac{{}^{*}\Psi^{max}}{m} \right] . \tag{2.189}$$

In an uniaxial test $\phi(\eta^{min})$ may be interpreted as the *area between the loading and the unloading curve* [Dorfmann & Ogden, 2003] correspondent to the *dissipated energy* during the loading-unloading cycle. Furthermore, $\Psi^{max} - \phi(\eta^{min}) = \Psi^{rec}$, is interpreted as the recoverable energy per deformation cycle as seen figure 2.9.

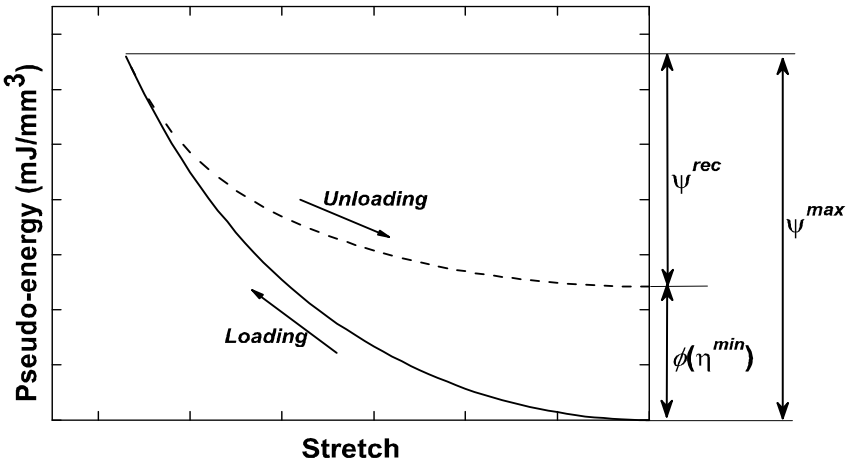


Figure 2.9: Pseudo-elastic strain energy function describing the uniaxial mechanical behaviour of a hysteretic material.

Note that in figure 2.9, the pseudo-energy is plotted against the uniaxial stretch λ, related with the uniaxial nominal strain ϵ, by $\lambda = \epsilon + 1$.

Zúñiga model In a more recent work, Elías-Zúñiga [2005] proposed a dissipation function ϕ of the form

$$-\phi'(\eta) = -1\left(\frac{1}{b}\ln\eta\right)^{1/n} + {}^{*}\Psi^{\max}\,, \tag{2.190}$$

where b is an adjustable material parameter and n a is positive material parameter chosen to best fit data for a given material.

After some algebraic manipulations we obtain

$$\eta = e^{-b\sqrt{{}^{*}\Psi^{\max} - {}^{*}\Psi^{0}(\lambda)}}. \tag{2.191}$$

Integrating (2.190) we obtain the dissipative energy function for the Zúñiga model given by

$$\begin{aligned}\phi(\eta) &= \int_1^{\eta}\left(\left(\frac{1}{b}\ln\eta\right)^2 - {}^{*}\Psi^{\max}\right)d\eta = \\ &= \frac{2}{b^2}\left[\eta\left(1 - \ln\eta + \frac{1}{2}(\ln\eta)^2\right) - 1\right] - {}^{*}\Psi^{\max}(\eta - 1).\end{aligned} \tag{2.192}$$

The minimum value for η is obtained for a stress-free configuration given by $\lambda = 1$ with ${}^*\Psi^0(1) = 0$. Substituting in (2.191) we obtain

$$\eta^{min} = e^{-b\sqrt{{}^*\Psi^{\max}}}. \tag{2.193}$$

2.5 Heat generation

The strain energy developed during the deformation process of a hysteretic material is not totally recovered during the unloading phase. This *residual energy* is converted in others form of energy such as *thermal energy* and irreversibly lost to the surroundings. For a better understanding we can think on a rigid ball that falls into a rubber plate. The potential energy of the ball is transformed into kinetic energy that is transferred to the rubber plate. Consequently, the ball deforms the rubber plate transforming the kinetic energy into strain energy absorbed by the rubber material. The ball is then bounced back to a height that in the case of dissipative materials is inferior to the original drop height. The fraction of original height recovered is a measure of the efficiency of energy restitution or resilience. Low resilience materials are normally associated with *energy dissipation* or *hysteretic effects*.

Hysteresis represents the non-recoverable part of the energy when a material is loaded to a point and then unloaded (see figure 2.7) and corresponds to the area between the loading and unloading curve. By performing a cyclic integration in the stress vs. strain uniaxial curve we obtain the area between the loading and unloading curve that corresponds to the dissipated energy density per cycle of deformation (hysteresis). Dissipated energy H is then given by

$$H = \oint \sigma d\epsilon. \tag{2.194}$$

Following the assumption made in (2.194), we can express the hysteresis value in a volumetric deformation test as

$$H = \oint p dJ \ , \tag{2.195}$$

where p is the pressure and J the volume ratio.

DMA-Dynamical Mechanical Analysis experimental tests are conducted to analyzed mechanical properties of materials subjected to high frequency solicitation schemes. In this experimental procedure the material sample is subjected to an alternating strain (or stress) and simultaneously measure the stress (or strain) applied. In the case of a purely elastic material the strains are in-phase with the applied stress in such a way

that the mechanical energy absorbed during a sinusoidal deformation cycle (1/4 of the period) is totally bounced back during the following recovery cycle in such a way that the material don't accumulate energy during the cyclic deformation. By other hand, viscoelastic (dissipative) materials are characterized by the lag between the applied stress (or strain) and strain (or stress) response. This out-of-phase response is responsible for the hysteretic (dissipative) effect. There are other material classes where the hysteretic behaviour is not associated with viscoelasticity but rather with internal dissipation effects.

When equilibrium is reached both the stress and strain varies sinusoidally with the applied radial frequency ω, but with a lag δ in the strain (or stress) response. Considering that the experimental procedure is driven by an imposed strain ϵ_0, we can write

$$\epsilon = \epsilon_0 \sin(\omega t) \tag{2.196}$$

and

$$\sigma = \sigma_0 \sin(\omega t + \delta). \tag{2.197}$$

The *phase angle* δ is given by

$$\operatorname{tg} \delta = \frac{E^{''}(\omega)}{E^{'}(\omega)} \ , \tag{2.198}$$

[see Ward & Hadley, 1996, Section 4.3] where $E^{'}(\omega)$ is the *storage modulus* (in phase response) defining the strain energy stored in the model and $E^{''}(\omega)$ corresponds to the *dissipative modulus* (out of phase response) that defines the dissipation of energy. In the complex plane the vectorial sum of the in phase $E^{'}(\omega)$ component with the out of phase component $E^{''}(\omega)$ gives the complex modulus E^{*}, expressed by

$$E^{*}(\omega) = E^{'}(\omega) + iE^{''}(\omega).$$

The magnitude of complex modulus $E^{*}(\omega)$ is then expressed by

$$||E^{*}|| = \sqrt{(E^{'}(\omega))^2 + (E^{''}(\omega))^2}. \tag{2.199}$$

From equation (2.198) is possible to conclude that tg δ is proportional to the dissipative modulus $E^{''}(\omega)$. A simple expression can be derived for determining the hysteretic loss (or dissipated energy) per cycle in sinusoidal experiments [Ferry, 1980, Chapter 19]. This expression is given by

$$H(\omega) = \pi E^{''}(\omega) {\epsilon_0}^2. \tag{2.200}$$

From expression (2.200) is visible that hysteresis is a dissipative phenomena dependent only the dissipative part of the complex modulus. Because this dissipated energy is not easily conducted away from the material it causes (especially in high frequency solicitation) a rise in the temperature whose magnitude depends on the thermal properties of the material (thermal conductivity, specific heat) and on the thermal boundary conditions (thermal radiation and convection).This internally generated thermal energy can cause in some cases thermal degradation and consequently failure of the material.

A simple way of calculating the heat build-up in a filled rubber is given in the book from [Ferry, 1980, Chapter 19], expressed by

$$\Delta T = c(1 - b_T v_f) \left[\frac{\omega \epsilon_0^2 E''(\omega, T_1)}{2} \right] ,$$

where ΔT is the temperature differential from the steady state-temperature, v_f is the volume fraction of filler, coefficients c and b_T are material dependent materials and T_1 is the steady-state temperature.

Heat build-up is normally studied in the bibliography for rubber or rubber-like materials and try to correlate its dependence with structural characteristics (crosslink density and structure) and composition of rubber or rubber-like materials. The work from Kamal & Anil [1997] and Park *et al.* [2000] studied the heat generation in samples (instrumented with thermocouples) made from vulcanized rubber subjected to cyclic deformations.

Heat build-up phenomena are not normally included in the definition of a finite element analysis problem. In the vast majority of the models the dissipative behaviour is introduced by the definition of a *fraction of the critical damping factor* ξ (obtained indirectly from DMA tests) or other forms of assigning damping such as the *Rayleigh damping* [see Clough & Penzien, 1993, Section 12-5] form, also dependent on ξ. This approach, models the dissipative part of the material's mechanical behaviour but can't model the heat build-up phenomena associated with hysteresis. Also, for large amplitude vibrations this concept is arguable.

Other works just account the dissipative properties for heat build-up calculations. The work from Lin & Hwang [2004] implemented an methodology for an uncoupled thermo-mechanical FEA simulation of tires that introduces the heat generation developed during the tire rolling as an external thermal load calculated from DMA tests.

This page is intentionally left blank.

Chapter 3

New Formulations

In this chapter will be discussed new formulations in terms of constitutive modelling obtained during this thesis, namely introduced for the modelling of dissipative effects.

In section 3.1 we will discuss a modified approach to the pseudo-elasticity theory that enables the modelling of materials with *separate deviatoric* and *volumetric dissipative behaviour*. In section 3.2 a new approach to model the *heat generation* in hysteretic materials is presented.

All the new formulations presented here were implemented in the finite element code ABAQUS® through user subroutines. These implementations are discussed with a more detail in section 4.3.

3.1 Modelling hysteresis in nonlinear elastic materials with deviatoric and volumetric dissipative behaviour

It was assumed, for the present work, that our material is *not affected by the Mullins effect* (described in section 2.4) and the energy dissipation revealed by the *quasi-static hysteretic cycles* are due to *internal mechanisms of energy dissipation*. The material will be treated as compressible, which introduces changes to the Dorfmann & Ogden [2003] and Ogden & Roxburgh [1999] theory formulations and enables a decoupled approach in terms of deviatoric and volumetric dissipative phenomena.

The approach followed in this work is a *purely phenomenological* one. Using the pseudo-elastic theory from Ogden & Roxburgh [1999] and the models introduced in Dorfmann & Ogden [2003] and Elías-Zúñiga [2005], our main aim is to describe the quasi-static loading-unloading process of the CPGC during uniaxial and volumetric deformation cases, accounting separately energy dissipation mechanisms due to *deviatoric* and *volumetric* de-

formation processes. For that, uniaxial *unconfined compression* and *confined compression* tests were performed in order to verify the existence of *separate volumetric* and *deviatoric energy dissipative phenomena* at the CPGC material.

For some compressible materials is usually benefical to split the overall deformation into a so-called volumetric and deviatoric parts. Performing a multiplicative decomposition of the deformation gradient $\mathbf{F}$ into a volumetric and deviatoric part, we obtain

$$\mathbf{F} = J^{1/3}\overline{\mathbf{F}}, \qquad \lambda_i = J^{1/3}\bar{\lambda}_i \ , \tag{3.1}$$

with

$$\det \overline{\mathbf{F}} = \bar{\lambda}_1\bar{\lambda}_2\bar{\lambda}_3 = 1. \tag{3.2}$$

The term $J^{1/3}$ is associated with *volume changing* deformations with J representing the volume ratio, while the modified deformation gradient $\overline{\mathbf{F}}$ is associated with *volume preserving* or deviatoric deformations. A decoupled strain energy function $\bar{\Psi}$ can be written based on the assumption (3.1) and perform an additive decomposition of the deviatoric and volumetric parts (see section 2.2.5), written by

$$\Psi(\mathbf{F}) = \bar{\Psi}(\overline{\mathbf{F}}, J) = \bar{\Psi}_{dev}(\overline{\mathbf{F}}) + \bar{\Psi}_{vol}(J). \tag{3.3}$$

The scalar-valued and objective functions, $\bar{\Psi}_{dev}(\overline{\mathbf{F}})$ and $\bar{\Psi}_{vol}(J)$, .describes the deviatoric (or isochoric) and volumetric (or dilatational) nonlinear elastic response of the material, respectively.

The decoupled strain energy function in equation (2.167) can be modified in order to include internal variables η_{dev} and η_{vol} that model the unloading path accounting separately the deviatoric and volumetric state of deformation, respectively. We can write that

$$\bar{\Psi}(\overline{\mathbf{F}}, J, \eta_{dev}, \eta_{vol}) \equiv \Psi(\mathbf{F}, \eta). \tag{3.4}$$

Decoupling the strain energy function in equation (3.4) into a volumetric and deviatoric part, we obtain

$$\bar{\Psi}(\overline{\mathbf{F}}, J, \eta_{dev}, \eta_{vol}) = \bar{\Psi}_{vol}(J, \eta_{vol}) + \bar{\Psi}_{dev}(\overline{\mathbf{F}}, \eta_{dev}). \tag{3.5}$$

Equation (3.5) is a typical decoupled strain energy function for compressible elastic materials modified with the inclusion of two internal variables, namely, η_{vol} and η_{dev}, that can be referred as a decoupled pseudo-energy function [Dorfmann & Ogden, 2003; Ogden & Roxburgh, 1999].

The resulting nominal stress (or first Piola-Kirchhoff stress) $\mathbf{P}$ for a compressible material is given by

$$\mathbf{P} = \mathbf{P}_{dev} + \mathbf{P}_{vol}. \tag{3.6}$$

For the cases which the internal variables η_{dev} and η_{vol} are inactive their values are set equal to unity. In theses cases the form of the decoupled strain energy function $\bar{\Psi}$ is not affected and a zero superscript is added to the definition of the strain energy function. With η_{dev} and η_{vol} inactive we can write the unmodified or primary strain energy function as

$$\bar{\Psi}^0(\overline{\mathbf{F}}, J) = \bar{\Psi}^0_{vol}(J, 1) + \bar{\Psi}^0_{dev}(\bar{\mathbf{F}}, 1). \tag{3.7}$$

The respective unmodified or primary nominal stress $\mathbf{P}^0$ is given by

$$\mathbf{P}^0 = \mathbf{P}^0_{dev} + \mathbf{P}^0_{vol} \ , \tag{3.8}$$

where the deviatoric and volumetric components of equation (3.8) are given respectively by

$$\mathbf{P}^0_{dev} = \frac{\partial \bar{\Psi}^0_{dev}(\overline{\mathbf{F}})}{\partial \mathbf{F}} = \frac{\partial \bar{\Psi}^0_{dev}(\overline{\mathbf{F}})}{\partial \overline{\mathbf{F}}} \frac{\partial \overline{\mathbf{F}}}{\partial \mathbf{F}} \tag{3.9}$$

and

$$\mathbf{P}^0_{vol} = \frac{\partial \bar{\Psi}^0_{vol}(J)}{\partial \mathbf{F}} = \frac{\partial \bar{\Psi}^0_{vol}(J)}{\partial J} \frac{\partial J}{\partial \mathbf{F}} \ , \tag{3.10}$$

where the primary or unmodified hydrostatic pressure p^0 is given by

$$p^0 = \frac{\partial \bar{\Psi}^0_{vol}(J)}{\partial J}. \tag{3.11}$$

The total unmodified nominal stress $\mathbf{P}^0$is given by the sum of the unmodified deviatoric and volumetric terms, given by

$$\mathbf{P}^0 = \frac{\partial \bar{\Psi}^0(\overline{\mathbf{F}}, J)}{\partial \mathbf{F}} = \frac{\partial \bar{\Psi}^0_{dev}(\overline{\mathbf{F}})}{\partial \overline{\mathbf{F}}} \frac{\partial \overline{\mathbf{F}}}{\partial \mathbf{F}} + \frac{\partial \bar{\Psi}^0_{vol}(J)}{\partial J} \frac{\partial J}{\partial \mathbf{F}}. \tag{3.12}$$

If η_{dev} and η_{vol} are active and dependent on $\overline{\mathbf{F}}$ and $\mathbf{J}$,respectively, we can write that

$$\eta_{dev} = \chi(\overline{\mathbf{F}}) \ , \qquad \text{and} \qquad \eta_{vol} = \chi(J). \tag{3.13}$$

The respective modified nominal stress $\mathbf{P}$ is given by

$$\mathbf{P} = \mathbf{P}_{dev} + \mathbf{P}_{vol} \ , \tag{3.14}$$

where the modified deviatoric and volumetric components can be written by

$$\mathbf{P}_{dev} = \frac{\partial \bar{\Psi}_{dev}(\overline{\mathbf{F}}, \eta_{dev})}{\partial \mathbf{F}} = \frac{\partial \bar{\Psi}_{dev}(\overline{\mathbf{F}}, \eta_{dev})}{\partial \overline{\mathbf{F}}} \frac{\partial \overline{\mathbf{F}}}{\partial \mathbf{F}} + \frac{\partial \bar{\Psi}_{dev}(\overline{\mathbf{F}}, \eta_{dev})}{\partial \eta_{dev}} \frac{\partial \eta_{dev}}{\partial \mathbf{F}} \tag{3.15}$$

and

$$\mathbf{P}_{vol} = \frac{\partial \bar{\Psi}_{vol}(J)}{\partial \mathbf{F}} = \frac{\partial \bar{\Psi}_{vol}(J, \eta_{vol})}{\partial J} \frac{\partial J}{\partial \mathbf{F}} + \frac{\partial \bar{\Psi}_{vol}(J, \eta_{vol})}{\partial \eta_{vol}} \frac{\partial \eta_{vol}}{\partial \mathbf{F}}. \tag{3.16}$$

The total modified nominal stress $\mathbf{P}$ is given by the sum of the deviatoric and volumetric term

$$\begin{aligned} \mathbf{P} = \frac{\bar{\Psi}(\overline{\mathbf{F}}, J, \eta_{dev}, \eta_{vol})}{\partial \mathbf{F}} = & \underbrace{\frac{\partial \bar{\Psi}_{dev}(\overline{\mathbf{F}}, \eta_{dev})}{\partial \overline{\mathbf{F}}} \frac{\partial \overline{\mathbf{F}}}{\partial \mathbf{F}} + \frac{\partial \bar{\Psi}_{dev}(\overline{\mathbf{F}}, \eta_{dev})}{\partial \eta_{dev}} \frac{\partial \eta_{dev}}{\partial \mathbf{F}}}_{deviatoric\ term} \\ & + \underbrace{\frac{\partial \bar{\Psi}_{vol}(J, \eta_{vol})}{\partial J} \frac{\partial J}{\partial \mathbf{F}} + \frac{\partial \bar{\Psi}_{vol}(J, \eta_{vol})}{\partial \eta_{vol}} \frac{\partial \eta_{vol}}{\partial \mathbf{F}}}_{volumetric\ term}. \end{aligned} \tag{3.17}$$

Following the work of Ogden & Roxburgh [1999] it follows that in equilibrium and in the absence of body forces

$$\frac{\partial \Psi(\mathbf{F}, \eta)}{\partial \eta} = 0. \tag{3.18}$$

For our particular case we can specialize the equation 3.18 for the decoupled energy function $\bar{\Psi}$. We can write that

$$\frac{\partial \bar{\Psi}_{dev}(\overline{\mathbf{F}}, \eta_{dev})}{\partial \eta_{dev}} = 0 \ , \qquad \text{and} \qquad \frac{\partial \bar{\Psi}_{vol}(J, \eta_{vol})}{\partial \eta_{vol}} = 0. \tag{3.19}$$

Substituting equations (3.19) in (3.17) we obtain the nominal stress $\mathbf{P}$ for the case which η_{vol} and η_{dev} are both active or inactive, given by

$$\mathbf{P} = \frac{\partial \bar{\Psi}_{dev}(\overline{\mathbf{F}}, \eta_{dev})}{\partial \overline{\mathbf{F}}} \frac{\partial \overline{\mathbf{F}}}{\partial \mathbf{F}} + J \frac{\partial \bar{\Psi}_{vol}(J, \eta_{vol})}{\partial J} \mathbf{F}^{-T}. \tag{3.20}$$

If the constants η_{dev} and η_{vol} are function of the deformation status (via the deformation gradient $\mathbf{F}$ at a current instant), we can write that

$$\eta_{dev} = \chi(\overline{\mathbf{F}}(\mathbf{F})) \ , \qquad \text{and} \qquad \eta_{vol} = \chi(J(\mathbf{F})). \tag{3.21}$$

The dependence on the deformation gradient $\mathbf{F}$ of the modified deformation gradient $\bar{\mathbf{F}}$ and volume ratio J, associated with the assumptions described in (3.21), allows the definition of a unique strain energy function φ, written by

$$\varphi(\mathbf{F}) = \bar{\Psi}(\overline{\mathbf{F}}(\mathbf{F}), J(\mathbf{F}), \eta_{dev}(\mathbf{F}), \eta_{vol}(\mathbf{F})). \tag{3.22}$$

3.1.1 Specialization to isotropic pseudo-elasticity

The strain energy function that describes the material behaviour is considered to be isotropic. This property is based on the equivalence of material's mechanical response when subjected to stress-strain experiments in different directions. Specializing the strain energy function $\bar{\Psi}$ in (3.4) for an isotropic response written as

$$\begin{aligned}\bar{\Psi}(\overline{\mathbf{F}}, J, \eta_{dev}, \eta_{vol}) &\equiv \bar{\Psi}(\bar{\lambda}_1, \bar{\lambda}_2, \bar{\lambda}_3, J, \eta_{dev}, \eta_{vol}) \\ &= \bar{\Psi}_{vol}(J, \eta_{vol}) + \bar{\Psi}_{dev}(\bar{\lambda}_1, \bar{\lambda}_2, \bar{\lambda}_3, \eta_{dev}).\end{aligned} \tag{3.23}$$

The respective Cauchy total principal stress $\boldsymbol{\sigma}$ is given by

$$\boldsymbol{\sigma} = \boldsymbol{\sigma}_{vol} + \boldsymbol{\sigma}_{dev}, \tag{3.24}$$

where the deviatoric and volumetric terms are written respectively by

$$\sigma_{i\,dev} = J^{-1}\left(\bar{\lambda}_i \frac{\partial \bar{\Psi}_{dev}(\bar{\lambda}_i, \eta_{dev})}{\partial \bar{\lambda}_i} - \frac{1}{3}\sum_{j=1}^{3} \bar{\lambda}_j \frac{\partial \bar{\Psi}_{dev}(\bar{\lambda}_j, \eta_{dev})}{\partial \bar{\lambda}_j}\right) \ , \quad i = 1, 2, 3 \tag{3.25}$$

and

$$\boldsymbol{\sigma}_{vol} = \frac{\partial \Psi_{vol}(J, \eta_{vol})}{\partial J}\mathbf{I} = p\mathbf{I} = \frac{1}{3}(\sigma_1 + \sigma_2 + \sigma_3) \ , \tag{3.26}$$

where $\mathbf{I}$ is the identity matrix. The combination of (3.25) and (3.26) results in a incompressible behaviour

The conditions in (3.19) can be specialized to the isotropic case through

$$\frac{\partial \bar{\Psi}_{dev}(\bar{\lambda}_1, \bar{\lambda}_2, \bar{\lambda}_3, \eta_{dev})}{\partial \eta_{dev}} = 0 \ , \qquad \text{and} \qquad \frac{\partial \bar{\Psi}_{vol}(J, \eta_{vol})}{\partial \eta_{vol}} = 0. \tag{3.27}$$

In parallel with the incompressible theory we can retain only two modified principal stretches as independent variables, by the definition in (3.2), we can write that $\bar{\lambda}_3 = \bar{\lambda}_1^{-1}\bar{\lambda}_2^{-1}$. The respective strain energy function can be expressed by

$$^{\star}\bar{\Psi}(\bar{\lambda}_1, \bar{\lambda}_2, J, \eta_{dev}, \eta_{vol}) \equiv \bar{\Psi}(\bar{\lambda}_1, \bar{\lambda}_2, \bar{\lambda}_1^{-1}\bar{\lambda}_2^{-1}, J, \eta_{dev}, \eta_{vol}). \tag{3.28}$$

The strain energy function $^{\star}\bar{\Psi}$ can be decoupled in volumetric and deviatoric terms through

$$^{\star}\bar{\Psi}(\bar{\lambda}_1, \bar{\lambda}_2, J, \eta_{dev}, \eta_{vol}) \equiv {}^{\star}\bar{\Psi}_{vol}(J, \eta_{vol}) + {}^{\star}\bar{\Psi}_{dev}(\bar{\lambda}_1, \bar{\lambda}_2, \eta_{dev}). \tag{3.29}$$

Cauchy's deviatoric stress differences are written by

$$\begin{aligned} \sigma_{1\ dev} - \sigma_{3\ dev} &= J^{-1}\bar{\lambda}_1 \frac{\partial^{\star}\bar{\Psi}_{dev}(\bar{\lambda}_1, \bar{\lambda}_2, \eta_{dev})}{\partial\bar{\lambda}_1} \ , \\ \sigma_{2\ dev} - \sigma_{3\ dev} &= J^{-1}\bar{\lambda}_2 \frac{\partial^{\star}\bar{\Psi}_{dev}(\bar{\lambda}_1, \bar{\lambda}_2, \eta_{dev})}{\partial\bar{\lambda}_2}. \end{aligned} \tag{3.30}$$

The volumetric Cauchy stress is given by equation (3.26). Specializing the equations expressed in (3.27) for the present case, we obtain

$$\frac{\partial^{\star}\bar{\Psi}_{dev}(\bar{\lambda}_1, \bar{\lambda}_2, \eta_{dev})}{\partial\eta_{dev}} = 0 \ , \qquad \text{and} \qquad \frac{\partial^{\star}\bar{\Psi}_{vol}(J, \eta_{vol})}{\partial\eta_{vol}} = 0. \tag{3.31}$$

Considering η_{vol} and η_{dev} inactive and equal to unity we can write the unmodified or primary strain energy function $^{\star}\bar{\Psi}^0$ as

$$^{\star}\bar{\Psi}^0(\bar{\lambda}_1, \bar{\lambda}_2) \equiv {}^{\star}\bar{\Psi}(\bar{\lambda}_1, \bar{\lambda}_2, J, 1, 1). \tag{3.32}$$

In the decoupled form the strain energy in equation 3.32 is given by

$$^{\star}\bar{\Psi}^0(\bar{\lambda}_1, \bar{\lambda}_2, J) = {}^{\star}\bar{\Psi}^0_{dev}(\bar{\lambda}_1, \bar{\lambda}_2) + \ {}^{*}\bar{\Psi}^0_{vol}(J). \tag{3.33}$$

The respective unmodified deviatoric Cauchy stress differences are given through

$$\sigma^0_{1\ dev} - \sigma^0_{3\ dev} = J^{-1}\bar{\lambda}_1 \frac{\partial^{\star}\bar{\Psi}^0_{dev}(\bar{\lambda}_1, \bar{\lambda}_2)}{\partial\bar{\lambda}_1} \qquad \text{and} \qquad \sigma^0_{2\ dev} - \sigma^0_{3\ dev} = J^{-1}\bar{\lambda}_2 \frac{\partial^{\star}\bar{\Psi}^0_{dev}(\bar{\lambda}_1, \bar{\lambda}_2)}{\partial\bar{\lambda}_2} \ , \tag{3.34}$$

with the volumetric unmodified Cauchy stress given by

$$\boldsymbol{\sigma}^0_{vol} = \frac{\partial\Psi^0_{vol}(J)}{\partial J}\mathbf{I} = p^0\mathbf{I} = \frac{1}{3}(\sigma^0_1 + \sigma^0_2 + \sigma^0_3) \ , \tag{3.35}$$

where $\sigma^0_{i\ dev}$ and p^0 are the unmodified deviatoric Cauchy stress and unmodified hydrostatic pressure, respectively.

3.1.1.1 Simple uniaxial compression case (unconfined deformation)

For the uniaxial solicitation analysis is important having in mind that experimental testing conducted to evaluate the mechanical response of the material is also uniaxial, through unconfined and confined deformation procedures.

Considering a simple uniaxial compression and consequently a pure deviatoric behaviour we define only one independent modified principal stretch. In simple tension we have $\sigma_1 = \sigma$ and $\sigma_2 = \sigma_3 = 0$. In terms of modified principal stretches we can write that $\bar{\lambda}_1 = \bar{\lambda}$ with $\bar{\lambda}_2 = \bar{\lambda}_3 = \bar{\lambda}^{-1/2}$. The strain energy function for the uniaxial case ${}^*\bar{\Psi}$ can be written by

$$ {}^*\bar{\Psi}(\bar{\lambda}, J, \eta_{dev}, \eta_{vol}) \equiv {}^\star\bar{\Psi}(\bar{\lambda}, \bar{\lambda}^{-1/2}, J, \eta_{dev}, \eta_{vol}). \tag{3.36} $$

In the decoupled form we obtain for the uniaxial (compression) case we obtain

$$ {}^*\bar{\Psi}(\bar{\lambda}, J, \eta_{dev}, \eta_{vol}) = {}^*\bar{\Psi}_{vol}(J, \eta_{vol}) + {}^*\bar{\Psi}_{dev}(\bar{\lambda}, \eta_{dev}). \tag{3.37} $$

The respective deviatoric and volumetric Cauchy stress for the compression (uniaxial) case are given by

$$ \sigma_{dev} = J^{-1}\bar{\lambda}\frac{\partial^*\bar{\Psi}_{dev}(\bar{\lambda}, \eta_{dev})}{\partial\bar{\lambda}} - \frac{1}{3}J^{-1}\bar{\lambda}\frac{\partial^*\bar{\Psi}_{dev}(\bar{\lambda}, \eta_{dev})}{\partial\bar{\lambda}} \ , \tag{3.38} $$

and

$$ \boldsymbol{\sigma}_{vol} = \frac{\partial\Psi_{vol}(J)}{\partial J}\mathbf{I} = p\mathbf{I} = \frac{1}{3}\sigma. \tag{3.39} $$

The specializations of equation (3.31) for the uniaxial case are given by

$$ \frac{\partial^*\bar{\Psi}_{dev}(\bar{\lambda}, \eta_{dev})}{\partial\eta_{dev}} = 0 \ , \qquad \text{and} \qquad \frac{\partial^*\bar{\Psi}_{vol}(J, \eta_{vol})}{\partial\eta_{vol}} = 0. \tag{3.40} $$

For the case of inactive η_{vol} and η_{dev} we obtain the unmodified strain energy function ${}^*\bar{\Psi}^0$ for the uniaxial case given by

$$ {}^*\bar{\Psi}^0(\bar{\lambda}, J) \equiv {}^*\bar{\Psi}(\bar{\lambda}, J, 1, 1). \tag{3.41} $$

In the decoupled form we obtain

$$ {}^*\bar{\Psi}^0(\bar{\lambda}, J, \eta_{dev}, \eta_{vol}) = {}^*\bar{\Psi}^0_{vol}(J, \eta_{vol}) + {}^*\bar{\Psi}^0_{dev}(\bar{\lambda}, \eta_{dev}). \tag{3.42} $$

The unmodified deviatoric and volumetric Cauchy stress are given by

$$\sigma^0_{dev} = J^{-1}\bar{\lambda}\left(\frac{\partial^*\bar{\Psi}^0_{dev}(\bar{\lambda},\eta_{dev})}{\partial\bar{\lambda}} - \frac{1}{3}\frac{\partial^*\bar{\Psi}^0_{dev}(\bar{\lambda},\eta_{dev})}{\partial\bar{\lambda}}\right) , \tag{3.43}$$

and

$$\boldsymbol{\sigma}^0_{vol} = \frac{\partial\Psi^0_{vol}(J)}{\partial J}\mathbf{I} = p^0\mathbf{I} = \frac{1}{3}\sigma^0. \tag{3.44}$$

3.1.1.2 Uniaxial volumetric compression case (confined deformation)

In the uniaxial volumetric test the material specimen is confined inside a rigid container. The specimen top surface is compressed by a rigid piston inducing a compressive loading and consequently hydrostatic pressure.

For a pure hydrostatic pressure test we have $\lambda_1 = \lambda_2 = \lambda_3 = \lambda_v$ and therefore only volumetric deformations are present stated by $\bar{\lambda}_1 = \bar{\lambda}_2 = \bar{\lambda}_3 = 1$. The strain energy function ${}^{\diamond}\bar{\Psi}$ for the volumetric deformation case is given by.

$${}^{\diamond}\bar{\Psi}(J,\eta_{vol}) \equiv \bar{\Psi}(1,1,1,J,1,\eta_{vol}). \tag{3.45}$$

For the present case it was considered that energy dissipation associated with deviatoric effects is negligible. By so η_{dev} was set equal to the unity.

Following the same decoupling methodology followed in previous strain energy functions we obtain

$${}^{\diamond}\bar{\Psi}(J,\eta_{vol}) = {}^{\diamond}\bar{\Psi}_{vol}(J,\eta_{vol}). \tag{3.46}$$

For a pure hydrostatic pressure state we have

$$\boldsymbol{\sigma} = \boldsymbol{\sigma}_{vol} + \underbrace{\boldsymbol{\sigma}_{dev}}_{0}. \tag{3.47}$$

The components of the volumetric Cauchy stress tensor are given by

$$\boldsymbol{\sigma}_{vol} = \frac{\partial^{\diamond}\bar{\Psi}(J)}{\partial J} = p\mathbf{I}. \tag{3.48}$$

Considering the volume ratio $J = det(\mathbf{F}) = \lambda_1\lambda_2\lambda_3$ and knowing that in the uniaxial volumetric state we have $\lambda_1 = \lambda v$ with $\lambda_2 = \lambda_3 = 1$, we can write that

$$J = det(\mathbf{F}) = \lambda_v. \tag{3.49}$$

Following this assumption, a new strain energy function ${}^{\bullet}\bar{\Psi}$ for the uniaxial volumetric

case can be written by

$$^{\bullet}\bar{\Psi}(\lambda_v, \eta_{vol}) = {}^{\diamond}\bar{\Psi}(J, \eta_{vol}). \tag{3.50}$$

Substituting this statement in equation (3.51) we have that

$$\boldsymbol{\sigma}_{vol} = p\mathbf{I} = \frac{\partial^{\bullet}\bar{\Psi}(\lambda_v)}{\partial\lambda_v} = \frac{\partial^{\diamond}\bar{\Psi}(J)}{\partial J}. \tag{3.51}$$

For the pure volumetric deformation case, the statement in (3.19) can be specialized through

$$\frac{\partial^{\diamond}\bar{\Psi}(J, \eta_{vol})}{\partial\eta_{vol}} = 0. \tag{3.52}$$

Considering the constant η_{vol} inactive and set equal to unity, we can write

$${}^{\diamond}\bar{\Psi}^0(J) = {}^{\diamond}\bar{\Psi}(J, 1). \tag{3.53}$$

The respective unmodified pressure is given by

$$\boldsymbol{\sigma}^0_{vol} = \frac{\partial^{\diamond}\bar{\Psi}^0(J, \eta_{vol})}{\partial J} = p^0\mathbf{I}. \tag{3.54}$$

3.1.2 Modelling the hysteretic cycle

The hysteretic cycle can be modeled using a pseudo-elastic constitutive law that enables a suitable scheme to describe loading and unloading paths. The starting point for this approach was the work of Ogden & Roxburgh [1999] for the analysis of stress softening related with the Mullins effect. In the present case we shall assume that the Mullins effect does not occurs in our material. The pseudo-elasticity theory is used for modelling the purely hysteretic behaviour associated with loading-unloading cycles. This approach is similar to that used in the work of Dorfmann & Ogden [2003] who model the hysteretic behaviour for an incompressible material assuming that the Mullins effect is not present (removed by pre-conditioning).The pseudo-elastic model proposed by Ogden & Roxburgh [1999] for an incompressible material in a biaxial state defined with a primary strain energy function $\tilde{\Psi}^0$ can be written by

$$\Psi(\lambda_1, \lambda_2, \eta) = \eta\tilde{\Psi}^0(\lambda_1, \lambda_2) + \phi(\eta)\ , \tag{3.55}$$

where $\phi(\eta)$ is a smooth function of η that is subjected to

$$\phi(1) = 0. \tag{3.56}$$

Considering the decoupled strain energy function described by (3.29)

$$^{\star}\bar{\Psi}(\bar{\lambda}_1, \bar{\lambda}_2, J, \eta_{dev}, \eta_{vol}) = {}^{\star}\bar{\Psi}_{vol}(J, \eta_{vol}) + {}^{\star}\bar{\Psi}_{dev}(\bar{\lambda}_1, \bar{\lambda}_2, \eta_{dev}) \ , \tag{3.57}$$

we can also write the pseudo-energy function $^{\star}\bar{\Psi}$ in (3.55) to describe the loading-unloading behaviour of the material in the decoupled form, accounting separately, energy dissipation from the deviatoric and volumetric deformations processes. The pseudo-energy function for the deviatoric behaviour takes the form

$$^{\star}\bar{\Psi}_{dev}(\bar{\lambda}_1, \bar{\lambda}_2, \eta_{dev}) = \eta_{dev}{}^{\star}\bar{\Psi}^0_{dev}(\bar{\lambda}_1, \bar{\lambda}_2) + \phi_{dev}(\eta_{dev}) \ , \qquad \phi_{dev}(1) = 0 \ , \tag{3.58}$$

where $^{\star}\bar{\Psi}^0_{dev}$ is the unmodified deviatoric strain energy and $\phi(\eta_{dev})$ is a function that ,in the context of hysteretic cycles, accounts the energy dissipation in the deviatoric deformation process.

The pseudo-energy function for the volumetric behaviour is written by

$$^{\star}\bar{\Psi}_{vol}(J, \eta_{vol}) = \eta_{vol}{}^{\star}\bar{\Psi}^0_{vol}(J) + \phi_{vol}(\eta_{vol}), \qquad \phi_{vol}(1) = 0 \ , \tag{3.59}$$

where $^{\star}\bar{\Psi}^0_{vol}$ is the unmodified volumetric strain energy and $\phi(\eta_{vol})$ is a function that accounts the energy dissipation at a purely volumetric deformation process (confined deformation). We can now write the pseudo-energy function for the total deformation process (volumetric and deviatoric) through

$$\begin{aligned} ^{\star}\bar{\Psi}(\bar{\lambda}_1, \bar{\lambda}_2, J, \eta_{dev}\eta_{vol}) = \eta_{dev}{}^{\star}\bar{\Psi}^0_{dev}(\bar{\lambda}_1, \bar{\lambda}_2) + \phi_{dev}(\eta_{dev}) + \\ + \eta_{vol}{}^{\star}\bar{\Psi}^0_{vol}(J) + \phi_{vol}(\eta_{vol}). \end{aligned} \tag{3.60}$$

Considering the pseudo-elastic deviatoric energy function described in equation (3.58), the deviatoric components of the Cauchy stress tensor are equal to

$$\sigma_{i\ dev} = J^{-1}\lambda_i \frac{\partial {}^{\star}\bar{\Psi}_{dev}(\bar{\lambda}_1, \bar{\lambda}_2, \eta_{dev})}{\partial \lambda_i}. \tag{3.61}$$

Applying equation (3.61) in the deviatoric pseudo-elastic model in (3.58) we obtain

$$\sigma_{i\ dev} = J^{-1}\lambda_i \left(\eta_{dev} \frac{\partial {}^{\star}\bar{\Psi}^0_{dev}(\bar{\lambda}_1, \bar{\lambda}_2)}{\partial \lambda_i} \right) \ , \qquad i = 1, 2, 3. \tag{3.62}$$

Considering that for the case η_{dev} is active, equation (3.62) can be written by

$$\sigma_{i\ dev} = \eta_{dev} \left(\underbrace{J^{-1}\lambda_i \frac{\partial^\star \bar{\Psi}^0_{dev}(\bar{\lambda}_1, \bar{\lambda}_2)}{\partial \lambda_i}}_{\boldsymbol{\sigma}^0_{i\ dev}} \right). \tag{3.63}$$

The deviatoric Cauchy stress differences can now be given through

$$\sigma_{1\ dev} - \sigma_{3\ dev} = \eta_{dev} \left(\sigma^0_{1\ dev} - \sigma^0_{3\ dev} \right) \ , \tag{3.64}$$

and

$$\sigma_{2\ dev} - \sigma_{3\ dev} = \eta_{dev} \left(\sigma^0_{2\ dev} - \sigma^0_{3\ dev} \right). \tag{3.65}$$

Equations in (3.64) and (3.65) can be presented in the following form:

$$\sigma_{1\ dev} - \sigma_{3\ dev} = \eta_{dev} \left(J^{-1}\bar{\lambda}_1 \frac{\partial^\star \bar{\Psi}^0_{dev}(\bar{\lambda}_1, \bar{\lambda}_2)}{\partial \bar{\lambda}_1} \right) \ , \tag{3.66}$$

$$\sigma_{2\ dev} - \sigma_{3\ dev} = \eta_{dev} \left(J^{-1}\bar{\lambda}_2 \frac{\partial^\star \bar{\Psi}^0_{dev}(\bar{\lambda}_1, \bar{\lambda}_2)}{\partial \bar{\lambda}_2} \right). \tag{3.67}$$

The hydrostatic pressure is given by

$$\boldsymbol{\sigma}_{vol} = \frac{\partial^\star \bar{\Psi}_{vol}(J)}{\partial J}\mathbf{I} = p\mathbf{I}. \tag{3.68}$$

Applying (3.68) to the volumetric pseudo-elastic function described in (3.59), we obtain

$$\boldsymbol{\sigma}_{vol} = \eta_{vol} \frac{\partial^\star \bar{\Psi}^0_{vol}(J)}{\partial J}. \tag{3.69}$$

Considering an active η_{vol}, we can write equation 3.69 as follows

$$\boldsymbol{\sigma}_{vol} = \eta_{vol} \underbrace{\frac{\partial^\star \bar{\Psi}^0_{vol}(J)}{\partial J}}_{p^0} = \eta_{vol} p^0 \mathbf{I}. \tag{3.70}$$

Equation 3.70 can be written simply by

$$p\mathbf{I} = \eta_{vol} p^0 \mathbf{I}. \tag{3.71}$$

The deviatoric and volumetric energy dissipation functions are written by

$$\phi_{dev}(\eta_{dev}) = {}^\star\bar{\Psi}_{dev}(\bar{\lambda}_1, \bar{\lambda}_2, \eta_{dev}) - \eta_{dev}\, {}^\star\bar{\Psi}^0_{dev}(\bar{\lambda}_1, \bar{\lambda}_2) \tag{3.72}$$

and

$$\phi_{vol}(\eta_{vol}) = {}^{\star}\bar{\Psi}_{vol}(J, \eta_{vol}) - \eta_{vol}{}^{\star}\bar{\Psi}^{0}_{vol}(J). \tag{3.73}$$

Using the equations described in (3.31) and applying them to the equations in (3.72) and (3.73) we can write

$$\frac{\partial \phi_{dev}(\eta_{dev})}{\partial \eta_{dev}} = -{}^{\star}\bar{\Psi}^{0}_{dev}(\bar{\lambda}_1, \bar{\lambda}_2) \ , \tag{3.74}$$

and

$$\frac{\partial \phi_{vol}(\eta_{vol})}{\partial \eta_{dev}} = -{}^{\star}\bar{\Psi}^{0}_{vol}(J). \tag{3.75}$$

Equations (3.74) and (3.75) implicitly define the value of the constants η_{dev} and η_{vol} in terms of the deviatoric and volumetric current state the modified principal stretches $\bar{\lambda}$ and the volume ratio J respectively. In the undeformed configuration the volumetric and deviatoric unmodified strain energy functions attain its minimum value that must increases monotonically with the applied deformation. The following constraints are applied in the definition of the unmodified deviatoric and volumetric strain energy functions:

$${}^{\star}\bar{\Psi}^{0}_{dev}(\bar{\lambda}_1, \bar{\lambda}_2) \geq 0 \ , \tag{3.76}$$

$${}^{\star}\bar{\Psi}^{0}_{vol}(J) \geq 0. \tag{3.77}$$

3.1.2.1 Simple uniaxial compression cycle (unconfined deformation)

A special case for the pseudo-energy function described in (3.60) is the uniaxial loading (compression). The pseudo-elastic strain energy function for the uniaxial solicitation can be written following the same methodology used in (3.60) as

$$\begin{aligned} {}^{*}\bar{\Psi}(\bar{\lambda}, J, \eta_{dev}, \eta_{vol}) = \eta_{dev}{}^{*}\bar{\Psi}^{0}_{dev}(\bar{\lambda}) + \phi_{dev}(\eta_{dev}) + \\ + \eta_{vol}{}^{*}\bar{\Psi}^{0}_{vol}(J) + \phi_{vol}(\eta_{vol}) \ , \end{aligned} \tag{3.78}$$

with

$${}^{*}\bar{\Psi}_{dev}(\bar{\lambda}, \eta_{dev}) = \eta_{dev}{}^{*}\bar{\Psi}^{0}_{dev}(\bar{\lambda}) + \phi_{dev}(\eta_{dev}) \ , \qquad \phi_{dev}(1) = 0 \ , \tag{3.79}$$

and

$${}^{*}\bar{\Psi}_{vol}(J, \eta_{vol}) = \eta_{vol}{}^{*}\bar{\Psi}^{0}_{vol}(J) + \phi_{vol}(\eta_{vol}) \ , \qquad \phi_{vol}(1) = 0. \tag{3.80}$$

The respective Cauchy deviatoric uniaxial stress is given by

$$\sigma_{dev} = \eta_{dev} \underbrace{\left(J^{-1}\lambda \frac{\partial^* \bar{\Psi}^0_{dev}(\bar{\lambda})}{\partial \lambda} \right)}_{\sigma^0_{dev}}. \tag{3.81}$$

The deviatoric uniaxial nominal stress component is obtained through

$$P_{dev} = \eta_{dev} \underbrace{\left(\frac{\partial^* \bar{\Psi}^0_{dev}(\bar{\lambda})}{\partial \lambda} \right)}_{P^0_{dev}}. \tag{3.82}$$

In terms of the volumetric stress component we have

$$\boldsymbol{\sigma}_{vol} = p\mathbf{I} = \eta_{vol} \underbrace{\left(\frac{\partial^* \bar{\Psi}^0_{vol}(J)}{\partial J} \right)}_{p^0}, \tag{3.83}$$

where p^0 is the unmodified hydrostatic pressure given by $p^0 = \frac{1}{3}\sigma^0$.

It is now possible to state that for modelling the unloading behaviour the constants η_{vol} and η_{dev} must be less than unity in order to allow the stress decrease for the same deformation level during the unloading path (hysteretic behaviour). It should be noticed that the values for η_{vol} and η_{dev} are set constant and equal to unity during the loading path.

$$\eta_{dev} = \begin{cases} 1, & if\ loading \\ < 1, & if\ unloading \end{cases}$$

$$\eta_{vol} = \begin{cases} 1, & if\ loading \\ < 1, & if\ unloading \end{cases}$$

Regarding the uniaxial compression case we can write the deviatoric dissipation function ϕ_{dev} as

$$\phi_{dev}(\eta_{dev}) = {}^*\bar{\Psi}_{dev}(\bar{\lambda}, \eta_{dev}) - \eta_{dev}{}^*\bar{\Psi}^0_{dev}(\bar{\lambda}). \tag{3.84}$$

The volumetric dissipation function ϕ_{vol} for the uniaxial compression case is given by

$$\phi_{vol}(\eta_{vol}) = {}^*\bar{\Psi}_{vol}(J, \eta_{vol}) - \eta_{vol}{}^*\bar{\Psi}^0_{vol}(J). \tag{3.85}$$

Differentiating ϕ_{vol} and ϕ_{dev} by η_{vol} and η_{dev}, and using (3.40) we obtain

$$\frac{\partial \phi_{dev}(\eta_{dev})}{\partial \eta_{dev}} = \phi'(\eta_{dev}) = -{}^*\bar{\Psi}^0_{dev}(\bar{\lambda}), \tag{3.86}$$

$$\frac{\partial \phi_{vol}(\eta_{vol})}{\partial \eta_{vol}} = \phi'(\eta_{vol}) = -{}^{*}\bar{\Psi}^{0}_{vol}(J). \tag{3.87}$$

Differentiating (3.86) by the stretch ratio λ and substituting (3.86) we obtain

$$\frac{\partial \phi'_{dev}(\eta_{dev})}{\partial \lambda} = -\underbrace{\frac{\partial {}^{*}\bar{\Psi}^{0}_{dev}(\bar{\lambda})}{\partial \lambda}}_{P^{0}_{dev}} = \underbrace{\frac{\partial \phi'_{dev}(\eta_{dev})}{\partial \eta_{dev}}}_{\phi''(\eta_{dev})} \frac{\partial \eta_{dev}}{\partial \lambda}. \tag{3.88}$$

Assuming $P_{dev} < 0$ for compression and knowing that the variable η_{dev} decreases with unloading (increasing λ) we can state that $\frac{\partial \eta_{dev}}{\partial \lambda} < 0$ and therefore

$$\phi''(\eta_{dev}) < 0. \tag{3.89}$$

Applying the same methodology to the volumetric dissipation function in (3.87) with the help of (3.88) we obtain

$$\frac{\partial \phi'_{vol}(\eta_{vol})}{\partial J} = \underbrace{\frac{\partial \phi'_{vol}(\eta_{vol})}{\partial \eta_{vol}}}_{\phi''(\eta_{vol})} \frac{\partial \eta_{vol}}{\partial J} = -\underbrace{\frac{{}^{*}\bar{\Psi}^{0}_{vol}(J)}{\partial J}}_{p^{0}}. \tag{3.90}$$

Associating $p < 0$ for compressive hydrostatic pressure ($J < 1$) and associating unloading with decreasing η_{vol} and increasing J it follows that $\frac{\partial \eta_{vol}}{\partial J} < 0$ and for signal consistency we obtain

$$\phi''(\eta_{vol}) < 0. \tag{3.91}$$

Referring to (3.86), (3.87) and the positiveness of the deviatoric and volumetric strain energy functions, we can conclude that ϕ'_{dev} and ϕ'_{vol} are monotonically decreasing functions. We can conclude also, that the value of η_{dev} and η_{vol} is dependent of the maximum energy value attained during the loading path.

Noting that the maximum energy is achieved at $\bar{\lambda}_{max}$ for a pure deviatoric behaviour and J_{max} for a pure volumetric behaviour. Setting $\eta_{vol} = \eta_{dev} = 1$ at any point on the loading path from where unloading is initiated, we can write

$$\phi'(1) = {}^{*}\bar{\Psi}^{0}_{dev}(\bar{\lambda}, 1) = -{}^{*}\bar{\Psi}^{max}_{dev} \tag{3.92}$$

and

$$\phi'(1) = {}^{*}\bar{\Psi}^{0}_{vol}(J, 1) = -{}^{*}\bar{\Psi}^{max}_{vol}, \tag{3.93}$$

where ${}^{*}\bar{\Psi}^{max}_{dev}$ and${}^{*}\bar{\Psi}^{max}_{vol}$ are the maximum values of strain energy obtained in the deviatoric and volumetric regime, respectively.

When the material is fully unloaded $\bar{\lambda} = 1$ and $J = 1$ the constants η_{vol} and η_{dev} attain its minimum value, say η_{vol}^{min} and η_{dev}^{min}. Inserting these values in (3.86) and (3.87, we can write

$$\phi'(\eta_{dev}^{min}) = -{}^*\bar{\Psi}_{dev}^0(1, \eta_{dev}^{min}) = 0 \tag{3.94}$$

and

$$\phi'(\eta_{vol}^{min}) = -{}^*\bar{\Psi}_{vol}^0(1, \eta_{vol}^{min}) = 0. \tag{3.95}$$

The functions ϕ_{dev} and ϕ_{vol} depends on the point of unloading through the value of ${}^*\bar{\Psi}_{dev}^{max}$ and ${}^*\bar{\Psi}_{vol}^{max}$.The pseudo-energy function described in (3.78) have a residual value that is equal to the sum of the deviatoric and volumetric dissipation parts, obtained for the undeformed final configuration (final of the unloading process).

$${}^*\bar{\Psi}(1, 1, \eta_{dev}^{min}, \eta_{vol}^{min}) = \underbrace{\phi(\eta_{dev}^{min}) + \phi(\eta_{vol}^{min})}_{\phi(\eta_{total}^{min})}. \tag{3.96}$$

The residual energy can be interpreted as the energy dissipated during the loading-unloading cycles. In an uniaxial test $\phi(\eta_{total}^{min})$ may be interpreted as the *area between the loading and the unloading curve.*

3.1.2.2 Volumetric deformation cycle (confined deformation)

Considering the volumetric strain energy function in (3.46) we can write a pseudo-elastic model for modeling purely volumetric behaviour through

$${}^\diamond\bar{\Psi}(J, \eta_{vol}) = \eta_{vol}{}^\diamond\bar{\Psi}^0(J) + \phi_{vol}(\eta_{vol}). \tag{3.97}$$

The dissipation function ϕ_{vol} is given by (3.85). The respective volumetric Cauchy stress $\boldsymbol{\sigma}_{vol}$ is given by

$$\boldsymbol{\sigma}_{vol} = p\mathbf{I} = \eta_{vol} \underbrace{\left(\frac{\partial^\diamond \bar{\Psi}^0(J)}{\partial J} \right)}_{p^0}, \tag{3.98}$$

where p^0 is the unmodified hydrostatic pressure given by $p^0 = \frac{1}{3}(\sigma_1^0 + \sigma_2^0 + +\sigma_3^0)$ and the unloading response is affected only by the value of η_{vol}.

3.1.3 Modified Dorfmann-Ogden model

In their work Dorfmann & Ogden [2003] proposed a dissipation function $\phi(\eta)$ based on the dissipation function used by Ogden & Roxburgh [1999] to model the energy dissipation induced by the Mullins effect in incompressible rubber given by:

$$-\phi'(\eta) = m\ \tanh^{-1}[r(\eta-1)] + \Psi^{max}\ , \tag{3.99}$$

where r and m are adjustable material parameters and Ψ_{max} represents the maximum strain energy density achieved during the loading.

The model in (3.99) do not distinguish between the mechanisms of energy dissipation, namely, its volumetric or deviatoric nature. The dissipation function can be modified to separately model the deviatoric and volumetric dissipation. The deviatoric dissipation term can be written by

$$-\phi'_{dev}(\eta_{dev}) = m_{dev}\ \tanh^{-1}[r_{dev}(\eta_{dev}-1)] + \bar{\Psi}^{max}_{dev}\ , \tag{3.100}$$

while the volumetric model is given by

$$-\phi'_{vol}(\eta_{vol}) = m_{vol}\ \tanh^{-1}[r_{vol}(\eta_{vol}-1)] + \bar{\Psi}^{max}_{vol}. \tag{3.101}$$

From (3.100) and (3.101), applying (3.86) and (3.87), we obtain, after some algebraic manipulation, the expressions for the deviatoric η_{dev} and volumetric η_{vol} dissipation factors for a simple uniaxial case, given by equations (3.102) and (3.103), respectively, written as

$$\eta_{dev} = 1 - \frac{1}{r_{dev}} \tanh\left[\frac{\bar{\Psi}^{max}_{dev} - {}^{*}\bar{\Psi}^{0}_{dev}(\bar{\lambda})}{m_{dev}}\right]\ , \tag{3.102}$$

and

$$\eta_{vol} = 1 - \frac{1}{r_{vol}} \tanh\left[\frac{\bar{\Psi}^{max}_{vol} - {}^{*}\bar{\Psi}^{0}_{vol}(J)}{m_{vol}}\right]. \tag{3.103}$$

Integrating (3.100) and (3.101) we obtain ϕ_{dev} and ϕ_{vol}, for the Dorfmann and Ogden model, expressed respectively by

$$\phi_{dev}(\eta_{dev}) = \int_1^{\eta_{dev}} (-m_{dev}\ \tanh^{-1}[r_{dev}(\eta_{dev}-1)] - \bar{\Psi}^{max}_{dev})\ d\eta_{dev} = \tag{3.104}$$

$$= -\frac{m_{dev}}{2r_{dev}} \ln\left[1 - (\eta_{dev} r_{dev} - r_{dev})^2\right] - \bar{\Psi}^{max}_{dev}(\eta_{dev}-1)$$

$$- m_{dev} \tanh^{-1}\left[r_{dev}(\eta_{dev}-1)\right](\eta_{dev}-1) \tag{3.105}$$

and

$$\phi_{vol}(\eta_{vol}) = \int_1^{\eta_{vol}} (m_{vol}\ \tanh^{-1}[r_{vol}(\eta_{vol}-1)] + \bar{\Psi}_{vol}^{max})\ d\eta_{vol} = \tag{3.106}$$

$$= -\frac{m_{vol}}{2r_{vol}} \ln\left[1-(\eta_{vol}r_{vol}-r_{vol})^2\right] - \bar{\Psi}_{vol}^{max}(\eta_{vol}-1)$$

$$- m_{vol} \tanh^{-1}\left[r_{vol}(\eta_{vol}-1)\right](\eta_{vol}-1). \tag{3.107}$$

The minimum value for η_{dev} and η_{vol} are obtained for a stress-free configuration given by $\bar{\lambda}=1$ and $J=1$, respectively. Consequently, ${}^*\bar{\Psi}_{dev}^0(1)=0$ and ${}^*\bar{\Psi}_{vol}^0(1)=0$. Substituting into (3.102) and (3.103), we obtain the minimum values for the scalars η_{dev} and η_{vol}, expressed by

$$\eta_{dev}^{min} = 1 - \frac{1}{r_{dev}} \tanh\left[\frac{\bar{\Psi}_{dev}^{max}}{m_{dev}}\right]\ , \tag{3.108}$$

and

$$\eta_{vol}^{min} = 1 - \frac{1}{r_{vol}} \tanh\left[\frac{\bar{\Psi}_{vol}^{max}}{m_{vol}}\right]. \tag{3.109}$$

3.1.4 Modified Zúñiga model

More recently, Elías-Zúñiga [2005] using the pseudo-elastic model by Ogden & Roxburgh [1999], proposed a dissipation function $\phi(\eta)$ of the form:

$$-\phi'(\eta) = -1\left(\frac{1}{b}\ln\eta\right)^{1/n} + \Psi_{max}\ , \tag{3.110}$$

where b is a material parameter and n a is positive material parameter chosen to best fit data. In his work, Elías-Zúñiga [2005] set the value $n=1/2$ in order to best fit experimental data for a given rubber-like material. Following the same assumptions used in (3.100) and (3.101), for the Dorfmann-Ogden model, we can rewrite the Zuñiga model to account for deviatoric and volumetric energy dissipation, to be equal to

$$-\phi'_{dev}(\eta_{dev}) = -1\left(\frac{1}{b_{dev}}\ln\eta_{dev}\right)^{1/n} + \bar{\Psi}_{dev}^{max} \tag{3.111}$$

and

$$-\phi'_{vol}(\eta_{vol}) = -1\left(\frac{1}{b_{vol}}\ln\eta_{vol}\right)^{1/n} + \bar{\Psi}_{vol}^{max}. \tag{3.112}$$

Applying (3.86) and (3.87), we obtain, after some algebraic manipulations, the expressions for the deviatoric and volumetric dissipation factors. For the uniaxial case we

obtain

$$\eta_{dev} = e^{-b_{dev}\sqrt{\bar{\Psi}^{max}_{dev} - {}^*\bar{\Psi}^0_{dev}(\bar{\lambda})}} \tag{3.113}$$

and

$$\eta_{vol} = e^{-b_{vol}\sqrt{\bar{\Psi}^{max}_{vol} - {}^*\bar{\Psi}^0_{vol}(J)}}. \tag{3.114}$$

Integrating (3.111) and (3.112) we obtain the dissipative energy functions ϕ_{dev} and ϕ_{vol}, for the Zuñiga model, given by

$$\begin{aligned}\phi_{dev}(\eta_{dev}) &= \int_1^{\eta_{dev}} \left(\left(\frac{1}{b_{dev}} \ln \eta_{dev} \right)^2 - \bar{\Psi}^{max}_{dev} \right) d\eta_{dev} = \\ &= \frac{2}{b^2_{dev}} \left[\eta_{dev} \left(1 - \ln \eta_{dev} + \frac{1}{2} (\ln \eta_{dev})^2 \right) - 1 \right] - \bar{\Psi}^{max}_{dev}(\eta_{dev} - 1) \ ,\end{aligned} \tag{3.115}$$

and

$$\begin{aligned}\phi_{vol}(\eta_{vol}) &= \int_1^{\eta_{vol}} \left(\left(\frac{1}{b_{vol}} \ln \eta_{vol} \right)^2 - \bar{\Psi}^{max}_{vol} \right) d\eta_{vol} = \\ &= \frac{2}{b^2_{vol}} \left[\eta_{vol} \left(1 - \ln \eta_{vol} + \frac{1}{2} (\ln \eta_{vol})^2 \right) - 1 \right] - \bar{\Psi}^{max}_{vol}(\eta_{vol} - 1).\end{aligned} \tag{3.116}$$

The minimum values for η_{dev} and η_{vol} are obtained for a stress-free configuration given by $\bar{\lambda} = 1$ and $J = 1$, respectively. Consequently, ${}^*\bar{\Psi}^0_{dev}(\bar{\lambda}) = 0$ and ${}^*\bar{\Psi}^0_{vol}(J) = 0$. Substituting in (3.113) and (3.114), we obtain

$$\eta^{min}_{dev} = e^{-b_{dev}\sqrt{\bar{\Psi}^{max}_{dev}}} \tag{3.117}$$

and

$$\eta^{min}_{vol} = e^{-b_{vol}\sqrt{\bar{\Psi}^{max}_{vol}}}. \tag{3.118}$$

3.2 Modelling heat generation in nonlinear elastic materials

Cyclic deformations of rubber or rubber-like materials can give rise to a temperature increase due to *internal heat generation* associated with *energy dissipative phenomena*. In

this thesis we propose a *thermomechanical model* that models the hysteretic behaviour of nonlinear elastic materials and the consequent *heat build-up* in a *fully coupled* thermomechanical way. The theory was implemented for the mechanical modelling of the loading/unloading behaviour of the compressible CPGC material.

The modifications to the pseudo-elastic theory proposed in section 3.1, introduced in order to decouple deviatoric and volumetric dissipative mechanisms that were found to affect the CPGC mechanical behaviour when subjected to cyclic deformations, are the basis of this thermomechanical approach.

The obtained thermomechanical model was implemented in a nonlinear finite element code (ABAQUS®) via user subroutines to simulate a total loading-unloading cycle and the consequent internal heat generation due to energy dissipative (hysteretic) considering affection of material parameters. The numerical implementation of this procedure will be discussed in more detail at section 4.3.3.

3.2.1 Heat build-up modelling

As stated in section 2.5, the dissipative effects in a material are responsible for the heat build-up during cyclic deformations. From the approach followed in section 3.1 we can decouple the dissipative mechanisms in deviatoric and volumetric terms. For simplicity reasons we focus our attention on the uniaxial case, from which we obtain the deviatoric and volumetric dissipative energy values given by $\phi_{dev}(\eta_{dev})$ and $\phi_{vol}(\eta_{vol})$, respectively.

If both deviatoric and volumetric dissipative effects are present at the material, the total dissipated energy for one loading-unloading cycle is given by

$$\phi_{total} = \phi_{vol}(\eta_{vol}) + \phi_{dev}(\eta_{dev}). \tag{3.119}$$

The *thermal energy rate* per unit volume during the dissipative process is given by

$$r_h = \frac{d\phi_{total}}{dt} \ , \tag{3.120}$$

where r_h is the *volumetric heat flux* described in expression (2.61). This term the describes thermal energy generated per unit time and unit volume during the dissipative process and it is responsible for the heat build-up in the material.

For the present work it was considered that all the dissipated energy generated during the loading-unloading cycle and expressed by ϕ_{total}, is *totally converted in heat*.

With (3.120) and its implementation at the finite element code, in conjunction with the procedure discussed in section 3.1, we are able to define a fully-coupled thermomechanical model that accounts hysteretic effects in cyclic deformations and the consequent material temperature increase through the monitoring of dissipative energy values.

This page is intentionally left blank.

Chapter 4

Constitutive Modelling

The nonlinear elastic behaviour of materials is commonly described by constitutive equations based on strain energy functions as described in section 2.2. In this work a *purely phenomenological approach*, describing the *macroscopic behaviour* of CPGC material is used. Within this approach we are mainly concerned with the methodology to perform a purely mathematical fitting of hyperelastic models to a set of experimental data that characterize the mechanical behaviour of the CPGC.

Considering that the CPGC will be submitted mainly to *uniaxial solicitations* in practical cases (shoe insoles, seat cushions, vibration dampers, etc...), a experimental methodology defined by *simple uniaxial compression* (unconfined deformation) and *volumetric compression* (confined deformation) experimental tests was defined. The real behaviour of the CPGC was evaluated through an experimental procedure defined by simple uniaxial compression tests (loading-unloading cycles) at different temperatures ($T = 23^oC$, $T = 100^oC$ and $T = -10^oC$) and volumetric compression tests at $T = 23^oC$. Five formulations of CPGC (varying the amount of incorporated cork) as summarized in table 4.1, were experimentally evaluated. The experimental procedure is discussed in more detail in section 4.1.

In section 4.2 is discussed the material parameters fitting procedure adopted for the modelling both the *loading path* and the *hysteretic* (loading-unloading path) cycle. Also,

Table 4.1: CPGC formulations characteristics.

Formulations	*php*	% in cork weight	Apparent density (kg/m^3)
A	25	6	751.4
B	50	11	660.1
C	75	16	623.2
D	0	0	957.8
F	100	20	584.5

in section 4.2, the special constitutive equations for uniaxial and volumetric compression as the basis for the numerical fitting procedure adopted for the modelling of the loading path are presented. Numerical fitting of the hysteretic cycle through the implementation of a *modified form of the Dorfmann-Ogden model* [Dorfmann & Ogden, 2003] and *modified form of Zúñiga model* [Elías-Zúñiga, 2005] are also discussed in section 4.2.

The finite element method (FEM) implementation of the constitutive equations developed especially for the CPGC material are discussed in section 4.3, nominally, the definition of *material subroutines* that allows the modelling of *hysteretic cycles* and the consequent *heat build-up* using nonlinear finite element tools. Simple finite element (FE) models that replicates the experimental procedure (uniaxial and volumetric deformation) and its numerical correlation with experimentally obtained results are also discussed in section 4.3.

4.1 Experimental methodology and results

4.1.1 Simple uniaxial compression

The mechanical behaviour of different CPGC formulations, varying the amount of incorporated cork, was evaluated by simple uniaxial (compression) loading-unloading cycles considering three different temperatures ($T = 23^oC$, $T = 100^oC$ and $T = -10^oC$) and four formulations of CPGC (A, B, D and F). The different cork incorporations for those formulations are summarized in table 4.1. The simple uniaxial compression tests were conducted in CPGC material buttons ($\varnothing = 29.0mm,\ h = 13.1mm$) following the standard test method for rubber properties in compression *ASTM D575-91*. In order to minimize the barrelling effect in the material specimen that would cause deviations from the homogeneous axial deformation state, lubricated plates were used during the compression test. Experimental tests were conducted in an Instron® 4505 machine equipped with a thermal chamber Instron®. The axial force was measured by a standard loading cell (50 kN) and the nominal stress was obtained for each specimen as the ratio of the measured force to the initial undeformed area. The cross-head speed was set to 12 mm/min and the maximum compressive strain set to $\epsilon \simeq 0.55$.

The uniaxial tests were repeated ten times for each formulation and temperature and the numerical data obtained was treated using the software OriginPro® 7.5.

4.1.1.1 Simple uniaxial compression results (loading path)

In this section the experimental results for the different CPGC formulations tested are compared considering for now, only the loading path resulting from the *truncation* of the

experimentally obtained deformation cycles. The experimental results for the complete cycle (loading and unloading path) are described later in section 4.1.1.2.

Figure 4.1 show a comparison between the mechanical behaviour of four formulations of CPGC tested considering $T = 23^oC$. Is visible an increase in stiffness followed by a continuous linearization of the mechanical response of the CPGC material with the incorporation of cork. The stiffer formulation is formulation F that corresponds to an maximum in the cork incorporation (20% in cork weight). By other hand, the softer material corresponds to formulation D characterized by a non incorporation of cork.

Note that for this section, the nominal stress and nominal strain values are given in absolute values.

In figures 4.2 and 4.3, is plotted the mechanical behaviour of the CPGC formulations considering $T = 100^oC$ and $T = -10^oC$, respectively.

The temperature dependence of formulations A, B and F can be seen in figures 4.4, 4.5 and 4.6, where is visible the decrease in the material stiffness with the increase in temperature, for all tested formulations.

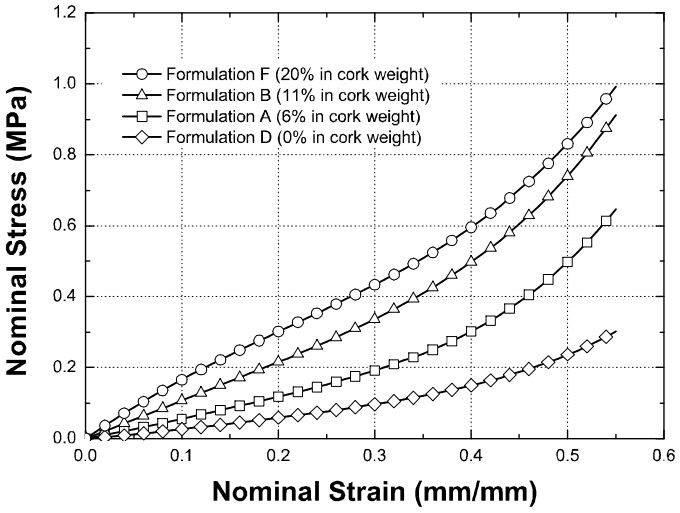


Figure 4.1: Uniaxial nominal stress plotted against nominal strain, considering $T = 23^oC$.

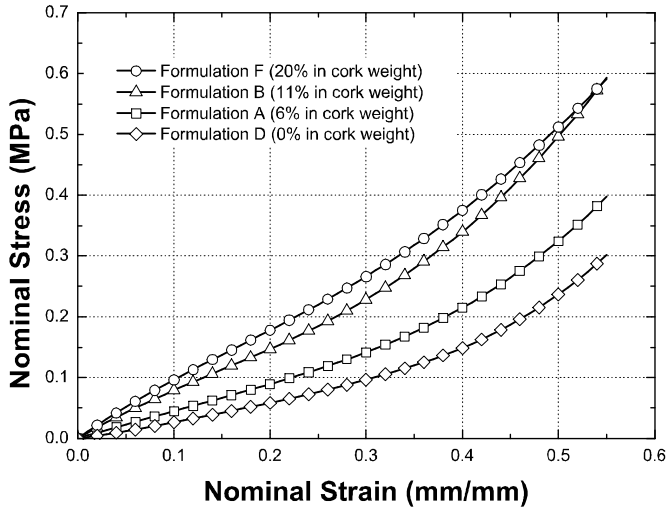


Figure 4.2: Uniaxial nominal stress plotted against nominal strain, considering $T = 100^oC$.

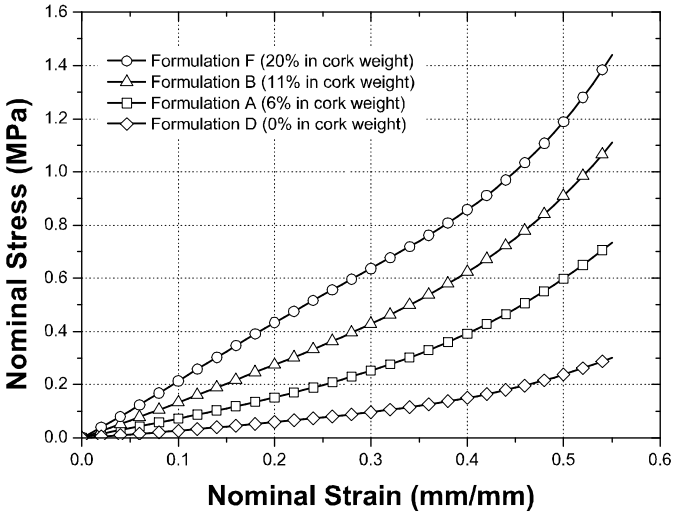


Figure 4.3: Uniaxial nominal stress plotted against nominal strain, considering $T = -10^oC$.

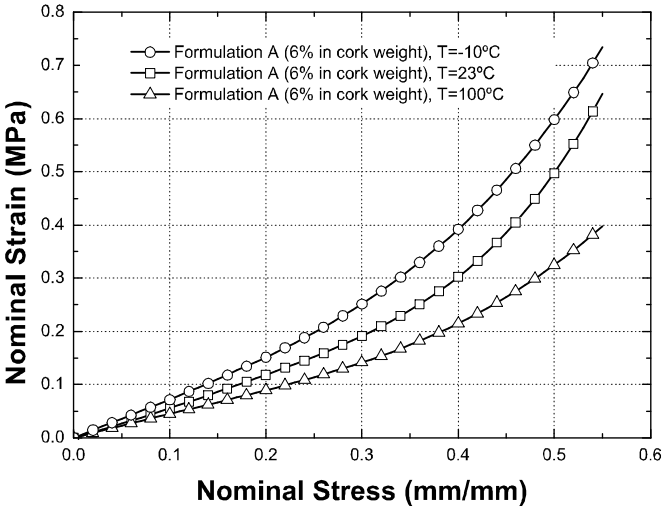


Figure 4.4: Uniaxial nominal stress plotted against nominal strain considering formulation A, with $T = 23^oC$, $T = 100^oC$ and $T = -10^oC$.

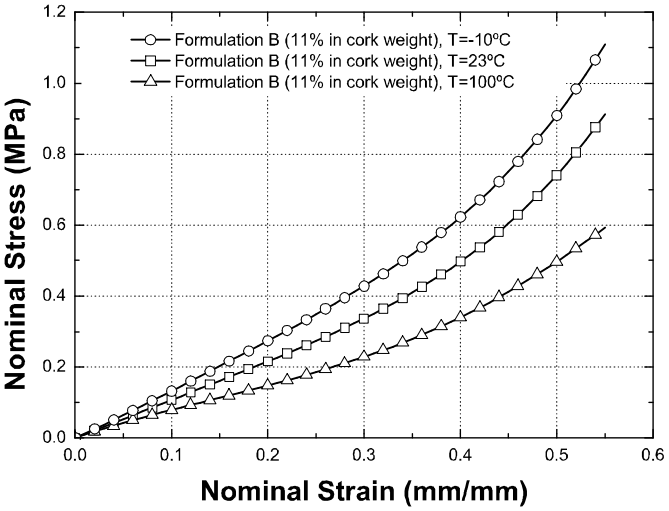


Figure 4.5: Uniaxial nominal stress plotted against nominal strain considering formulation B, with $T = 23^oC$, $T = 100^oC$ and $T = -10^oC$.

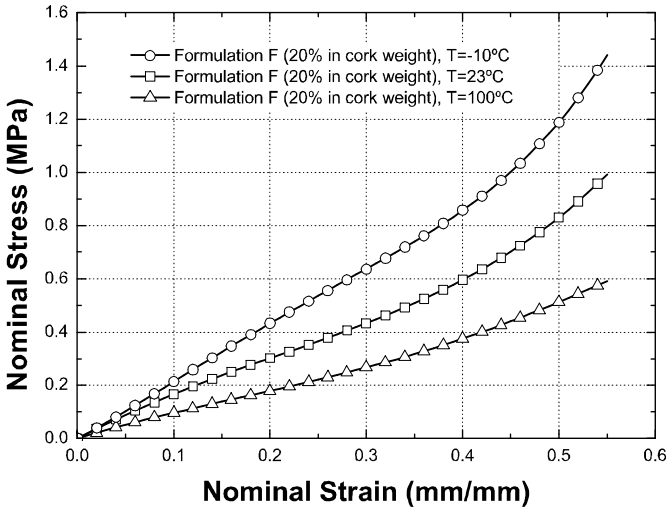


Figure 4.6: Uniaxial nominal stress plotted against nominal strain considering formulation F, with $T = 23^oC$, $T = 100^oC$ and $T = -10^oC$.

4.1.1.2 Simple uniaxial compression results (loading-unloading path)

As expressed in section 4.1.1, the material mechanical behaviour was evaluated through a simple uniaxial loading-unloading cycle up to a nominal strain $\epsilon \simeq 0.55$. For a better understanding of the hysteresis dependence with cork incorporation, the next figures show the total deformation cycle (loading-unloading) imposed during the uniaxial compression tests considering $T = 23^oC$ and not only the loading path as already seen in figure 4.1.

From figures 4.7-4.10, is possible to conclude that material hysteresis increases with the incorporation of cork as it is maximum for formulation F (figure 4.10) and minimum for formulation D (figure 4.9). Performing a cyclic integral in the experimental nominal stress-nominal strain loop we obtain the area between the loading and the unloading curve correspondent to the amount of dissipated energy per deformation cycle (see equation 2.194). These energy values are summarized in table 4.2.

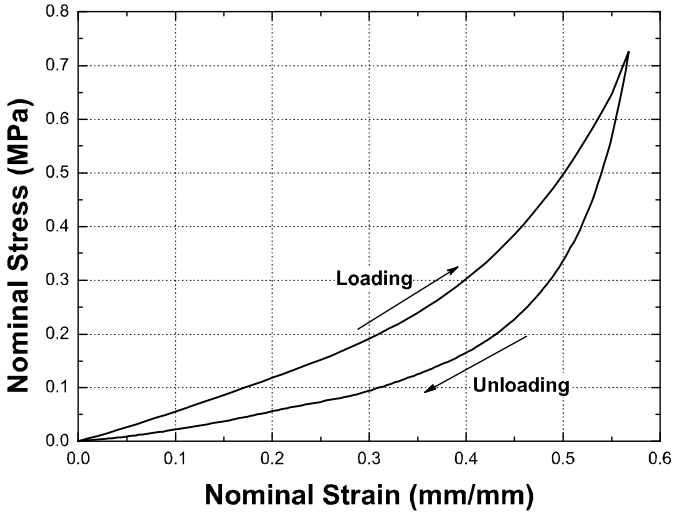


Figure 4.7: Uniaxial loading-unloading cycle obtained for formulation A, considering $T = 23^oC$.

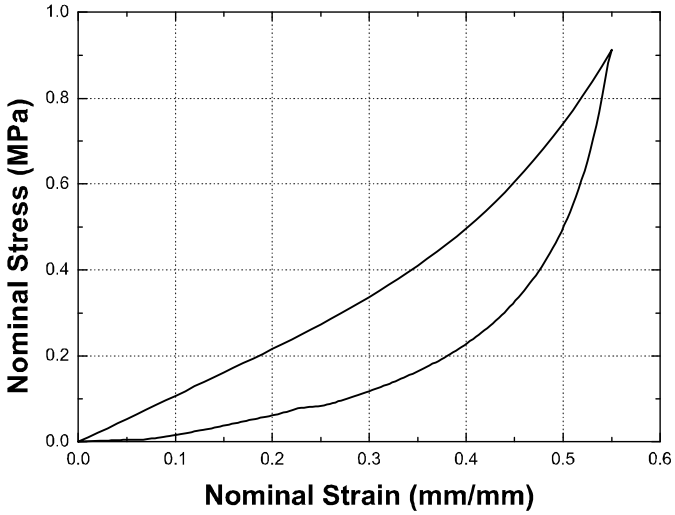


Figure 4.8: Uniaxial loading-unloading cycle obtained for formulation B, considering $T = 23^oC$.

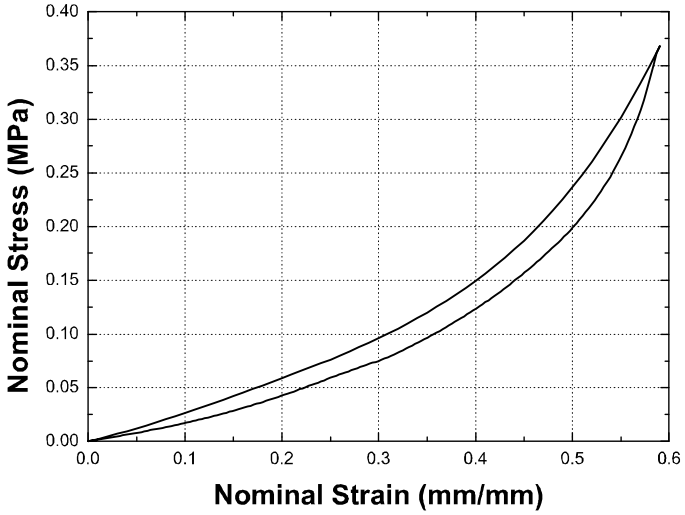


Figure 4.9: Uniaxial loading-unloading cycle obtained for formulation D, considering $T = 23^oC$.

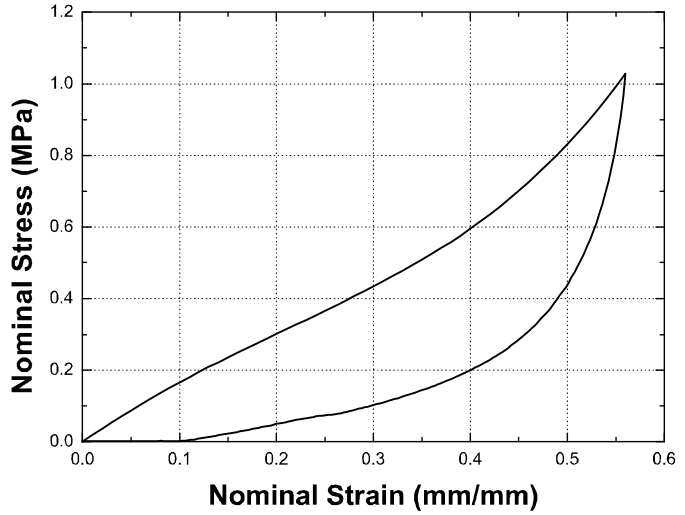


Figure 4.10: Uniaxial loading-unloading cycle obtained for formulation F, considering $T = 23^oC$.

Table 4.2: Hysteresis (dissipated energy density per deformation cycle) values for CPGC formulations.

Formulation	*php*	% in cork weight	Hysteresis ($mJmm^{-3}$)
A	25	6	0.049
B	50	11	0.095
D	0	0	0.011
F	100	20	0.153

4.1.2 Volumetric compression

The volumetric tests were conducted using cylindrical material specimens ($\varnothing = 18.8mm$, $h = 25.3mm$) that fits snugly in a rigid container whose top surface is compressed with a rigid piston. The compressive stress imposed by the piston is effectively the hydrostatic pressure developed inside the container. The volume ratio J, is calculated from the piston displacement and is a measure of the volumetric strain developed in the sample. This test is important to quantify the CPGC mechanical response when highly confined and the material behaviour is ruled mainly by the volumetric mechanical characteristics of the material.

Notice that is common in experimental procedures, rewrite the volume ratio defined at expression (2.19), in terms of current sample's volume V_c and initial sample's volume V_0. This volumetric relation is given by

$$J = \frac{V_c}{V_0}. \tag{4.1}$$

4.1.2.1 Volumetric compression results (loading path)

Three material formulations (A, B and C) were tested considering $T = 23^oC$. In figure 4.11 is shown a comparison of the volumetric mechanical response for the tested formulations, where is visible an increase in compressibility (decrease in the *tangent bulk modulus*) with the incorporation of cork. This behaviour is due to the high degree of compressibility that characterizes the cork which influences the overall volumetric mechanical response of the CPGC material formulations.

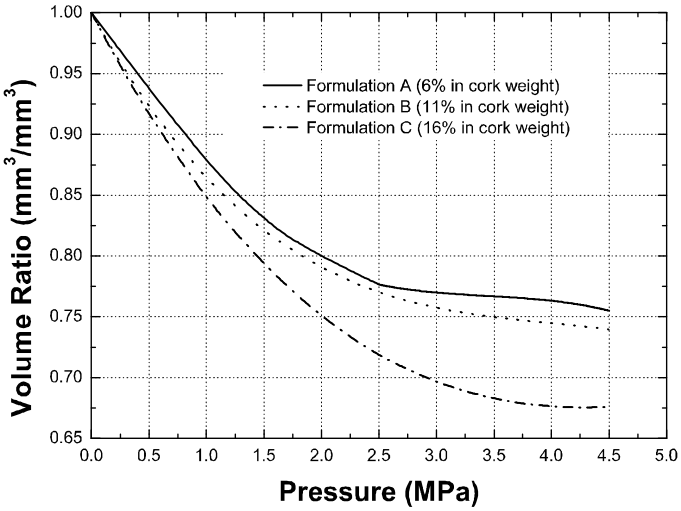


Figure 4.11: Volume ratio plotted against hydrostatic pressure for formulations of CPGC, considering $T = 23^oC$.

Note that this experimental procedure do not account the temperature dependence as did in section 4.1.1 for the simple uniaxial compression experimental procedure. It was observed that during the tests at $T = 100^oC$ the material flows out of the container's cavity leading to variations in the sample's mass, introducing major experimental errors.

4.1.2.2 Volumetric compression results (loading-unloading path)

In figure 4.11 we showed the volumetric behaviour for three formulations of CPGC considering only the loading path. In order to quantify the purely volumetric dissipative behaviour of the material we need to perform a loading-unloading deformation cycle maintaining the material in a confined space. The experimental apparatus for measuring the purely volumetric CPGC's mechanical behaviour described in section 4.1.2, do not allow to perform in a reproducible manner loading-unloading cycles. Due to the mechanical construction of the experimental apparatus and the mechanical characteristics of the CPGC the piston tends to be stucked inside the rigid container during the unloading phase. For that reason, and to be able to numerically implement the new formulation for modelling hysteresis described in section 3.1, the volumetric dissipative behaviour of formulation A was evaluated in a purpose build bulk modulus measuring apparatus at the *University of the West of England* [Coveney *et al.*, 2008]. The apparatus consists of a dilatometer (specimen covered by a primary pressurizing fluid) within a pressurized vessel. The changes in the volume of the sample were measured by changes in the level

of the primary fluid. This measuring technique allows the output of "clean" pressurizing-depressurizing curves that reproduces the purely volumetric behaviour of the material in a loading-unloading case scenario. For this experimental procedure the maximum applied pressure was set equal to approximately $1.0MPa$.

The experimental purely volumetric loading-unloading cycle is shown in figure 4.12, where is possible to see that under confined deformation, the CPGC's mechanical response is characterized by a hysteretic behaviour.

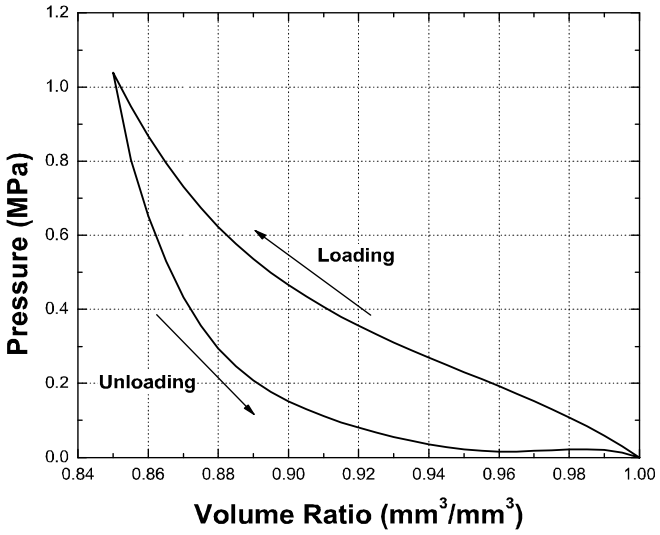


Figure 4.12: Volumetric (confined deformation) loading-unloading curve for formulation A, considering $T = 23^oC$.

4.2 Material parameters fitting

Constitutive equations for hyperelastic materials are based on *strain energy functions* (see section 2.2.1) whose adjustable *material parameters* are calculated in order to best reproduce the real behaviour of a material. As seen in section 2.3, the wide variety and different fitting capabilities of strain energy functions, make indispensable a systematic *numerical fit procedure* in order to best predict the mechanical behaviour of a material in particular.

In this section is discussed the numerical fitting methodology followed for the reproduction of the CPGC's experimental data for loading path and hysteretic cycles. Also in this section, a tool for predicting the mechanical behaviour of non-tested formulations of CPGC based on *interpolation of material parameters* is presented.

4.2.1 Fitting the loading path

4.2.1.1 Simple uniaxial compression stress

The experimental results discussed in section 4.1.1.1 are the basis for the numerical fit procedure followed for the calculation of material parameters that are calibrated for best reproducing, in this particular case, the uniaxial mechanical behaviour of CPGC. For this procedure we use the material parameters calibration tool available in the nonlinear finite element package ABAQUS®. This package have *in-built* both phenomenological and physical hyperelastic models and is capable of calculating material parameters for hyperelastic models based on uniaxial, equibiaxial, pure shear and volumetric stress experimental data.

For a given experimental data set, ABAQUS® calculates the material parameters through a *least-square procedure* that tries to minimize the error E in stress, between the experimental stress values P_{test} and the stress values predicted from the constitutive equations P_{theo}. The error E is expressed by

$$E = \sum_{i=1}^{n} \left(1 - \frac{P_{theo}}{P_{test}}\right)^2 , \tag{4.2}$$

where n is the number of nominal stress-nominal strain data pairs.

MATLAB® was also used for the calibration of the volumetric material parameters through *linear least square fitting procedure* considering different *expansion orders* in the volumetric term of the strain energy function. This issue will be discussed with more detail later in this section.

Polynomial models such as Mooney-Rivlin, Second order polynomial, Neo-Hookean and Yeoh are linear in the coefficients C_{ij} (see section 2.3) and for those models a linear least-square fitting procedure is used for the calibration of the material parameters. By other hand, the Ogden model is nonlinear in the coefficients α_i necessitating for the material parameters calibration, a *nonlinear least-square procedure*.

Special care must be taken during the calibration of material parameters in order to avoid *instabilities* that could lead to *nonphysical* behaviour, such as inversion of the *monotonicity* in the stress-strain curve. In ABAQUS®, the material parameters are not numerically constrained and must be the user to discard non-physical solutions *a posteriori*. The model stability is checked by the *Drucker stability condition* and this stability condition requires that a infinitesimal change in stress $d\boldsymbol{\sigma}$ followed by an infinitesimal change in strain $d\boldsymbol{\epsilon}$ satisfies the inequality expressed by

$$d\boldsymbol{\sigma} : d\boldsymbol{\varepsilon} > 0. \tag{4.3}$$

It must be the user to check if the *stability limit* is in the range of the expected deformations and to perform a test in a simple FE model in order to check the stability of the calibrated model in the considered range of deformation.

The constitutive equations used for the calibration of material parameters are reformulated for each experimental stress state induced in the material sample. Since we are interested on the calibration based on the experimental simple uniaxial stress data we will outline here the principal phenomenological constitutive equations used in the calibration of material parameters for the CPGC material. In figure 4.13 is shown the stress state induced by a compressive load.

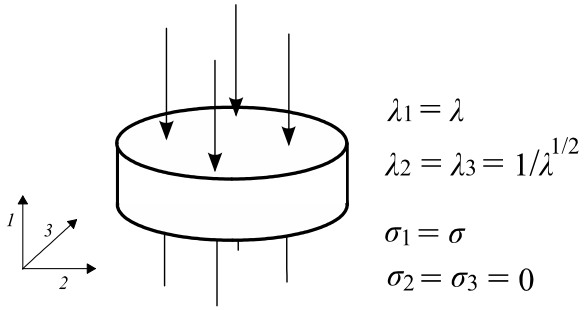


Figure 4.13: Simple uniaxial compression stress state (unconfined deformation).

Rivlin's model Hyperelastic models in ABAQUS® are written in the decoupled form (see section 2.2.5) and it assumes incompressibility of the material for the numerical fitting process [see ABAQUS®, 2006, Theory Manual, Section 4.6.2], except for the calibration of volumetric material parameters.

The constitutive equation for the Rivlin's model is given by

$$P_{theo} = 2\left(\lambda - \frac{1}{\lambda^2}\right)\left[\frac{\partial \Psi_{dev}}{\partial \bar{I}_1} + \frac{1}{\lambda}\frac{\partial \Psi_{dev}}{\partial \bar{I}_2}\right]. \tag{4.4}$$

where λ is the uniaxial stretch as seen in figure 4.13 and $\bar{I}_1$ and $\bar{I}_2$ are the modified strain invariants already defined in section 2.2.6. The constitutive equation expressed in (4.4) is valid for the Mooney-Rivlin model and the Second order polynomial model.

Reduced Polynomial Model The reduced polynomial model is given by expression (2.145) and is the basis of the Neo-Hookean ($N = 1$) model and Yeoh model ($N = 3$). In ABAQUS® is possible to calculate material parameters based on the reduced polynomial model up to the polynomial expansion order $N = 6$.

For the reduced polynomial model the constitutive equation for the uniaxial stress state is given by

$$P_{theo} = 2\left(\lambda - \frac{1}{\lambda^2}\right)\sum_{i=1}^{N} iC_{i0}\left(\bar{I}_1 - 3\right)^{i-1}. \tag{4.5}$$

Ogden model For a uniaxial stress state the constitutive equation for the Ogden model is expressed by

$$P_{theo} = \sum_{i=1}^{N} \frac{\mu_i}{\alpha_i}(\lambda^{\alpha_i - 1} - \lambda^{\left(-\frac{1}{2}\alpha_i - 1\right)}). \tag{4.6}$$

From constitutive equation (4.6) is possible to conclude that the parameters α_i must be calibrated using nonlinear fitting procedures.

4.2.1.2 Volumetric compression stress

In ABAQUS® the volumetric term of all the *in-built* phenomenological strain energy functions is given by

$$\Psi_{vol} = \sum_{i=1}^{N} \frac{1}{D_i}(J-1)^{2i}\ , \tag{4.7}$$

where D_i is the adjustable volumetric material parameter and J, the volume ratio expressed in equation (4.1). The volumetric stress state induced in the CPGC cylindrical sample is plotted in figure 4.14.

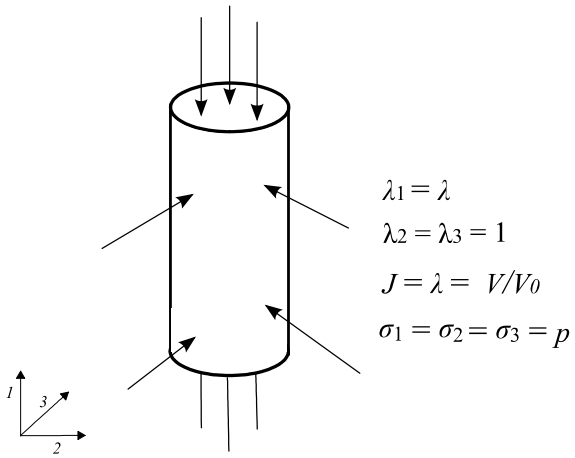


Figure 4.14: Uniaxial volumetric stress compression case (confined deformation).

Experimental data shown in figure 4.11 reproduces the purely volumetric behaviour of the CPGC material and was used to calibrate the volumetric material parameters D_i through a linear least-square procedure.

Later in this text (section 4.3.1.2) we present a user subroutine implemented in ABAQUS® that allows to unlink the volumetric polynomial expansion N_{vol} from the deviatoric polynomial expansion order N_{dev}. This capability is not assured by default by the ABAQUS® finite element code and can be useful when the volumetric mechanical response is highly nonlinear and a higher polynomial expansion order is needed to model the volumetric behaviour of the material.

Regarding the volumetric term of the strain energy function expressed in (4.7) and equation (2.127), we obtain the constitutive equation for the hydrostatic pressure p_{theo}, through

$$p_{theo} = -\frac{\partial \Psi_{vol}}{\partial J} = -\sum_{i=1}^{N} 2i \frac{1}{D_i}(J-1)^{2i-1}. \tag{4.8}$$

4.2.1.3 Numerical fitting procedure

Simple uniaxial compression data The uniaxial experimental data was used to calibrate material parameters for three types of phenomenological hyperelastic models in order to understand the numerical fitting capabilities of that hyperelasic models to the CPCG experimental uniaxial data.

In table 4.3 are summarized the results obtained for each tested hyperelastic model, nominally, the stability condition for the considered experimental deformation range and the mean relative error obtained for the numerical fit of each formulation experimentally tested considering $T = 23^oC$.

It is possible to observe from the numerical fit results summarized in table 4.3, that the models expanded to the first polynomial order ($N = 1$) have the worst fitting capabilities as expressed by the higher mean relative error values (see Mooney-Rivlin, Ogden ($N = 1$) and Neo-Hookean models). The model accuracy increases with the increase in the expansion order and it is maximum for the Ogden ($N = 6$) model. On other hand the fitting accuracy is minimum for the reduced polynomial models as expressed by the high mean relative errors for all the polynomial expansion orders considered and a general unstable behaviour obtained for $N = 2, 4$ and 6.

As it will be discussed in section 4.2.2 it was developed during this work a numerical tool for the prediction of the mechanical behaviour of non-tested formulations that can have a great practical importance. This methodology is based on linear interpolation of material parameters. For this procedure to be correctly implemented the material parameters must follow a clear tendency with the incorporation of cork. By other words, the model must be linear in the adjustable material parameters and this is not the case for the Ogden model

Table 4.3: Numerical fit of CPGC uniaxial experimental data, considering $T = 23^oC$.

	Formulation A		Formulation B		Formulation D		Formulation F		General behaviour	
Models	Stability	Rel. error	Stability	Rel. error	Stability	Rel. error	Stability	Rel. error	Stability	Rel. error
Mooney-Rivlin	Stable	7.638%	Stable	8.586%	Stable	6.587%	Stable	14.403%	Stable	9.30%
Second order polynomial	Stable	1.647%	Stable	0.262%	Stable	2.762%	Stable	2.450%	Stable	1.78%
Ogden (N=1)	Stable	8.306%	Stable	16.833%	Stable	6.587%	Stable	27.874%	Stable	14.90%
Ogden (N=2)	Stable	1.628%	Stable	0.457%	Stable	2.762%	Stable	2.498%	Stable	1.84%
Ogden (N=3)	Stable	1.759%	Stable	0.457%	Stable	2.690%	Stable	2.502%	Stable	1.85%
Ogden (N=4)	Stable	1.627%	Stable	0.278%	Stable	2.700%	Stable	1.981%	Stable	1.65%
Ogden (N=5)	Stable	1.759%	Stable	0.333%	Stable	1.676%	Stable	0.441%	Stable	1.05%
Ogden (N=6)	Stable	0.621%	Stable	0.294%	Stable	0.902%	Stable	0.408%	Stable	0.56%
Neo-Hookean (N=1)	Stable	8.406%	Stable	16.852%	Stable	6.588%	Stable	27.875%	Stable	14.93%
Reduced polynomial (N=2)	Stable	5.849%	Stable	8.803%	Stable	3.884%	Unstable	15.789%	Unstable	8.58%
Yeoh Model (N=3)	Stable	3.648%	Stable	5.331%	Stable	2.686%	Stable	9.948%	Stable	5.40%
Reduced polynomial (N=4)	Stable	2.684%	Unstable	3.697%	Stable	2.388%	Unstable	6.691%	Unstable	3.86%
Reduced polynomial (N=5)	Stable	2.261%	Stable	2.979%	Stable	2.430%	Stable	4.896%	Stable	3.14%
Reduced polynomial (N=6)	Stable	2.109%	Stable	2.561%	Stable	2.410%	Unstable	3.824%	Unstable	2.73%

It must be clearly understand that the Ogden model could be used for the modelling of the mechanical behaviour of CPGC since it is valid in the required range of deformation and fits very well to the experimental data but the nonlinearity at the material parameters α_i do not allow the use of interpolation tools for the prediction of mechanical behaviour for non-tested formulations. For that reason the second order polynomial model (linear at parameters C_{ij}) and also characterized by a very low mean relative error (1.78%) was chosen as the basis model for modelling the mechanical response of CPGC and consequently for the implementation of the material parameters interpolative scheme.

Figure 4.15 shows the excellent numerical fitting obtained for the second order polynomial, considering for this example the experimental results for formulation A. In figure 4.16 is plotted the relative error against the nominal strain obtained for the fit process of formulation A to the second order polynomial model.

The fitting of the simple uniaxial compression data for CPGC obtained for formulations B, D and F is plotted in figures 4.17, 4.19 and 4.21, respectively. The respective relative errors obtained for the numerical fit are expressed in figures 4.18, 4.20 and 4.22.

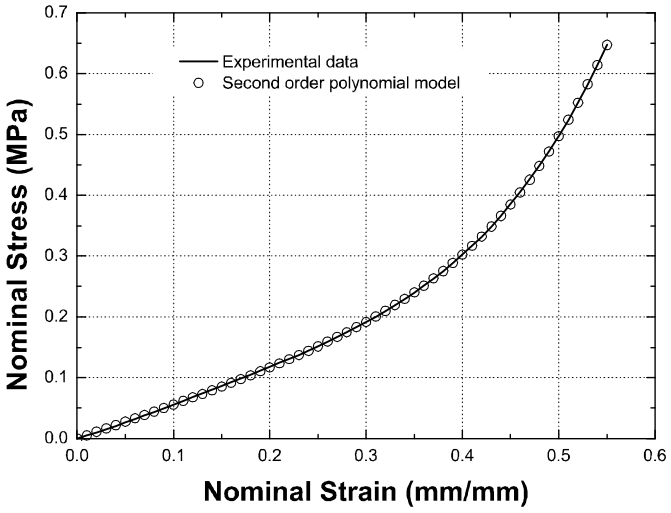


Figure 4.15: Fit to the uniaxial compression experimental data from formulation A to the second order polynomial hyperelastic model, considering $T = 23^oC$.

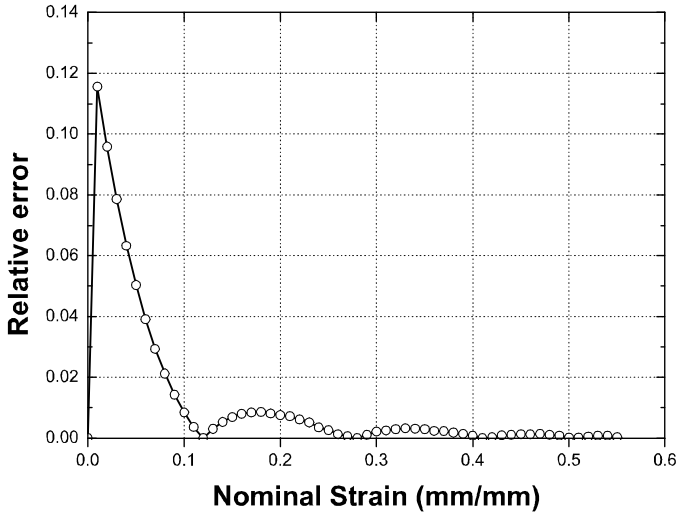


Figure 4.16: Relative error plotted against nominal strain, for the fit of uniaxial compression data from formulation A.

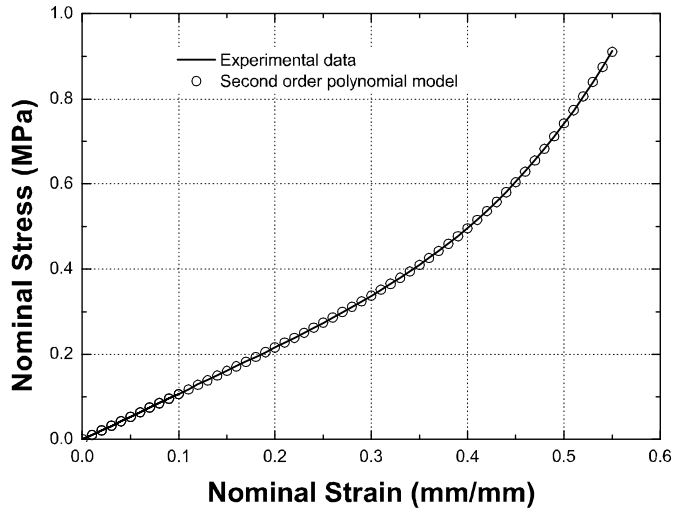


Figure 4.17: Fit to the uniaxial compression experimental data from formulation B to the second order polynomial hyperelastic model, considering $T = 23^oC$.

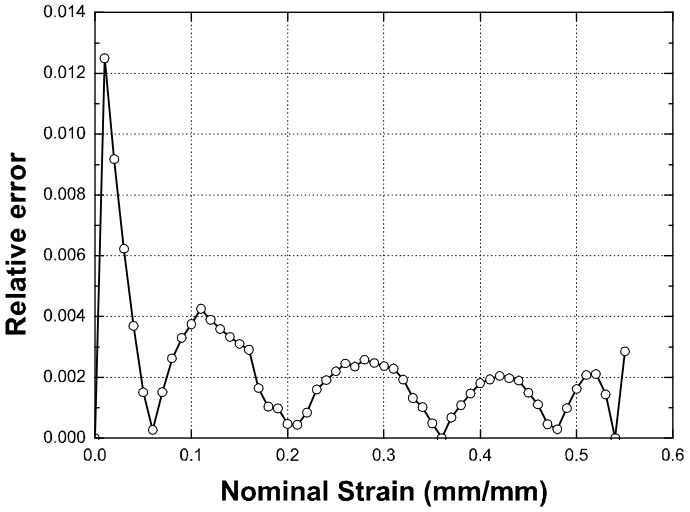


Figure 4.18: Relative errors plotted against nominal strain, for the fit of uniaxial compression data from formulation *B*.

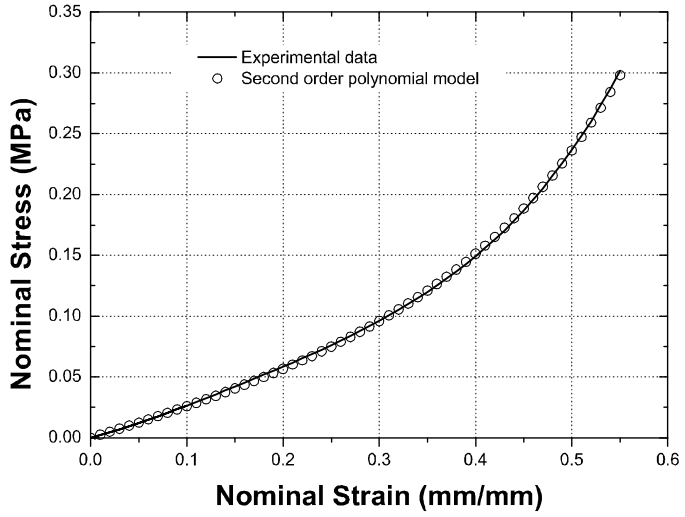


Figure 4.19: Fit to the uniaxial compression experimental data from formulation D to the second order polynomial hyperelastic model, considering $T = 23^oC$.

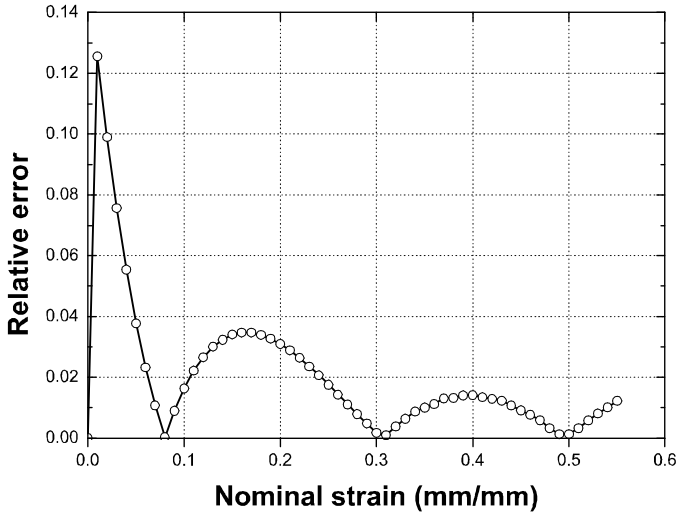


Figure 4.20: Relative error plotted against nominal strain, for the fit of uniaxial compression data from formulation *D*.

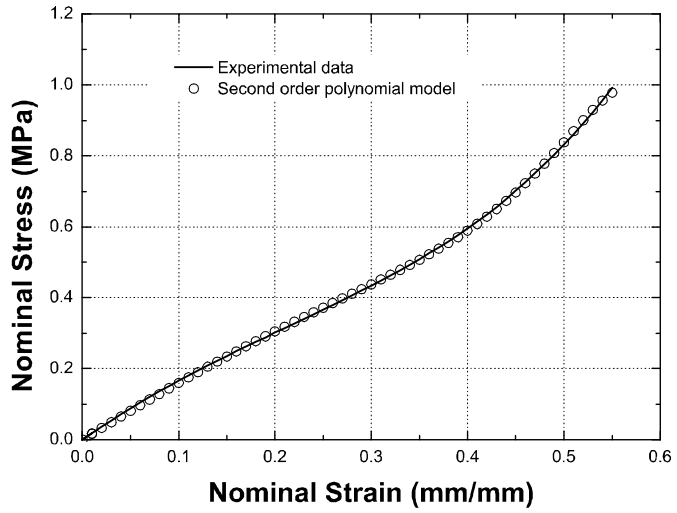


Figure 4.21: Fit to the uniaxial compression experimental data from formulation F to the second order polynomial hyperelastic model, considering $T = 23^oC$.

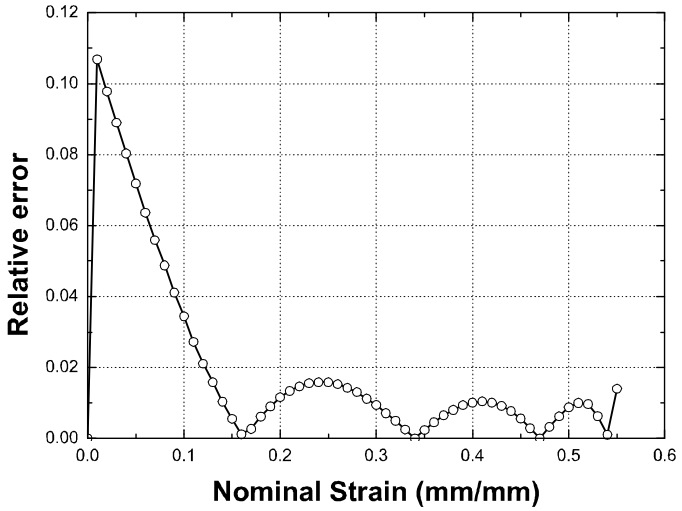


Figure 4.22: Relative error plotted against nominal strain, for the fit of uniaxial compression data from formulation *F*.

Considering the second order polynomial model as the basis model for the modelling of the mechanical response of the CPGC, a new numerical fitting procedure was effectuated for the experimental uniaxial compression results obtained at $T = 100^oC$ and $T = -10^oC$.

The quality of the numerical fitting of CPGC experimental data to the second order polynomial model is summarized in table 4.4.

Table 4.4: Numerical fit of CPGC uniaxial experimental data to the second order polynomial model, considering $T = 100^oC$ and $T = -10^oC$.

	Formulation *A*		Formulation *B*		Formulation *F*		General behaviour	
Temp.	Stability.	Error	Stability	Error	Stability	Error	Stability	Error
100^{o}C	Stable	1.337%	Stable	3.117%	Stable	2.916%	Stable	2.46%
-10^{o}C	Stable	0.239%	Stable	0.926%	Stable	1.889%	Stable	1.02%

The second order polynomial model material parameters C_{ij}, that calibrates the second order polynomial model for reproducing the mechanical behaviour of CPGC at $T = 23^oC$ are given in table 4.5. Material parameters for $T = 100^oC$ and $T = -10^oC$ are summarized in tables 4.6 and 4.7,respectively.

Table 4.5: Deviatoric material parameter values (MPa) for the second order polynomial model, considering $T = 23^oC$.

Formulation	C_{10}	C_{01}	C_{20}	C_{11}	C_{02}
A	0.17306013	-0.08149739	-0.01592234	0.04407064	-0.01219079
B	0.35444008	-0.17757937	-0.03354625	0.08103747	-0.02176274
D	0.07726427	-0.03392411	0.01481363	-0.00546274	0.00147543
F	0.60229052	-0.32782088	-0.23539651	0.31855866	-0.08398760

Table 4.6: Deviatoric material parameter values (MPa) for the second order polynomial model, considering $T = 100^oC$.

Formulation	C_{10}	C_{01}	C_{20}	C_{11}	C_{02}
A	0.15624587	-0.08246075	-0.00407284	0.03113852	-0.00934143
B	0.29393111	-0.16449149	-0.03373282	0.08856770	-0.02596343
D	0.07726427	-0.03392411	0.01481363	-0.00546274	0.00147543
F	0.35651657	-0.19774760	-0.05886092	0.11378074	-0.03151476

Table 4.7: Deviatoric material parameter values (MPa) for the second order polynomial model, considering $T = -10^oC$.

Formulation	C_{10}	C_{01}	C_{20}	C_{11}	C_{02}
A	0.23919204	-0.12138389	0.06296112	-0.02117186	0.00336226
B	0.42384338	-0.20463189	-0.00502419	0.05100597	-0.01271140
D	0.07726427	-0.03392411	0.01481363	-0.00546274	0.00147543
F	0.66381986	-0.30664070	-0.20197565	0.23482219	-0.05409386

Volumetric compression data Experimental data obtained from the experimental procedure described in section 4.1.2.1 was used for the calibration of volumetric material parameters D_i. The numerical fitting procedure was done using the linear least-square capabilities of MATLAB® software. The material parameters were calculated considering the polynomial expansion order of the volumetric strain energy function expressed by (4.7) in the range $N = [1, 4]$. The evolution of the mean relative error with the polynomial expansion order is summarized in table 4.8.

From table 4.8 is possible to conclude that the relative error decreases with the expansion order for all tested formulation, as it is minimum for $N = 4$.

For a highly nonlinear volumetric behaviour the increase in the polynomial expansion order can contribute for a better prediction of the material's mechanical behaviour, especially in cases where the material is highly confined. The increase in the fitting accuracy with the increase in the polynomial expansion order of the volumetric strain energy function is visible in figure 4.23 considering for a term of comparison, $N = 2$ and $N = 4$.

The evolution of the relative error with volume ratio for formulation A is plotted in figure 4.24.

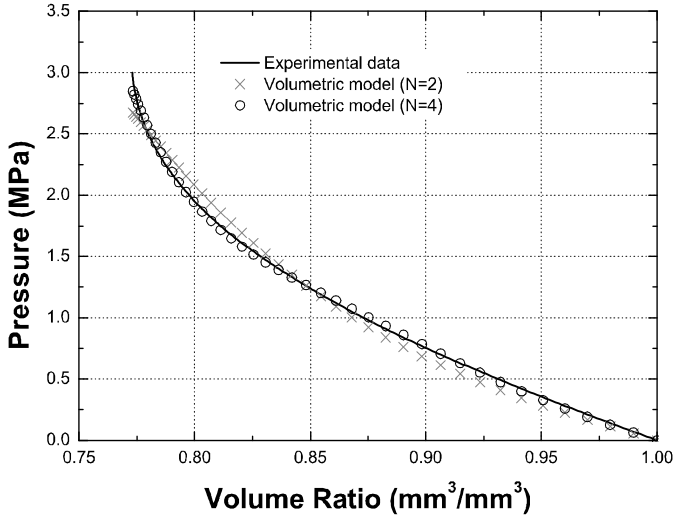


Figure 4.23: Effect of the expansion order in the fit of the volumetric experimental data from formulation A to the volumetric polynomial model, considering $N = 2$ and $N = 4$.

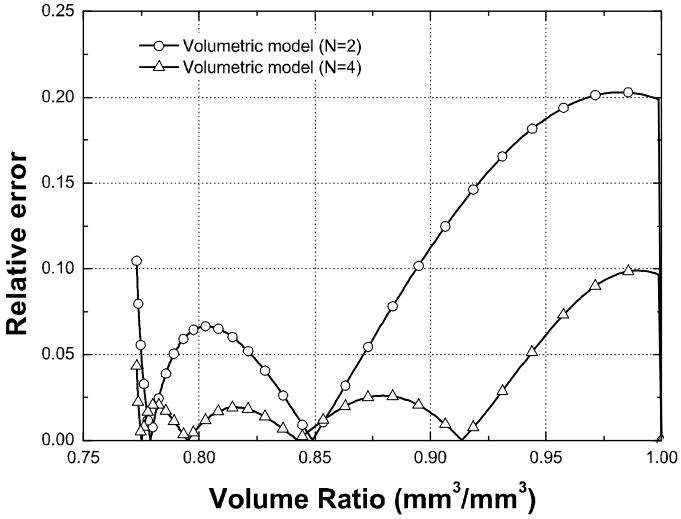


Figure 4.24: Relative error plotted against volume ratio for the fit of volumetric data from formulation A to the volumetric polynomial model, considering $N = 2$ and $N = 4$.

Table 4.8: Mean relative errors considering different polynomial expansion orders.

Formulation	$N = 1$	$N = 2$	$N = 3$	$N = 4$
A	23.117%	7.932%	4.708%	2.472%
B	25.917%	5.403%	2.940%	0.636%
C	19.506%	2.342%	1.617%	0.248%

The fit of experimental curves from formulations B and C are reported in figures 4.25 and 4.27, respectively, where is possible to visualize a better fitting accuracy with the increase in the polynomial expansion order. Respective relative errors are shown in figures 4.26 and 4.28.

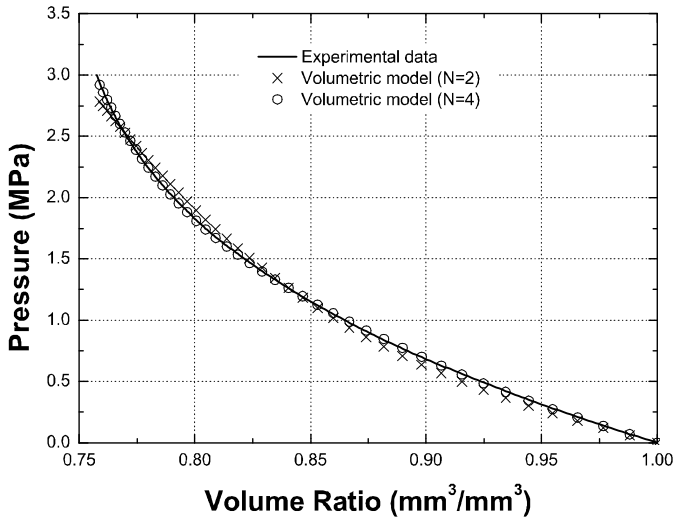


Figure 4.25: Effect of the expansion order in the fit of the volumetric experimental data from formulation B to the volumetric polynomial model, considering $N = 2$ and $N = 4$.

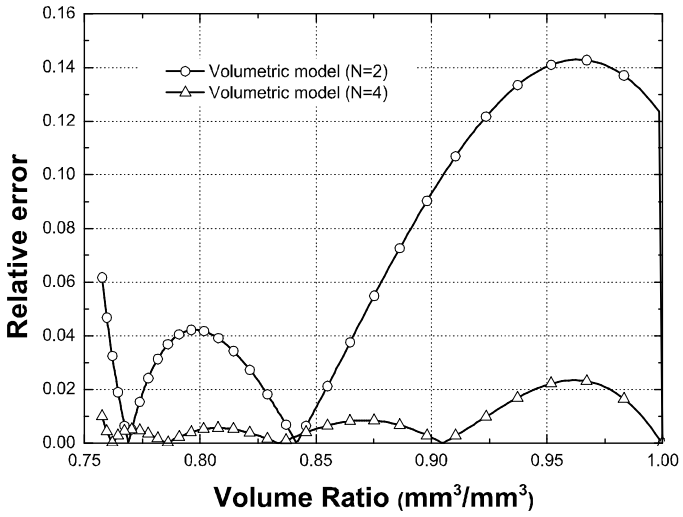


Figure 4.26: Relative error plotted against volume ratio for the fit of volumetric data from formulation B to the volumetric polynomial model, considering $N = 2$ and $N = 4$.

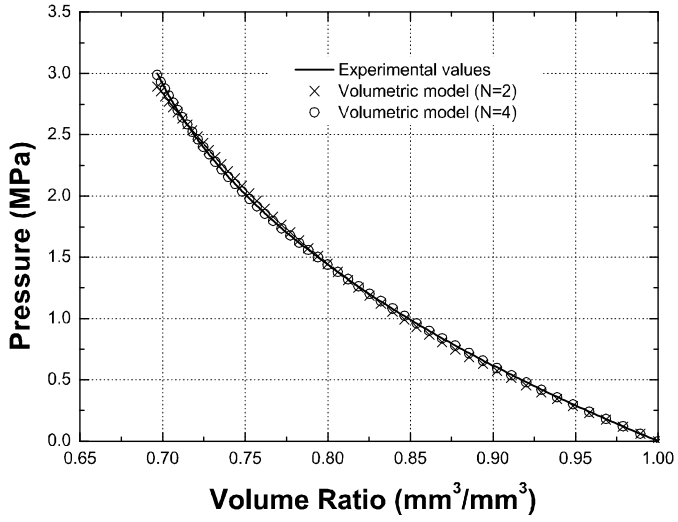


Figure 4.27: Effect of the expansion order in the fit of the volumetric experimental data from formulation C to the volumetric polynomial model, considering $N = 2$ and $N = 4$.

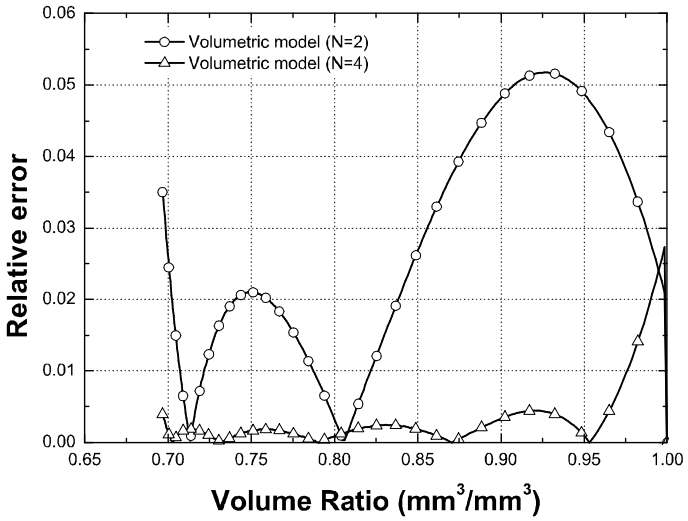


Figure 4.28: Relative error plotted against volume ratio for the fit of volumetric data from formulation C to the volumetric polynomial model, considering $N = 2$ and $N = 4$.

From expression $\frac{\partial^2 \psi_{vol}}{\partial J^2}$, we compute the tangent bulk modulus. Figure 4.29 show the evolution of the tangent bulk modulus calculated from the volumetric term of the strain energy function Ψ_{vol}, considering the polynomial expansion order $N = 4$, for formulations A, B and C. Note that for $J = 1$ (undeformed state) we obtain the initial bulk modulus K_0 given by expression (2.144).

As plotted in figure 4.29, the mechanical behaviour of formulation A in a pure volumetric deformation state is characterized by a more stiff response when compared with formulations B and C. On the other hand, formulation C is the more compressible formulation as evidenced by the lowest values of tangent bulk modulus, resulting from a higher incorporation of cork.

From the evolution of the tangent bulk modulus with volumetric deformation it is possible to check the stability of the calibrated model by monitoring inversions in the monotonicity of the curve and the existence of negative bulk modulus values that can lead to non-physical mechanical behaviors.

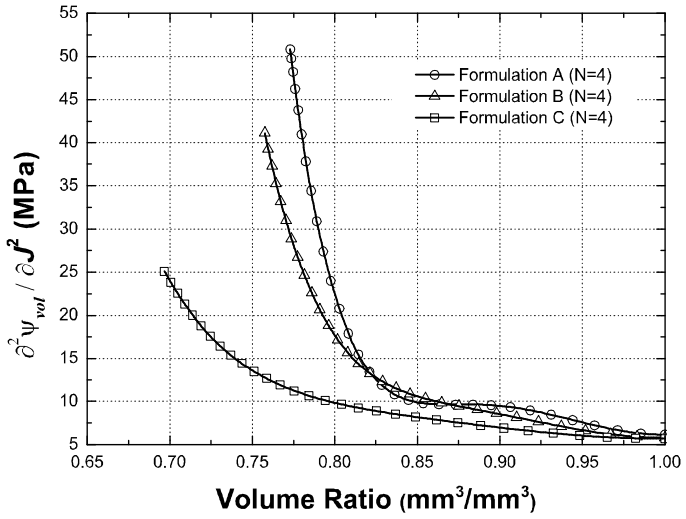


Figure 4.29: Tangent bulk modulus plotted against volume ratio for formulations A, B and C, considering $N = 4$.

In tables 4.9, 4.10 and 4.11 are summarized the volumetric material parameters for formulations A, B and C, respectively.

Table 4.9: Volumetric material parameters values (MPa^{-1}) for formulation A, considering different polynomial expansion orders.

Material parameter	$N = 1$	$N = 2$	$N = 3$	$N = 4$
D_1	0.19394	0.3661600	0.2446300	0.32465000
D_2	-	0.0324080	-0.0487880	0.01795200
D_3	-	-	0.0018991	-0.00070458
D_4	-	-	-	0.00006222

Table 4.10: Volumetric material parameters values (MPa^{-1}) for formulation B, considering different polynomial expansion orders.

Material parameter	$N = 1$	$N = 2$	$N = 3$	$N = 4$
D_1	0.20322	0.393030	0.29282	0.34494000
D_2	-	0.036026	-0.69752	0.03057200
D_3	-	-	0.0037283	-0.00198570
D_4	-	-	-	0.00017642

Table 4.11: Volumetric material parameter values (MPa^{-1}) for formulation C, considering different polynomial expansion orders.

Material parameter	$N = 1$	$N = 2$	$N = 3$	$N = 4$
D_1	0.24117000	0.36890000	0.32782000	0.35159000
D_2	-	0.08923800	0.27319000	0.07908400
D_3	-	-	0.02203400	-0.01146400
D_4	-	-	-	0.00158050

4.2.2 Interpolation of material parameters

The material parameter's dependence with the incorporation of cork can be a very useful information for the construction of *"virtual"* uniaxial compression or volumetric curves through linear interpolation of material parameters fitted to a set of experimental data. Following the work from Antunes *et al.* [2008a,b], this method allows the mechanical definition of material formulations that were not experimentally evaluated. In the case of CPGC, this procedure can be very useful since it permits the prediction of mechanical characteristics of a given formulation (varying the incorporation of cork) without the need of performing experimental tests for each produced CPGC formulation.

MATLAB® software was used to define the material parameters interpolation routine and to output the numerical results in graphical terms.

This methodology is applied for the construction of both uniaxial and volumetric curves as discussed bellow.

4.2.2.1 Simple uniaxial compression behaviour

The deviatoric material parameters C_{ij} dependence with the incorporation of cork weight for $T = 23^oC$ can be seen in figure 4.30. Is visible from figure 4.30 that an increase in the incorporation of cork is followed by an increase in the absolute values of the adjustable deviatoric material parameters. Note that the values of incorporation of cork are written in a reduced format.

As an example, the mechanical behaviour was predicted for a non-tested CPGC formulation with a cork incorporation equal to $35php$ ($\approx 8.5\%$ in cork weight). In Figure 4.31 is plotted the *"virtual"* stress-stretch curve (simple uniaxial compression) and in figure 4.32 the corresponding strain energy density plotted against the uniaxial stretch λ. Note that in figure 4.31 the stress is plotted in negative (compressive) values and not in absolute values.

It is possible to observe that the *"virtual"* compression and deviatoric strain energy density curves are positioned between the experimental curves correspondent to cork incorporation equal to $25php$ and $50php$, since the material parameter values for the new

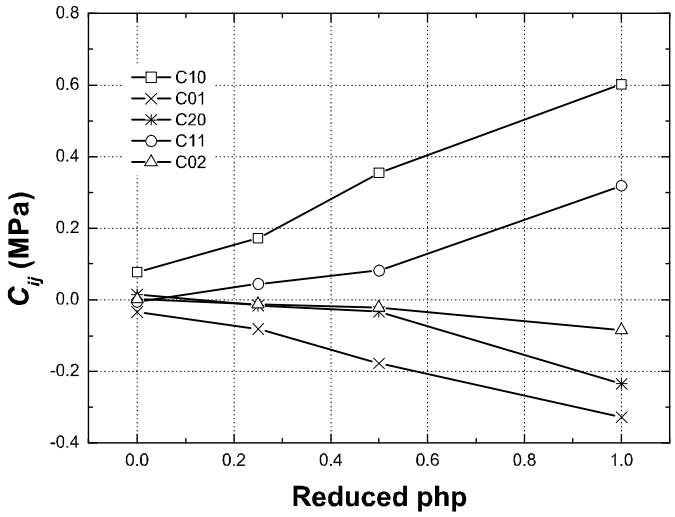


Figure 4.30: Deviatoric material parameters C_{ij} plotted against incorporation of cork, considering $T = 23^oC$.

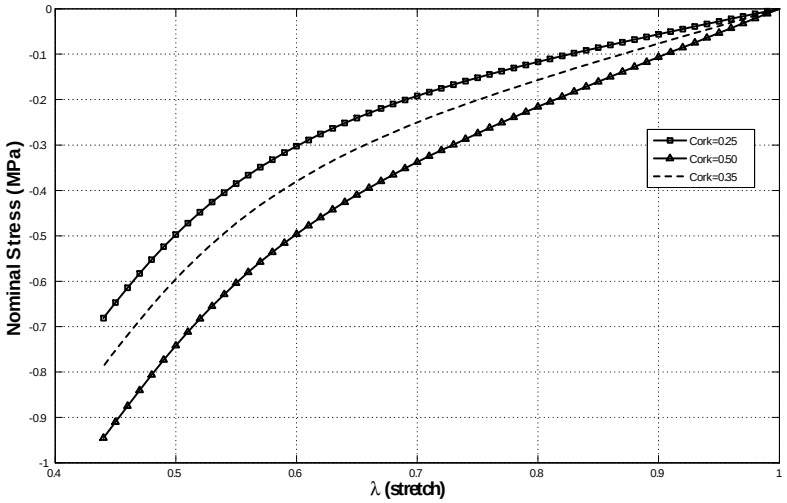


Figure 4.31: Nominal stress plotted against stretch for interpolated CPGC formulation with 35*php* in cork *(represented with dashed line).*

formulation are interpolated from that values of cork incorporation.

In figures 4.33 and 4.34 is shown the material parameter's dependence with cork incorporation for $T = 100^oC$ and $T = -10^oC$, respectively.

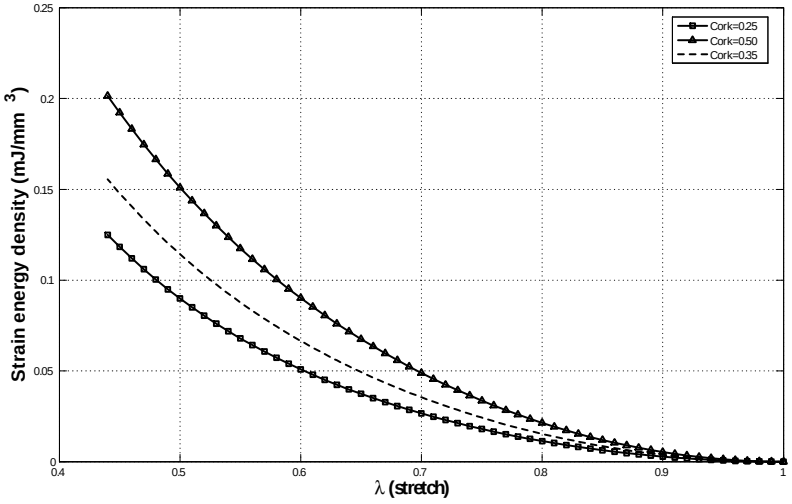


Figure 4.32: Deviatoric strain energy density plotted against stretch for interpolated CPGC formulation with *35php* in cork *(represented with dashed line).*

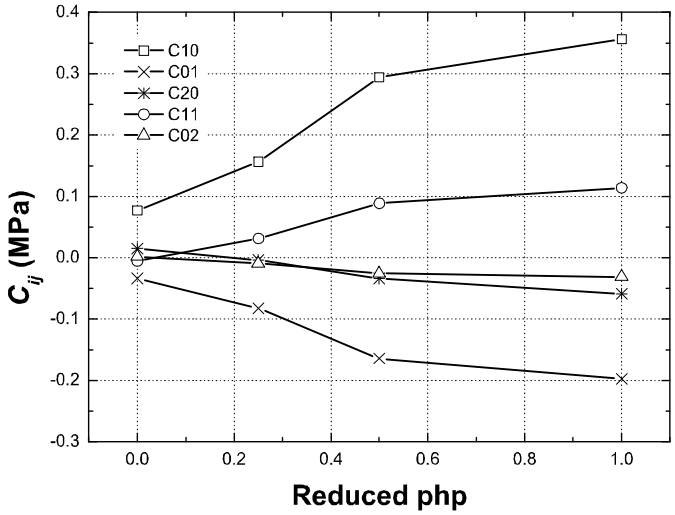


Figure 4.33: Deviatoric material parameters C_{ij} plotted against incorporation of cork, considering $T = 100^oC$.

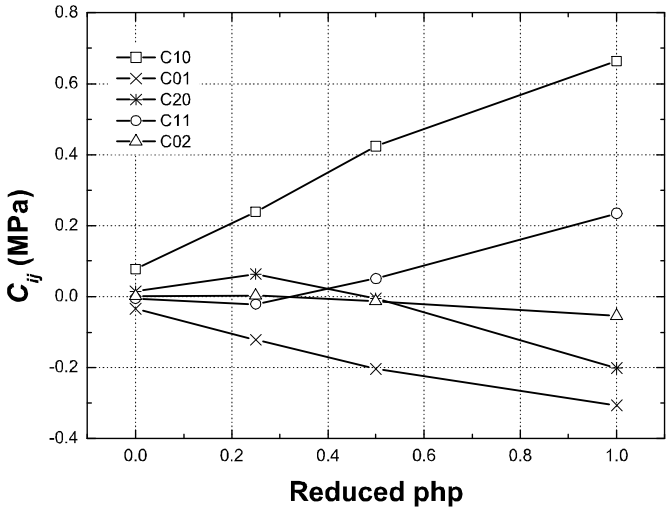


Figure 4.34: Deviatoric material parameters C_{ij} plotted against incorporation of cork, considering $T = -10^oC$.

The new material parameters are automatically calculated by the implemented routine and are summarized in table 4.12.

Table 4.12: Interpolated deviatoric material parameters (MPa) for a non-tested formulation with 35*php* in cork.

Formulation	C_{10}	C_{01}	C_{20}	C_{11}	C_{02}
35 php (8.5% in cork weight)	0.2456	-0.1199	-0.0230	0.0589	0.0589

4.2.2.2 Volumetric compression behaviour

The same methodology followed for the construction of *"virtual"* uniaxial compression curves can be applied for computing the volumetric mechanical response of non-tested CPGC formulations by knowing the volumetric material parameters D_i dependence with the incorporation of cork. Figure 4.35 show the parameters evolution with the incorporation of cork, considering for this case an volumetric expansion order $N = 2$.

Defining again a new formulation with a cork incorporation equal to 35*php* we can compute the volumetric mechanical response for this formulation, that is given by figure 4.36, where the hydrostatic pressure is plotted against the volume ratio. In figure 4.37 the respective volumetric strain energy density is plotted against the considered range of volumetric deformation.

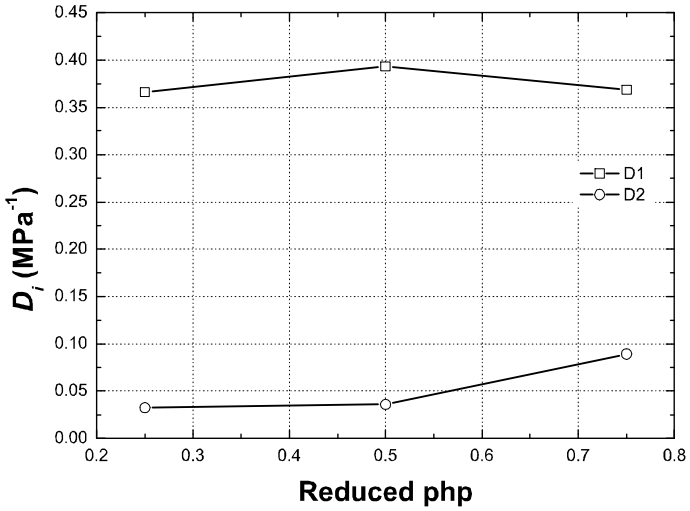


Figure 4.35: Volumetric material parameters D_i plotted against incorporation of cork, considering $T = 23^oC$.

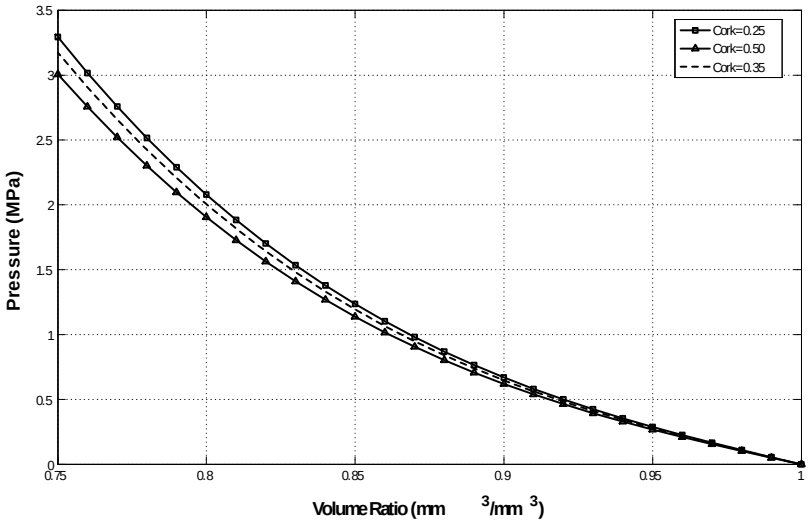


Figure 4.36: Hydrostatic pressure plotted against volume ratio for interpolated CPGC formulation with 35*php* in cork *(represented with dashed line)*.

In table 4.13 are summarized the volumetric material parameters calculated for the non-tested CPGC formulation (35*php*). These values are interpolated from the experimental data obtained for the formulations A and B since the non-tested formulation is characterized by a cork incorporation value located in the cork incorporation range

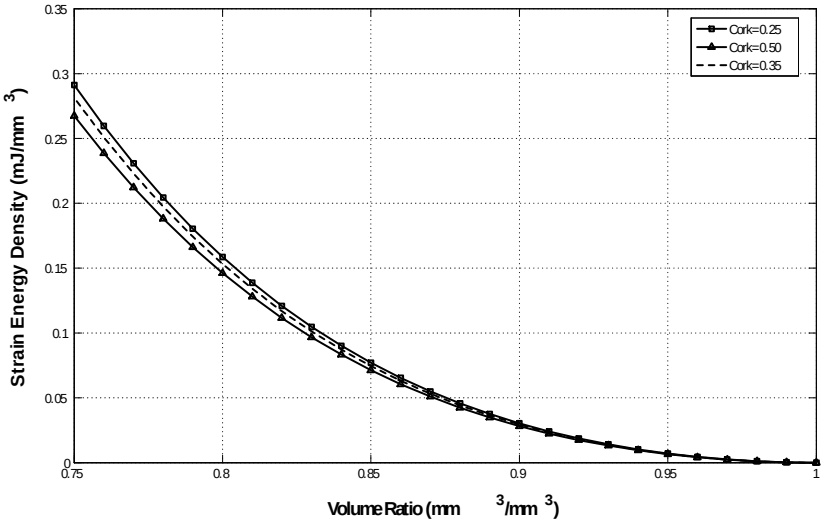


Figure 4.37: Volumetric strain energy density plotted against volume ratio for interpolated CPGC formulation with 35*php* in cork *(represented with dashed line).*

defined by formulations A and B.

Table 4.13: Interpolated volumetric material parameters (MPa^{-1}) for a non-tested formulation with 35*php* in cork.

Formulation	D_1	D_2
35 php (8.5% in cork weight)	0.37691	0.033855

4.2.3 Modelling the hysteretic cycle

As already discussed in section 3.1, a new formulation based on a modification of the *Pseudo-elasticity theory* is proposed for modelling hysteretic cycles accounting separately deviatoric and volumetric dissipative effects.

In the case of the CPGC material, the experimental data collected from simple uniaxial compression (unconfined deformation) tests as seen in section 4.1.1.2 and the volumetric compression (confined deformation) tests summarized in section 4.1.2.2, reveals that the CPGC is a material characterized by a hysteretic behaviour in both confined and unconfined deformation processes.

For the modelling of the hysteretic cycle (loading-unloading path) a modified form of the models proposed by Dorfmann & Ogden [2003] and Elías-Zúñiga [2005], was used in order to study the model that best reproduce the CPGC's hysteretic cycle. The modified Dorfmann-Ogden model is expressed by equations (3.102) and (3.103), while the Modified

Zúñiga model is expressed by (3.113), and (3.114).

In the next sections is discussed the material parameter fitting methodology followed for the calibration of the modified Dorfmann-Ogden and Zúñiga models in order to reproduce both confined and unconfined deformation hysteretic cycles of the CPGC material.

4.2.3.1 Unconfined deformation hysteretic cycle (purely deviatoric behaviour)

The material parameters r_{dev} and m_{dev} for the modified Dorfmann-Ogden model and parameter b_{dev} for the modified Zúñiga model were obtained through the numerical fitting of simple uniaxial compression (unloading path) curves using the nonlinear least square fitting capabilities of MATLAB® software. It must be noticed that for the present work it was considered that the simple uniaxial compression (unconfined deformation) deformation case is characterized by a purely deviatoric deformation state.

The nominal stress relations described in (3.82) was used for the numerical fit procedure. Material parameters obtained for the calibration of the modified Dorfmann-Ogden and modified Zúñiga models are summarized in table 4.14.

Table 4.14: Material parameters obtained for the modified Dorfmann-Ogden and Zúñiga models, considering a purely deviatoric behaviour.

Formulation	r_{dev}	$m_{dev}(mJmm^{-3})$	$b_{dev}(mJmm^{-3})^{-1/2}$
A	1.8823	0.059933	1.9138
B	1.4061	0.091458	2.2892
D	5.2187	0.019	1.0182
F	1.2897	0.079588	2.9641

In table 4.15 are summarized the mean relative errors obtained for the fit of the experimentally tested formulations.

Table 4.15: Mean relative errors for the fit of the uniaxial unloading path, considering the Dorfmann-Ogden and Zúñiga models.

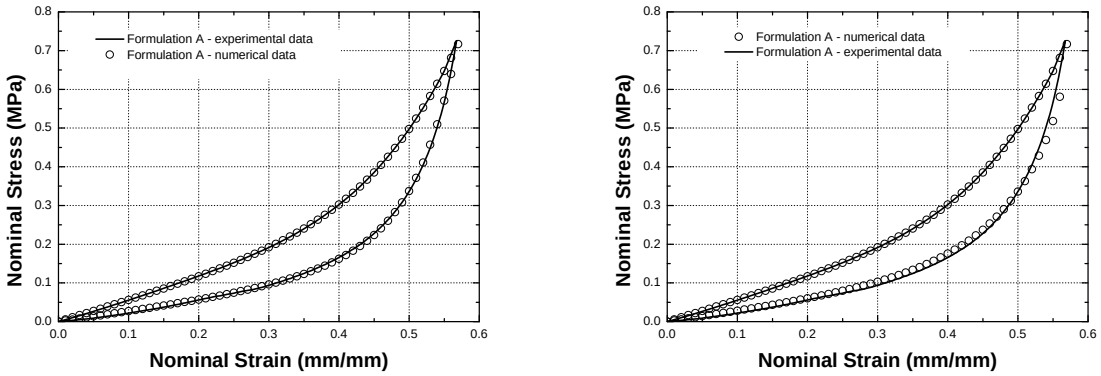
Formulation	Dorfmann-Ogden model	Zúñiga model
A	11.6%	12.5%
B	20.6%	27.8%
D	10.9%	8.9%
F	33.3%	33.6%

Observing table 4.15 and figures 4.38-4.45 we can conclude that the modified Dorfmann-Ogden model is the most indicated model for the reproduction of the loading-unloading cycles for formulations *A*, *B* and *F*. On the other hand, for formulation *D*, the

modified Zúñiga model have a better fit capability to the experimental hysteretic uniaxial compression cycle.

The correspondent relative error obtained for the fit of formulation *A*, using the modified Dorfmann-Ogden and Zúñiga models, is shown in figure 4.39.

Figures 4.40, 4.42 and 4.44 show the fit to the experimental data obtained for formulations *B*, *D* and *F*, respectively. The respective fit relative errors are plotted in figures 4.41, 4.43 and 4.45.



(a) (b)

Figure 4.38: Modelling the uniaxial (unconfined deformation) hysteretic cycle of formulation *A*, considering a) the modified Dorfmann-Ogden model and b) the modified Zúñiga model.

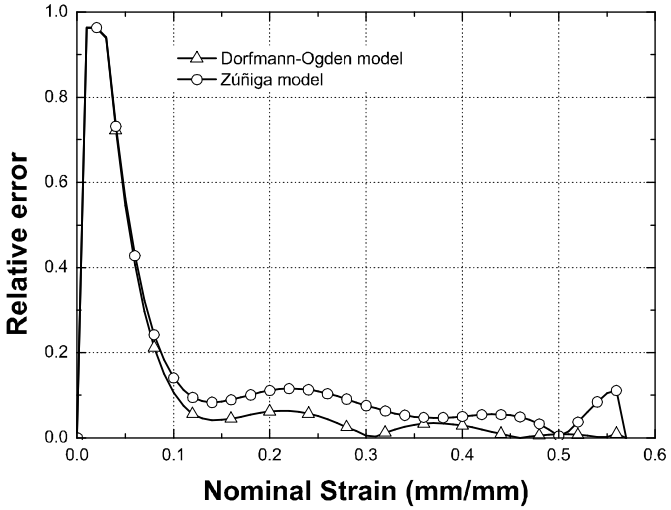
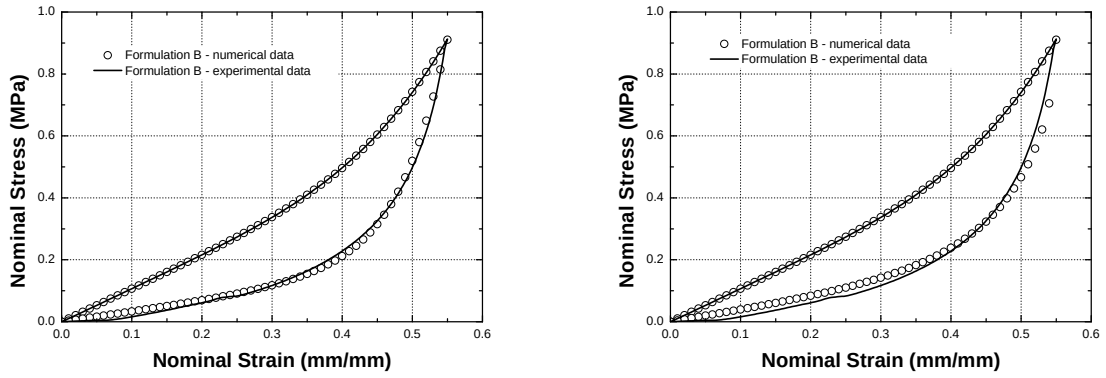


Figure 4.39: Relative error plotted against nominal strain for the fit of uniaxial data from formulation *A* to the modified Dorfmann-Ogden and Zúñiga models.



(a) (b)

Figure 4.40: Modelling the uniaxial (unconfined deformation) hysteretic cycle of formulation *B,* considering a) the modified Dorfmann-Ogden model and b) the Modified Zúñiga model.

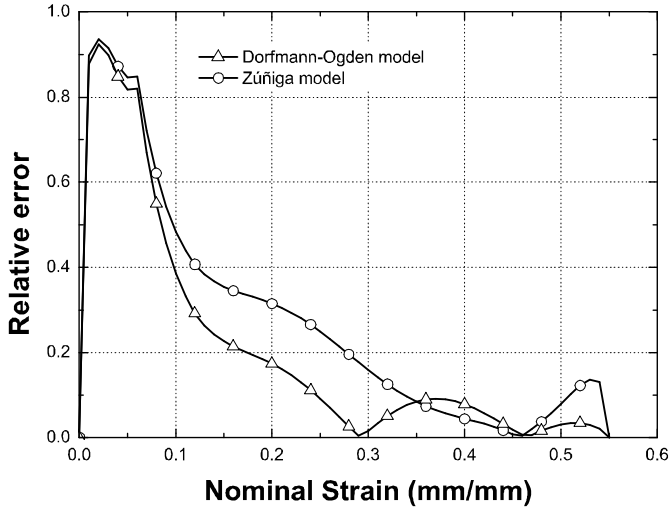
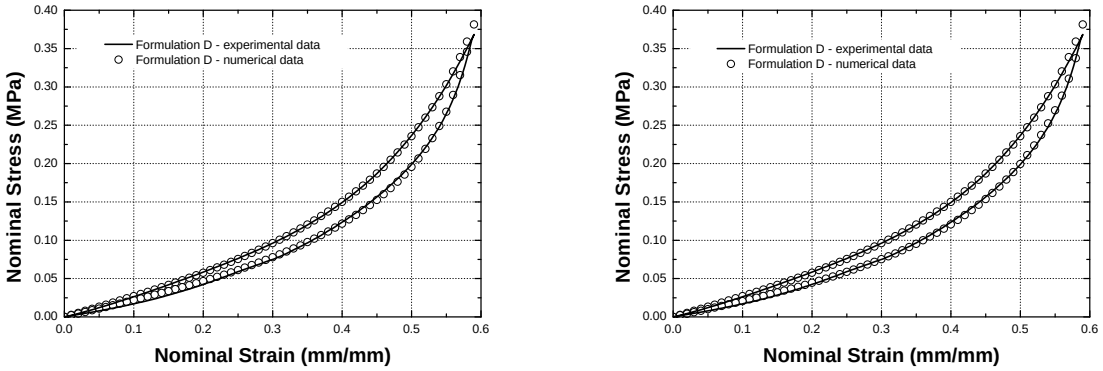


Figure 4.41: Relative error plotted against nominal strain for the fit of uniaxial data from formulation *B* to the modified Dorfmann-Ogden and Zúñiga models.



(a) (b)

Figure 4.42: Modelling the uniaxial (unconfined deformation) hysteretic cycle of formulation D, considering a) the Dorfmann-Ogden model and b) the Zúñiga model.

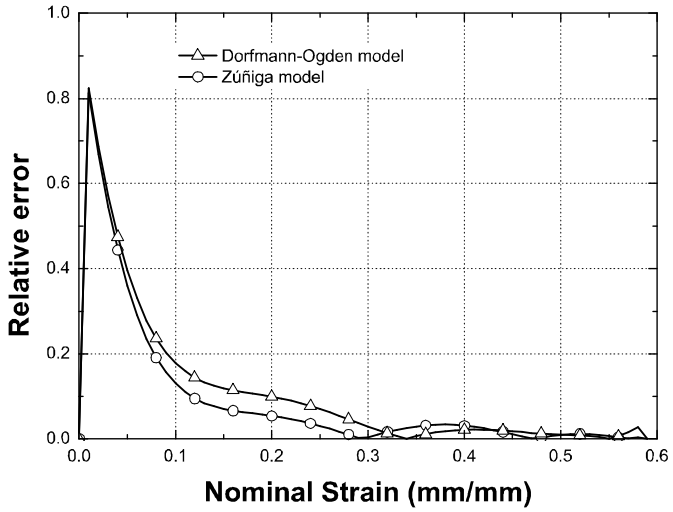
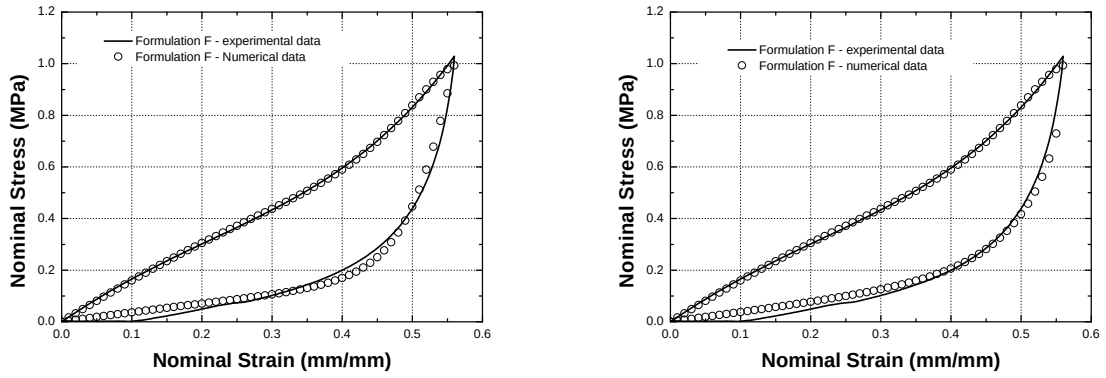


Figure 4.43: Relative error plotted against nominal strain for the fit of uniaxial data from formulation D to the modified Dorfmann-Ogden and Zúñiga models.



(a) (b)

Figure 4.44: Modelling the uniaxial (unconfined deformation) hysteretic cycle of formulation *F,* considering a) the modified Dorfmann-Ogden model and b) the modified Zúñiga model.

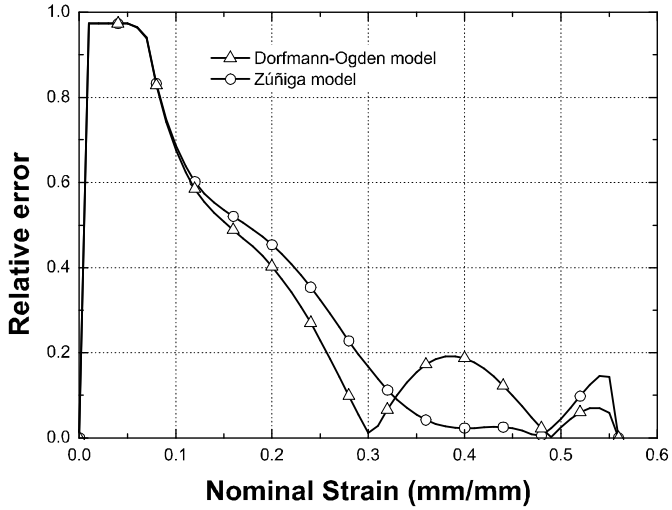


Figure 4.45: Relative error plotted against nominal strain for the fit of uniaxial data from formulation F to the modified Dorfmann-Ogden and Zúñiga models.

The pseudo-energy developed during the deformation process defined by (3.79) for the present loading-unloading cycle, is obtained using the modified Dorfmann-Ogden or Zúñiga models, respectively expressed by (3.100) and (3.111).

In figure 4.46 is plotted the pseudo-energy variation for formulation A considering the modified Dorfmann-Ogden model as it is the model that best fit to the experimental data of formulation A. It is apparent from figure 4.46 an increase in the strain energy values until the load reversal which occurs at approximately $\epsilon = 0.57$ ($\lambda = 0.43$). As already discussed in section 3.1.2, the intersection of the pseudo-energy curve with the vertical axis at nominal strain $\epsilon = 0$, gives the amount of dissipated energy (hysteresis): equal to the area between the loading and unloading curves.

In figures 4.47, 4.48 and 4.49, are plotted the pseudo-energy values against the nominal strain for formulations B, D and F, respectively, considering a simple uniaxial compression cycle.

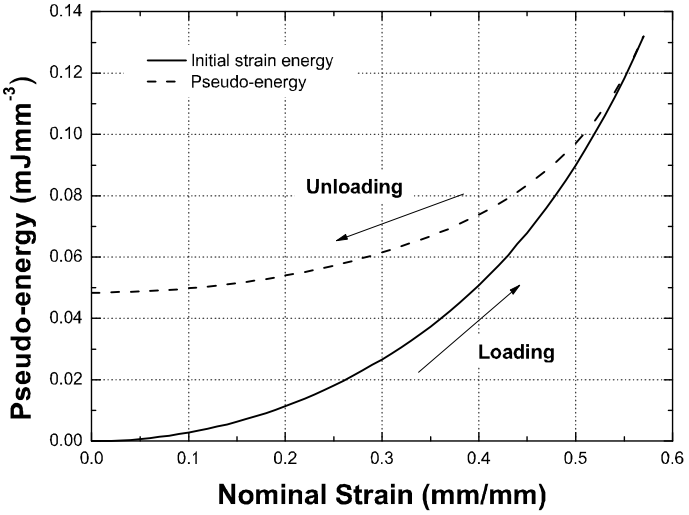


Figure 4.46: Plot of the pseudo-energy function against the nominal strain during loading-unloading cycle, considering formulation A at $T = 23^oC$.

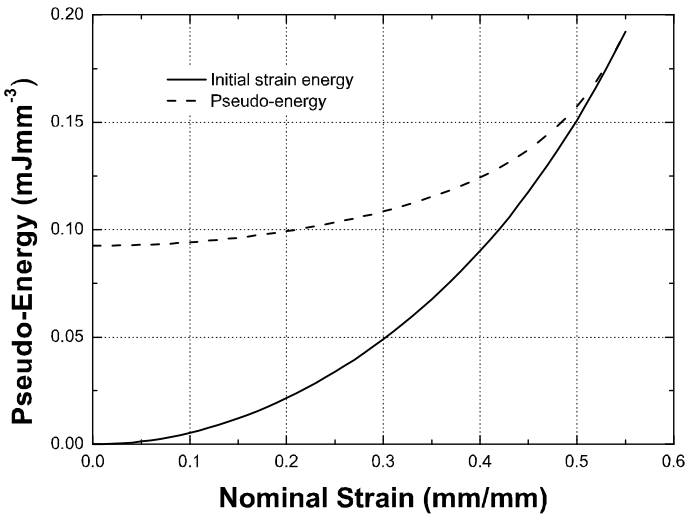


Figure 4.47: Plot of the pseudo-energy function against the nominal strain during loading-unloading cycle, considering formulation B at $T = 23^oC$.

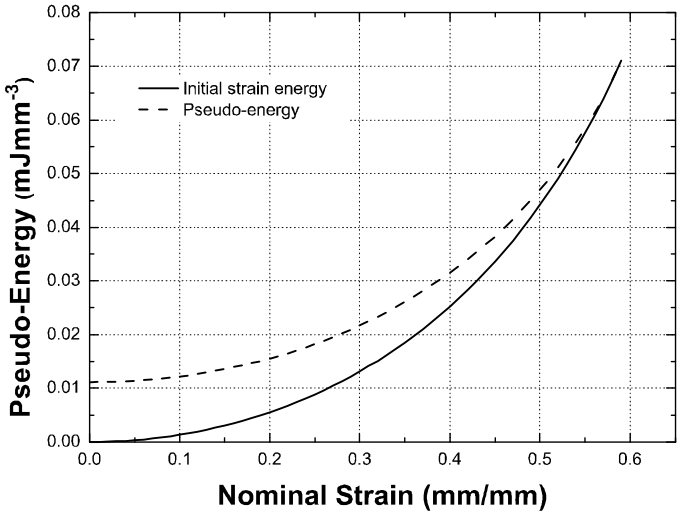


Figure 4.48: Plot of the pseudo-energy function against the nominal strain during loading-unloading cycle, considering formulation D at $T = 23^oC$.

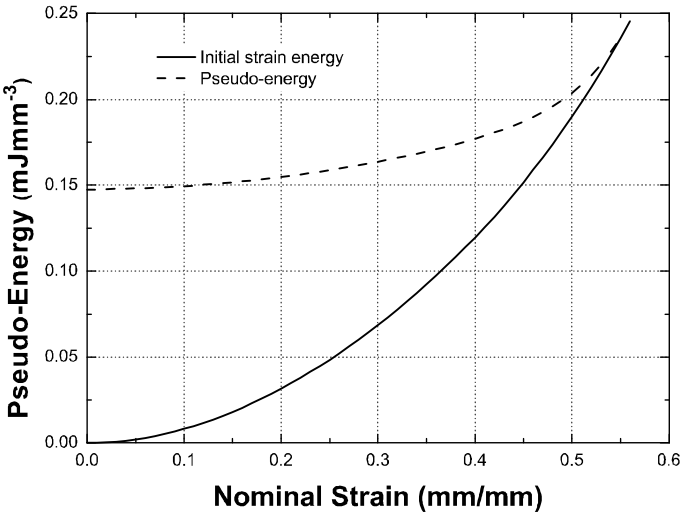


Figure 4.49: Plot of the pseudo-energy function against the nominal strain during loading-unloading cycle, considering formulation F at $T = 23^oC$.

4.2.3.2 Confined deformation hysteretic cycle (purely volumetric behaviour)

The same numerical approach was followed to find the material parameters r_{vol} and m_{vol} and $_{bvol}$ in order to characterize the purely volumetric unloading mechanical response and consequently the volumetric dissipative behaviour. Experimental data discussed in section 4.1.2.2 was the basis of the numerical fitting procedure followed in the present section.

The relation expressed by (3.83) was used for the numerical fit procedure. A nonlinear least square technique was used to calculate the material parameters referred above using the MATLAB® software.

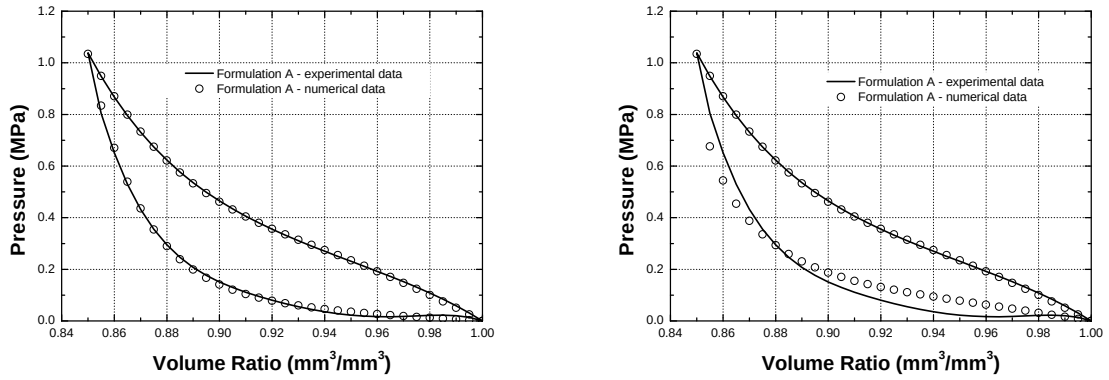
In table 4.16 are summarized the material parameters for the modified Dorfmann-Ogden and Zúñiga models, considering the experimental data from formulation A as this formulation was the only to be submitted to confined deformation loading-unloading cycles.

Table 4.16: Material parameters obtained for the modified Dorfmann-Ogden and Zúñiga models, considering a purely volumetric behaviour.

Formulation	r_{vol}	$m_{vol}(mJmm^{-3})$	$b_{vol}(mJmm^{-3})^{-1/2}$
A	1.0156	0.0399	4.8264

Figure 4.50 show the theoretical modelling of the volumetric hysteresis cycle for the formulation A given by the modified Dorfmann-Ogden and Zúñiga models. The unloading occurs at a volume ratio equal to approximately $J = 0.85$ that corresponds to a hydrostatic pressure approximately equal to 1.0 MPa.

Figure 4.51 show the evolution of the fitting relative error obtained for the considered volumetric deformation range.



(a) (b)

Figure 4.50: Modelling the volumetric (confined deformation) hysteretic cycle of formulation A, considering a) the Dorfmann-Ogden model and b) the Zúñiga model.

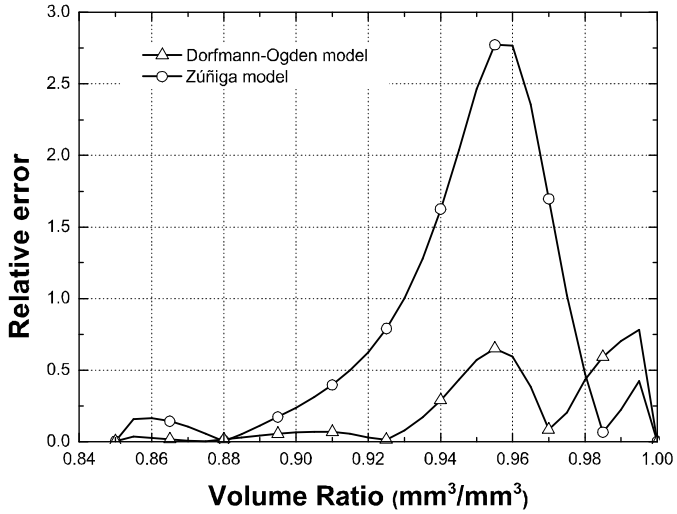


Figure 4.51: Relative error plotted against nominal strain for the fit of volumetric data from formulation A to the modified Dorfmann-Ogden and Zúñiga models.

In table 4.17 are summarized the mean relative errors obtained for the fit of the modified Dorfmann-Ogden and Zúñiga models to the volumetric deformation experimental data (unloading path) obtained for formulation A.

Table 4.17: Mean relative errors for the fit of the volumetric unloading path considering, the Dorfmann-Ogden and Zúñiga models.

Formulation	Dorfmann-Ogden model	Zúñiga model
A	21.7%	80.1%

Based on table 4.17 and in figures 4.50 and 4.51, we can conclude that the modified Dorfmann-Ogden model have a better fit capability when compared with the fit capabilities of the modified Zúñiga model.

The plot of the pseudo energy function expressed in (3.80) for the purely volumetric deformation case is given in figure 4.52 where, in the same way as described for the simple uniaxial compression case (unconfined deformation), the intersection of the pseudo-energy curve with the vertical axis at $J = 1$ gives the amount of dissipated energy for a purely volumetric deformation process.

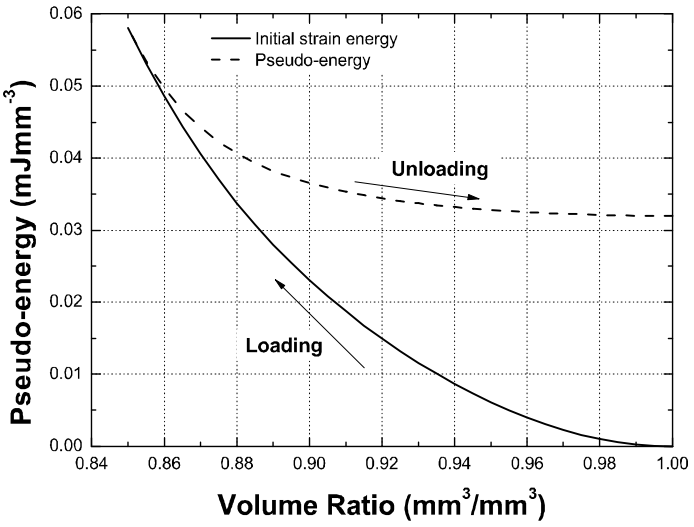


Figure 4.52: Plot of the pseudo-energy function against the volume ratio during a loading-unloading (confined deformation) cycle considering formulation A at $T = 18^oC$.

4.3 Constitutive modelling implementation

In this section we discuss the FEM implementation of the constitutive laws that characterize the CPGC's mechanical behaviour. The modelling of the loading path, hysteretic cycles (loading-unloading cycles) and heat generation effects due to energy dissipation phenomena, will be treated separately in this section in order to best explain our constitutive modelling implementation approach.

4.3.1 Modelling the loading path

4.3.1.1 Simple uniaxial compression case

To evaluate the suitability of the chosen strain energy function for nonlinear finite element analysis (FEA) procedures, a axisymetrical FE model (figure 4.53) that replicates the uniaxial experimental test was modelled, considering mean dimensions of the material samples corresponding to $\varnothing = 29.0mm$ and $h = 13.1mm$. The maximum nominal uniaxial strain ϵ was set equal to approximately 55% ($\simeq 7mm$ in displacement). The reaction force imposed by the CPGC material button to the superior plate displacement, was monitored and compared with the experimental test data in the raw format (force against displacement) in order to avoid comparing nominal stress data obtained from the experimental tests with true stress (Cauchy stress) data outputted from the finite element analysis procedure.

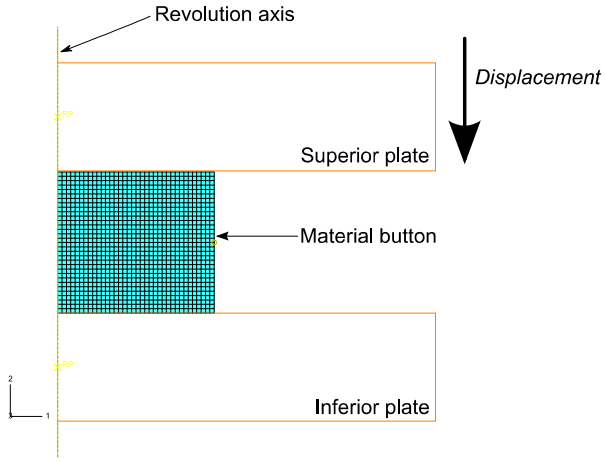


Figure 4.53: Axisymetrical FE model (simple uniaxial compression case).

Frictionless tangential behaviour in the interface plate/material was considered in the definition of the FE model in order to replicate the lubricated sample/plate interface at the experimental procedure. A linear, hybrid reduced integration axisymetrical finite element

formulation (CAX4RH) was used in the definition of the FE model that replicates the material button. This element formulation assured a good convergence within the applied deformation range.

In figure 4.54 is plotted the deformed shape of the CPGC sample for the maximum axial displacement of the upper plate.

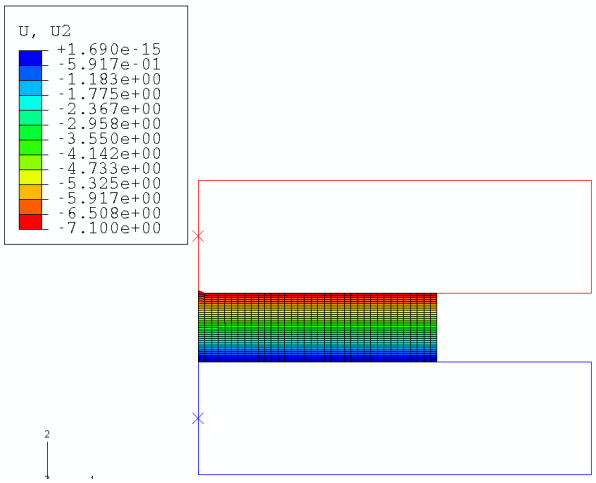


Figure 4.54: Nodal axial displacement FEA values (mm) obtained for the simple uniaxial compression case.

Material parameters summarized in tables 4.5, 4.6 and 4.7 were introduced for the calibration of the second order polynomial model in order to study the model's numerical response for different CPGC material formulations and applied thermal conditions.

Figures 4.55, 4.56, 4.57 and 4.58, shown the results obtained for formulations A, B, D and F, respectively, considering $T = 23^oC$ and respective material parameters summarized on table 4.5. These figures compare the obtained FEA results with the obtained experimental data. Is visible that the correlation between the experimental uniaxial results at $T = 23^oC$ and the results obtained through finite element analysis is acceptable for the considered range of deformation.

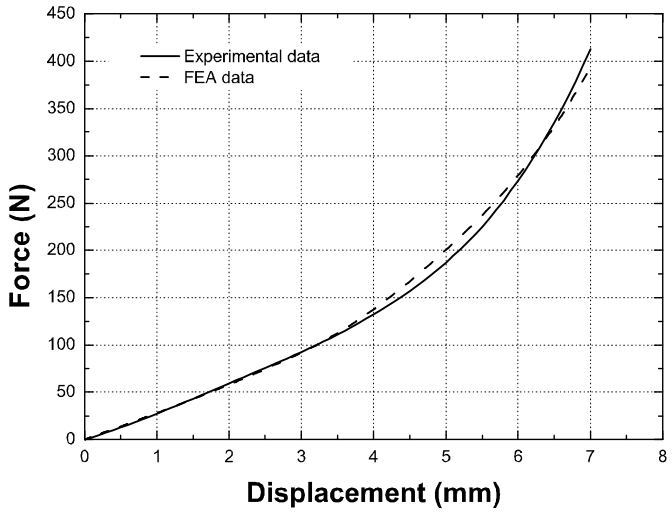


Figure 4.55: Comparison of FEA results with uniaxial compression experimental data from formulation A, considering $T = 23^oC$.

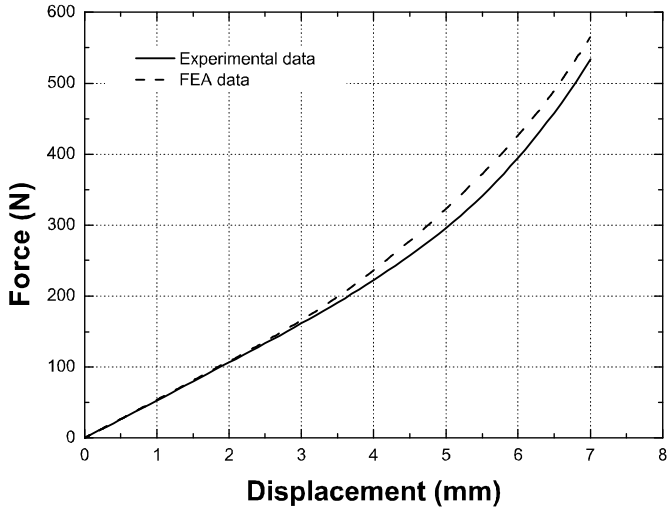


Figure 4.56: Comparison of FEA results with uniaxial compression experimental data from formulation B, considering $T = 23^oC$.

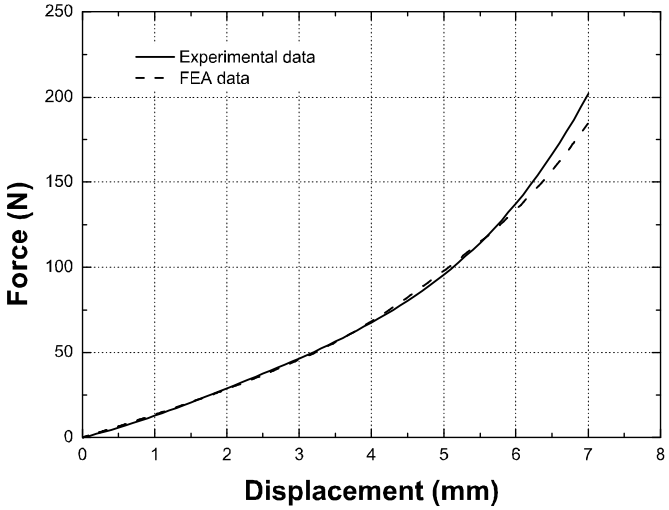


Figure 4.57: Comparison of FEA results with uniaxial compression experimental data from formulation D, considering $T = 23^oC$.

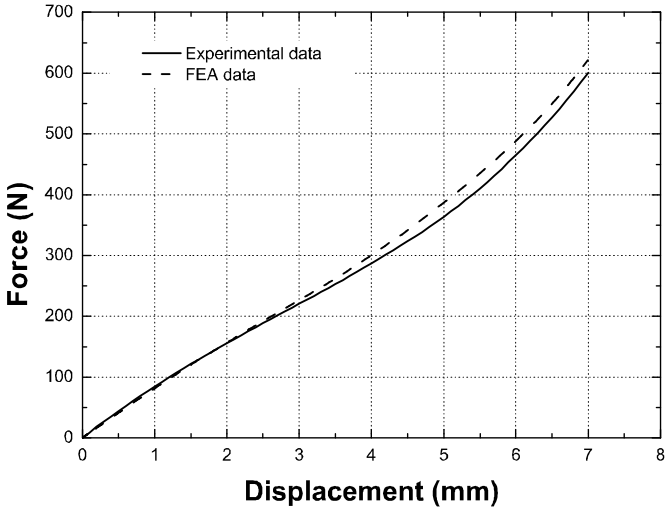


Figure 4.58: Comparison of FEA results with uniaxial compression experimental data from formulation F, considering $T = 23^oC$.

Considering the material parameters obtained for $T = 100^oC$, expressed in table 4.6, we compare the obtained FEA results with the uniaxial compression experimental data in figures 4.59, 4.60 and 4.61, for formulations A, B and F, respectively.

FEA results obtained considering material parameters obtained for $T = -10^oC$, summarized in table 4.7, are shown in figures 4.62, 4.63 and 4.64 for formulations A, B and F, respectively.

From the comparison between experimental data and obtained FEA results, is possible to conclude that the second order polynomial model is suitable for the reproduction of the CPGC's mechanical behaviour in nonlinear finite element method analysis considering material temperature equal to $T = 100^oC$ and $T = -10^oC$.

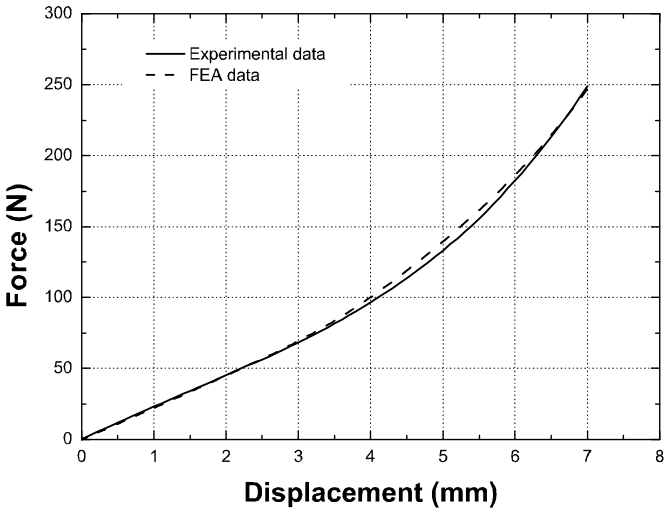


Figure 4.59: Comparison of FEA results with uniaxial compression experimental data from formulation A, considering $T = 100^oC$.

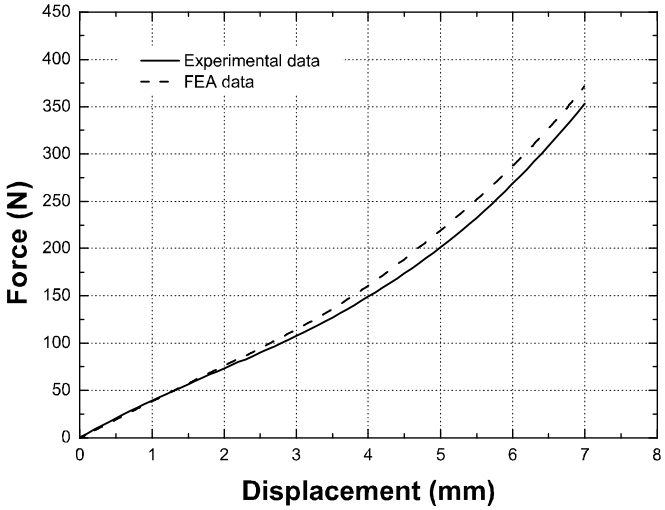


Figure 4.60: Comparison of FEA results with uniaxial compression experimental data from formulation B, considering $T = 100^oC$.

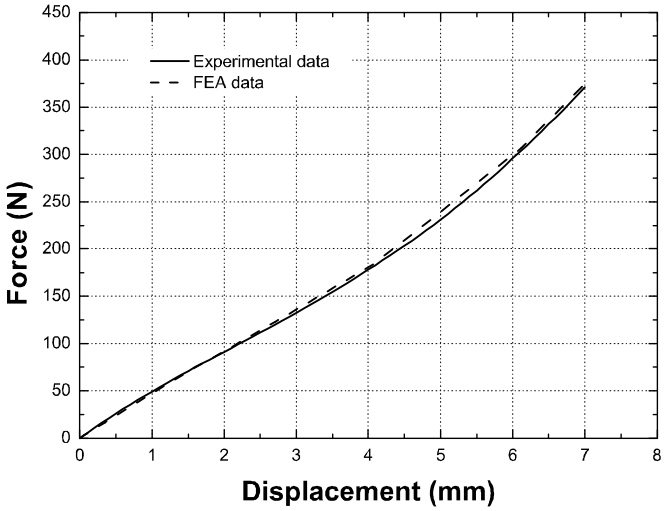


Figure 4.61: Comparison of FEA results with uniaxial compression experimental data from formulation F, considering $T = 100^oC$.

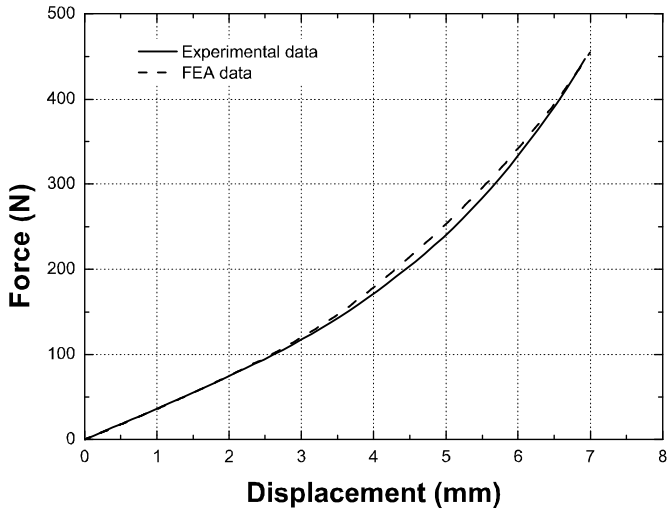


Figure 4.62: Comparison of FEA results with uniaxial compression experimental data from formulation A, considering $T = -10^oC$.

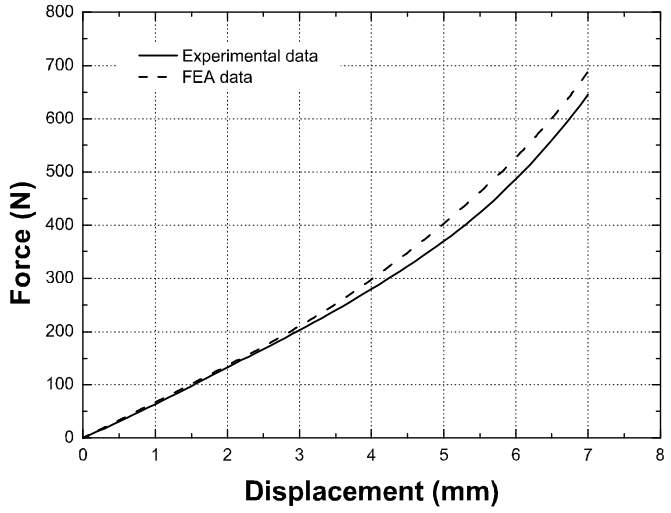


Figure 4.63: Comparison of FEA results with uniaxial compression experimental data from formulation B, considering $T = -10^oC$.

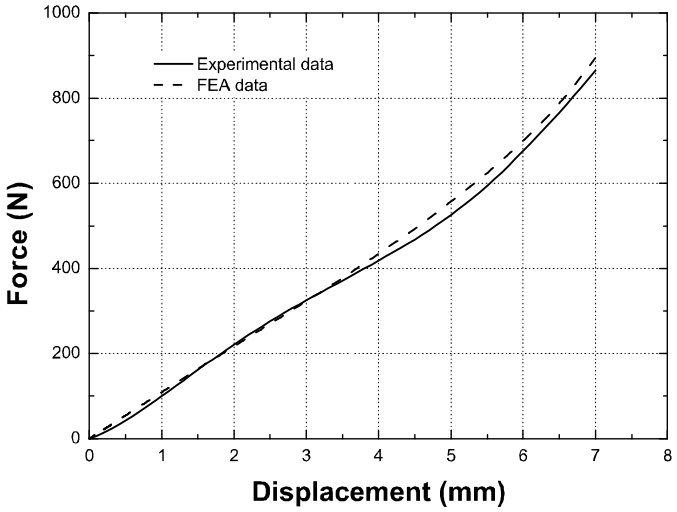


Figure 4.64: Comparison of FEA results with uniaxial compression experimental data from formulation F, considering $T = -10^{o}C$.

4.3.1.2 Volumetric compression case

As already pointed out in section 4.2.1.2, a FORTRAN® user subroutine was implemented in the nonlinear finite element code ABAQUS® allowing an independent polynomial expansion order N_{vol} of the volumetric term that defines the strain energy function. This capability is not assured by the finite element code that by default equals the volumetric polynomial expansion order to the deviatoric term expansion order ($N_{vol} = N_{dev}$). The implemented user subroutine *UHYPER allows the decoupling of the deviatoric and volumetric polynomial expansion orders ($N_{vol} \neq N_{dev}$), which can be very useful for modelling materials with highly nonlinear volumetric behaviour, through an independent increase in the volumetric expansion order. With the implemented user subroutine, the decoupled form of the Rivlin model (see expression 2.142) implemented in ABAQUS® can be reformulated and expressed by

$$\bar{\Psi} = \underbrace{\sum_{i+j=1}^{N_{dev}} C_{ij}(\overline{I}_1 - 3)^i(\overline{I}_2 - 3)^j}_{\Psi_{dev}} + \underbrace{\sum_{i+j=1}^{N_{vol}} \frac{1}{D_i}(J-1)^{2i}}_{\Psi_{vol}} \cdot \tag{4.9}$$

The pseudo-code of the implemented subroutine is described in algorithm 1.

For evaluating the CPGC's volumetric response in FE analysis and its dependence with the volumetric term polynomial expansion order, an unitary dimension hexahedron

Algorithm 1 Pseudo-code user subroutine for an independent control of the volumetric polynomial expansion order, N_{vol}

SUBROUTINE UHYPER {*Call ABAQUS subroutine UHYPER*}
———————————Block 1 (Material parameters)
INPUT C_{10}, C_{01}, C_{20}, C_{11}, C_{02} {*Pass in deviatoric material parameters* C_{ij} *via *.INP file*}
INPUT N_{vol} {*Define polynomial expansion order (volumetric term) via *.inp file*}
INPUT D_i,...D_N {*Pass in volumetric material parameters* D_i *via *.INP file*}
for $i = 1$ to N **do**
  {*Construction of the volumetric material parameter* $D(i)$ *array*}
  $D(i)$ = PROPS(i+6)
end for
———————————Block 2 (Definition of volumetric strain energy function)
INITIALIZE WV, $WV1$, $WV2$ and $WV3$
while $i \leq N$ **do**
  $WV = WV + \frac{1}{D(i)}(J-1)^{2i}$ {*Definition of volumetric term* $\bar{\Psi}_{vol}$}
  $WV1 = WV1 + \frac{2i}{D(i)}(J-1)^{2i-1}$ {*First derivative of volumetric term* $\frac{\partial \bar{\Psi}_{vol}}{\partial J}$}
  $WV2 = WV2 + \frac{4i^2-2i}{D(i)}(J-1)^{2i-2}$ {*Second derivative of volumetric term* $\frac{\partial^2 \bar{\Psi}_{vol}}{\partial J^2}$}
  $WV3 = WV3 + \frac{8i^3-12i^2+4i}{D(i)}(J-1)^{2i-3}$ {*Third derivative of volumetric term* $\frac{\partial^3 \bar{\Psi}_{vol}}{\partial J^3}$}
  $i = i + 1$
end while
———————————Block 3 (Strain energy function $\bar{\Psi} = \bar{\Psi}(\bar{I}_1, \bar{I}_2, J)$ and its derivatives)
if Compressible material **then**
  $U(1) = \bar{\Psi} = \underbrace{C_{10}(\bar{I}_1-3) + C_{01}(\bar{I}_2-3) + C_{20}(\bar{I}_1-3)^2 + C_{11}(\bar{I}_1-3)(\bar{I}_2-3) + C_{02}(\bar{I}_2-3)^2}_{\bar{\Psi}_{dev}} + \underbrace{WV}_{\bar{\Psi}_{vol}}$
  ELSE [Incompressible material]
  $U(1) = \bar{\Psi} = C_{10}(\bar{I}_1-3) + C_{01}(\bar{I}_2-3) + C_{20}(\bar{I}_1-3)^2 + C_{11}(\bar{I}_1-3)(\bar{I}_2-3) + C_{02}(\bar{I}_2-3)^2$
end if
——————————— {*First derivatives...*}
$UI1(1) = \frac{\partial \bar{\Psi}}{\partial \bar{I}_1} = C_{10} + 2C_{20}(\bar{I}_1-3) + C_{11}(\bar{I}_2-3)$
$UI1(2) = \frac{\partial \bar{\Psi}}{\partial \bar{I}_2} = C_{01} + 2C_{02}(\bar{I}_2-3) + C_{11}(\bar{I}_1-3)$
$UI1(3) = \frac{\partial \bar{\Psi}_{vol}}{\partial J} = WV1$
——————————— {*Second derivatives and cross derivatives...*}
$UI2(1) = \frac{\partial^2 \bar{\Psi}}{\partial \bar{I}_1^2} = 2C_{20}$
$UI2(2) = \frac{\partial^2 \bar{\Psi}}{\partial \bar{I}_2^2} = 2C_{02}$
$UI2(3) = \frac{\partial^2 \bar{\Psi}}{\partial J^2} = WV2$
$UI2(4) = \frac{\partial^2 \bar{\Psi}}{\partial \bar{I}_1 \partial \bar{I}_2} = C_{11}$
$UI2(5) = \frac{\partial^2 \bar{\Psi}}{\partial \bar{I}_1 \partial J} = 0$
$UI2(6) = \frac{\partial^2 \bar{\Psi}}{\partial \bar{I}_2 \partial J} = 0$
——————————— {*Third derivatives and cross derivatives...*}
$UI3(1) = \frac{\partial^3 \bar{\Psi}}{\partial \bar{I}_1^2 \partial J} = 0$
$UI3(2) = \frac{\partial^3 \bar{\Psi}}{\partial \bar{I}_2^2 \partial J} = 0$
$UI3(3) = \frac{\partial^3 \bar{\Psi}}{\partial \bar{I}_1 \partial \bar{I}_2 \partial J} = 0$
$UI3(4) = \frac{\partial^3 \bar{\Psi}}{\partial \bar{I}_1 \partial J^2} = 0$
$UI3(5) = \frac{\partial^3 \bar{\Psi}}{\partial \bar{I}_2 \partial J^2} = 0$
$UI3(6) = \frac{\partial^3 \bar{\Psi}}{\partial J^3} = WV3$
———————————

($V_0 = 1mm^3$) was modelled using a hexahedral finite element with a quadratic, hybrid, reduced integration formulation (C3D20RH). A volumetric state of deformation was achieved by constraining the lateral displacements of the element and applying a displacement boundary condition at the top face (in red) of the hexahedral element as seen in figure 4.65.

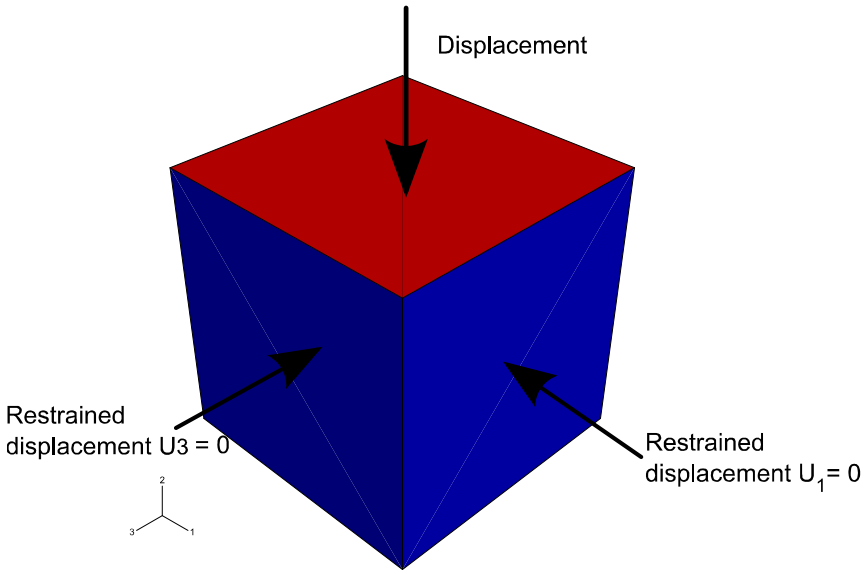


Figure 4.65: Boundary conditions applied to the hexahedral finite element for reproducing a volumetric (confined) deformation state.

A set of FE simulations were done considering the formulations A, B and C at $T = 23^oC$. In this numerical procedure were considered different polynomial expansion orders N_{vol}. The volumetric material parameters D_i defined as input for the implemented user subroutine are summarized in tables 4.9, 4.10 and 4.11.

In figures 4.66, 4.67 and 4.68, are compared the pressure values obtained through FE analysis with the experimentally obtained data. It is observable that the fitting accuracy is improved with the implementation of the *UHYPER user subroutine. The improvement in the reproduction of the experimental volumetric behaviour is more pronounced for formulation A, as this formulation is characterized by a higher degree of nonlinearity in the purely volumetric mechanical response.

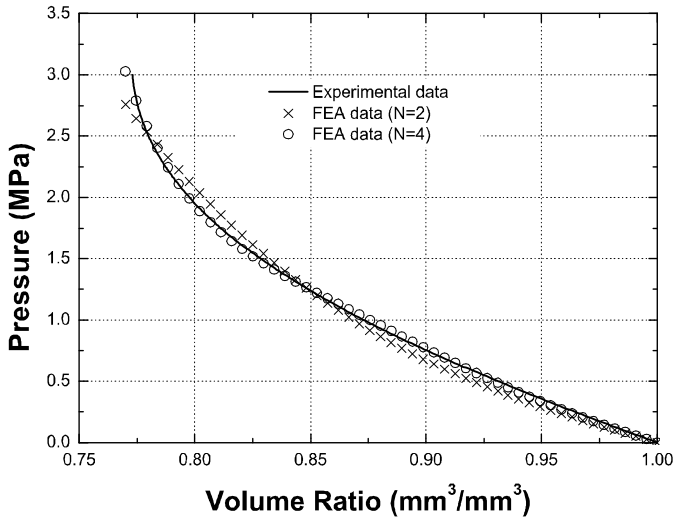


Figure 4.66: FEA results obtained for formulation A, considering $N_{vol} = 2$ and $N_{vol} = 4$, plotted against volumetric deformation experimental data at $T = 23^oC$.

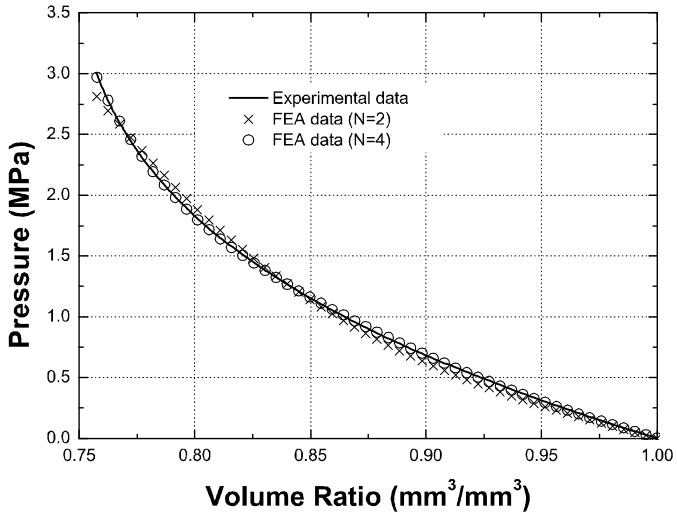


Figure 4.67: FEA results obtained for formulation B, considering $N_{vol} = 2$ and $N_{vol} = 4$, plotted against volumetric deformation experimental data at $T = 23^oC$.

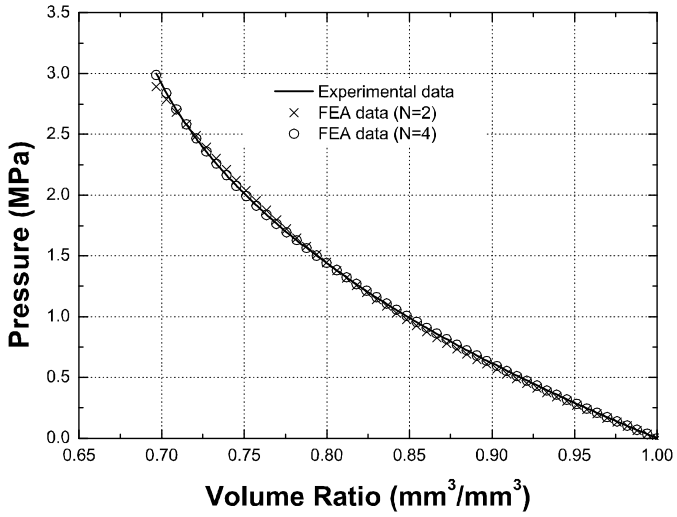


Figure 4.68: FEA results obtained for formulation *C*, considering $N_{vol} = 2$ and $N_{vol} = 4$, plotted against volumetric deformation experimental data at $T = 23^oC$.

4.3.2 Modelling hysteretic cycles using a modified pseudo-elasticity theory

The new formulation for describing hysteretic cycles discussed in section 3.1 was implemented in the finite element code ABAQUS® using inbuilt user subroutines. For the present case, CPGC's formulation *A* was chosen as the material formulation to be modelled. For this example, total loading-unloading cycles were considered (no partial unloading). *UHYPER was the basis user subroutine for this numerical implementation and *SDVINI and *UVARM were used as auxiliary subroutines to manage the output of nominal stress values, for posterior comparison with experimental data

The primary strain energy function $\bar{\Psi}^0$ implemented in this subroutine is expressed by (4.10) and as already discussed in section 4.2.1, this model was chosen for describing the loading (unmodified) mechanical behaviour of CPGC material.

$$\begin{aligned}\bar{\Psi}^0(\bar{I}_1, \bar{I}_2, J) = {} & C_{10}(\overline{I}_1 - 3) + C_{01}(\overline{I}_2 - 3) + C_{20}(\overline{I}_1 - 3)^2 \\ & + C_{11}(\overline{I}_1 - 3)(\overline{I}_2 - 3) + C_{02}(\overline{I}_2 - 3)^2 + \sum_{i=1}^{N_{vol}} \frac{1}{D_i}(J-1)^{2i}.\end{aligned} \tag{4.10}$$

The subroutine implements the pseudo-energy function described in (3.78) allowing the

decoupling of the deviatoric and volumetric effects during loading-unloading cycles. The unloading behaviour was modelled with the implementation of the modified Dorfmann-Ogden model, considering the best fit capabilities to the experimental data obtained with this model as already discussed in section 4.2.3.

In order to better capture the unmodified (primary) volumetric behaviour of CPGC, the present subroutine incorporate instructions from the subroutine already discussed and proposed in algorithm 1.

The pseudo-code of the implemented subroutine is divided in two parts and is expressed in algorithms 2 and 3.

Two simple deformation cases were considered for validation of the finite element implementation. First, an uniaxial (unconfined) compression cycle was simulated, given predominantly the deviatoric deformation effects. In the element of figure 4.69 a displacement boundary condition was applied at the upper and bottom faces (in red) of the unitary element. The nodal displacements at the lateral faces (in orange) were not restrained allowing a free expansion of the material.

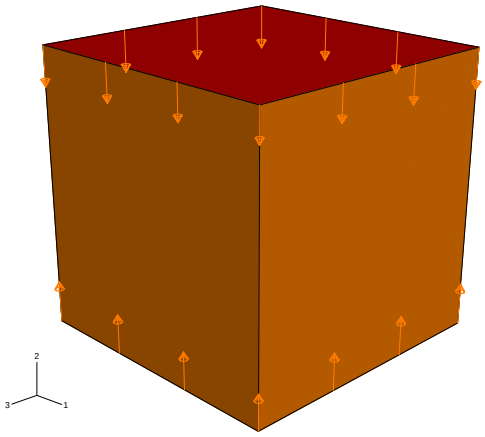


Figure 4.69: Boundary conditions defined to simulate loading-unloading uniaxial compression cycles.

For simulating the confined deformation cycle and consequently, affecting mainly volumetric mechanical aspects of the material, the FE model represented in figure 4.65 was used.

A new linear least square procedure was performed to calculate the volumetric material parameters D_i in order to find the volumetric material parameters that best model the loading (unmodified) volumetric deformation curve for formulation A obtained for the volumetric deformation cycle expressed in figure 4.12. A good approximation to the

Algorithm 2 Pseudo-code for modelling hysteretic cycles

SUBROUTINE UHYPER {*Call ABAQUS subroutine UHYPER*}
———————————Block 1 (Material parameters)
INPUT C_{10}, C_{01}, C_{20}, C_{11}, C_{02} {*Deviatoric material parameters* C_{ij}}
INPUT N_{vol} {*Define polynomial expansion order* N_{vol}}
INPUT D_i,...D_N {*Volumetric material parameters* D_i}
for $i = 1$ to N **do**
  $D(i)$ = PROPS(i+6)
end for
INPUT $r_{dev}, m_{dev}, r_{vol}, m_{vol}$ {*Unloading parameters (Modified Dorfmamm-Ogden model)*}
———————————Block 2 (Compute initial strain energy values)
INITIALIZE $\bar{\Psi}^0_{vol}$ {*Initial volumetric strain energy*}
$i = 1$
while $i \leq N$ **do**
  $\bar{\Psi}^0_{vol} = \bar{\Psi}^0_{vol} + \frac{(J-1)^{2i}}{D(i)}$
  $i = i + 1$
end while
$\bar{\Psi}^0_{dev} = C_{10}(I_1 - 3) + C_{01}(I_2 - 3) + C_{20}(I_1 - 3)^2 + C_{11}(I_1 - 3)(I_2 - 3) + C_{02}(I_2 - 3)^2$ {*Initial deviatoric strain energy*}
———————————{*Block for triggering multiple loading-unloading cycles*}
if MultiloopFlag=ON and $I_1 = 3$, $I_2 = 3$, $J = 1$ **then**
  Modelling multi-loops procedure active (reset energy values)
end if
———————————Block 3 (Block for triggering the unloading point)
INITIALIZE *Old* $\bar{\Psi}^0_{dev}$ and *Old* $\bar{\Psi}^0_{vol}$ {*Deviatoric and volumetric energy value for the past increment*}
if $\bar{\Psi}^0_{dev} \geq$ *Old* $\bar{\Psi}^0_{dev}$ **then**
  $\eta_{dev} = 1$ {*Loading phase*}
  Old $\bar{\Psi}^0_{dev} = \bar{\Psi}^0_{dev}$ {*Store current deviatoric strain energy value for the next increment*}
  STORE *Old* $\bar{\Psi}^0_{dev}$ {*Define state variable (pass to next increment)*}
else {Unloading phase}
  $\bar{\Psi}^{max}_{dev}$ = *Old* $\bar{\Psi}^0_{dev}$ {*Store maximum deviatoric energy at unloading point*}
  $\eta_{dev} = 1 - \frac{1}{r_{dev}} tanh\left[\frac{\bar{\Psi}^{max}_{dev} - \bar{\Psi}^0_{dev}}{m_{dev}}\right]$
  STORE $\bar{\Psi}^{max}_{dev}$ {*Define state variable (pass to next increment)*}
end if
if $\bar{\Psi}^0_{vol} \geq$ *Old* $\bar{\Psi}^0_{vol}$ **then**
  $\eta_{vol} = 1$ {*Loading phase*}
  Old $\bar{\Psi}^0_{vol} = \bar{\Psi}^0_{vol}$ {*Store current volumetric strain energy value for the next increment*}
  STORE *Old* $\bar{\Psi}^0_{vol}$ {*Define state variable (pass to next increment)*}
else {Unloading phase}
  $\bar{\Psi}^{max}_{vol}$ = *Old* $\bar{\Psi}^0_{vol}$ {*Store maximum volumetric energy at unloading point*}
  $\eta_{vol} = 1 - \frac{1}{r_{vol}} tanh\left[\frac{\bar{\Psi}^{max}_{vol} - \bar{\Psi}^0_{vol}}{m_{vol}}\right]$
  STORE $\bar{\Psi}^{max}_{vol}$ {*Define state variable (Pass to next increment)*}
end if
———————————Block 4 (Deviatoric and volumetric dissipative energy)
COMPUTE $\phi_{dev}(\eta_{dev}) = -\frac{m_{dev}}{2r_{dev}} \ln[1 - (\eta_{dev} r_{dev} - r_{dev})^2] - \bar{\Psi}^{dev}_{max}(\eta_{dev} - 1) - m_{dev} \tanh^{-1}[r_{dev}(\eta_{dev} - 1)](\eta_{dev} - 1)$ {*Deviatoric dissipative energy*}
COMPUTE $\phi_{vol}(\eta_{vol}) = -\frac{m_{vol}}{2r_{vol}} \ln[1-(\eta_{vol} r_{vol} - r_{vol})^2] - \bar{\Psi}^{vol}_{max}(\eta_{vol} - 1) - m_{vol} \tanh^{-1}[r_{vol}(\eta_{vol} - 1)](\eta_{vol} - 1)$ {*Volumetric dissipative energy*}
COMPUTE $\phi_{total} = \phi_{dev}(\eta_{dev}) + \phi_{dev}(\eta_{vol})$ {*Total dissipative energy*}
STORE ϕ_{total} {*Define state variable*}
———————————

Algorithm 3 Pseudo-code for modelling hysteretic cycles (continued)

———————————Block 5 (Definition of volumetric strain energy function)

INITIALIZE WV, $WV1$, $WV2$ and $WV3$

while $i \leq N$ **do**

$WV = WV + \frac{1}{D(i)}(J-1)^{2i}$ {*Definition of volumetric term* $\bar{\Psi}_{vol}$}

$WV1 = WV1 + \frac{2i}{D(i)}(J-1)^{2i-1}$ {*First derivative of volumetric term* $\frac{\partial \bar{\Psi}_{vol}}{\partial J}$}

$WV2 = WV2 + \frac{4i^2-2i}{D(i)}(J-1)^{2i-2}$ {*Second derivative of volumetric term* $\frac{\partial^2 \bar{\Psi}_{vol}}{\partial J^2}$}

$WV3 = WV3 + \frac{8i^3-12i^2+4i}{D(i)}(J-1)^{2i-3}$ {*Third derivative of volumetric term* $\frac{\partial^3 \bar{\Psi}_{vol}}{\partial J^3}$}

$i = i + 1$

end while

———————————Block 6 (Definition of pseudo-energy function and its derivatives)

if Compressible material **then**

$U(1) = \bar{\Psi} = \eta_{dev}[\underbrace{C_{10}(\bar{I}_1-3) + C_{01}(\bar{I}_2-3) + C_{20}(\bar{I}_1-3)^2 + C_{11}(\bar{I}_1-3)(\bar{I}_2-3) + C_{02}(\bar{I}_2-3)^2}_{\bar{\Psi}^0_{dev}}] +$

$\eta_{vol}\underbrace{WV}_{\bar{\Psi}^0_{vol}} + \phi_{dev} + \phi_{vol}$

else {Incompressible material}

$U(1) = \bar{\Psi} = \eta_{dev}[(C_{10}(\bar{I}_1-3) + C_{01}(\bar{I}_2-3) + C_{20}(\bar{I}_1-3)^2 + C_{11}(\bar{I}_1-3)(\bar{I}_2-3) + C_{02}(\bar{I}_2-3)^2)]$

end if

———————————{*First derivatives...*}

$UI1(1) = \frac{\partial \bar{\Psi}}{\partial \bar{I}_1} = \eta_{dev}[C_{10} + 2C_{20}(\bar{I}_1-3) + C_{11}(\bar{I}_2-3)]$

$UI1(2) = \frac{\partial \bar{\Psi}}{\partial \bar{I}_2} = \eta_{dev}[C_{01} + 2C_{02}(\bar{I}_2-3) + C_{11}(\bar{I}_1-3)]$

$UI1(3) = \frac{\partial \bar{\Psi}_{vol}}{\partial J} = \eta_{vol} WV1$

———————————{*Second derivatives and cross derivatives...*}

$UI2(1) = \frac{\partial^2 \bar{\Psi}}{\partial \bar{I}_1^2} = \eta_{dev} 2C_{20}$

$UI2(2) = \frac{\partial^2 \bar{\Psi}}{\partial \bar{I}_2^2} = 2\eta_{dev} C_{02}$

$UI2(3) = \frac{\partial^2 \bar{\Psi}}{\partial J^2} = \eta_{vol} WV2$

$UI2(4) = \frac{\partial^2 \bar{\Psi}}{\partial \bar{I}_1 \partial \bar{I}_2} = \eta_{dev} C_{11}$

$UI2(5) = \frac{\partial^2 \bar{\Psi}}{\partial \bar{I}_1 \partial J} = 0$

$UI2(6) = \frac{\partial^2 \bar{\Psi}}{\partial \bar{I}_2 \partial J} = 0$

———————————{*Third derivatives and cross derivatives...*}

$UI3(1) = \frac{\partial^3 \bar{\Psi}}{\partial \bar{I}_1^2 \partial J} = 0$

$UI3(2) = \frac{\partial^3 \bar{\Psi}}{\partial \bar{I}_2^2 \partial J} = 0$

$UI3(3) = \frac{\partial^3 \bar{\Psi}}{\partial \bar{I}_1 \partial \bar{I}_2 \partial J} = 0$

$UI3(4) = \frac{\partial^3 \bar{\Psi}}{\partial \bar{I}_1 \partial J^2} = 0$

$UI3(5) = \frac{\partial^3 \bar{\Psi}}{\partial \bar{I}_2 \partial J^2} = 0$

$UI3(6) = \frac{\partial^3 \bar{\Psi}}{\partial J^3} = \eta_{vol} WV3$

———————————Block 7 (Compute compressive nominal stres)

SUBROUTINE UVARM {*Call ABAQUS subroutine UVARM*}

$P_2 = J\lambda_2^{-1}\sigma_2$ {*Stress transformation*}

WRITE P_2 stress component to results file *.ODB

———————————

experimental pressure vs. volume ratio curve was obtained considering the volumetric polynomial expansion order $N_{vol} = 4$. The volumetric material parameters for formulation A are given in table 4.18.

Also in table 4.18 is expressed the initial Poisson's ratio υ_0 for formulation A calculated from expressions (2.143), (2.144) and (2.98) with material parameters given by tables 4.5 and 4.18. The initial Poisson's ratio for formulation A is quite high, defining an almost-incompressible volumetric behaviour for this formulation.

Table 4.18: Volumetric material parameter values (MPa^{-1}) for formulation A and correspondent initial Poisson's ratio.

Formulation	D_1	D_2	D_3	D_4	υ_0
A	0.39258	-0.019409	0.000327	-3.2183 x10^{-5}	0.482

4.3.2.1 Simple uniaxial compression (unconfined deformation)

An unitary dimensional hexahedra element, with a quadratic, hybrid, reduced integration (C3D20RH) formulation was used to evaluate the numerical response of the subroutine in a simple uniaxial compression (unconfined deformation) case. For the present case the primary energy function $\bar{\Psi}^0$ is described by (4.10) calibrated with deviatoric constants C_{ij} expressed for formulation A in table 4.5. The volumetric material parameters D_i that characterize the volumetric behaviour are summarized in table 4.18.

The deviatoric unloading behaviour was modelled using the modified Dorfmann-Ogden model through the definitions of unloading constants r_{dev}, m_{dev}, r_{vol} and m_{vol} summarized in tables 4.14 and 4.16, respectively.

A displacement boundary condition was applied at two parallel faces of the element as seen in figure 4.69, simulating a homogeneous deformation process for a total loading-unloading cycle. The element was uniaxially loaded until $\epsilon = 0.57$ ($\lambda = 0.43$) and then released to the unstressed configuration $\epsilon = 0$ ($\lambda = 1$) performing one loading-unloading cycle. In figure 4.70 is displayed the FEA nominal stress obtained for one total loading-unloading cycle plotted against the experimentally obtained nominal stress for formulation A It is possible to observe from figure 4.70, that the FE results obtained through the subroutine implemented in ABAQUS® gives a very good fit to the experimental hysteretic cycle.

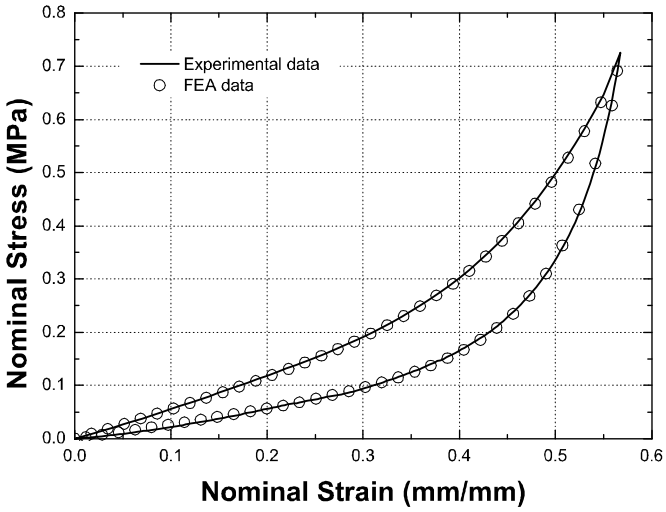


Figure 4.70: FEA results plotted against experimental data considering a total loading-unloading compression cycle.

Figure 4.71 show the pseudo-energy curve for a complete loading-unloading cycle obtained for the FE simulation plotted against the numerical values obtained during the fit process of the hysteretic cycle as discussed in section 4.2.3.1.

The predominance of deviatoric effects in the present deformation case (unconfined deformation) is evident in figure 4.72. From these results it is possible to conclude that the effect of deviatoric dissipative parameter η_{dev} in the mechanical response of the material during the unloading phase is much more pronounced then the effect of the volumetric dissipative parameter η_{vol}, resulting from higher deviatoric strain energy values obtained during the uniaxial (unconfined) deformation process.

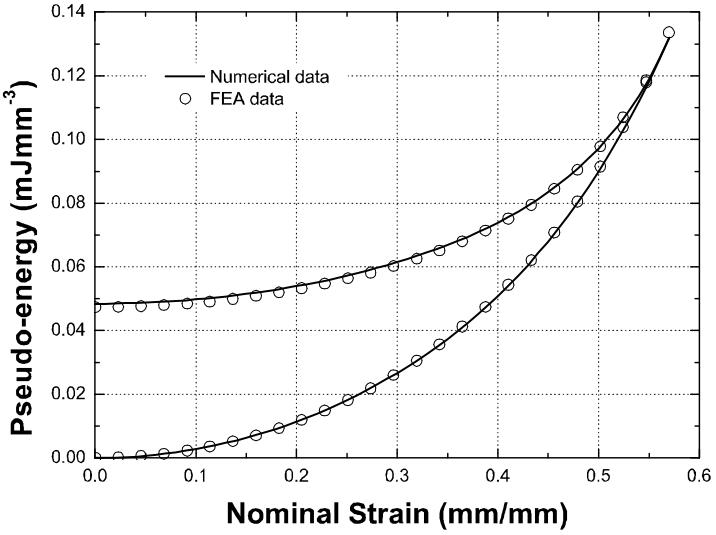


Figure 4.71: Pseudo-energy plotted against nominal strain, considering simultaneously numerical data obtained from the fitting process and FEA data.

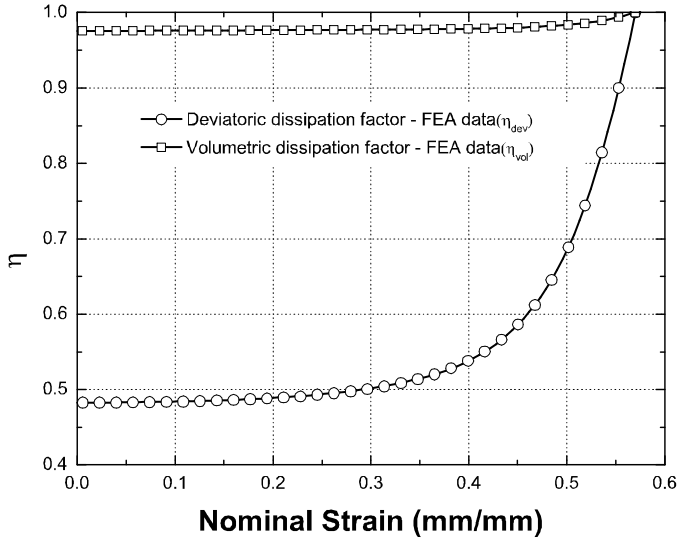


Figure 4.72: Deviatoric and volumetric dissipation factors plotted against nominal strain, considering a uniaxial (unconfined) compression case.

4.3.2.2 Volumetric compression (confined deformation)

For simulating the volumetric or confined deformation, an unitary dimensional hexahedra quadratic element ($V_0 = 1mm^3$) was defined. The applied boundary conditions defines a volumetric deformation state by applying displacement at one of the faces of the element and constraining the other displacement components on the other faces of the unitary cube as seen in figure 4.65. A volumetric deformation cycle was applied until $J = 0.85$ is obtained and then released to the unstressed configuration $J = 1$. The deviatoric and volumetric material parameters for modelling the loading path are given in tables 4.5 and 4.18, respectively. Unloading parameters r_{dev}, m_{dev}, r_{vol} and m_{vol} for formulation A are summarized in tables 4.14 and 4.16. The results obtained from the FE model are shown in figure 4.73, in which the pressure is plotted against the volume ratio for the entire volumetric deformation cycle. It is observable that the FEA results obtained through the implemented subroutine predicts very well the experimental volumetric hysteric cycle.

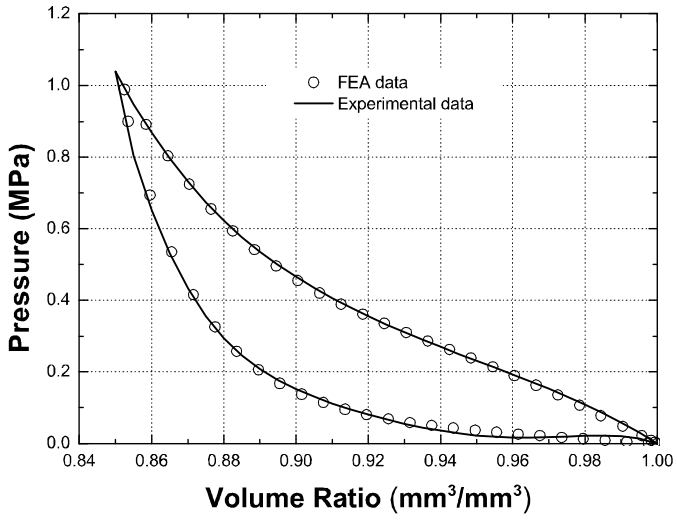


Figure 4.73: FEA results plotted against experimental data considering a total loading-unloading volumetric compression cycle.

The evolution of the strain pseudo-energy values with the volumetric deformation cycle is shown in figure 4.74. In this figure are compared the numerical results obtained for fit process of the volumetric hysteretic cycle as discussed in section 4.2.3.2 with the results obtained via the implemented subroutine.

Figure 4.75 show the major effect of the volumetric dissipation factor η_{vol} in the modelling of the unloading behaviour when the material is highly confined. This behaviour

is the opposite from that obtained in section 4.3.2.1 for the uniaxial (unconfined) deformation case, in which the volumetric dissipative factor have a minor effect on the global mechanical response.

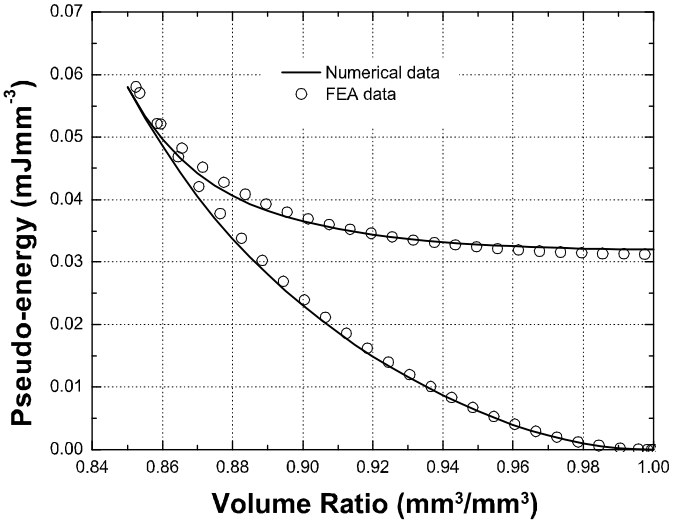


Figure 4.74: Pseudo-energy plotted against volume ratio considering simultaneously numerical data obtained from the fitting process and FEA data.

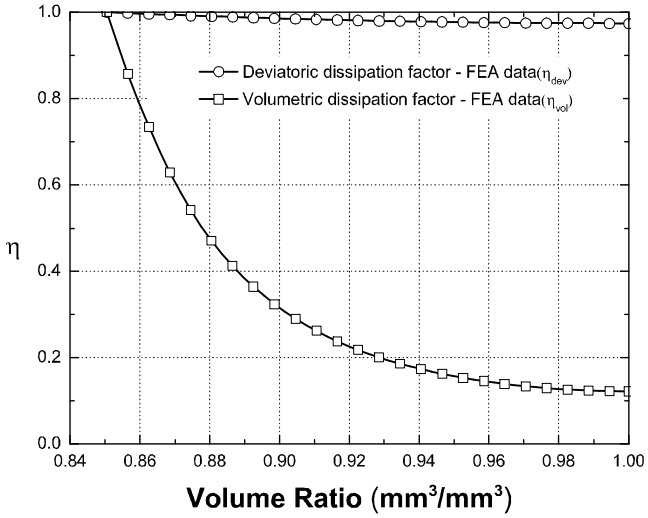


Figure 4.75: Deviatoric and volumetric dissipation factors plotted against volume ratio considering a volumetric deformation state.

4.3.3 Modelling heat generation

A transient fully coupled thermal-stress finite element procedure for evaluation of the internal heat generation during a loading-unloading cycle was implemented in the nonlinear finite element code ABAQUS®, using inbuilt subroutine programing capabilities.

For the present case it was assumed that during the loading process *all the energy is absorbed by the material as strain energy* (recoverable strain energy) and heat is generated only during the *unloading process* in consequence of the hysteresis loss.

The internal heat build up generation was implemented by the use of the user subroutine *HETVAL. This subroutine is (as the *UHYPER subroutine) called at each element's integration point and allows, for the dependence of internal heat generation, variables that evolve with the solution of the problem such as the total dissipative energy ϕ_{total} per hysteretic cycle expressed by equation (3.119). Subroutine *HETVAL is called (for each increment) after the material constitutive subroutine *UHYPER [see ABAQUS®, 2006, User Subroutine Reference Manual, Section 1.1.12] which allows the update of all state variables passed into subroutine *HETVAL.

The thermal energy generated per unit time and unit volume during the dissipative process is, in our case, given by the *volumetric heat flux term* r_h (see equation 2.61). It follows that

$$r_h = \frac{d(\phi_{dev}(\eta_{dev}) + \phi_{vol}(\eta_{vol}))}{dt} = \frac{d\phi_{total}}{dt} \ , \tag{4.11}$$

where r_h is given in units of power per unit of volume.

Observing equation (3.120) and as mentioned before in section 3.2.1, we state for the present approach, that the total dissipated energy ϕ_{total} *is totally converted into heat.*

The pseudo-code for the subroutine that model heat generation from hysteretic cycles, is expressed in algorithm 4.

4.3.3.1 Thermomechanical finite element model description

For simulate the heat build-up during a loading-unloading cycle was defined an unitary dimensional FE model ($V_0 = 1mm^3$) subjected to uniaxial compression cycles. The model was descritized by four coupled temperature-displacement 3D continuum quadratic hexahedral elements (C3D20RHT). The model was defined for two different thermal situations, *adiabatic* (no boundary heat flux) and *non-adiabatic* (convection and thermal radiation fluxes). For the non-adiabatic case was considered that the surroundings temperature was equal to 23^oC and the convective heat phenomena in the model boundaries was assumed to be free. The convective heat transfer coefficient was set to $h_{air} = 10Wm^{-2}K^{-1}$. Thermal radiation emitted by the boundary surfaces of the model during the deformation

Algorithm 4 Pseudo-code for modelling heat generation

SUBROUTINE HETVAL {*Call ABAQUS subroutine *HETVAL*}
INITIALIZE *Old* ϕ_{total} {*Dissipative energy value for the past increment*}
if $\phi_{total} = 0$ **then**
  $r(1) = 0$
  $r(2) = 0$
else
  $d\phi_{total} = \phi_{total}$ - *Old* ϕ_{total} {*Incremental difference in dissipated energy* $(\frac{mJ}{mm^3})$}
  $r(1) = \frac{d\phi_{total}}{dt}$ {*Incremental internal volumetric heat flux* $(\frac{mJ}{mm^3 s})$}
  $r(2) = 0$ {*Variation of volumetric heat flux with temperature*}
end if
Old $\phi_{total} = \phi_{total}$ {*Store current dissipative energy value*}
STORE *Old* ϕ_{total} {*Define state variable (pass to next increment)*}

cycle was also considered ($\epsilon_{rad} = 0.8$).

CPGC's indicative thermal properties and material density used as input for the fully coupled thermal-stress analysis, are summarized in table 4.19.

Table 4.19: Material thermal properties [Silva *et al.*, 2005] and density applied in the definition of the FE thermomechanical model.

Formulation	Thermal conductivity k_t	Specific heat c_p	Density ϱ
A	0.043 $Wm^{-1}K^{-1}$	350 $Jkg^{-1}K^{-1}$	751.4 kgm^{-3}

For the present case, the primary energy function was described by (4.10) using the deviatoric constants C_{ij} expressed for formulation A in table 4.5 and for volumetric constants D_i, the values expressed in table 4.18. The deviatoric and volumetric unloading behaviour was modelled using the modified Dorfmann-Ogden model through the definitions of unloading constants r_{dev}, m_{dev}, and r_{vol}, m_{vol} summarized at tables 4.14 and 4.16, respectively.

A displacement boundary condition was applied at the upper face of the element simulating a homogeneous deformation process The element was loaded until $\epsilon = 0.57$ and then released to the unstressed configuration considering for the present loading case a multi-cycle approach. In table 4.20 are described the loading conditions applied to the FE model for evaluating the thermal response of the model to a different set of loading conditions (varying the loading frequency and loading time) and thermal conditions.

Multiple cycles in table 4.20 refers to complete loading-unloading cycles up to $\epsilon = 0.57$ while *nested cycles* corresponds to three cycles up to $\epsilon = 0.57$, $\epsilon = 0.45$ and $\epsilon = 0.35$ in a total of 9 loading-unloading cycles. Figure 4.76 show the FEA results obtained for an simple uniaxial deformation case considering a nested cycle loading procedure.

Table 4.20: Thermomechanical characteristics of the FE models.

Load type	FE Model	f (Hz)	Number cycles	Time (s)	Thermal conditions
Multiple cycles	1	1	10	10	Adiabatic
Multiple cycles	2	1	10	10	Non-adiabatic
Nested cycles	3	1	9	9	Non-adiabatic
Multiple cycles	4	10	10	1	Adiabatic
Multiple cycles	5	10	10	1	Non-adiabatic
Nested cycles	6	10	9	0.9	Non-adiabatic
Multiple cycles	7	10	100	10	Non-adiabatic
Multiple cycles	8	100	10	0.1	Adiabatic
Multiple cycles	9	100	10	0.1	Non-adiabatic
Nested cycles	10	100	9	0.09	Non-adiabatic
Multiple cycles	11	100	1000	10	Non-adiabatic

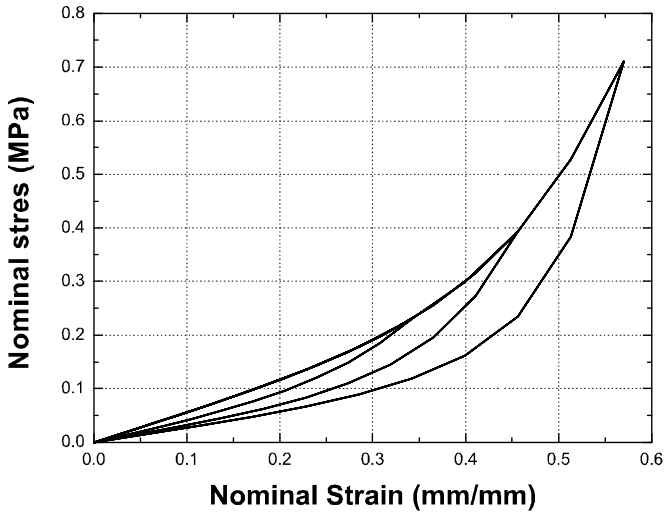


Figure 4.76: Nominal stress plotted against nominal strain for formulation A, considering a nested cycle loading condition.

4.3.3.2 Thermomechanical FEA results

Figures 4.77, 4.78 and 4.79, show the influence of thermal conditions (adiabatic and non-adiabatic) in the thermal response of the model through the monitoring of the temperature at the centroid of the element. As expected, in the non-adiabatic case the rise in temperature is more pronounced in result of the inexistence of heat transfer to the surroundings. It is also observable that for the adiabatic case after the 10 loading-unloading cycles, the same final temperature is achieved for the three imposed frequencies. It must be noticed

that the same final temperature is reached in different time scales due to the increase in the volumetric heat flux term r_h (see equation 4.11) with the imposed frequency.

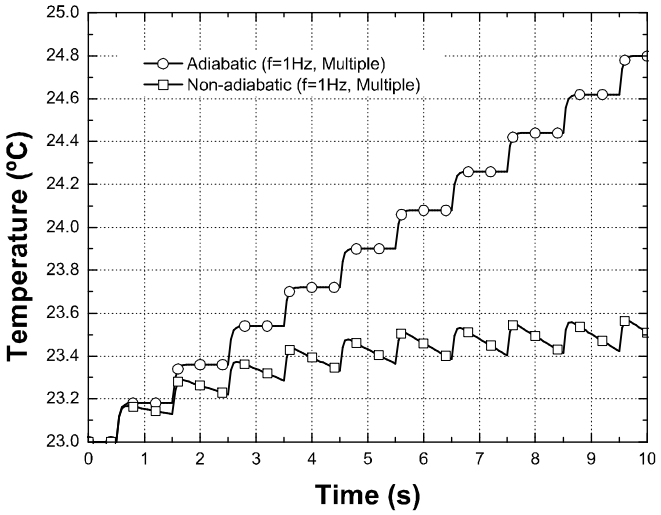


Figure 4.77: Material temperature plotted against simulation time for 10 loading-unloading cycles, considering $f = 1Hz$ *(models 1 and 2).*

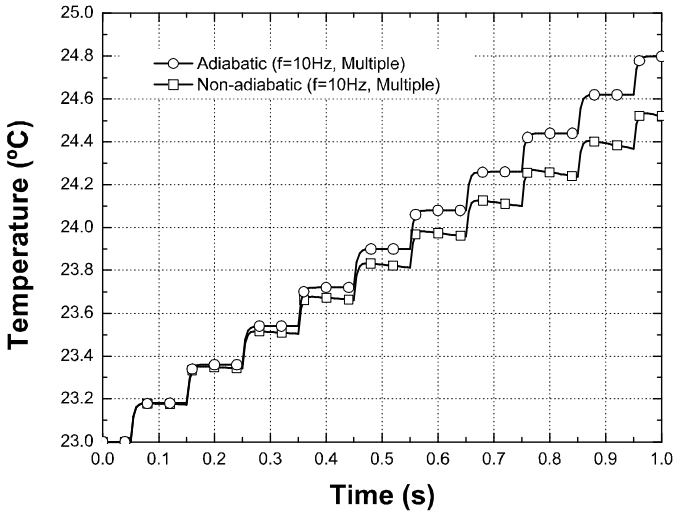


Figure 4.78: Material temperature plotted against simulation time for 10 loading-unloading cycles, considering $f = 10Hz$ *(models 4 and 5).*

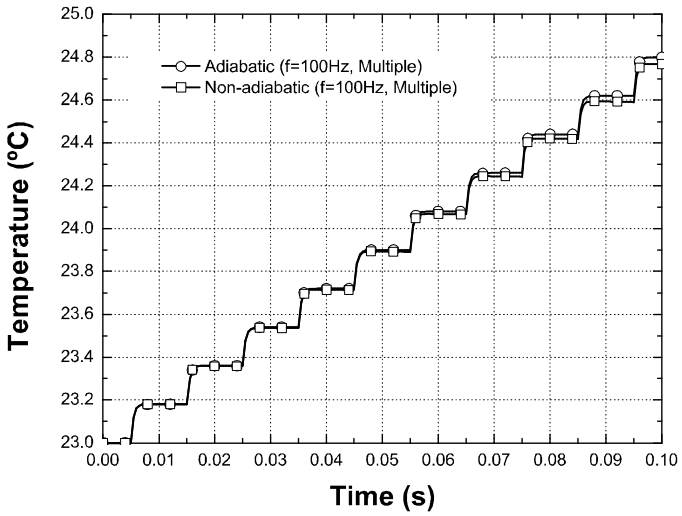


Figure 4.79: Material temperature plotted against simulation time for 10 loading-unloading cycles, considering $f = 100Hz$ *(models 8 and 9).*

Considering the FEA results obtained from models 2, 7 and 11 (see table 4.20) we can compare the final temperature obtained for the same time scale ($t = 10s$), considering different loading frequencies. The obtained results are expressed in figure 4.80.

The final temperature is maximum for $f = 100Hz$ as result of the highest number of loading-unloading cycles (1000 cycles) obtained with that loading frequency. The increase in the number of cycles directly affects the amount of dissipated energy as ϕ_{total} is calculated for each loading-unloading cycle.

The effect of the loading type in the heat generation is obtained by comparing the results obtained for FE simulations 2 and 3 (see table 4.20) considering for this study a non-adiabatic thermal condition. It is observable from figure 4.81 that the definitions of a nested cycle load scenario have influence in the final material temperature achieved. The final temperature is lower for the nested cycle loading when compared with the temperature obtained with a multiple loading-unloading case. This behaviour is due to the fact that the strain energy absorbed by the material during the defined 6 internal cycles ($\epsilon = 0.45$ and $\epsilon = 0.35$) is less than the strain energy absorbed by the loading-unloading cycles defined up to $\epsilon = 0.57$. This behaviour have a direct influence in the dissipated energy generated for each hysteretic cycle and consequently on the heat generation.

For loading frequencies $f = 10Hz$ and $f = 100Hz$ the thermal behaviour is similar for that obtained for $f = 1Hz$ with a decrease in the final temperature when nested cycles are imposed to the material. These results are expressed in figures 4.82 and 4.83.

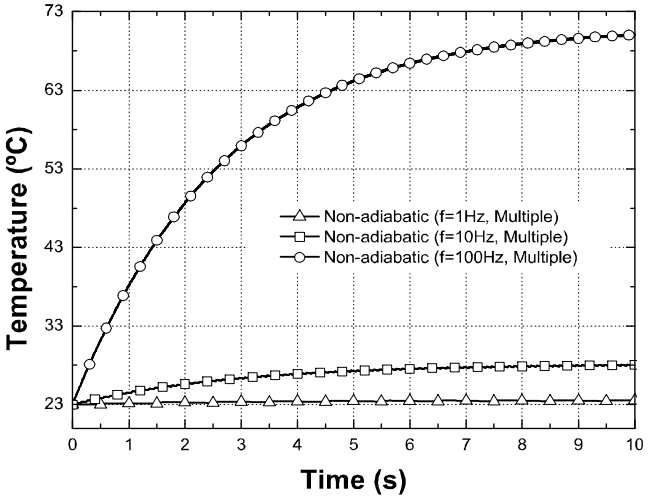


Figure 4.80: Temperature plotted against simulation time considering multiple loading-unloading cycles, for $f = 1Hz$, $f = 10Hz$ and $f = 100Hz$ *(models 2, 7 and 11).*

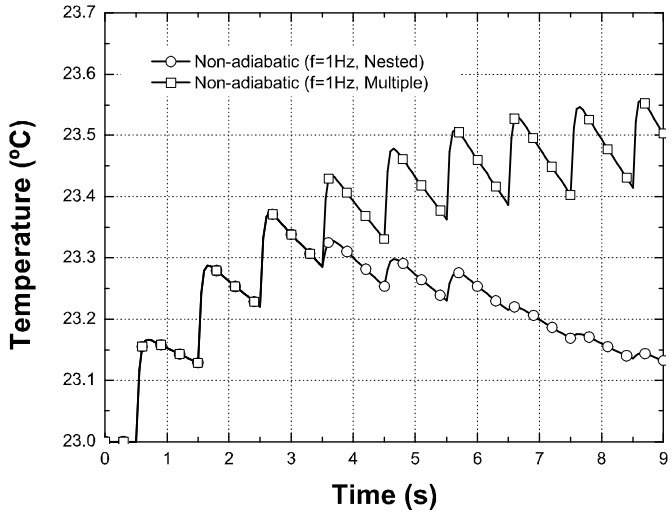


Figure 4.81: Temperature plotted against simulation time considering multiple and nested loading-unloading cycles, for $f = 1Hz$ *(models 2 and 3).*

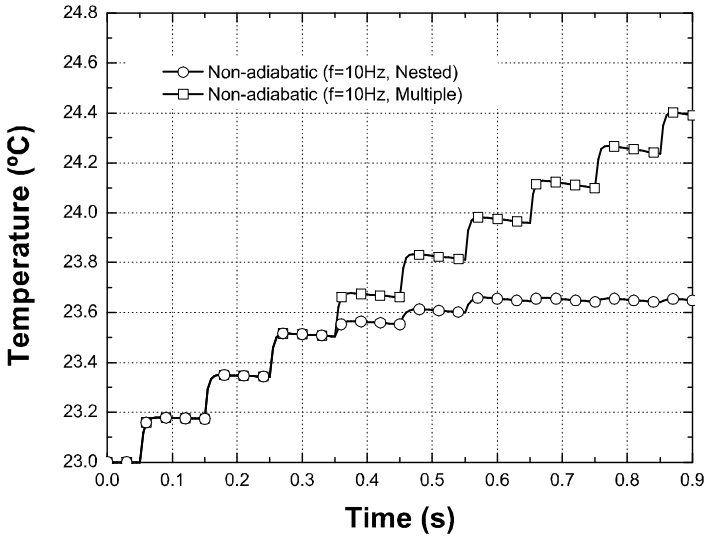


Figure 4.82: Temperature plotted against simulation time considering multiple and nested loading-unloading cycles, for $f = 10Hz$ *(models 5 and 6).*

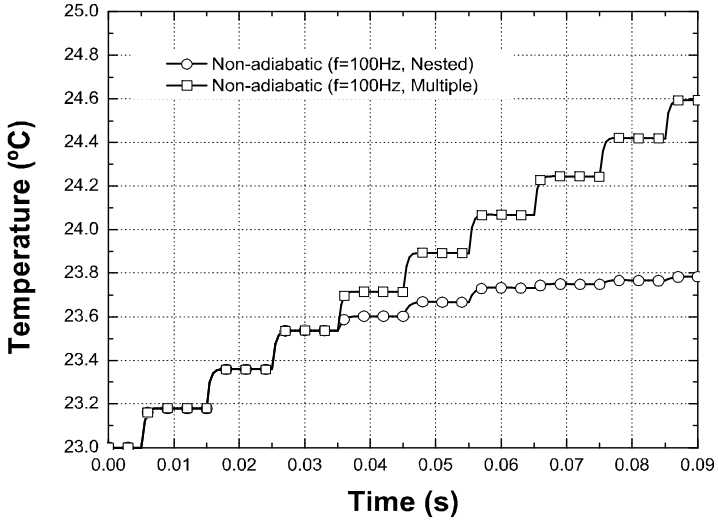


Figure 4.83: Temperature plotted against simulation time considering multiple and nested loading-unloading cycles, for $f = 100Hz$ *(models 9 and 10).*

A modification to the user subroutine expressed in algorithm 5 was done, in order to change (with temperature) the deviatoric material properties C_{ij}, during the loading-unloading cycles.

Algorithm 5 Pseudo-code for interpolation of material parameters

INPUT $C_{ij}(23^0C)\{$*Material parameters for* $T = 23^0C\}$
INPUT $C_{ij}(100^0C)\{$*Material parameters for* $T = 100^0C\}$
INPUT T_0 and T_1 $\{$*Temperature range for interpolation*$\}$
MONITOR *Temperature* $\{$*Monitor current temperature at the element*$\}$
COMPUTE $C_{ij} = C_{ij}(23^0C) + (Temperature - T_0)\frac{[C_{ij}(100^0C) - C_{ij}(23^0C)]}{(T_1 - T_0)}$

During the analysis the temperature is monitored at each element integration point and a linear interpolative scheme was defined for computing new material parameters based on the material parameters expressed for $T = 23^oC$ and $T = 100^oC$ in tables 4.5 and 4.6, respectively.

Considering, for example, a multiple loading-unloading case with $f = 10Hz$ and $t = 10s$, we monitored the evolution of the nominal stress-nominal strain curves as expressed in figure 4.84, where it is visible a *"softening"* in the stress-curves considering the first and the last loading-unloading cycle.

The stress *"softening"* have also effect in the heat generation of the material as seen in figure 4.85. The softening induced by the heat build-up, originate a decrease in the strain energy absorbed by the material for the same level of deformation. This effect have a direct influence on the amount of dissipated energy per deformation cycle and consequently on the material temperature that is lower for the case where thermal affection of material parameters was considered.

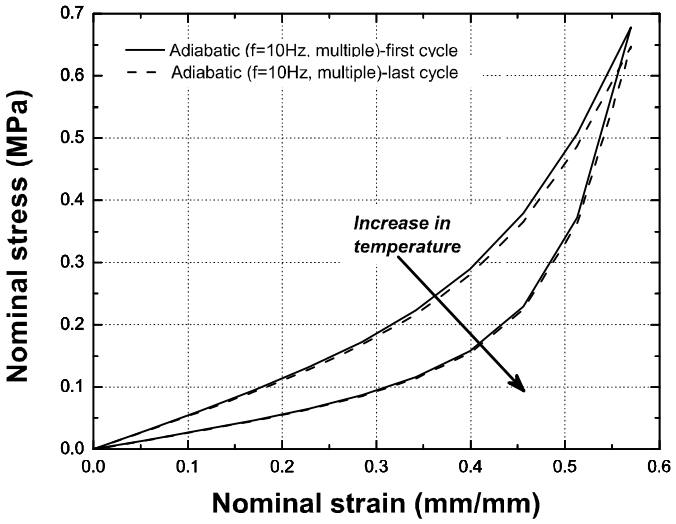


Figure 4.84: Nominal stress plotted against nominal strain for multiple cycles ($f = 10Hz$), considering the effect of temperature on the material parameters C_{ij}.

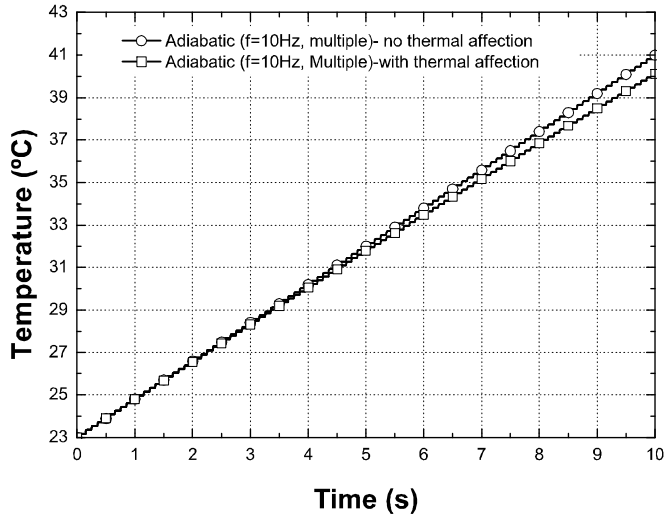


Figure 4.85: Temperature plotted against time for multiple loading-unloading cycles ($f = 10Hz$), considering thermal and no thermal effect on the material parameters C_{ij}.

Chapter 5

Applications/Examples

In this chapter are discussed two case-studies where the CPGC was used as the basis material. The first case-study is described in section 5.1 and corresponds to comfort evaluation of CPGC *shoe insoles* using for that procedure an anatomically detailed *FE model of the human foot* [Antunes *et al.*, 2008c]. In that section, the modelling methodology applied in the definition of the foot model geometry, loads, boundary conditions, interactions and material constitutive modelling are discussed in detail.

The second practical example is discussed in section 5.2 and implied the use of the subroutines developed during this work that model *hysteretic cycles* and *heat generation* when cyclic loads are applied to the CPGC material. For this practical example, a structure similar to the structures used to quantify the dissipative behaviour of rubber materials was defined.

5.1 Comfort evaluation of CPGC shoe insoles (FE model of the foot)

In this section is described the methodology applied in the definition of a nonlinear three-dimensional foot FE model to serve as a tool for foot orthotic (shoe insoles) design optimization through the monitoring of *plantar contact pressure* distribution during a *balanced standing* loading case.

For studying the dependence on the contact pressure generated at the foot plantar area with the changes in the contact stiffness at the insole/foot interface, simple CPGC's flat insoles were geometrically defined and implemented in the FE model. This study allowed the quantification of variations in contact pressure and contact area for different CPGC formulations and insole thicknesses.

5.1.1 Background

Detailed anatomical virtual models are of increasing importance in the process of designing new products with interaction with the human body. The combination of growing computer power with new modelling tools makes possible the development of Computer Aided Engineering (CAE) methodologies for geometrical or material formulation *optimization of orthotic devices*.

Orthotic devices like CPGC shoe insoles can act as contact pressure reducers and minimize the effects associated with high values of contact pressure (normal stress) at the foot plantar area, such as *pain, callus* or even *ulceration* in diabetic patients [Raspovic *et al.*, 2000]. Specially designed orthotic devices are often used to reduce the plantar contact pressure values through the increase in the contact area, namely, for diabetic patients. Several articles [Tsung *et al.*, 2004; Lord & Hosein, 1994; Birke *et al.*, 1999] studied the influence of insole material properties and insole geometrical design in the redistribution of plantar contact pressures.

Common approaches to reduce the plantar pressure, namely, in diabetic patients, can include prescription of running shoes [Perry *et al.*, 1995] or prescription of custom made orthopedic shoes [Janninck *et al.*, 2005]. Normally, the design of custom insoles is based on empirical basis and therefore, dependent on the individual experiences of podologists or orthopedic shoe technicians.

The well established pressure measuring technique using in-shoe podological pressure measuring equipment can be used as a tool for the optimization of shoe insoles. However, this approach can be very time-consuming; since it depends on numerous trials to obtain statistical representative values and on the manufacturing of insoles for the tests.

Another approach to the optimization of shoe insoles and other anatomic interacting devices is the virtual analysis of geometrically representative anatomic structures. In fact, several authors have used the finite element method for determining the load distribution at the foot plantar area and stress/strains at the bone structure. Certain simplifications are normally considered in these models. They arise normally from the geometrical simplification of the foot structure, namely, the ligamentar and muscular structure, material properties and limited or absent cartilaginous relative movement. In this works, Gefen [2003], Lemmon *et al.* [1997] and Erdemir *et al.* [2005], considered a 2D foot model defined by planar cross-sectional geometries. The foot three-dimensional geometry was considered in the works by Cheung *et al.* [2005], Chen *et al.* [2001] and Gefen *et al.* [2000]. FE models can be a very valuable tool for studying systems that interact with the human anatomy in particular with the foot, in this case shoe insoles design is clearly a practical application of finite element analysis. Within this framework Cheung & Zhang [2006, 2005] and Hsu *et al.* [2008], studied the insole influence in the redistribution of plantar contact pressure

using a three-dimensional foot FE model.

Based on the work results from Lemmon *et al.* [1997] is possible to conclude that soft tissues are characterized by a nonlinear elastic behaviour which must be accounted in the definition of the finite element model, although some models consider a linear-elastic behaviour for the soft tissues [Shanti & Mothiram, 1999; Chen *et al.*, 2001] this approach normally imply a relatively stiff behaviour for the soft tissues [Cheung *et al.*, 2005].

5.1.2 3D modelling methodology

The complex mechanical behaviour of the foot and the necessity of obtaining accurate results for retrospective validation with experimental values implies an adequate modelling of the foot structure in terms of 3D anthropometric characteristics and material constitutive modelling. The initial stage concerning the foot anthropometrical definition was a *CT scan* of the foot region of a 26 year old male in a Phillips® Brilliance CT equipment. The *DICOM* images generated in the CT scan were then processed with a medical imaging and editing software (MIMICS® 9.1) that was used to obtain the primary 3D models using *density segmentation techniques*. The primary 3D models were then exported as geometrical files for a CAD system (CATIA®) that allowed the assembly and some 3D geometrical operations. Finally, the CAD model was exported to a nonlinear FEA package (ABAQUS® Version 6.6) where the foot model was prepared for the nonlinear finite element analysis, namely through the definitions of loads, boundary conditions, material constitutive models, kinematic constraints and mesh discretization processes. The modelling methodology applied in the definition of the foot model is summarized in figure 5.1.

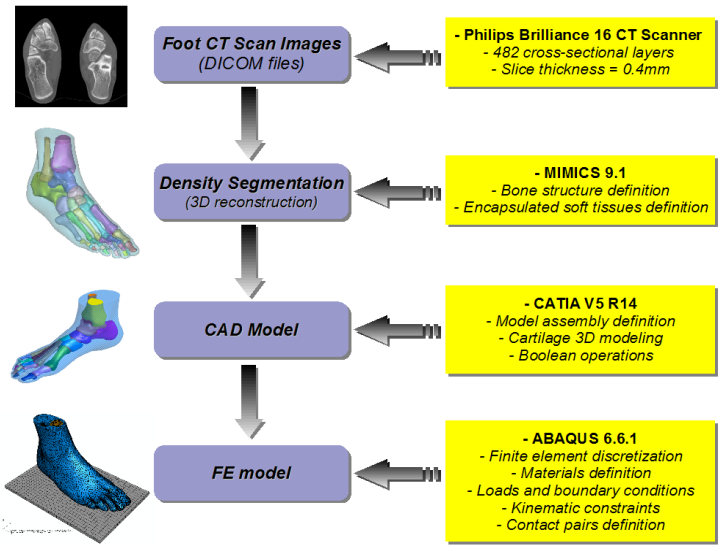
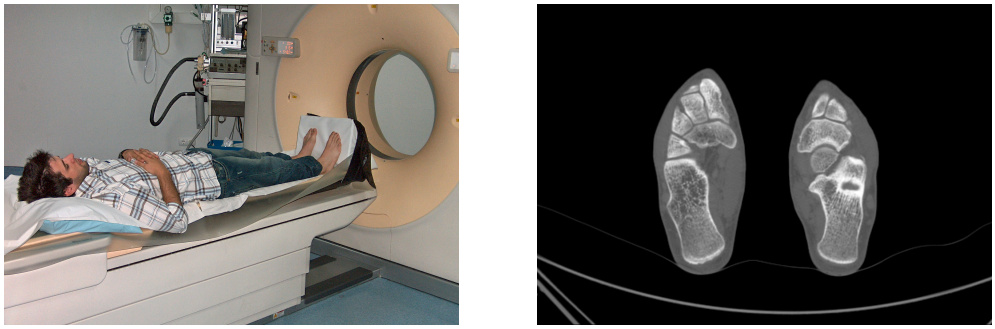


Figure 5.1: Modelling methodology applied in the FE model definition.

5.1.2.1 Medical image data generation

A CT scan was performed in a 26 year old male weighing $75kg$, in a Phillips® Brilliance 16 CT equipment, as show in figure 5.2(a). The scan was realized for both foot at the *neutral posture* in which there is the least tension or pressure on tendons, muscles and bones and was defined by 482 cross-sectional cuts with a slice distance of $0.4mm$ and a field of view (FOV) of $346mm$. The medical images (figure 5.2(b)) were exported from the CT equipment in the *DICOM* format with an image area of 1024x1024 pixels. The high image resolution associated with the reduced distance between slices assures a good geometrical definition of the primary 3D models in future density segmentation operations.



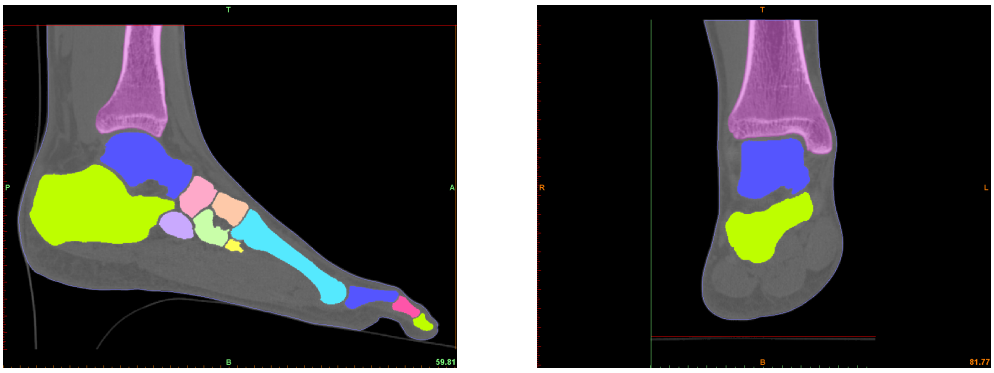
(a) (b)

Figure 5.2: Medical image data aquisition detailing a) the CT scan equipment and b) a CT scan medical image.

5.1.2.2 Density segmentation operations

For the reconstruction of the primary 3D anthropometrical models (bone structure and encapsulated soft tissues volume) was used the MIMICS® 9.1 medical imaging density segmentation software. The DICOM image files are constituted by pixels with different gray intensities corresponding to different material densities presented at the anatomic foot structure, namely, soft tissues, bone and cartilage. Notice that in a CT scan it is also possible to distinguish tendon and ligamentar structure, but for the present case these structures were not accounted in the density segmentation operations. The separated 3D reconstruction of each bone segment was accomplished with manual editing operations of the density masks, which allowed the construction of *separated masks* for each foot bone as seen in figure 5.3

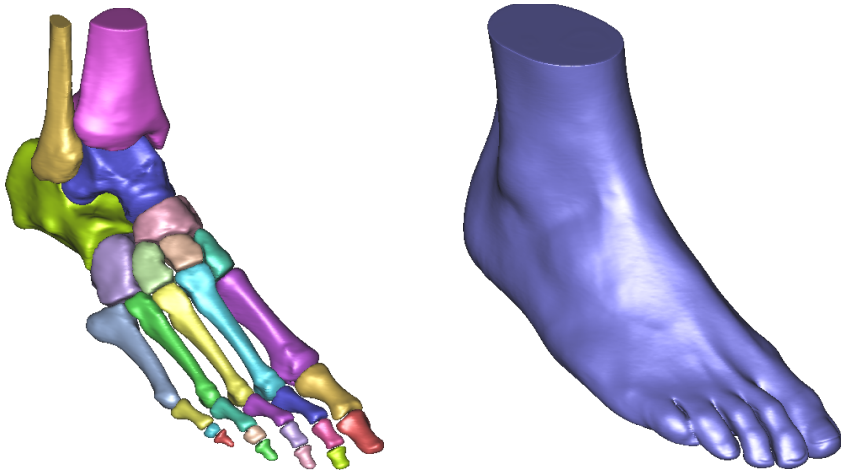
The reconstruction of the encapsulated soft tissues was easier due to the high difference of densities between the soft tissues and the surrounding air. Thresholding based on *Hounsfield Units (HU)* was used to separate each bone from the bone structure and also in the definition of the encapsulated soft tissues volume. In order to include all the *cortical*



(a) (b)

Figure 5.3: Density segmentation masks detailing a) sagittal view and b) coronal view.

and *trabecular* bone at the bone structure and exclude the *cartilaginous structure*, a lower limit of $250HU$ and an upper limit of $2000HU$ were defined [MIMICS®, 2005]. The soft tissues volume was generated accounting a lower limit of $-200HU$ and an upper limit of $3071HU$. The 3D reconstruction is based on 3D interpolation techniques that transform the 2D images (cross-sectional images) into 3D models. Each model was exported to a *.STL file allowing future CAD operations. Figures 5.4(a) and 5.4(b) show the bone structure and soft tissues primary models, respectively, as the final result of the density segmentation operations. Figure 5.5 show the final density segmentation assembly model incorporating both the bone structure and the encapsulated soft tissues volume.



(a) (b)

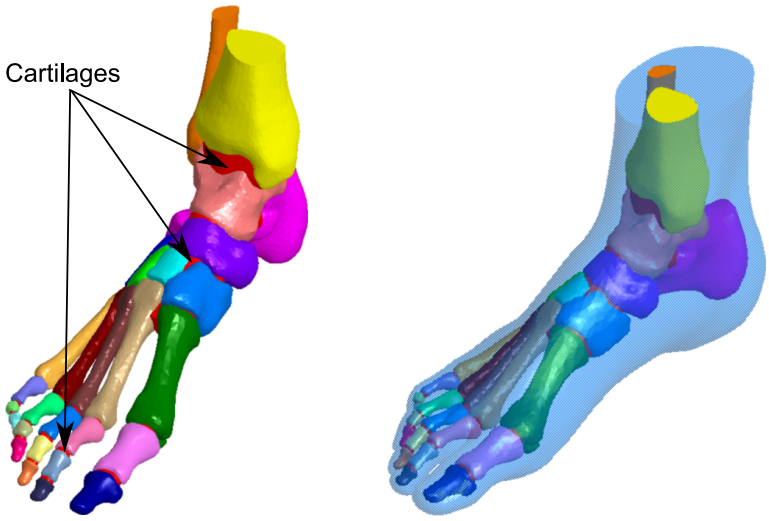
Figure 5.4: Density segmentation 3D models considering a) the bone structure and b) the soft tissues volume.



Figure 5.5: Density segmentation model incorporating both bone structure and soft tissues volume.

5.1.2.3 3D CAD modelling

The *.STL files generated in MIMICS® software were imported into CATIA® CAD package. All the parts imported were assembled together. The cartilages that were not reconstructed in the segmentation process were modelled in order to connect the bones and fill the cartilaginous space as visible in figure 5.6(a).



(a) (b)

Figure 5.6: Final CAD models detailing a) bone and cartilaginous structure and b) encapsulated soft tissues volume, bone and cartilaginous structure.

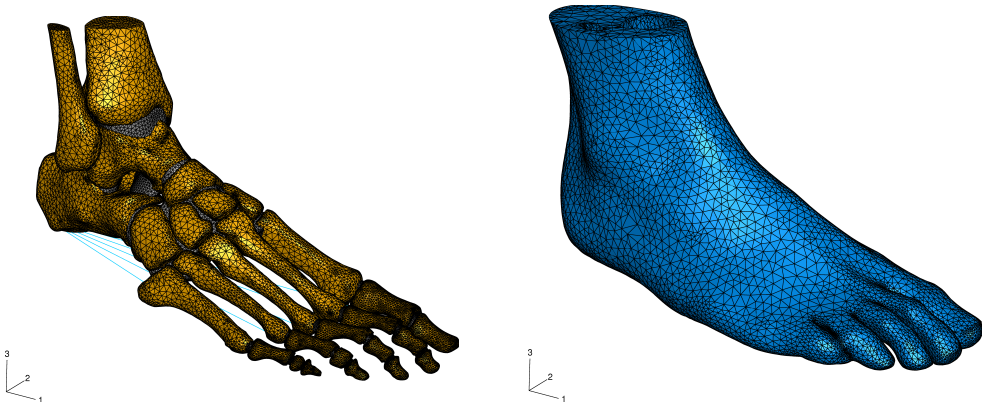
After the cartilage modelling process, volume *boolean operations* were performed to achieve a volume of soft tissues that corresponds to the subtraction of the bone structure coupled with the cartilages. As final result of the CAD operations, the foot bone structure

coupled with the modelled cartilages was assembled together with the boolean generated encapsulated soft tissues as shown in figure 5.6(b).

5.1.3 Nonlinear FE foot model definition

5.1.3.1 Geometrical definition

The FE bone structure model of the right foot consisted of 28 bone parts, that includes all the *distal, medial and proximal phalanges, cuneiforms, talus, calcaneus, cuboid, navicular, distal tibia and fibula* bones. *Tetrahedral elements* that are more versatile to capture the irregularly shapes of the bone structure and the encapsulated soft tissues volume, were used to mesh the model. Bone and cartilaginous structure were *bonded* together forming a unique structure (figure 5.7(a)) that was *tied* to the encapsulated soft tissues volumetric mesh (figure 5.7(b)) through the definition of *mesh tie kinematic constraints*.

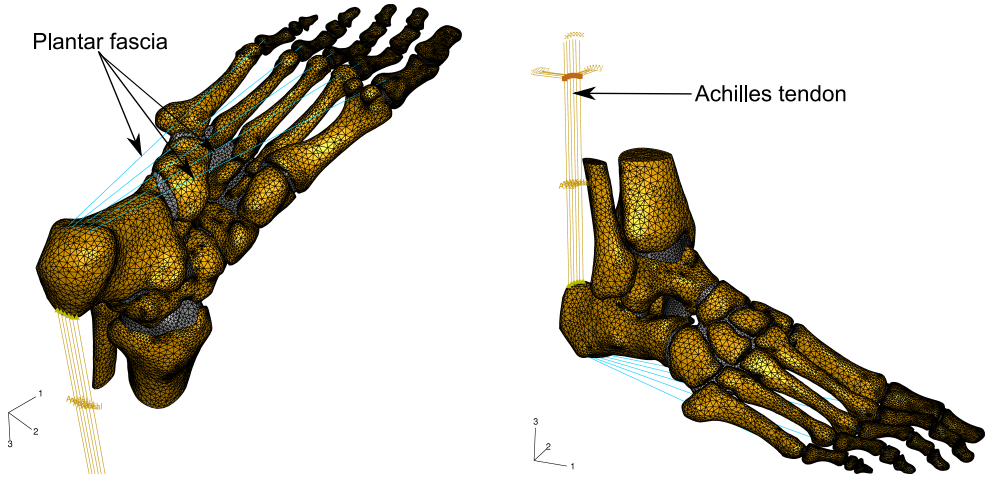


(a) (b)

Figure 5.7: Mesh discretization of the foot geometry with a) corresponding to the volumetric meshes of bone and cartilaginous structure and b) to the encapsulated soft tissues.

The *plantar fascia* (figure 5.8(a)) and *Achilles tendon* (figure 5.8(b)) were geometrically simplified and included in the FE model by *truss* and *axial connector* elements, respectively. The plantar fascia is one of the major stabilization structures of the longitudinal arch of the human foot and sustains high tensions during the weight application [Gefen, 2002]. The definition of the Achilles tendon allowed the simulation of the load applied in the calcaneus during balanced standing.

The *foot/ground interface* was defined through contact surfaces, which allowed the load transmission between ground and foot model. A *small-sliding tracking* approach associated with a *surface to surface contact formulation* was defined to model the interaction tangential behaviour. A static friction coefficient was set to 0.6, using the *Coulomb*



(a) (b)

Figure 5.8: FE modelling procedures detailing a) plantar fascia modelling through the definition of truss elements and b) modelling of Achilles tendon incorporating axial connector elements.

friction model [Zhang & Mak, 1999]. An *augmented Lagrange* constraint enforcement method was implemented in the definition of the interaction normal behaviour.

5.1.3.2 Loads and boundary conditions

A vertical force corresponding to half of the body weight was applied at the ground reference point and Achilles tendon load was applied at the end of the axial elements for simulating the balanced standing loading case as show in figure 5.9.

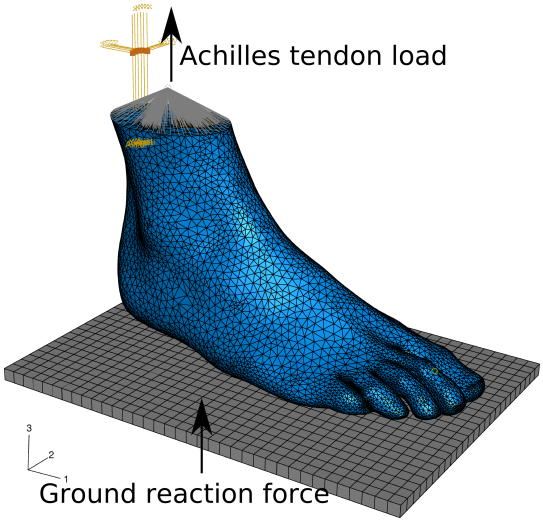


Figure 5.9: Balanced standing loading case scheme.

Load at the *posterior-superior aspect of the calcaneus* is generated by involuntary contraction of the *triceps surae* muscle group in order to stabilize the foot during standing [Gefen, 2002]. The value of the Achilles tendon force is not easy to be experimentally measured and for that reason, some analytical assumptions concerning the Achilles tendon load are made in the bibliography, which estimates the load to be ranging between one half to two thirds the weight applied on the foot. The study of Simkin [1982] arrives to a force on the Achilles tendon of approximately 50% of the body load during standing. This model was considered for some computational analysis in the literature [Cheung *et al.*, 2005; Gefen, 2003], although Cheung *et al.* [2006] concluded that an Achilles force of 75% of the total weight provides a closer match to the experimentally measured centre of pressure.

A magnitude of $187.5N$ was calculated for the Achilles tendon force, following the model of Simkin [1982], for a vertical reaction force equal to $375N$. The upper surfaces of the soft tissues, tibia and fibula were fixed via *kinematic constraints*, while the boundary conditions applied at the ground reference point restrained horizontal movements of the ground.

5.1.3.3 Material properties

The materials at the foot model were considered *isotropic* and *linear-elastic* except the soft tissues that are mechanically characterized by an isotropic *nonlinear elastic behaviour*. The bone material behaviour was linearly defined with a Young's Modulus and Poisson's ratio, equal to $7300MPa$ and 0.3, respectively. These values were obtained by weighing cortical and trabecular bone elasticity according to Nakamura *et al.* [1981] and Gefen *et al.* [2000]. The mechanical properties of the cartilage [Shanti & Mothiram, 1999; Gefen, 2003] and plantar fascia [Cheung *et al.*, 2005], were selected from the literature.

Specifically, the soft tissues nonlinear elastic behaviour definition was based on the uniaxial nominal stress-nominal strain data obtained from *in vivo* tests of the heel pad obtained from the work of Lemmon *et al.* [1997], expressed in figure 5.10.

This mechanical approach can model more accurately the soft tissues mechanical behaviour in areas where the soft tissues deformation is higher and therefore, not ruled by a linear mechanical behaviour. Although some authors [Shanti & Mothiram, 1999; Chen *et al.*, 2001] consider the soft tissues as a linear elastic material, the nonlinear mechanical approach can model more accurately the foot mechanical behaviour, especially at the foot plantar area. The soft tissues mechanical behaviour was defined through a second order polynomial strain energy function according to Lemmon *et al.* [1997] and Cheung *et al.* [2005].

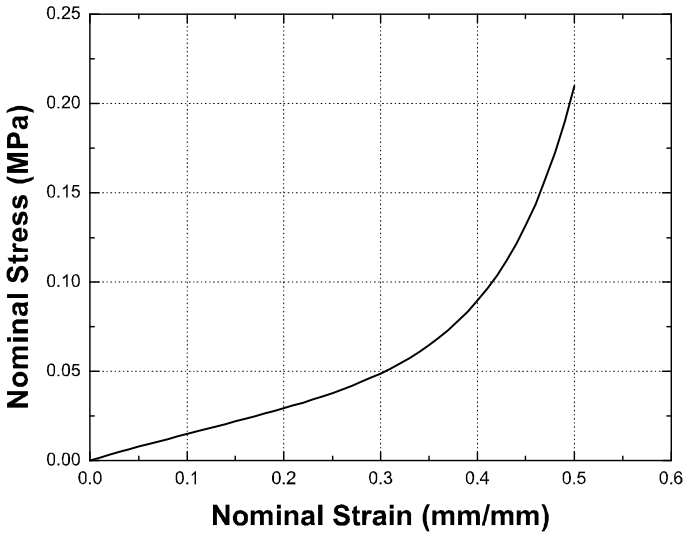


Figure 5.10: Soft tissues nonlinear mechanical behaviour obtained from *in vivo* experimental tests of the heel pad in: Lemmon *et al.* [1997].

In table 5.1 are summarized the material properties and element's topology and *formulation* used in the definition of the FE foot model.

Table 5.1: Material properties and element topology/formulation.

Components	El. topology	El. formulation	Young's Modulus (MPa)	υ	Cross-sectional area (mm^2)
Bone structure	3D-Tetrahedra	Linear	7300	0.3	-
Cartilage	3D-Tetrahedra	Linear	10	0.4	-
Soft tissues	3D-Tetrahedra	Linear, Hybrid	Hyperelastic	-	-
Achilles tendon	1D-Connector	Linear	∞	-	-
Plantar Fascia	1D-Truss	Linear	350	-	58.6
Ground	Quadrilateral	Rigid	∞	-	-

Material parameters used for the calibration of the second order hyperelastic model associated with the mechanical behaviour of the soft tissues, are presented in table 5.2. Units are MPa and MPa^{-1} for C_{ij} and D_i material parameters, respectively.

Table 5.2: Material parameters of the hyperelastic model used for the soft tissues [Cheung *et al.*, 2005].

C_{10}	C_{01}	C_{20}	C_{11}	C_{02}	D_1	D_2
0.08556	-0.05841	0.03900	-0.02319	0.00851	3.65273	0

5.1.4 FEA results

The FE model predicts a maximum plantar contact pressure equal to $0.111MPa$ ($11.1Ncm^{-2}$) for the present loading case, at the heel region as seen in figure 5.11.

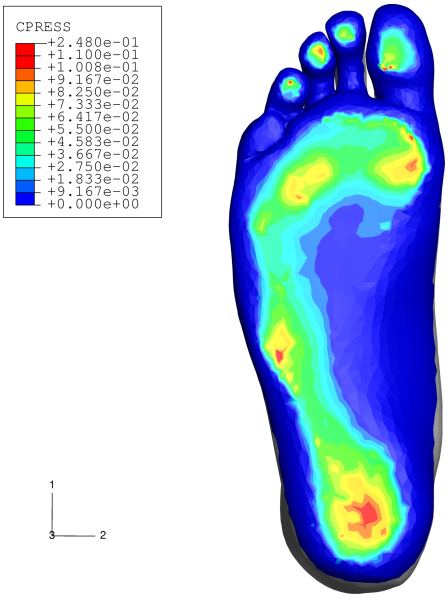
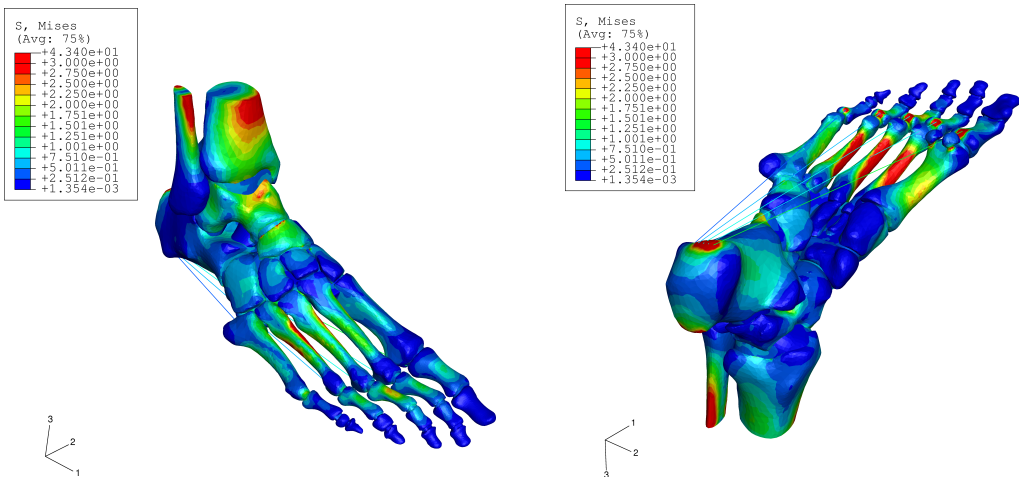


Figure 5.11: Foot plantar contact pressure values (MPa) obtained through FE analysis.

Figure 5.12(a) show that at the bone structure, peak of stress are present at the metatarsal and talus bones. Maximum levels of stress are also predicted for the tibia and fibula bones due to the nodal displacement restrictions imposed (local increase of geometrical stiffness). The insertion points of the plantar fascia truss elements at the plantar region of the metatarsophalangeal articulations and calcaneus bone tuberosity, experienced large stress as seen in figure 5.12(b), due to the generated fascia plantar tension. In table 5.3 are presented indicative nodal contact pressure values beneath the metatarsal heads and heel regions. The FE predicted centre of pressure for the balanced standing model was approximately located under the 2^{nd} cuneiform bone.



(a) (b)

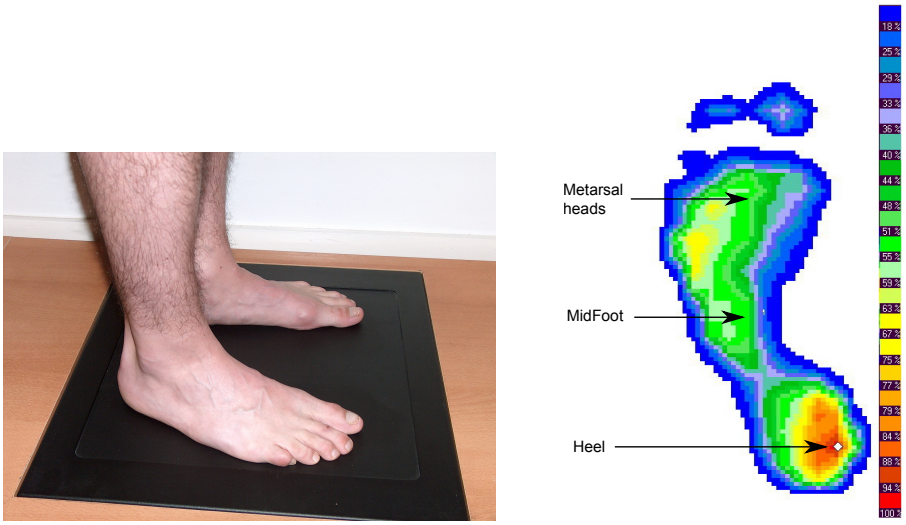
Figure 5.12: von Mises stress criteria at the bone structure detailing a) upper view and b) posterior view.

Table 5.3: FEA nodal contact pressure values (MPa) beneath metatarsal heads and calcaneus bones.

1^{st} metatarsal	2^{nd} metatarsal	3^{th} metatarsal	4^{th} metatarsal	5^{th} metatarsal	Calcaneus (heel)
0.083	0.051	0.084	0.083	0.041	0.111

5.1.5 Experimental validation

For a quantitative evaluation of the contact pressure generated at the plantar area, the same individual that volunteered for the CT scan was used to experimentally evaluate the plantar pressure distribution. A *podologic pressure measuring equipment* from Eclipse 2000® was used for the experimental analysis as seen in figure 5.13(a). A *barefoot* balanced standing posturologic test was conducted during $10s$ where the contact pressure values were evaluated 200 times in that time range. This procedure was repeated 5 times in order to improve the results accuracy and reproducibility. During the test, the individual focused a point in space and kept its arms next to the body in order to achieve a more *static posture*. Figure 5.13(b) show the experimental contact pressure values for the right foot balanced standing situation.



(a) (b)

Figure 5.13: Experimental measuring of foot plantar contact pressure values detailing a) the podologic pressure measuring equipment and b) the experimentally obtained foot plantar contact pressure values.

An experimental contact pressure peak of about $0.071MPa$ ($7.1Ncm^{-2}$) was measured at the heel region. The FE model (figure 5.11) predicted a maximum value for the same area but greater and equal to $0.111MPa$ ($11.1Ncm^{-2}$). In a midfoot indicative point as displayed in figure 5.13(b), the experimental contact pressure is approximately equal to $0.038MPa$ ($3.8Ncm^{-2}$), while the correspondent FEA predicted contact pressure for approximately the same point is equal to $0.049MPa$ ($4.9Ncm^{-2}$). Beneath the metatarsal heads, experimental contact pressure values of about 0.033, 0.039, 0.045, 0.387 and $0.045MPa$ from the 1^{st} to 5^{th} metatarsal head were measured, while the correspondent FEA nodal contact pressure values were about the following ranges: $[0.103, 0.053]$, $[0.051, 0.041]$, $[0.088, 0.051]$, $[0.098, 0.039]$ and $[0.067, 0.041]MPa$, for approximately the same foot regions. Notice that the FEA values are taken in a min/max form due to the difficulty in obtaining a single contact pressure value for those zones. The FEA predicted contact area was approximately equal to $89cm^2$, compared to $138cm^2$ obtained from the experimental measurements.

5.1.6 Contact stiffness dependence

In order to study the foot plantar contact pressure and contact area dependence with changes in the contact stiffness, a FE model with incorporation of flat insoles at the plantar/ground interface was prepared as shown in figure 5.14. Three CPGC (Cork-Polyurethane Gel Composite) formulations, produced by *ACC-Amorim Cork Composites*

and three different insole thicknesses (4, 8 and 12mm)were used for evaluation.

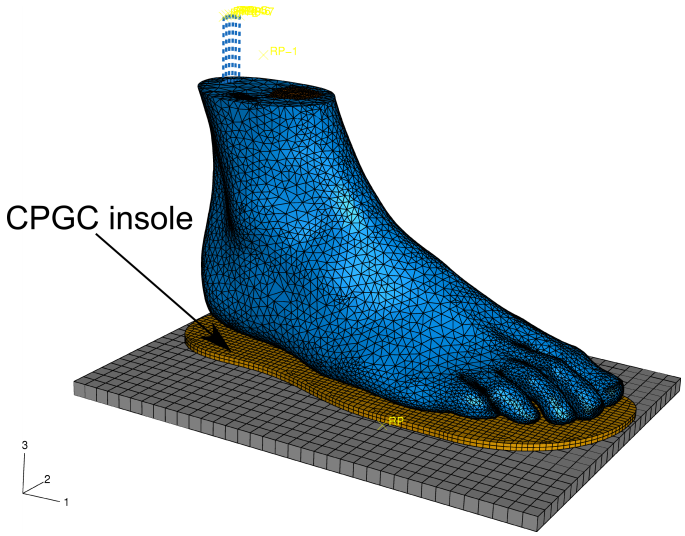


Figure 5.14: Foot FE model with incorporation of a CPGC flat insole.

5.1.6.1 Material properties

The mechanical behaviour of CPGC formulations was evaluated by uniaxial compression (unconfined deformation) considering three different temperatures (23^oC, 100^oC and -10^oC) and four different cork incorporations ($G-0php$, $A-25php$, $B-50php$ and $F-100php$) and by volumetric tests that were conducted at 23^oC for three formulations ($A-25php$, $B-50php$ and $C-75php$). The followed experimental methodology and experimental results can be seen in more detail in section 4.1.

The nonlinear elastic behaviour of the CPGC material was modelled by a hyperelastic constitutive model based on a second order polynomial strain energy function as already discussed in section 4.2.1.

For the present work, three formulations ($B-50php$, $G-12.5php$ and $H-90php$) were evaluated. The mechanical behaviour of formulations $G-12.5php$ and $H-90php$ that were not experimentally evaluated, was predicted based on a *linear interpolation of the material parameters* (see section 4.2.2) obtained for the experimentally evaluated formulations. In table 5.4 are summarized the interpolated material parameters for formulations G and H.

Table 5.4: Interpolated material parameter values (MPa) for non-tested CPGC formulations G and H.

Formulation	C_{10}	C_{01}	C_{20}	C_{11}	C_{02}
G ($12.5php$)	0.1252	-0.0577	-0.0006	0.0193	-0.0054
H ($90php$)	0.5527	-0.2978	-0.1950	0.2711	-0.0715

Although the CPGC material formulations evidence some degree of compressibility it was assumed for the present simulations that the material has an incompressible behaviour. In fact, for applications where the deformation is not highly confined, the modelling of the compressibility degree is normally non crucial. However, for simulation cases where the insole deformation process is highly confined, for instance, inside a shoe, the degree of compressibility must be adequately defined and introduced.

5.1.6.2 FEA results

The maximum values of contact pressure, namely, beneath the first metatarsal head, decrease with the introduction of flat insoles as shown in figure 5.15. The contact area value is maximum for the formulation $G - 12.5php$ (softer formulation) made insole thickness with $12mm$ thickness as seen in figure 5.16, corresponding to a minimum in the contact pressure value.

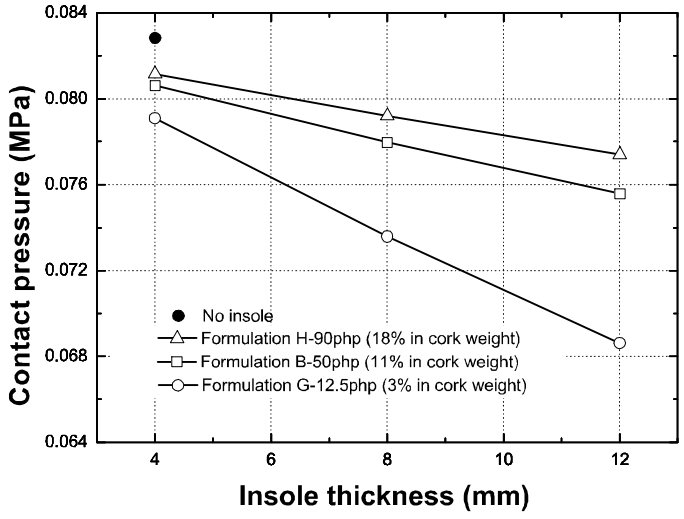


Figure 5.15: Nodal contact pressure values beneath the 1^{st} metatarsal head plotted against insole thickness.

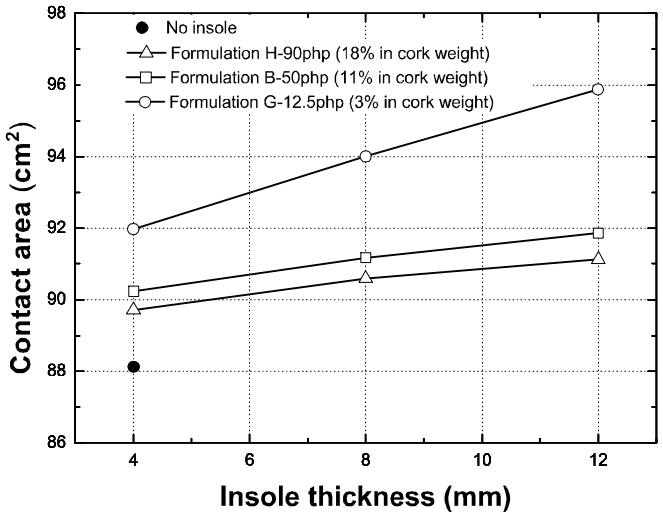


Figure 5.16: Foot plantar contact area plotted against insole thickness.

5.1.7 Results discussion

The experimental plantar pressure distribution is qualitatively comparable with the predicted FEA results, nominally, the peak pressure values zones at the heel region and beneath the metatarsal heads. However in the quantitative point of view, the FEA results are higher than the experimental results. This difference may be caused by the resolution of the pressure sensors that report an average pressure over a sensor area while the FE model reports the contact pressure as calculated from nodal constraints associated with the contact formulation, with an averaging procedure controlled by the analyst. However, in this case, the reference areas associated with the sensors and the typical dimension of the element mesh are significantly different, therefore, is expected that the FEA contact pressure values to be higher than the experimental ones.

The FEA predicted contact area values for balanced standing ($89cm^2$) are proportionally comparable with the results obtained by Cheung *et al.* [2005], who reported a contact area equal to $68cm^2$ for a $1.74m$ and $70kg$ male with normal soft tissues stiffness. The higher contact area values obtained in our experimental results can be due to the contact area acquisition mode and sensors resolution at the podologic pressure measuring equipment.

The FEA results showed that at the heel region and beneath the metatarsal heads the contact pressure values are maximum, which indicate the regions that most probably ignite foot pain and ulcer development. These results are in accordance with the observation

of foot ulcers appearance at the medial forefoot and heel regions of the diabetic patients [Mueller *et al.*, 1994; Raspovic *et al.*, 2000].

The difficulty in obtaining a completely static posture that replicates the FEA model load conditions was a major experimental difficulty encountered and an aspect that must be accounted during the results discussion. In fact, the continuous individual displacement originated by the involuntary muscle contraction during balanced standing, can affect the foot load bearing and consequently the experimental contact pressure distribution.

The change on the contact stiffness through the implementation of flat insoles, alter the values of contact pressure and contact area at the foot plantar region. A decrease in the material stiffness through the reduction in cork weight minimizes the value of contact pressure as a consequence of the increase in the foot plantar contact area. This contact pressure reduction effect is also visible for the same material formulation when the insole thickness increases. This effect is due to a decrease in the geometrical stiffness and a consequent increase in the insole deformability.

In conclusion we can conclude that the FE model capability in predicting the stress state in the foot, namely the contact pressure at the foot plantar area, makes suitable the application of the present FE model in comfort optimization of CPGC shoe insoles or other foot support devices.

5.2 Vibration control

In this case-study the capability of modelling loading-unloading cycles in nonlinear FE analysis through the implementation of *user subroutines* defined in section 4.3.2 is applied in a practical example. For the present case, the capability of modelling in a fully *coupled thermomechanical* form the loading-unloading mechanical response of the CPGC and the consequent heat build-up originated from the dissipated energy is demonstrated.

5.2.1 FE model

The FE model defined for this case study is composed by an aluminium structure that supports steel weights which in turn compress the CPGC samples as seen in figure 5.17. A transient fully coupled thermal-stress finite element procedure was implemented using the nonlinear FEA package ABAQUS® in order to model the thermomechanical behaviour of the CPGC.

With this FE model we intend to verify the thermomechanical response of the material in complete loading-unloading cycles by monitoring the force and the material temperature during the loading-unloading deformation cycles.

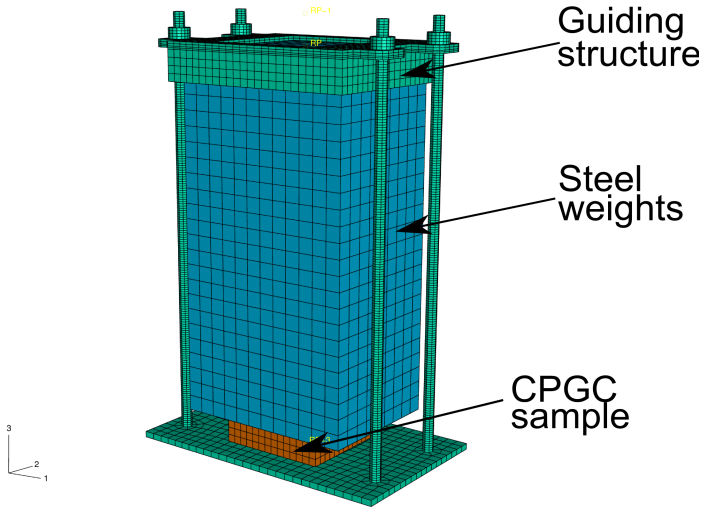


Figure 5.17: FE model assembly with indication of the principal parts.

In order to study the effect of *thermal affection* of material parameters during the loading scenario, two FE models were created considering for one of these models the capability of interpolating new values for the deviatoric material parameters in function of the actual material temperature, as already discussed in more detail in section 4.3.3.2. A loading frequency equal to $100Hz$ for a total loading time of $5s$ was defined for both models.

The general characteristics of the FE models used for this case-study are summarized in table 5.5.

Table 5.5: Thermomechanical characteristics of the FE models.

FE model	$f(Hz)$	Time (s)	Cycles	Thermal conditions	Thermal affection
1	100	5	500	Non-adiabatic	No
2	100	5	500	Non-adiabatic	Yes

5.2.1.1 Material properties

For this case-study was considered the formulation A of the CPGC material whose deviatoric material parameters are summarized in tables 4.5 and 4.6, for $T = 23^oC$ and $T = 100^oC$, respectively. Volumetric material parameters for formulation A are expressed in table 4.18. Thermal material properties used for the definition of the thermal behaviour of formulation A are expressed in table 4.19.

The CPGC sample part in the FE model was descritized by coupled temperature-

displacement 3D continuum linear hybrid elements (C3D8RHT) in a total of 784 hexahedral elements.

Other material properties (thermal and mechanical) and element topology/formulation used in the definition of the FE model, particularly the materials that define the structure are expressed in tables 5.6 and 5.7, respectively.

Table 5.6: Material properties and element topology/formulation.

Components	Material	El. topology	El. formulation	Young's Modulus (GPa)	υ	Density (kgm^{-3})
Structure	Aluminium	Hexahedra	Linear	207	0.35	2700
Weights	Steel	Hexahedra	Linear	70	0.3	7500

Table 5.7: Material thermal properties [Incropera & DeWitt, 1996] used in the definition of the FE model.

Material	Thermal conductivity k_t	Specific heat c_p
Steel	$60.5 Wm^{-1}K^{-1}$	434 $Jkg^{-1}K^{-1}$
Aluminium	$177 Wm^{-1}K^{-1}$	875 $Jkg^{-1}K^{-1}$

5.2.1.2 Loads and boundary conditions

In order to define the complete loading-unloading cycles imposed to the CPGC sample a displacement boundary condition (triangular wave) is imposed at the weights as shown in figure 5.18. The generated reaction force to the imposed displacement is monitored at the basis of the aluminium structure. The basis movement of the aluminium structure basis was constrained in all directions and the weights can only move in the downward direction.

This loading scenario results in the deformation of the CPGC sample as is shown by figure 5.19 where is plotted the nodal displacement values in the axial direction at the moment of maximum vertical displacement.

The material's initial and surroundings temperatures were set equal to 23^oC. Thermal boundary conditions were applied at the external faces of the sample in order to define a non-adiabatic case. Convective phenomena in the sample boundaries was assumed to be free and the convection coefficient equal to $h_{air} = 10 Wm^{-2}K^{-1}$. Thermal emissivity factor was set equal to $\epsilon_{rad} = 0.8$.

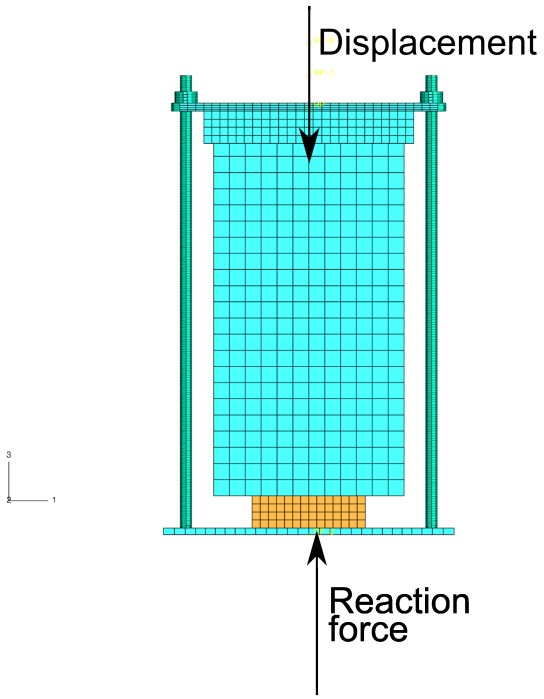


Figure 5.18: Mechanical boundary conditions applied in the definition of the FE model.

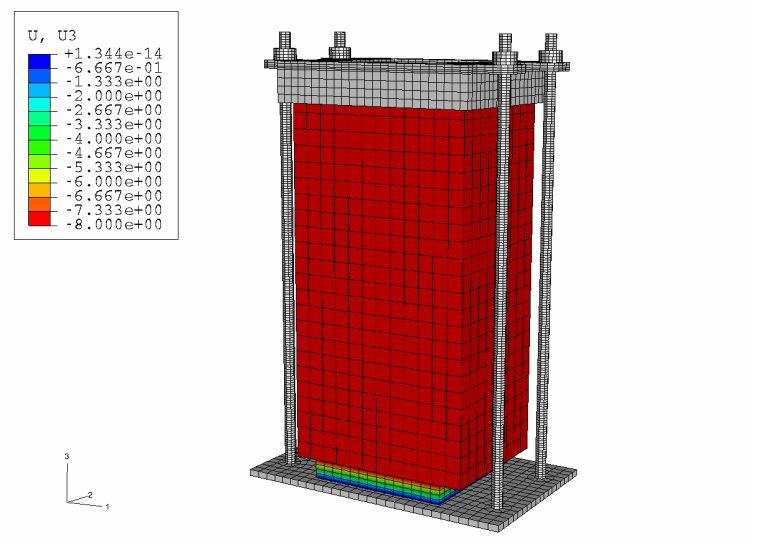


Figure 5.19: Nodal axial displacement FEA values (mm).

5.2.1.3 Mechanical and thermal interactions

The mechanical interaction between the CPGC sample and the weights and aluminium structure the was modeled assuming a *node to surface constraint* enforcement method associated to a *finite sliding tracking formulation*. The *direct constraint enforcement*

method associated to a *hard contact pressure-overclosure* relationship was introduced to define the interaction normal behaviour.

Heat flux between the sample and external structure (guiding structure and weights) was accounted in the FE model by introducing the thermal conductance term in the definition of the thermal contact properties. Thermal conductance in the interfaces was approximated for the present case, based on the work by Marotta *et al.* [2002] and set equal to $h_{con} = 1345.2 W m^{-2} K^{-1}$.

5.2.2 FEA results

In this section are discussed the results obtained for FE models 1 and 2 (see table 5.7) detailing the mechanical and thermal results obtained.

Figure 5.20 show the evolution of the reaction force monitored at the base of the aluminium structure for model 1. It is observable in that figure the hysteretic loop obtained during the applied loading-unloading cycles.

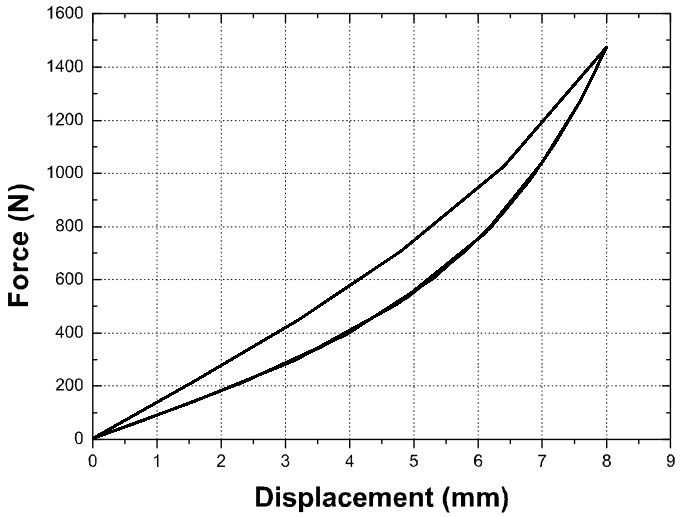
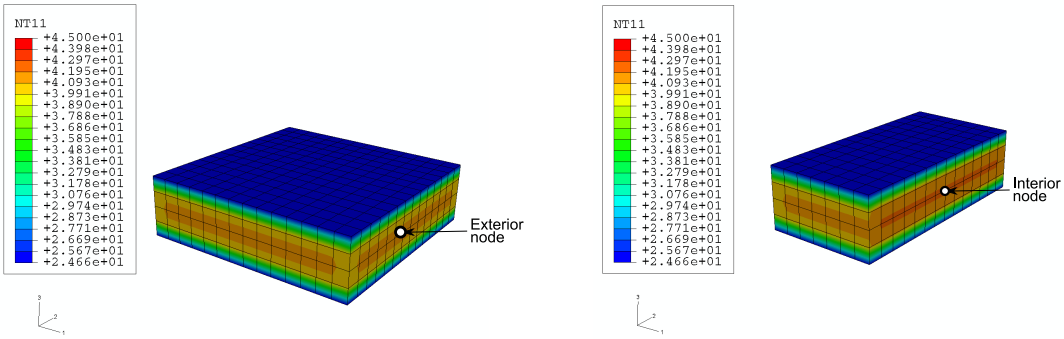


Figure 5.20: Reaction force values obtained for FE model 1 plotted against nodal displacement *(model 1)*.

In figure 5.22 is plotted the material nodal temperature evolution with time for FE model 1 considering one external node and one internal node as indicated in figures 5.21(a) and 5.21(b), respectively. The achieved final temperature at the external node is lower than that obtained for the internal node due to the more pronounced effect of convection and radiation phenomena at the exterior faces of the sample.



(a) (b)

Figure 5.21: Final nodal temperatures obtained in the material sample detailing a) facet temperature and b) internal temperature (cross-section).

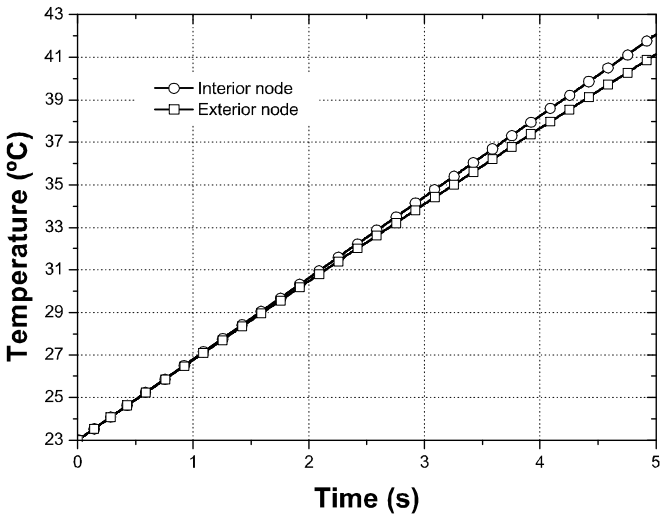


Figure 5.22: Nodal temperature values plotted against loading time *(model 1)*.

Considering the results obtained for the model 2 in which the deviatoric material parameters are affected by the material temperature we can observe in figure 5.23 the softening effect induced by the material heat build-up comparing for this example the reaction forces obtained for the first and the last loading-unloading cycles.

The softening effect induced by the heat build-up have a direct effect on the final temperature achieved. In fact, the reduction in the material stiffness due to the increase in temperature implies a reduction in the strain energy absorbed by the material for the same level of deformation. This effect have direct influence on the dissipated energy

(and consequently on the material temperature) during the unloading cycle, that, for this case, is less then the dissipated energy obtained for the FE model with no thermal affection of material parameters. In figure 5.24 this effect is visible when compared the final temperature obtained for the models with and without material parameters thermal affection, resulting in higher final temperature values for the model with no thermal effect on the material parameters (model 1).

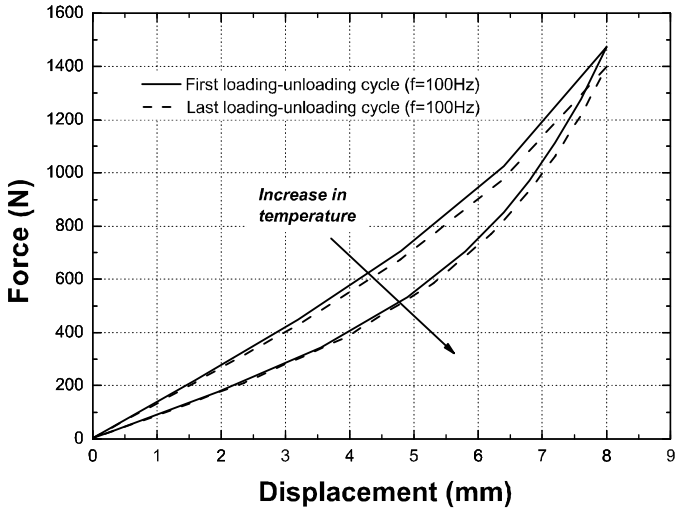


Figure 5.23: Reaction force plotted against displacement considering the first and the last loading-unloading cycle *(model 2)*.

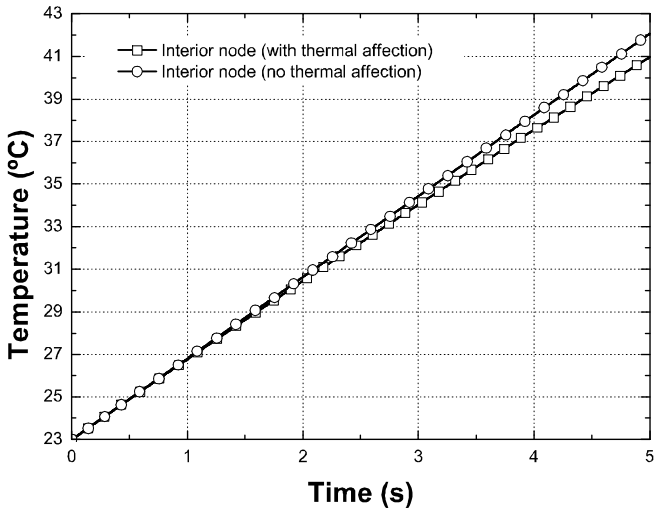


Figure 5.24: Temperature at the internal node plotted against loading time, considering thermal and no thermal effect on the material parameters *(models 1 and 2)*.

This page is intentionally left blank.

Chapter 6

Conclusions/Further work

The nonlinear elastic behaviour of the CPGC was modelled by a second order polynomial model whose material parameters were obtained through numerical fit of several hyperelastic constitutive equations to experimental simple uniaxial compression and volumetric data (see section 4.2.1). As discussed in section 4.3.1, simple FE models that simulate the confined and unconfined deformation experimental tests were modelled in order to evaluate the strain energy function response in the considered range of deformation.

In section 3.1, new formulations for modelling hysteresis based on a modified form of the pseudo-elastic theory were presented and discussed. The main aim of this approach was to describe the quasi-static loading-unloading process of the CPGC material during uniaxial and volumetric deformation cases, accounting separately energy dissipation mechanisms due to deviatoric and volumetric deformation processes. This theory was implemented in the nonlinear finite element code package ABAQUS®, via user subroutines (see section 4.3.2) allowing the reproduction of material hysteresis when submitted to loading-unloading cycles.

The results obtained with the proposed model allowed a good description of the hysteretic cycles for simple uniaxial compression and volumetric compression cases as can be seen in figures 4.70 and 4.73, respectively, considering total loading-unloading cycles.

The theory developed in this thesis for modelling hysteresis do not account the possibility of partial unloading (the material must be completely unloaded for the next deformation cycle) and consequent reloading. This aspect is intended to be treated in future modifications to the present theory, and for that, a new experimental methodology must be implemented in order to characterize the CPCC's mechanical response when internal loading-unloading cycles are applied. New models based on expressions (3.102) and (3.103), with the incorporation of internal variables calibrated for describing internal loading-unloading cycles must also be deduced.

In this work we also proposed also a thermomechanical model (see section 3.2) that,

in a fully-coupled thermomechanical form, model the heat build-up in the material, as consequence of the dissipated energy arise from the hysteretic cycles. The proposed model, as seen in figure 4.80, predicts the heat build-up in the material and its dependence with the frequency of mechanical solicitation. As expected, the heat build-up is maximum for the highest solicitation frequency ($f = 100Hz$) defined for the finite element analysis procedure.

As seen in section 4.2.2, *"virtual"* compression and volumetric curves can now be calculated for non-tested CPGC formulations based on experimental data through linear interpolation of hyperelastic material parameters. This procedure can have a great practical importance for the mechanical behaviour's prediction of untested CPGC formulations.

As discussed in section 4.3.1.2, an user's material subroutine *UHYPER was implemented in the finite element code ABAQUS® in order to improve the numerical fitting of the volumetric constitutive equation to experimental data, enabling a more versatile way in the modelling of highly nonlinear volumetric behaviour.

In section 5.1, as anatomically detailed human foot FE model was presented as a case-study related with comfort evaluation of CPCG's shoe insoles. This model intends to serve as a tool for future industrial projects, where CPGC's insoles are geometrically modified in order to enhance human comfort. The introduction of the foot ligamentar and muscular structure is predicted to be incorporated in future FE modelling works, in order to dynamically model the human gait. This work can have a great importance for the prediction of the stresses developed at both the bone structure and soft tissues during walking and consequently in the insole's optimization procedure.

The capability of modelling in a fully coupled thermomechanical form the loading-unloading mechanical response of the CPGC through the implemented finite element subroutines was demonstrated in the second practical case-study (see section 5.2), in which a CPGC's sample was submitted to complete loading-unloading cycles and the mechanical and thermal behaviour of the material monitored during the simulation time.

Bibliography

ABAQUS®. 2006. ABAQUS® Version 6.6 Documentation. Dassault Systémes.

Antunes, P.J., Dias, G.R., Coelho, A.T., Rebelo, F., & Pereira, T. 2008a. Hyperelastic Analysis of Cork-Polyurethane Gel Composites. *Pages 373–378 of:* Boukamel, A., Laiarinandrasana, L., Méo, S., & Verron, E. (eds), *Constitutive Models for Rubber V*. Taylor & Francis.

Antunes, P.J., Dias, G.R., Coelho, A.T., Rebelo, F., & Pereira, T. 2008b. Hyperelastic Modelling of Cork-Polyurethane Gel Composites: Non-linear FEA Implementation in 3D Foot Model. *Materials Science Forum*, **587-588**, 700–705.

Antunes, P.J., Dias, G.R., Coelho, A.T., Rebelo, F., & Pereira, T. 2008c. Nonlinear 3D foot FEA modeling from CT scan medical images. *Pages 135–141 of:* Tavares, João, & Natal, Jorge (eds), *Computational Vision and Medical Image Processing*. Taylor & Francis.

Arruda, Ellen M., & Boyce, Mary C. 1993. A Three-Dimensional Constitutive Model for the Large Stretch Behavior of Rubber Elastic Materials. *Journal of the Mechanics and Physics of Solids*, **41, No. 2**, 389–412.

Attard, M.M. 2004. Finite strain - isotropic hyperelasticity. *International Journal of Solids and Structures*, **40**, 4353–4378.

Banks, H.T., Pintér, G.A., & Potter, L.K. 1999. Modeling of Nonlinear Hysteresis in Elastomers under Uniaxial Tension. *Journal of Intelligent Materials Systems and Structures*, **10**, 116.

Belytschko, Ted, Liu, Wing Kam, & Moran, Brian. 2006. *Nonlinear Finite Elements for Continua and Structures*. West Sussex, England: John Wiley and Sons, Ltd.

Bergström, J.S., & Boyce, M.C. 1999. Constitutive Modeling fo the Large Strain Time-Dependent Behavior of Elastomers. *Journal of Mechanics Physics and Solids*, **46**, 931–354.

Bergström, J.S., & Boyce, M.C. 2000. Large strain time-dependent behavior of filled elastomers. *Mechanics of Materials*, **32**, 627–644.

Bilgili, Ecevit. 2004. Restricting the Hyperelastic Models for Elastomers Based on Some Thermodynamical, Mechanical, and Empirical Criteria. *Journal of Elastomers and Plastics*, **36**, 159–175.

Birke, J.A., Foto, J.G., & Pfiefer, L.A. 1999. Effect of Orthosis Material Hardness on Walking Pressure in High-Risk Diabetes Patients. *Journal of Prosthetics and Orthotics*, **11**, 43–46.

Blatz, P.J., & Ko, W.L. 1962. Application of Finite Elasticity Theory to the Deformations of Rubbery Materials. *Transactions of the Society of Rheology*, **VII**, 223–252.

Çengel, Yunus A., & Boles, Michael A. 1989. *Thermodynamics-An Engineering Approach.* New York, USA: McGraw-Hill International Editions.

Chen, W.P., F.T., Tang, & Ju, C.W. 2001. Stress Distribution of the foot during mid-stance to push-off in barefoot gait: a 3-D finite element analysis. *Clinical Biomechanics*, **16**, 614–620.

Cheung, J.T., & Zhang, M. 2005. A 3-Dimensional Finite Element Model of the Human Foot and Ankle for Insole Design. *Archives of Physical Medicine and Rehabilitation*, **86**, 353–358.

Cheung, J.T., & Zhang, M. 2006. Finite Element Modeling of the Human Foot and Footwear. *In: Proceedings of 19th Annual Worldwide ABAQUS Users Conference.*

Cheung, J.T., M., Zhang, Leung, A.K.L., & Y.B., Fan. 2005. Three Dimensional Analysis of the Foot During Standing - A Material Sensitivity Study. *Journal of Biomechanics*, **38**, 1045–1054.

Cheung, J.T., Zhang, M., & An, K. 2006. Effect of Achilles Tendon Loading on Plantar Fascia Tension in the Standing Foot. *Clinical Biomechanics*, **21**, 194–203.

Clough, Ray W., & Penzien, Joseph. 1993. *Dynamics of Structures.* New York, USA: McGraw-Hill International Editions.

Coveney, V.A., Johnson, D.E, Keavey, M.A., & Townsend, N. 2008. Time-dependent dilatational and multiaxial deviatoric behaviour of rubbery materials. *Pages 327–330 of:* Boukamel, A., Laiarinandrasana, L., Méo, S., & Verron, E. (eds), *Constitutive Models for Rubber V*. Taylor & Francis.

Diani, J., Brieu, M., Vacherand, J.-M., & Rezgui, A. 2004. Directional model for isotropic and anisotropic hyperelastic rubber-like materials. *Mechanics of Materials*, **36**, 313–321.

Dorfmann, A., & Ogden, R.W. 2003. A Pseudo-Elastic Model for Loading, Partial Unloading, and Reloading of Particle-Reinforced Rubber. *International Journal of Solids and Structures*, **40**, 2699–2714.

Dorfmann, A., & Ogden, R.W. 2004. A constitutive model for the Mullins effect with permanent set in particle-reinforced rubber. *International Journal of Solids and Structures*, **41**, 1855–1878.

Dorfmann, A., Fuller, K.N.G., & Ogden, R.W. 2003. Shear, compressive and dilatational response of rubberlike solids subject to cavitation damage. *International Journal of Solids and Structures*, **39**, 1845–1861.

Dunne, Fionn, & Petrinic, Nik. 2005. *Introduction to Computational Plasticity*. New York, USA: Oxford University Press.

Elías-Zúñiga, A. 2005. A phenomenological energy-based model to characterize stress-softening effect in elastomers. *Polymer*, **46**, 3496–3506.

Erdemir, A., Saucerman, J.J., Lemmon, D., Loppnow, B., Turso, B., Ulbrecht, J.S., & Cavanagh, P.R. 2005. Local plantar pressure relief in therapeutic footwear: design guidelines from finite element models. *Journal of Biomechanics*, **38**, 1798–1806.

Ferry, John D. 1980. *Viscoelastic Properties of Polymers*. New York, USA: John Wiley and Sons, Ltd.

Fu, Y.B., & Ogden, R.W. 2002. *Nonlinear Elasticity, Theory and Applications*. Cambridge, United Kingdom: Cambridge University Press.

Fung, Y.C. 1981. *Biomechanics: Mechanical Properties of Living Tissue*. New-York, USA: Springer.

Gefen, A. 2002. Stress Analysis of the Standing Foot Following Surgical Plantar Fascia Release. *Journal of Biomechanics*, **35**, 629–637.

Gefen, A. 2003. Plantar Soft Tissue Loading Under the Medial Metatarsals in the Standing Diabetic Foot. *Medical Engineering & Physics*, **25**, 491–499.

Gefen, A., Megido-Ravid, M., Itzchak, Y., & Arcan, M. 2000. Biomechanical Analysis of the Three-Dimensional Foot Structure During Gait: A Basic Tool for Clinical Applications. *Transactions of the ASME*, **122**, 630–639.

Gendy, A.S., & Saleeb, A.F. 2000. Nonlinear material parameter estimation for characterizing hyperelastic large strain models. *Computational Mechanics*, **25**, 66–77.

Gent, A.N. 1996. A New Constitutive Relation for Rubber. *Rubber Chemical Technology*, **59**, 59–61.

Holzapfel, Gerhard A. 2005. *Nonlinear Solid Mechanics*. London: John Wiley and Sons, Ltd.

Hsu, Yu-Chun, Gung, Yih-Wen, Shih, Shih-Liang, Feng, Chi-Kuang, Wei, Shun-Hwa, Chung-Huang, Yu, & Chen-Sheng, Chen. 2008. Using an Optimization Approach to Design an Insole for Lowering Plantar Fascia Stress A Finite Element Study. *Annals of Biomedical Engineering*, **36**(8), 1345–1352.

Incropera, Frank P., & DeWitt, David P. 1996. *Fundamentals of Heat and Mass Transfer*. Fourth edn. New York, USA: John Wiley and Sons, Ltd.

Itskov, M., & Askel, N. 2004. A class of orthotropic and transversely isotropic hyperelastic constitutive models based on a polyconvex strain energy function. *International Journal of Solids and Structures*, **41**, 3833–3848.

James, A.G., Green, A., & Simpson, G.M. 1975. Strain Energy Functions of Rubber. 1. Characterization of Gum Vulcanizates. *Journal of Applied Polymer Science*, **19**, 2033–2058.

Janninck, M.J., Ijzerman, M.J., Groothuis-Oudshoorn, K., Stewart, R.E., Groothoff, J.W., & Lankhorst, G.J. 2005. Use of Orthopedic Shoes in Patients with Degenerative Disorders of the Foot. *Archives of Physical Medicine and Rehabilitation*, **86**, 687–692.

Kaliske, M., & Rothert, H. 1998. Constitutive Approach to Rate-Independent Properties of Filled Elastomers. *International Journal of Solids and Structures*, **35**, 2057–2071.

Kamal, K. Kar, & Anil, K. Bhowmick. 1997. Hysteresis Loss in Filled Rubber Vulcanizates and Its Relationship with Heat Generation. *Journal of Applied Polymer Science*, **64**, 1541–1555.

Kilian, H. G. 1981. Equation of state of real networks. *Polymer*, **22**, 209–227.

Kilian, H. G., Enderle, H. F., & Unseld, K. 1986. The use of the van der Waals model to elucidate universal aspects of structure-property relationships in simply extended dry and swollen rubbers. *Colloid and Polymer Science*, **264**, 866–879.

Lemmon, D., Shiang, T.Y., Hashmi, A., Ulbrecht, J.S., & Cavanagh, P.R. 1997. The Effect of Shoe Insoles in Therapeutic Footwear - A Finite Element Approach. *Journal of Biomechanics*, **30**, 615–620.

Lin, Yeong-Jyh, & Hwang, Sheng-Jye. 2004. Temperature Prediction of rolling tires by computer simulation. *Mathematics and Computers in Simulation*, **67**, 235–249.

Lord, M., & Hosein, R. 1994. Pressure redistribution by molded inserts in diabetic footwear: A pilot study. *Journal of Rehabilitation Research and Development*, **31**, 214–221.

Marckmann, Gilles. 2004. *Contribution à l'Étude des Élastomèrs et des Membranes Soufflées*. Ph.D. thesis, Université de Nantes.

Marotta, E.E., LaFontant, S., McClafferty, D., Mazzuca, S., & Norley, J. 2002. The Effect of Interface Pressure on Thermal Joint Conductance for Flexible Graphite Materials: Analytical and Experimental Study. *In: ITherm2002 - Eighth Intersociety Conference on Thermal and Thermomechanical Phenomena in Electronic Systems*.

Mase, George E. 1970. *Schaum's Outline of Theory and Problems of Continuum Mechanics*. New York, USA: McGraw-Hill.

Merodio, José, Ogden, Ray W., & Saccomandi, Giuseppe. 2005 (16-19 August). *Innovative Applications of Rubber-Like Mechanics in Material Science and Biomechanics*. Summer Course of Cantabria's University.

Mills, N.J., & Gilchrist, A. 2000. Modelling the indentation of low density polymer foams. *Cellular Polymers*, **19**, 389–412.

MIMICS®. 2005. MIMICS® 9.1 Reference Guide. Materialise N.V.

Mooney, M.S. 1940. A theory of large elastic deformation. *Journal of Applied Physics*, **11**, 582–592.

Mueller, M.J., Sinacore, D.R., Hoogstrate, S., & Daly, L. 1994. Hip and ankle walking strategies:effect on peak plantar pressures and implications for neuropathic ulceration. *Archives of Physical Medicine and Rehabilitation*, **75**, 1196–1200.

Mullins, L. 1947. Effect of stretching on the properties of rubber. *Journal of Rubber Research*, **16**, 275–289.

Muralidharan, Vijayanand. 2002. *Large Deformation Isotropic Elasticity in the context of Rubberlike Solids*. Tech. rept. Cornell University.

Nakamura, S., Crowninshield, R.D., & R.R., Cooper. 1981. An Analysis of Soft Tissue Loading in the Foot: a preliminary report. *Bulletin of Prosthetics Research*, **18**, 27–34.

Nam, Tran Huu. 2004. *Mechanical properties of the composite material with elastomeric matrix reinforced by textile cords*. Ph.D. thesis, Technical University of Liberec.

Ogden, R.W. 1972a. Large deformation isotropic elasticity:on the correlation of theory and experiment for compressible rubberlike solids. *Proceedings of the Royal Society of London*, **A328**, 567–583.

Ogden, R.W. 1972b. Large deformation isotropic hyperelasticity: on the correlation of theory and experiment for incompressible rubberlike solids. *Proceedings of the Royal Society of London*, **A326**, 565–584.

Ogden, R.W. 2005. *Nonlinear Elastic Deformations*. London: Dover.

Ogden, R.W., & Roxburgh, D.G. 1999. A Pseudo-Elastic Model for the Mullins Effect in Filled Rubber. *Proceedings of the Royal Society of London*, **A455**, 2861–2877.

Ogden, R.W, Saccomandi, G., & Sgura, I. 2004. Fitting hyperelastic models to experimental data. *Computational Mechanics*.

Paige, Ryan E., & Mars, Will V. 2004. Implications of the Mullins Effect on the Stiffness of a Pre-loaded Rubber Component. *In: Abaqus User's Conference*.

Park, Dong Myung, Hong, Won Hi, Kim, Sang Goo, & Kim, Hwi Joong. 2000. Heat generation of filled rubber vulcanizates and its relationship with vulcanizate rubber structures. *European Polymer Journal*, **36**, 2429–2436.

Perry, J.E., Ulbrecht, J.S., Derr, J.A., & Cavanagh, P.R. 1995. The use of running shoes to reduce plantar pressure in patients who have diabetes. *The Journal of Bone and Joint Surgery*, **77**, 1819–1828.

Pucci, E., & Saccomandi, G. 2002. A note on the Gent model for rubber-like materials. *Rubber Chemistry and Technology*, **75**, 839–851.

Raspovic, A., Newcombe, L., Lloyd, J., & Dalton, E. 2000. Effect of customized insoles on vertical plantar pressures in sites of previous neuropathic ulcerations in the diabetic foot. *The Foot*, **10**, 133–138.

Rivlin, R.S. 1948. Large elastic deformations of isotropic materials. IV. Further developments of the general theory. *Philosophical Transactions of the Royal Society of London*, **A241**, 251–288.

Rivlin, R.S., & Saunders, D.W. 1951. Large elastic deformations of isotropic materials. VII. Experiments on the deformation of rubber. *Philosophical Transactions of the Royal Society of London*, **A243**, 251–288.

Saccomandi, Giuseppe. *Phenomenology of Rubber-Like Materials*. Tech. rept. Universitá di Lecce.

Shanti, J., & Mothiram, K. P. 1999. Three Dimensional Foot Modelling and Analysis of Stresses in Normal and Early Stage Hansen's Disease with Muscle Paralysis. *Journal of Rehabilitation Research & Development*, **36**.

Silva, S.P., Sabino, M.A., Fernandes, E.M., Correlo, V.M., Boesel, L.F., & Reis, R.L. 2005. Cork: properties, capabilities and applications. *International Materials Reviews*, **5**(6), 345–365.

Simkin, A. 1982. *Structural Analysis of the Human Foot in Standing Posture*. Ph.D. thesis, Tel Aviv University.

Treloar, L.R.G. 1975. *The physics of rubber elasticity*. Third edn. Oxford: Claredon Press.

Truesdell, Clifford, & Noll, Walter. 2004. *The Non-Linear Field Theories of Mechanics*. Third edn. Berlin, Germany: Springer.

Tsung, B.Y.S., Zhang, M., Mak, A.F.T., & Wong, M.W.N. 2004. Effectiveness of insoles on plantar redistribution. *Journal of Rehabilitation Research and Development*, **41**, 167–174.

Valanis, K.C., & Landel, R.F. 1967. The strain-energy function of a hyperelastic material in terms of extension ratios. *Journal of Applied Physics*, **38**, 2997–3002.

Varga, O.H. 1966. *Stress-strain behavior of elastic materials, Selected problems of large deformations*. New-York, USA: Wiley-Interscience.

Ward, I.M., & Hadley, D.W. 1996. *An Introduction to the Mechanical Properties of Solid Polymers*. West Sussex, England: John Wiley and Sons, Ltd.

Yeoh, O.H. 1990. Characterization of elastic properties of carbon-black-filled rubber vulcanizates. *Rubber Chemistry and Technology*, **63 No.5**, 792–805.

Zhang, M., & Mak, A.F.T. 1999. In vivo skin frictional properties. *Prosthetics and Orthotics International*, **23**, 135–141.